National Library
of Canada

Acquisitions and
Bibliographic Services Branch

395 Wellington Street
Ottawa, Ontario
K1A 0N4

Bibliothèque nationale
du Canada

Direction des acquisitions et
des services bibliographiques

395, rue Wellington
Ottawa (Ontario)
K1A 0N4

Your file Votre référence

Our file Notre référence

NOTICE

The quality of this microform is heavily dependent upon the quality of the original thesis submitted for microfilming. Every effort has been made to ensure the highest quality of reproduction possible.

If pages are missing, contact the university which granted the degree.

Some pages may have indistinct print especially if the original pages were typed with a poor typewriter ribbon or if the university sent us an inferior photocopy.

Reproduction in full or in part of this microform is governed by the Canadian Copyright Act, R.S.C. 1970, c. C-30, and subsequent amendments.

AVIS

La qualité de cette microforme dépend grandement de la qualité de la thèse soumise au microfilmage. Nous avons tout fait pour assurer une qualité supérieure de reproduction.

S'il manque des pages, veuillez communiquer avec l'université qui a conféré le grade.

La qualité d'impression de certaines pages peut laisser à désirer, surtout si les pages originales ont été dactylographiées à l'aide d'un ruban usé ou si l'université nous a fait parvenir une photocopie de qualité inférieure.

La reproduction, même partielle, de cette microforme est soumise à la Loi canadienne sur le droit d'auteur, SRC 1970, c. C-30, et ses amendements subséquents.

Canada

University of Alberta

ORIGIN OF BANDBROADENING ON A POROUS POLYMERIC HPLC PACKING

by ©

JINGYI LI

A thesis

submitted to the faculty of Graduate Studies and Research in partial fulfillment of the requirements for the degree of DOCTOR OF PHILOSOPHY

Department of Chemistry

Edmonton, Alberta

Fall, 1995

National Library of Canada
Acquisitions and Bibliographic Services Branch
395 Wellington Street
Ottawa, Ontario
K1A 0N4

Bibliothèque nationale du Canada
Direction des acquisitions et des services bibliographiques
395, rue Wellington
Ottawa (Ontario)
K1A 0N4

Your file Votre référence

Our file Notre référence

THE AUTHOR HAS GRANTED AN IRREVOCABLE NON-EXCLUSIVE LICENCE ALLOWING THE NATIONAL LIBRARY OF CANADA TO REPRODUCE, LOAN, DISTRIBUTE OR SELL COPIES OF HIS/HER THESIS BY ANY MEANS AND IN ANY FORM OR FORMAT, MAKING THIS THESIS AVAILABLE TO INTERESTED PERSONS.

L'AUTEUR A ACCORDE UNE LICENCE IRREVOCABLE ET NON EXCLUSIVE PERMETTANT A LA BIBLIOTHEQUE NATIONALE DU CANADA DE REPRODUIRE, PRETER, DISTRIBUER OU VENDRE DES COPIES DE SA THESE DE QUELQUE MANIERE ET SOUS QUELQUE FORME QUE CE SOIT POUR METTRE DES EXEMPLAIRES DE CETTE THESE A LA DISPOSITION DES PERSONNE INTERESSEES.

THE AUTHOR RETAINS OWNERSHIP OF THE COPYRIGHT IN HIS/HER THESIS. NEITHER THE THESIS NOR SUBSTANTIAL EXTRACTS FROM IT MAY BE PRINTED OR OTHERWISE REPRODUCED WITHOUT HIS/HER PERMISSION.

L'AUTEUR CONSERVE LA PROPRIETE DU DROIT D'AUTEUR QUI PROTEGE SA THESE. NI LA THESE NI DES EXTRAITS SUBSTANTIELS DE CELLE-CI NE DOIVENT ETRE IMPRIMES OU AUTREMENT REPRODUITS SANS SON AUTORISATION.

ISBN 0-612-06246-5

Canada

University Of Alberta

Library Release Form

Name Of Author:	JINGYI LI
Title of Thesis:	ORIGIN OF BANDBROADENING ON A POROUS POLYMERIC HPLC PACKING
Degree:	Doctor of Philosophy
Year this Degree Granted:	1995

Permission is hereby granted to the University of Alberta Library to reproduce single copies of this thesis and to lend or sell such copies for private, scholarly or scientific research purposes only.

The author reserves all other publication and other rights in association with the copyright in the thesis, and except as herein before provided, neither the thesis nor any substantial portion thereof may be printed or otherwise reproduced in any material form whatever without the author's prior written permission.

Jingyi Li

Wen Hua West Road
West Village 3122
Jinan, Shandong, P. R. China

Date: October 2, 1995

University of Alberta

Faculty of Graduate Studies and Research

The undersigned certify that they have read, and recommend to the Faculty of Graduate Studies and Research for acceptance, a thesis entitled ORIGIN OF BANDBROADENING ON A POROUS POLYMERIC HPLC PACKING submitted by JINGYI LI in partial fulfillment of the requirements for the degree of DOCTOR OF PHILOSOPHY.

F. F. Cantwell

Dr. F. F. Cantwell

Dr. N. J. Dovichi

Dr. L. Li

G R Loppnow

Dr. G.R. Loppnow

Daniel W Smith

Dr. D. W. Smith

Larry D Bowers

Dr. L. D. Bowers
(External Examiner)

This thesis is dedicated to my loving parents
Thank you for the opportunity, for the support, and for the understanding

Abstract

Hamilton PRP-1 is a commercially available, spherical microparticulate porous poly(styrene-divinylbenzene) with a 10μm diameter particle. It demonstrates greater chemical stability at pH of 1-13 than silica based packings. However, it produces broad asymmetric peaks for polyaromatic sample compounds. Slow intraparticle sorption is investigated as a possible cause using the aromatic compound naphthalene as sample in 85% MeOH/H_2O.

The intraparticle sorption rate measurements are made under the "infinite solution volume" condition by the shallow bed technique in which about a milligram of PRP-1 is used in a bed that is about 0.3 mm in height and 3 mm diameter. The sorption rate curve, a plot of moles sorbed in the bed *versus* time, is successfully fit to an empirical tri-exponential equation which contains three first order sorption rate constants k_1, k_2, k_3 and three pre-expoential parameters n_1, n_2 and n_3.

In the theoretical calculation of eluted peak shapes using the six constants, the chromatographic column is imagined to consist of three "hypothetical columns" placed in series. The shapes of the three separate peaks predicted to elute from each hypothetical column are calculated using a theoretical model. The overall theoretically predicted elution peak is obtained by mathematical convolution of the three hypothetical peaks. For comparison, the observed elution peaks are measured from an analytical HPLC column of PRP-1.

The good agreement between predicted and observed peaks demonstrates that slow intra-particle sorption is the major contribution to the excessive bandbroadening.

The nature of the slow intraparticle sorption is investigated by describing the sorption rate curve of naphthalene on PRP-1 with a monodisperse pore diffusion model (Crank) and a bidisperse pore diffusion model (Ruckenstein). The latter gives a better description of the overall sorption rate. The macropore and micropore effective diffusion

coefficients are calculated from the Ruckenstein model. Micropore diffusion is diffusion into the polymer matrix.

Hamilton PRP-∞, a nominally spherical nonporous poly(styrene-divinylbenzene) with 20μm diameter, might reasonable be expected to possess diffusion property similar to the matrix of PRP-1. The sorption rates of naphthalene on PRP-∞ are measured with the shallow bed technique and successfully fit to the Crank monodisperse model from which the micropore diffusion coefficient is calculated. Comparison of the diffusion coefficients of naphthalene in the matrices of PRP-1 and PRP-∞ suggests that diffusion in the former is much more hindered because of smaller size of the micropores. A hydrodynamic model is used to calculate the sizes of micropores in both PRP-1 and PRP-∞ using the experimentally measured diffusion coefficients. It shows that the two PS-DVB packings have a very similar micropore size. A slight decrease in sizes of the micropores causes a significant decrease in the micropore diffusion coefficient.

The sorption isotherms of naphthalene on PRP-1 and PRP-∞ are also studied by the "column equilibrium method" using the shallow bed apparatus. The high sorption amount suggests that naphthalene penetrates into the micropores in PRP-∞.

Acknowledgments

I would like to thank my research supervisor, Dr. Cantwell, for his invaluable guidance and help through the course of the research presented in this thesis. I would also like to thank David Gowanlock who wrote the computer programs used in the calculations, and to Dr. Jordan, Dr McClung and Dr. Horlick for their help in allowing the use of a computer program and the Lab-NB data acquisition board. Many thanks to the staff of the Machine Shop in the Chemistry department for making the shallow bed apparatus.

Finally, I would like to thank the Department of Chemistry at University of Alberta for financial assistance.

Table of Contents

Chapter Page

Chapter 1 Introduction

1.1 High Performance Liquid Chromatography on Poly (styrene-diviylbenzene) 1

1.2 Background to the Bandbroadening on PS-DVB 5

1.3 Scope of the Present Work 8

Chapter 2 Experimental Section

2.1 Introduction 11

2.2 Sorbents 11

2.3 Chemicals 12

2.4 Sample and Eluent Solutions 12

2.5 Sorption Rate Measurement 14

2.5.1 Apparatus 14

2.5.2 A Switching Valve to Control the Exposure Time 17

2.5.3 Shunting off Flow When the Shallow Bed is being Pulled from One Position to the Other 18

2.5.4 The Slider Valve 19

2.5.5 Procedures 21

2.6 The Hold-up Volume Measurement 22

2.7 Injector Loop Calibration 25

2.8 Naphthalene Sorption Isotherm Measurement 25

2.9 Elution Chromatography 26

2.10 Extra-Column Bandbroadening 30

Chapter Page

Chapter 3 **Naphthalene Sorption Isotherms**

3.1 Introduction 35

3.2 Theory 35

3.3 Measurement of the Isotherms 40

3.4 Principle of the Column Equilibriation Method 44

3.5 Results and Discussion 45

3.5.1 Hold-up Volume for Naphthalene on PRP-1 45

3.5.2 Hold-up Volume for Naphthalene on PRP-∞ 46

3.5.3 Naphthalene Sorption Isotherm on PRP-1 46

3.5.4 Naphthalene Sorption Isotherm on PRP-∞ 51

Chapter 4 **Naphthalene Sorption Kinetics**

4.1 Introduction 59

4.2 Theory 60

4.2.1 Film Diffusion 60

4.2.2 Intraparticle Diffusion 61

4.2.3 Adsorption onto the Surface of the Pore Walls 62

4.2.4 The Shallow Bed Theory 62

4.2.5 Empirical Tri-exponential Equation 67

4.3 Measurement of the Sorption Rates 68

4.4 Results and Discussion 73

4.4.1 Testing Switching Valve,V2, to Control the Exposure Times 73

4.4.2 Shunting off the Sample Flow Through the Bed 76

4.4.3 Testing Shallow Bed Conditions in PRP-1 77

4.4.4 Sorption Rate Curves of Naphthalene on PRP-1 80

Chapter Page

Chapter 5 Prediction of the Elution Peaks from the Sorption Rate Curves

5.1 Introduction 91

5.2 Theory 92

5.2.1 Bandbroadening Processes in Liquid Chromatography 92

5.2.1.1 Longitudinal Diffusion 93

5.2.1.2 Eddy Diffusion 94

5.2.1.3 Resistance to Mass Transfer in the Mobile Phase 95

5.2.1.4 Coupling of the Eddy and the Lateral Diffusion Term 96

5.2.1.5 Resistance to Mass Transfer in the Stagnant Mobile Phase 97

5.2.1.6 Resistance to Mass Transfer in the Stationary Phase 98

5.2.1.7 Overall Column Bandbroadening 99

5.2.1.8 Extra-Column Bandbroadening 100

5.2.1.9 Total Plate Height 100

5.2.1.10 Concentration Overload Bandbroadening 101

5.2.1.11 Slow Kinetic Processes 102

5.2.2 Predicting Peaks from the Sorption Rate Curves 103

5.2.2.1 Selection of experimental conditions 104

5.2.2.2 Models of the Elution Chromatographic Profiles 106

5.2.2.3 Overall Predicted Peak from the Individual

Chapter Page

Contributions Using Mathematical Convolution 110

5.2.3 Characterization of the Elution Profiles 114

5.2.3.1 Statistical Moment Analysis of Chromatographic Peaks 114

5.2.3.2 Characteristics of Kinetic Effects 119

5.3 Results and Discussion 120

5.3.1 Extra-Column Bandbroadening 121

5.3.2 Concentration Overload Bandbroadening 127

5.3.3 Axial Dispersion and Non-Uniform Flow Pattern 136

5.3.4 The Elution Chromatograms of Naphthalene on PRP-1 142

5.3.5 Predicted Elution Peaks from the Sorption Rate Curves of Naphthalene on PRP-1 145

5.3.6 Comparison of the Predicted and the Observed Elution Profiles on PRP-1 155

5.3.7 The Plate Height in the Stagnant Mobile Phase from Giddings' Equation 167

5.3.8 Kinetic Tailing 171

5.3.9 Criteria for Selecting a Correct Combination of n_3 and k_3 for the Predicted Peaks 175

Chapter 6 Origin of Bandbroadening of Naphthalene on PRP-1

6.1 Introduction 183

6.2 Theory 185

6.2.1 Isothermal Macropore Diffusion Control (Crank Model) 185

6.2.2 Isothermal Micropore Diffusion Control (Crank Model) 187

6.2.3 Bidisperse Pore Diffusion Control (Ruckenstein Model) 188

Chapter Page

6.2.4 Comparison of Different Kinetic Equations 190

6.2.5 Hydrodynamic Theory for Hindered Diffusion 191

6.2.5.1 Introduction 191

6.2.5.2 Basic Assumptions 192

6.2.5.3 Physical Picture for a Rigid Spherical Uncharged Solute in a Cylindrical Pore 193

6.2.5.4 Hydrodynamic Coefficient, K^{-1}, in the Hydrodynamic Model 195

6.3 Results and Discussion 195

6.3.1 Intraparticle Monodisperse Pore Diffusion Model (Crank Model) for Naphthalene on PRP-1 195

6.3.2 Intraparticle Bidisperse Pore Diffusion Model (Ruckenstein Model) for Naphthalene on PRP-1 199

6.3.3 Comparison of Different Kinetic Models for Naphthalene on PRP-1 203

6.3.4 Calculation of the Diffusion Coefficient, D_m, of Naphthalene in the Bulk Solution 204

6.3.5 Effective Diffusion Coefficients of Naphthalene in the Macropores and Micropores of PRP-1 204

6.3.6 Sorption Rate Curves of Naphthalene on PRP-∞ 210

6.3.6.1 Testing the Shallow Bed Condition in PRP-∞ 210

6.3.6.2 Intraparticle Monodisperse Pore Diffusion Model (Crank Model) for Naphthalene on PRP-∞ 214

6.3.6.3 The Empirical Tri-exponential Equation for Naphthalene on PRP-∞ 214

6.3.6.4 Simplified Rate Law and the Empirical

Tri-exponential Equation 220
6.3.6.5 Intraparticle Diffusion Model Based on Linear Driving Force (Mono-exponential Equation) 225
6.3.6.6 Comparison of Different Kinetic Models for Naphthalene on PRP-∞ 227
6.3.6.7 Effective Diffusion Coefficient of Naphthalene in the Micropores of PRP-∞ 227
6.3.7 Hydrodynamic Model for the Hindered Diffusion of Naphthalene in the Micropores of PRP-∞ 229
6.3.8 Comparison of the Diffusion Coefficients in the Micropores of PRP-1 and PRP-∞ 232
6.3.9 Comparison of the Sorption Isotherms of Naphthalene on PRP-1 and PRP-∞ 239

Chapter 7 Conclusions and Future Work

7.1 Conclusions 240
7.2 Future Work 243

****

BIBLIOGRAPHY 244
APPENDIX 1 The program used in the tri-exponential fit to the sorption rate data 253
APPENDIX 2 The program used in the calculation of the predicted peaks 264
APPENDIX 3 The program used in the EMG curve fit 270
APPENDIX 4 The program used to fit the sorption rate of naphthalene

List of Tables

Table Page

2.1 The features of the shallow beds of PRP-1 and PRP-∞ in the sorption rate measurement 15

3.1 Experimental parameters for the measurement of the hold-up volume in the shallow bed of PRP-1 47

3.2 The areas, A_{bed}, from injection onto the shallow bed of PRP-1 and the areas, A_{inj}, from the injector 48

3.3 Experimental parameters for the measurement of the hold-up volume in the shallow bed of PRP-∞ 49

3.4 The areas, A_{bed}, from injection onto the shallow bed of PRP-∞ and the areas from the injector, A_{inj}. 50

3.5 Experimental parameters in the measurement of the sorption isotherm of naphthalene onto PRP-1 52

3.6 The data of the sorption isotherm of naphthalene on PRP-1 54

3.7 Experimental parameters in the measurement of the sorption isotherm of naphthalene onto PRP-∞ 56

3.8 The data of the sorption isotherm of naphthalene on PRP-∞ 58

4.1 The blank amount of phloroglucinol on PRP-1 at different times with valve V2 closed 74

4.2 The amount of phloroglucinol in a bed of PRP-1 at times less than 2 seconds 75

4.3a The dependence of flow rate, F2, through the dummy hole on the position of V3. The shallow bed was placed in the sample loading 78

4.3b The dependence of flow rate, F2, through the shallow bed on the position of V3. The shallow bed was placed in the sample elution 79

Table Page

4.4 Experimental parameters in the measurement of the shallow bed condition in the bed of PRP-1 81

4.5 Dependence of the initial sorption rates of naphthalene on the interstitial linear velocity through the shallow bed of PRP-1 82

4.6 Constants from the tri-exponential equation describing four separate sorption rate curves of naphthalene on a shallow bed of PRP-1 87

5.1 The non-interacting fraction $P_i'(t_s)$ at the four mobile phase linear velocities for run 1 115

5.2 Experimental parameters in the collection of the elution profiles of phloroglucinol from the extra-column components 122

5.3 The variance from the extra-column components for phloroglucinol and the total variances for naphthalene in a column of PRP-1 at four mobile phase linear velocities 125

5.4 The dependence of capacity factors on the concentrations of naphthalene in a column of PRP-1 130

5.5 The experimental parameters in the collection of the elution profiles of naphthalene in a column of PRP-1 132

5.6 The dependence of the plate heights on the concentrations of naphthalene in a column of PRP-1 134

5.7 The experimental parameters in the collection of the elution profiles of phloroglucinol in a column of PRP-1 138

5.8 The baseline setting in the measurement of the first moments of phloroglucinol peaks 140

5.9 The first and second moments of phloroglucinol peaks in a column of PRP-1 141

Table Page

5.10 Chromatographic figures of merit for the observed naphthalene peaks in a column of PRP-1 144

5.11 The capacity factors for naphthalene peaks in a column of PRP-1 at the four mobile phase linear velocities 147

5.12 Chromatographic figures of merit for the predicted elution profiles of naphthalene in a column of PRP-1 151

5.13 The predicted plate heights at four mobile phase linear velocities 153

5.14 The asymmetry factors calculated at 10% of the peak height for the predicted peaks of naphthalene on PRP-1 154

5.15 The relative differences in the figures of merit between the observed and the predicted peaks 161

5.16 The observed plate heights at the four mobile phase linear velocities 169

5.17 Comparison of the predicted, observed and the theoretical ($\overline{H}_{sm}$) plate heights 170

5.18 The asymmetry factors calculated at 10% of the peak heights for the observed peaks of naphthalene on PRP-1 172

5.19 The dependence of the kinetic characteristic of a tailed peak on the mobile phase linear velocity 173

5.20 The parameters used in the calculation of the kinetic characteristics for a tailed peak 174

5.21 The effects of the estimated input values of n_3 and k_3 on the observed values of n_3 and k_3 values 176

Table		Page
5.22	The values of n_0 and n_3 for the four runs with small error norms	182
6.1	The parameters from the Ruckenstein bidisperse pore diffusion model for the sorption of naphthalene on PRP-1	202
6.2	Comparison of different models for the sorption rate curves of naphthalene on a shallow bed of PRP-1	205
6.3	The macropore and the micropore effective diffusion coefficients for naphthalene in PRP-1	207
6.4	Dependence of the micropore effective diffusion coefficient for naphthalene in PRP-1 on the estimated radii of the microshperes	209
6.5	Experimental parameters in the measurement of the shallow bed condition in a bed of PRP-∞	211
6.6	Dependence of the initial sorption rates of naphthalene on interstitial linear velocity of a solution through the shallow bed of PRP-∞	213
6.7	Micropore effective diffusion coefficients and the sorption amount at equilibrium from Crank model for naphthalene on PRP-∞	219
6.8	Constants from the tri-exponential fit for naphthalene sorption rate curve on a shallow bed of PRP-∞	223
6.9	Comparison of different models for sorption rate curves of naphthalene on a shallow bed of PRP-∞	228
6.10	Dependence of hindrance diffusion coefficients, Di, on the values of λ and K	231
6.11	The parameters used in the estimation of micropore diffusion coefficients for naphthalene on PRP-1 and PRP-∞	234
6.12	The dependence of the micropore diffusion coefficients and of the micropore sizes on the microsphere radius in PRP-1	236

List of Figures

Figure		Page
2.1	Schematic diagram of synthesis of poly(styrene-divinylbenzene)	13
2.2	Schematic diagram of apparatus used in the measurement of the sorption rate	16
2.3	Schematic diagram of the slider valve	20
2.4	Schematic diagram of the whole shallow bed apparatus	22
2.5	Schematic diagram showing the sequence of positions of the slider	24
2.6	Schematic diagram of apparatus used in the collection of the experimental elution profiles	27
2.7	Chromatograms of phloroglucinol on a column of PRP-1 at a mobile phase linear velocity of 0.3 cm/s	29
2.8	Chromatograms of 4.688 x 10^{-5} M naphthalene on a column of PRP-1 at a mobile phase linear velocity of 0.3 cm/s	30
2.9	Chromatograms of 4.688 x 10^{-3} M naphthalene on a column of PRP-1 at a mobile phase linear velocity of 0.1 cm/s	32
2.10	Chromatogram of 3.135 x10-5 M naphthalene on a column of PRP-1 at a mobile phase linear velocity of 0.4 cm/s	33
2.11	Schematic diagram of apparatus used in the measurement of the extra-column bandbroadening	34
3.1	A typical sorption isotherm	38
3.2	Shapes of common sorption isotherms and the corresponding elution peaks in chromatography	39
3.3	A breakthrough curve	42
3.4	Frontal chromatograms	43
3.5	Naphthalene sorption isotherm on PRP-1 fit to Langmuir equation	53

Figure Page

3.6 The linear part of the naphthalene sorption isotherm on PRP-1 55

3.7 Naphthalene sorption isotherm on PRP-∞ 57

4.1 Schematic diagram showing some possible kinetic processes in a porous particle 61

4.2 Diagrammatic sorption rate curve 66

4.3 Testing the shallow bed condition in PRP-1 83

4.4 Sorption rate curve of run 1 and the three exponential components for naphthalene on PRP-1 86

4.5 Sorption rate curve of run 2 for naphthalene on PRP-1 88

4.6 Sorption rate curve of run 3 for naphthalene on PRP-1 89

4.7 Sorption rate curve of run 4 for naphthalene on PRP-1 90

5.1 Schematic diagram of a tailed peak and its component tail and a Gaussian portions 105

5.2 Schematic diagram of convolution of two impulse response functions 111

5.3 Approach in predicating of an elution peak using convolution 113

5.4 Chromatograms of phloroglucinol from the extra-column components 124

5.5 The predicted peaks of naphthalene with and without correction by the extra-column bandbroadening 126

5.6 The dependence of capacity factors on the concentrations of naphthalene in a column of PRP-1 129

5.7 The plate heights of naphthalene on PRP-1 as a function of the concentrations 133

5.8 Chromatograms of 4.688 x 10^{-3} M and 3.135 x 10^{-5} M naphthalene on a column of PRP-1 135

5.9 Elution profiles of phloroglucinol on a column of PRP-1 139

Figure Page

5.10 EMG fits of the elution profiles of 3.135×10^{-5} M naphthalene on PRP-1 143

5.11 The observed plate heights of 3.135×10^{-5} M naphthalene on a column of PRP-1 as a function of the mobile phase linear velocity 146

5.12 The predicted profiles from four replicate sorption rate measurements for naphthalene on PRP-1 at $\overline{U}_0$ of 0.3 cm/s 148

5.13 The EMG fits of the predicted profiles from the four replicate sorption rate measurements for naphthalene on PRP-1 at $\overline{U}_0$ of 0.3 cm/s 149

5.14 The plate heights of the predicted peaks as a function of the mobile phase linear velocities for naphthalene on PRP-1 152

5.15 The predicted profiles from run 1 and the observed peaks at four mobile phase linear velocities 156

5.16 The predicted profiles from run 2 and the observed peaks at four mobile phase linear velocities 157

5.17 The predicted profiles from run 3 and the observed peaks at four mobile phase linear velocities 158

5.18 The predicted profiles from run 4 and the observed peaks at four mobile phase linear velocities 159

5.19 The non-scaled probability distributions of P1, P2 and P3 163

5.20 The probability distribution P1 and the observed predicted peak 164

5.21 The probability distribution P2 and the observed predicted peak 165

5.22 The probability distribution P1_2 and the observed predicted peak 166

5.23 The observed and predicted plate heights as a function of the mobile phase linear velocity for naphthalene on PRP-1 168

Figure | Page

5.24 Two tri-exponential fits resulting from different input values of n_3 and k_3 177

5.25 Predicted elution profiles calculated from two tri-exponential fits from Figure 5.25 179

5.26 Two predicted peaks calculated using two similar sets of n_3 and k_3 181

6.1 Schematic diagram of a bidisperse sorbent particle consisting of macrospheres and microspheres 189

6.2 Schematic diagram of a spherical solute in a cylindrical pore 194

6.3 The experimental sorption rate data for naphthalene on PRP-1 fit to the Crank model with a single diffusion coefficient 197

6.4 The linearized version of the Crank model for naphthalene on PRP-1 198

6.5 The sorption rate curve of naphthalene on PRP-1 fit to Ruckenstein model and the two components 201

6.6 Testing the shallow bed condition in PRP-∞ 212

6.7 The sorption rate curve from run 1 fit to Crank model for naphthalene on PRP-∞ 215

6.8 The linearized version of the Crank model for naphthalene on PRP-∞ 216

6.9 The sorption rate curve from run 2 fit to Crank model for naphthalene on PRP-∞ 217

6.10 The sorption rate curve from run 3 fit to Crank model for naphthalene on PRP-∞ 218

6.11 The sorption rate curve from run 1 fit to tri-exponential equation for naphthalene on PRP-∞ 220

6.12 The sorption rate curve from run 2 fit to tri-exponential equation

Figure Page

for naphthalene on PRP-∞ 221

6.13 The sorption rate curve from run 3 fit to tri-exponential equation for naphthalene on PRP-∞ 222

6.14 The sorption rate curve fit to a mono-exponential equation for naphthalene on PRP-∞ 226

6.15 The sorption rates of naphthalene in 85% MeOH/H_2O in the micropores of PRP-∞ and PRP-1 235

6.16 The sorption isotherms of naphthalene on PRP-1 and PRP-∞ 239

List of Symbols

a	Constant in the Langmuir equation
a_G	Area of a Gaussian peak
a_T	Area of a tail
A	Pre-exponential factor in EMG function in Chapter 5
A	Constant in the van Deemter equation (mm)
$A_{hold\text{-}up\text{-}T}$	Area of peak of an unretained compound in the shallow bed
A_{inj}	Area of peak of an unretained compound in the injector loop of valve 4
A.F.	Asymmetry factor of a peak
b	Constant in the Langmuir equation
B	Constant associated with Longitudinal diffusion in the van Deemter equation (s^{-1})
C	Concentration of a sample collected in the calibration of injector loop in valve 4 (Mol/L)
$C_{i,m}$	Sample concentration in the mobile phase for compound i (Mol/L)
$C_{i,s}$	Sample concentration in the stationary phase for compound i (Mol/g)
C_m	Sample concentration in the mobile phase (Mol/L)
C_s	Sample concentration in the stationary phase (Mol/g)
C_0, C_L	Solute concentrations at a pore entrance and exit in chapter 6 (Mol/L)
C_0	Initial concentration of a sample in the mobile phase (Mol/L)
$\langle C_0 \rangle, \langle CL \rangle$	Average concentration of a solute at a pore entrance and exit (Mol/L)
$\overline{C}$	Mean value of internal concentration in a particle (Mol/L)
D_a	Macropore diffusion coefficient (cm^2/s)
$D_{a,eff}$	Effective diffusion coefficient in the macropores (cm^2/s)
D_i	Micropore diffusion coefficient (cm^2/s)

$D_{i,eff}$	Effective diffusion coefficient in the micropores (cm^2/s)
$C_{convolve}$	Convolution of any functions
D_{eff}	Effective diffusion coefficient in chapter 6
D_m	Diffusion coefficient in the mobile phase
d_p	Particle diameter (cm)
E	Potential energy for a solute in a pore (J)
f	Ratio of intraparticle porosity to the total porosity in chapter 5
f_∞, f	Molecular friction coefficients in the mobile phase and in the pores in chapter 6
f1, f2	Any function describing signal and time profiles
F	Flow rate through the shallow bed (ml/min)
h_{EMG}	Height of an exponentially modified Gaussian signal
h_G	Peak height of a parent Gaussian peak
h_T	Peak height of a tailed peak
EMG	Exponentially Modified Gaussian
$\overline{H}j$	Plate height associated with the jth kinetic process (mm)
$\overline{H}$	Average plate height (mm)
$\overline{H}_{Eddy}$	Plate heights associated with Eddy diffusion (mm)
$\overline{H}_{LD}$	Plate height associated with Longitudinal diffusion
$\overline{H}m$	Plate height associated with the resistance to mass transfer in the mobile phase (mm)
$\overline{H}sm$	Plate height associated with the resistance to mass transfer in the stagnant mobile phase (mm)
$\overline{H}s$	Plate height associated with the adsorption on the surface of the stationary phase (mm)
K '	Capacity factor
K_D	Distribution coefficient for a component (L/g)

$K_i^{'}$	Capacity factor associated with the ith hypothetical sorption sites
$k_{a,i}$, $k_{d,i}$	Adsorption and desorption rate constants for species i
k_r, k_f	Forward and reverse rate constants
$K_{a,D}$	Distribution coefficient in macropores (L/g)
$K_{i,D}$	Distribution coefficient in micropores (L/g)
K^{-1}	Hydrodynamic coefficient in chapter 6
L	Length of a column (cm)
M_0, M_1, M_2	The zero, first and second moments
M_b	Solute molar mass (g/Mole)
n_0	Number of moles sorbed at equilibrium in the tri-exponential equation
n_1, n_2, n_3	Number of moles sorbed in each hypothetical sites in the tri-exponential equation
N_{Elu}	Number of moles eluted from the shallow bed (Mol/g)
N_{sorb}	Number of moles sorbed on a sorbent in the shallow bed (Mol/g)
N	Plate number
$P_i^{'}$ (ts)	Probability associated with fraction of molecules not interacting with the ith hypothetical sorption sites
P_i (ts)	Probability associated with fraction of molecules interacting with the ith hypothetical sorption sites
$Q_{a,t}$	The amount of a solute sorbed in the stationary phase in the macropores (Mol/g) at time t
$Q_{a,\infty}$	The amount of a solute sorbed in the macropores at equilibrium (Mol/g)
$Q_{i,t}$	The amount of a solute sorbed in the micropores (Mol/g) at time t
$Q_{i,\infty}$	The amount of a solute sorbed in the micropores at equilibrium (Mol/g)
Q_{Ave}	Average amount of a solute sorbed in the stationary phase (Mol/g)
Q_0	Amount of a solute in the mobile phase at time zero (Mol/g)
R	Fraction of molecules in the mobile phase in chapter 3

R	Radius of a particle in chapter 6 (cm)
R_a	Radius of a macrosphere (i.e. of the paticle) (cm)
R_i	Radius of a microsphere (cm)
R	Gas constant in chapter 6 J mol^{-1} K^{-1}
R'	Equilibrium constant for instantaneous sorption
r	Radius of the shallow bed (cm)
r_0	Radius of a pore in chapter 6 (cm)
r_s	Radius of a solute in chapter 6 (cm)
t_a	Time a solute spends in macropores (s)
t_c	Center gravity of a profile (s)
t_i	Time a solute spends in micropores (s)
t_D	The time that diffusion occurs (s)
t_G	Retention time of the parent Gaussian peak (s)
t_m	The retention time of an unretained compound (s)
t_R	Retention time of a retained compound (s)
T	Temperature (K)
$\overline{U}$	Interstitial linear velocity through the shallow bed (cm/s)
$\overline{U}_i$	Average linear velocity of an unretained compound (cm/s)
$\overline{U}_0$	Mobile phase linear velocity (cm/s)
$V_{hold-up}$	Actual hold up volume of the shallow bed itself (ml)
$V_{hold-up-T}$	Total hold up volume in the shallow bed (ml)
V	Volume of a mixing or diffusion chamber (ml)
V_S	Volume of a stationary phase (ml)
V_{inj}	Volume of the injector loop in valve 4 (ml)
V_p	Pore volume for PRP-1 (cm^3/g)
V_m	Intra and interparticle volume (ml)
V_G	Retention volume of the parent Gaussian peak (ml)

$V\tau$	Characteristic volume of the exponential tail of a peak (ml)
Va	Molecular volume of naphthalene in chapter 6 (ml/Mole)
X	The distance a sample travels in a column (cm)
Z	Variable in EMG function in chapter 5
α	Constant in the bidisperse pore distribution model
β	Constant in the bidisperse pore distribution model
λ	Ratio of a solute radius to a pore radius
λ'	Hinderance factor in the macropores
ε	Fractional pore volume
ε_a	Fraction of macropore volume
ε_i	Fraction of micropore volume
Φ	Partition or distribution coefficient in chapter 6
$\delta (t_s)$	Delta function
γ	Constant in the bidisperse pore distribution model
γ'	Obstruction factor in a pore
η	Viscosity of a solvent (cp)
ψ	Solvent association factor
λ	Packing parameter
ω	Packing parameter
τ	Characteristic time of the exponential tail of an EMG function (s)
ρ_a	Density of a particle matrix (cm^3/g)
ρ_i	Density of a microsphere matrix (cm^3/g)
σ_x^2	Variance of an elution peak in unit of distance (cm^2)
$\sigma_{x,j}^2$	Variance associated with the jth kinetic process (cm^2)
σ_G^2	Variance of the parent Gaussian part of an EMG function (ml^2)
$\sigma_{V,G}^2$	Variance of the parent Gaussian part of an EMG function in volume unit (ml^2)

σ_t^2	Variance of an elution peak from EMG in time unit (s^2)
σ_T'	Tail length in chapter 5 (s)
θ	Tortuosity

Chapter 1

Introduction

1.1 High Performance Liquid Chromatography on Poly (styrene-divinylbenzene)

Reversed-Phase High Performance Liquid Chromatography (RP-HPLC) has become a broadly applicable and valuable analytical tool for scientists in diverse fields. It is estimated that more than 80% of HPLC applications are performed using a reversed-phase mode where a nonpolar stationary phase and a polar mobile phase are used [1]. The separation process occurs as the sample molecules distribute themselves between the stationary phase and the mobile phase. RP-HPLC is generally performed with a porous silica which is modified by chemically covalently bonding different organic alkyl groups with or without polar functional groups to its surface [2].

Silica-based stationary phases have excellent mechanical strength compared with liquid-liquid chromatography based on mechanically held stationary liquids. Among their advantages are good mass transfer properties in microparticulate packings which produces a narrow and symmetric peak, a variety of pore sizes, narrow particle size distributions, and widely available reagents to modify the silica surface [3, 4].

Although silica based packings provide these ideal characteristics, problems inherent in the silica support materials present limitations. First of all, the silica support matrix is not completely inert even after the silica surfaces are covered by a layer of organic groups and end-caped with a smaller silylating reagent, such as trimethychlorosilane. There are unreacted acidic silanol groups which are accessible to the sample and the mobile phase. These residual silanol groups can act as polar groups and acidic catalysts which can react with polar and basic samples. Amines show poor peak symmetry due to the acidity of the silanol groups [5-8]. Charged molecules also show tailing due to the polar interactions.

In addition, proteins have poor recovery due to interactions with the silanol groups [9]. Secondly, the pH range over which the silica bonded reversed phases are stable is between 2 and 7.5. Eluents of extremely low pH (< 2) attack the Si-C bonds, whereas highly basic solvents (pH> 8) lead to dissolution of the Si-O-Si silica matrix. Thus, ion suppression methods can not be employed with sample solutes having a pKa less than 2 and greater then 7. However, in order to get a high column efficiency, good selectivity and detection sensitivity in the separation of some biological compounds, either high or low pH, is required [2,3]. Thirdly, after gradient elution, silica-based columns may require some time to re-estabilish equilibrium before the next run [10].

Numerous attempts have been made to improve pH stability of silica based columns, including the use of bulk silane reagents and coating of polymers on the surface, but these materials still do not have the pH stability associated with polymer-based supports. Although there have been many recent reports on HPLC properties of more pH stable inorganic supports, such as zirconia [11] and alumina [12], these supports are not yet available in the same wide range of particle sizes and pore sizes as the silica gel and the polymer resins.

In order to circumvent these problems associated with silica base-bonded phases, an alternate family of RP supports, organic polymer materials, are used. One common organic polymer is poly (styrene-divinylbenzene) (PS-DVB).

Two types of polymeric structures, microporous and macroporous polymers, have been used in modern liquid chromatography [13]. "Microporous polymers" (sometimes called gels) are cross-linked copolymers in which the porosity is determined by the amount of crosslinking monomer, divinylbenzene. The lower the crosslinking, the larger the porosity, but the softer the resultant product. Low crosslinked polymers are usually not sufficiently rigid to be used in high pressure LC. These materials are still commercially available for low and medium pressure permeation chromatography and liquid chromatography.

The other type is macroporous polymers. In 1964, Moore [14] first synthesized a macroporous poly (styrene-divinylbenzene) copolymer with a high percentage of cross-linker, divinylbenzene. The macroporous polymer is usually synthesized by suspension polymerization in the presence of a "porogen", a compound which is soluble in monomers, but insoluble in the polymer. Upon polymerization, the inert porogen will intersperse and occupy a large part of the particle volume. After removing the porogen, rigid, spherical macroporous sorbent particles having relatively high specific surface area and aromatic hydrocarbonaceous surface are obtained [15].

Commercially available polystyrene-based microparticulate packings for RP chromatography include PRP-1 [16] (Hamilton, Reno, NV, USA) and PLRP-S [17] (Polymer Laboratories, Church Stretton, U.K.)

Although a wide range of compounds has been examined on PS-DVB columns, there has been an emphasis on separation of relatively polar samples, including alkyl substituted phenols, substituted benzoic acids and carboxylic acids, organic anions, amines, anilines and phenylalcohols. These separations were of particular interest because the surface of the polymer is free from silanol interactions, so that, tailing with polar samples, especially amines, was greatly reduced [18]. The polymer columns were also used for separation of less polar samples, including substituted benzenes, polyethers and polyaromatic compounds [19, 20]. The performance and retention characteristics for a variety of hydrocarbons, including a variety of shapes, sizes, rigidity and aromatic planarities have been studied on PS-DVB [21].

PS-DVB not only has the requirements which a reversed-phase must meet, such as mechanical stability at high pressure, chemical inertness toward chromatographic solvents and solutes, and narrow particle size distributions, but in addition, PS-DVB packings offer distinct advantages over silica packings for particular applications where chemical stability under extreme pH conditions are required [13]. The tolerance to extreme mobile phase pH allows selective chromatography of strong acids and bases. Therefore, enhanced detection sensitivity for protic samples and exceptional mobile phase selectivity are obtained. PS-DVB as a reversed-phase sorbent has been studied under a variety of mobile phase conditions, including pH [16, 22], electrolyte concentration [22, 23], and mobile phase modifiers [23-25].

Another advantage of PS-DVB is that the phenyl rings can be functionalized with a variety of organic moieties. The surface characteristics of the hydrophobic PS-DVB matrix can be altered by derivatization or coating to produce cation and anion exchange functionality. A strong anion exchanger PL-SAX 4000Å (Polymer) has been produced by coating the PLRP-S 4000Å with polyethyleneimine [15]. In order to be compatible with biological compounds, the surfaces of PS-DVB have been modified with different functional groups by covalently bonding hydrophilic functional groups to the matrix, such as nitro, diol, cyano, amino, hydroxyl, carboxylate, sulphonyl and carbonyl groups [8, 26-28].

Application of a PS-DVB packing material to separation of higher molecular weight peptides and proteins would require a large pore stationary phase or a non-porous material. In a large pore packing, solutes enter the interior of the stationary phase through a combination of convection and diffusion, so the mass transfer becomes fast. If there are no pores in the packings, the diffusion path length is minimized. However, if the molecules can diffuse into the polymer matrix, this can result in a low column efficiency. PS-DVB with large pore size are PLRP-S 300Å, 1000Å, 3000Å and 4000Å (Polymer Lab) and PRP-300Å (Hamilton) [15, 29].

Chromatography on PS-DVB is usually performed with MeOH/H_2O and CH_3CN/H_2O mobile phase. These are standard solvent systems for reversed-phase chromatography. However, in one case, PS-DVB modified by cyano and diol groups was used in a non-polar solvent system. The surface of cyano and diol derivatized PS-DVB are hydrophilic and the normal phase mode is achieved [28].

Because of these ideal characteristics, the commercially available PS-DVB packings of PRP-1 and PLRP-S have been widely used in the separation of biologically active species, such as proteins [30], penicillins [31], erythromycin A [32, 33], tetracycline [34, 35], antibiotics [36], cefadroxil [37], basic drugs [38], small chain peptides [39], and acidic herbicides [40]. PRP-1 was even used in the separation of carbon clusters of C_{60} and C_{70} [41] and in the study of the selectivity in the base-catalyzed hydrolysis of p-nitrophenyl esters [42].

The nonporous PS-DVB packing, PRP-∞ (Hamilton), has been used in the purification and separation of plasmid, chromosomal DNA, and nucleic acids [43, 44]. The C_{18} alkylated PRP-∞ has been used in the separation of oligonuclotides and DNA fragments with a good resolution and recovery [45, 46].

1.2 Background to Bandbroadening in PS-DVB

Despite their advantages, PS-DVB columns tend to demonstrate asymmetric and tailing peaks. Consequently, they have a lower column efficiency than silica-based packing materials, especially for non-polar aromatic, and polyaromatic hydrocarbons (PAHs) [13, 47].

Four possible reasons have been proposed to explain the very low efficiency observed in some combinations of solutes and mobile phases:

1. Stagnant zones in the pores of the packing material causes poor contact between the eluent and the polymer surface [25].

In the study of the effects of organic modifiers on the separation and efficiencies of several homologs on PLRP-S of 5μm, Smith and coworker [25] observed unusually poor efficiency in methanol-water eluent, with all peaks being distorted and tailed. The efficiency of each peak was found to be markedly dependent upon the organic components in the eluent. In methanol-water, all the compounds tested gave poor efficiency. In contrast, better efficiencies in THF-water and acetonitrile-water have been observed, with peak shapes comparable to those obtained with similar size particles of ODS-silica column. It was suggested that a low efficiency in methanol-water was due to the presence of stagnant zones in the pores of the packing materials which caused a poor contact between the eluent and the polymer surface.

2. Shrinking and swelling of the particles upon solvent switching which causes channeling in the bed [1].

This idea is based on the fact that PS-DVB, despite its high degree of crosslinking, is expected to swell somewhat when it comes in contact with an organic solvent even if no significant macroscopic swelling occurs. The lesser crosslinked regions near the pore walls are likely to swell in a non-uniform fashion due to a gradient of crosslinking normal to the pore walls. Shrinking and swelling are likely to occur when solvent gradient elution is performed. Solute molecules with dimension comparable to the swollen pore region can penetrate into it where the diffusion rate is low. Consequently, the rate of phase exchange and, as a result, the efficiency of the column is low. When the shrinking and swelling of particles is large enough, substantial channeling of the column packing happens. In addition, non-homogeneity of eluent flow can also cause a low column efficiency due to the channeling of the column.

3. Strong interactions of pi electrons in the underivatized PS-DVB with pi electrons in the solutes [13].

These pi-pi interactions, initially proposed by Benson and Woo [13] in the study of the retention characteristics for various hydrocarbons, may result in strong peak retention, tailing and broadening. Also, Tanaka and coworker [21] found that PLRP-S 300Å showed preferential retention for rigid and planar polynuclear aromatic hydrocarbons (PAHs) compared to the bulky aromatic compounds with rotational freedom of phenyl groups which in turn were retained more favorably than saturated hydrocarbons when compared with C_{18} silica [13].

The effects of the solute structures on the column performance were explained based on the pi-pi electron interactions. To decrease the effects of pi electron interactions on the chromatographic separation, the PS-DVB matrix was modified by introducing appropriate functional groups to reduce and screen the pi electrons in the matrix of PS-DVB. When (CH_2 $)_n$ groups were covalently bond to PS-DVB, the retention time decreased, and peak shape improved. Nitro and C_{18} groups were also introduced to the PS-DVB matrix and used to separate nitroarenes and PAHs, producing symmetric and narrow peaks with good resolution [13].

4. Slow diffusion of solutes into the polymer matrix or into the micropores [48, 49].

The physical characteristics, including the pore sizes and pore size distributions have been well studied for PS-DVB [50, 51]. These macroporous packings have large pores, i.e macro (> 500 Å)/mesopore (> 20Å and < 500 Å), between the microspheres and the aggregates due to the heterogeneity of the polymerization process. There are also present micropores (< 20 Å) between the polymer chains due to the size of the monomer, divinylbenzene. Under certain conditions, the solvents and solutes can penetrate into these micropores. It is also proposed that the transition from micropores to permanent pores is not discontinuous, but rather exists as a continuum from heavily crosslinked polymer chains, to less crosslinked polymer chains, to the permanent pores. The less crosslinked regions are possibly accessible to solutes and solvents. However, whether the heavily crosslinked region is accessible to solutes and solvents is not quite clear [52].

In characterization of PLRP-100Å and PLRP-300Å, Lloyd and coworkers [53] found that the column efficiencies with diethylphthalate and toluene increased with an increase of temperature. This phenomenon might be related to a decrease in the capacity factor, K', or to an increase in the diffusion coefficients in the polymer. By varying the compositions of the eluent, K' was then kept constant. An increase in the column efficiency at constant K' with increasing temperature was significant. Those results were explained by restricted diffusion of a solute in the stationary phase. The influence of the viscosity of the mobile phase on efficiency due to the temperature was small because a decrease in liquid viscosity on raising the temperature was balanced by increasing the concentration of water in the eluent in order to maintain relatively constant viscosity.

In another study [49], the effects of microporosity in PS-DVB on chromatographic performance have been extensively examined using PS-DVB of different pore sizes and different sizes of solutes. A phthalate homolog gave almost the same column efficiency for different pore sizes of PS-DVB, including a nonporous PS-DVB, although it was expected that a PS-DVB with a large pore size would give a better column efficiency for the same solute due to fast mass transfer. It was concluded that micropores were present in all PS-DVB packings due to the size of the monomer, divinylbenzene. The micropores can open up for some solutes which have the same solubility parameters as the polystyrene and for solvents which can completely wet polystyrene. The comparable values of term C in the van Deemter equation, the slope of the $\overline{H}$ vs $\overline{U}_0$ plot in the size exclusion and the reversed-phase mode for PS-DVB packings, indicated that the adsorption process itself could be sufficiently fast to be negligible compared with the restricted diffusion. This view can explain not only the sample dependence, but also the solvent dependence of column efficiency. As the micropores swell, the spaces in which the solutes diffuse increase, the restricted effects of the micropores decrease, and the mass transfer becomes fast, leading to a better column efficiency [49].

Deng and coworkers [48] found that PS-DVB packings have similar chromatographic performances even when the specific surface areas are quite different, which may indicate diffusion into the polymer matrix.

Among the suggested reasons for a low column efficiency on PS-DVB packings, reason 4 would lead to a slow "intraparticle sorption rate". This could be either a slow diffusion mass transfer in the stagnant mobile phase in the macro/mesopores, or a slow diffusion into the micropores, the polymer matrix.

1.3 Scope of the Present Work

First of all, the purpose of the research described in this thesis is to discover whether slow sorption rate is the major cause of bandbroadening and tailing for naphthalene on PRP-1. In this work, the peak shapes of naphthalene eluted from an analytical HPLC column of PRP-1 are predicted based on the sorption rate curves measured by the "shallow bed" technique on the same packing. The sorption rate curves are fit to an empirical tri-exponential equation, the parameters from the tri-exponential fit are then used in a theoretical model which relates the measured sorption rates to elution profiles.

Secondly, the origin of the slow sorption rates for naphthalene on PRP-1 was studied. What causes the severe tailing of naphthalene on PRP-1? Is it slow diffusion in the stagnant mobile phase present in the meso/macropores of PRP-1, or slow diffusion in the micropores of the polymer matrix? To answer this question, the sorption rates of naphthalene on PRP-1 are represented by a dual rate diffusion model, the Ruckenstein model, and from it, the diffusion coefficients in the macropores and micropores are calculated.

In addition, sorption rates on Hamilton PRP-∞, a 20μm spherical nonporous PS-DVB packing, was studied because it has the same chemical components used in the polymerization as PRP-1, but it contains no macropores and mesopores. The sorption rate of naphthalene on PRP-∞ is described by a different kinetic model from that which describes the diffusion in PRP-1. The micropore diffusion coefficients for naphthalene on PRP-1 and PRP-∞ were compared. A hydrodynamic model was used to calculate the sizes of micropores in both PRP-1 and PRP-∞ using the experimentally measured micropore diffusion coefficients.

Finally, the amount of naphthalene sorbed on both PRP-1 and PRP-∞ were measured by the "column equilibrium method".

A brief description of each chapter in this thesis is given below:

Chapter 2 describes the apparatus and the experimental procedures used in the measurement of the sorption kinetic curves and the sorption isotherms. The elution chromatography of naphthalene and phloroglucinol, including data acquisition, analysis and characterization, is described. Measurement of extra-column bandbroadening is also described.

Chapter 3 focuses on the measurement of the sorption isotherms of naphthalene on PRP-1 and PRP-∞.

Chapter 4 presents the results of sorption rate curves of naphthalene on PRP-1. The empirical tri-exponential fit is discussed.

Chapter 5 discusses the approaches used in the calculation of the predicted peaks. The results of characterization of the elution peaks, and the comparison of the predicted and the observed peaks are presented. The effects of the flow rates and the values of n_3 and k_3 in the tri-exponential fit on the shapes of the elution peaks are discussed.

Chapter 6 addresses the origin of the slow sorption processes of naphthalene on PRP-1. This includes the measurement of the sorption rates of naphthalene on PRP-∞ and theoretical description of the sorption rates of naphthalene on PRP-1 and PRP-∞ with various kinetic models, from which the macropore and micropore diffusion coefficients in PRP-1 and the micropore diffusion coefficient in PRP-∞ are calculated. The hydrodynamic model for hindered diffusion is used to calculate the sizes of micropores in PRP-1 and PRP-∞ using the experimentally measured micropore diffusion coefficients.

Chapter 7 gives some conclusions and future work.

Chapter 2

Experimental Section

2.1 Introduction

In this chapter, all the experiments that were carried out in this thesis are presented in detail. The design of the slider valve which contains the shallow bed is described. The shallow bed apparatus which was used in the measurement of the sorption rates and the isotherms of naphthalene on PRP-1 and PRP-∞ is presented. The elution chromatograph used with naphthalene and phloroglucinol is discussed, and the extra-column bandbroadening measurement is also presented.

2.2 Sorbents

PS-DVB is a non-polar copolymer. It is usually synthesized by suspension polymerization in water. Present in the suspension are the monomer, styrene, the crosslinking monomer, divinylbenzene; an initiator which can produce a radical and initiate polymerization; and a porogen, an inert diluent which is a good solvent for the monomers but is not a good solvent for the polymer formed in the reaction. These are stirred with water to produce organic phase droplets equivalent to the particle sizes of the polymer beads. Sometimes a stabilizer may be required to prevent the droplets from coalescing. The polymerization proceeds in the droplets of the organic phase with the growing polymer chains precipitating in the droplet as they reach a critical size upon polymerization. The inert diluent will intersperse and occupy a large part of the particle volume. After removing the diluent, a rigid, macroporous sorbent particle having a relatively high specific surface area and an aromatic hydrocarbonceous surface is obtained. Use of a crosslinking monomer results in the formation of a rigid three dimensional structure within the polymer matrix. By suitable choice of a porogen, the pore size, the pore size distribution, and the pore geometry can be optimized for HPLC. Similarly, a nominally nonporous PS-DVB packing is synthesized without adding any porogen. Figure 2.1 gives the synthesis scheme of PS-DVB.

PRP-1, a 10μm spherical macroporous particle and PRP-∞, a 20 μm spherical non-porous particle, are poly(styrene-divinylbenzene) copolymers which were donated by Hamilton (Reno, NV), and were used in the sorption kinetic studies using the shallow bed technique.

2.3 Chemicals

Naphthalene (Norwood, OH) was recrystallized from methanol before use. Phloroglucinol (Fisher Scientific Co.) was recrystallized from water. Anthraquinone, (97% , Aldrich) was used to calibrate the injector loop. Methanol (Fisher Scientific Co.) was reagent grade and distilled before use. Water was distilled and deionized (Barnstead NANO pure system, Boston, MA).

2.4 Sample and Eluent Solutions

In the measurement of the sorption rates, the sorption isotherms and the elution chromatograms, 85% MeOH/H_2O was used as the solvent for naphthalene and as the eluent. To measure the hold-up volumes in the shallow beds containing PRP-1 or PRP-∞, 7.068×10^{-5} M phloroglucinol, an unretained compound, was used. A 4.899×10^{-6} M solution of naphthalene was used to measure the sorption rates on PRP-1 and on PRP-∞ with the shallow bed technique. In the elution chromatographic experiments, phloroglucinol of 5.145×10^{-4} M was used to determine the mobile phase linear velocity.

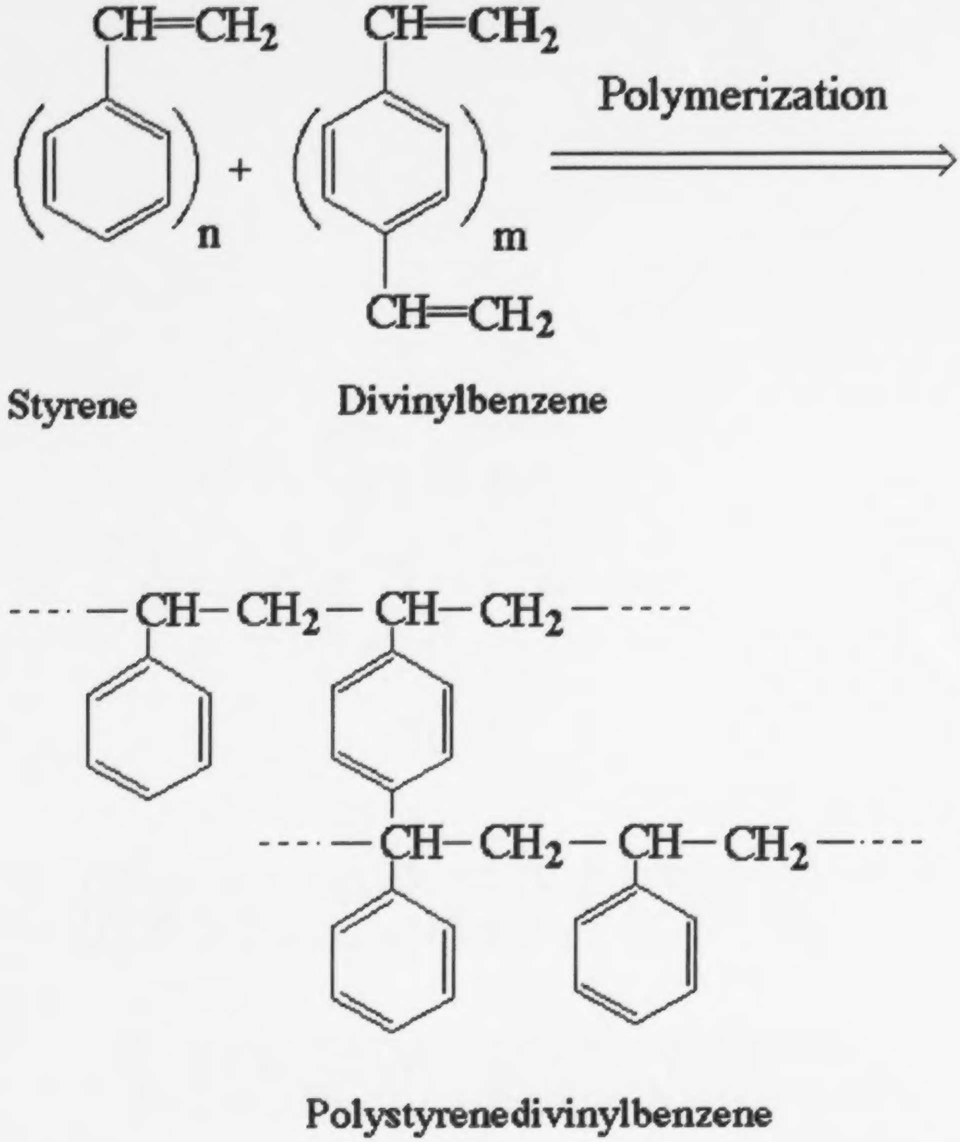
CH=CH2
CH=CH2
Polymerization
+
n
m
CH=CH2
Styrene
Divinylbenzene
CH–CH2–CH–CH2
CH–CH2–CH–CH2
Polystyrenedivinylbenzene

Figure 2.1 Schematic diagram of synthesis of poly(styrene-divinylbenzene).

Phloroglucinol of 5.057 x 10^{-4} M was used to measure the extra-column contribution, and naphthalene of 3.135 x 10^{-5} M was used to obtain the observed elution peaks from the PRP-1 HPLC column. Both the eluent and solvent were filtered through a 0.45 μm pore size Nylon 66 filter (Mandel Scientific Company Ltd.) before use.

2.5 Sorption Rate Measurement

2.5.1 Apparatus

The shallow bed dimensions for PRP-1 and PRP-∞ are shown in Table 2.1. Figure 2.2 is a schematic diagram of the apparatus for the measurement of the sorption rate curves. Two aluminum cylinders, R1 and R2 pressurized by N_2, contained naphthalene and phloroglucinol solution respectively. The solutions passed through inline stainless steel filter holders labeled IF (part XX4404700, Millipore, Mississauga, Ont.) containing Durapore HV membrane filters of 0.45 μm pore diameter (part HVLP04700, Millipore, Mississauga, Ont.) before reaching an ALTEX 6-way rotary valve (204-01), V1. The setting of V1 determines which solution will enter the left-hand inlet of the slider valve. The two aluminum cylinders, the two inline filter holders, and all of the connecting tubing were immersed in a constant temperature water bath thermostated by a circulating Haake D3 temperature controller (Fisher Scientific Co.) which was set to 25°C ± 0.2 °C.

The slider valve containing the shallow bed was mounted on an aluminum back plate which was attached inside a small plexiglass tank which was placed inside the front part of the constant temperature water bath and thermostated separately at 25°C ± 0.2 °C by a circulating Colora Ultra-Thermostat (NB34784, Germany).

Table 2.1 The features of shallow beds of PRP-1 and PRP-∞ in the sorption rate measurement.

Packing	PRP-1	PRP-∞
Weight (mg)	1.09 ± 0.02	3.20 ± 0.03
Bed Height (mm)	~0.34	~0.43
Packing Volume(μL)	~2.4	~3.1
$V_{\text{hold-up}}$ (μL)	8.3 ± 0.8	5.8 ± 0.5

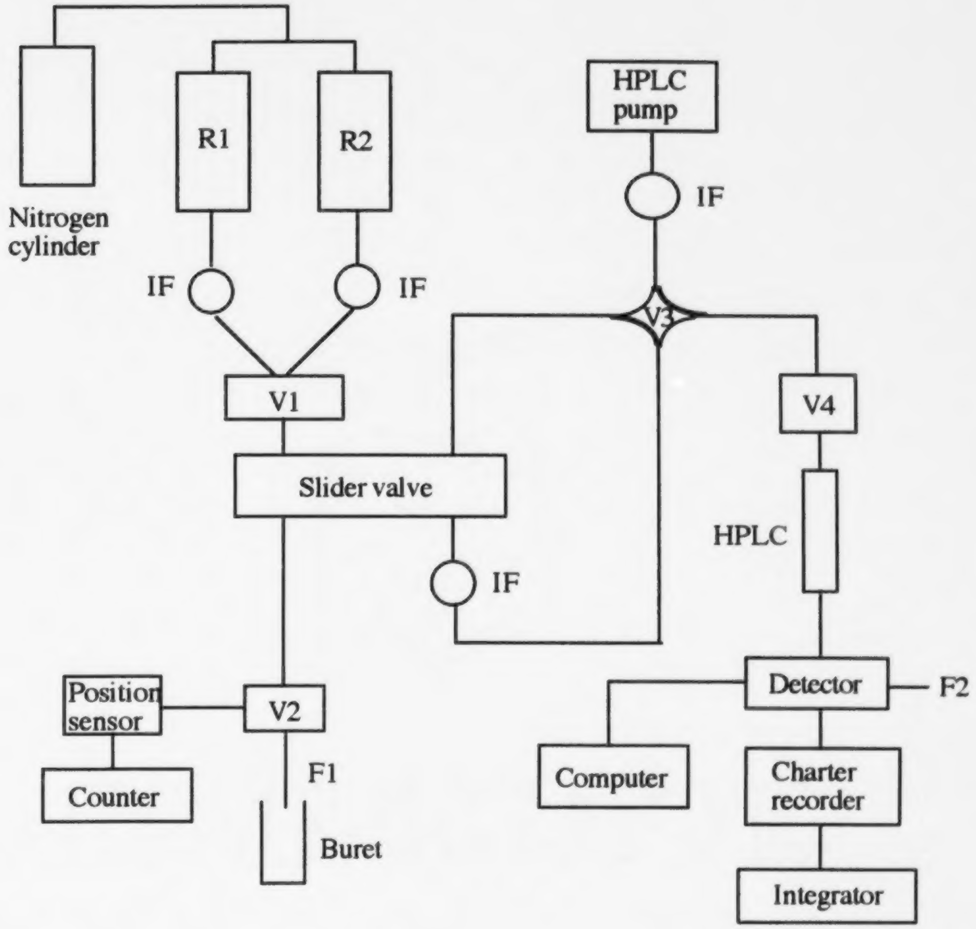
Nitrogen cylinder
R1
R2
HPLC pump
IF
IF
IF
V3
V1
V4
Slider valve
HPLC
IF
Position sensor
V2
Detector
F2
Counter
F1
Computer
Charter recorder
Buret
Integrator

Figure 2.2 Schematic diagram of apparatus used in the measurement of the sorption rate curves. Details see section 2.5.

The slider valve has two inlets which are stainless steel tubes of 3 mm i.d. The lefthand inlet was fed by a constant pressurized N_2 cylinder which drove the solution through the bed. The outflow from the leftside of the slider valve passed through a Cheminert 6-way rotary valve, V2 (R 6031V6, LDC, Riviera Beach, FA). A small infra-red generator/detector position sensor unit (ECG 3101 P312, Dorval, Quebec) attached to this valve was activated when the valve was switched to the position which allowed flow and was deactivated when the valve was turned to the off position. Valve V2 was used to control the time during which solutions flow through the bed. The time was recorded with an electronic counter (5321B Hewlett packard) set to display to ± 0.1ms. The righthand inlet of the slider valve was fed by a SP8000 HPLC pump (Spectra-Physics, Santa Clara, CA) in a constant flow mode. The flow rate was set to be 0.5-0.6ml/min at which the slider valve seals well. The outlet from the righthand side is a narrow bore (0.002" i.d.) stainless steel tubing leading to a Rheodyne inline filter (part 7315, Rheodyne, Berkeley, CA) and an analytical column (150 x 4.6mm) packed with μBondapak phenyl (part 086680, Waters, Mississauga, Ont.). The column was used to keep a constant back pressure and also to separate any impurity peak from naphthalene.

A Cheminert four way slider valve, V3 (CAV 4031, LDC, Riviera Beach, FA), was used to control the eluent from the HPLC pump. The setting of V3 determined whether the eluent passed through or bypassed the bed. V3 was set to bypass the bed when the slider was being moved from the righthand inlet, (the sample elution position), to the lefthand inlet, (the sample loading position), and the reverse. This avoided the disturbance of bed packing and occasional loss of packing during the moving of the slider valve from the loading position to the elution position and the reverse.

2.5.2 A Switching Valve to Control the Exposure Time

In the measurement of the sorption rates, valve V2, a six way rotary valve, was used to control the time during which the sorbent was exposed to the sample solution. Because the sorption rate of naphthalene on PRP-1 is very fast, the initial exposure times should be very short in order to accurately measure the initial sorption rates.

In the previous study [54], the exposure time was controlled by pulling the slider from the loading position to the elution position. There are two disadvantages associated with this method. First, the slider is sealed tightly under a high pressure by four tension adjustment screws as shown in Figure 2.3, so that a lot of force and a relatively long time was involved in pulling the slider from the loading position to the elution position. The minimum time was reported to be 0.4 seconds [54]. That time was too long for measuring the initial sorption rates of naphthalene on PRP-1 accurately. During the 0.4 seconds, about 70% of naphthalene has been sorbed as shown in the newly designed system. Therefore, the amount sorbed before that time can not be determined accurately.

Secondly, the particles in the shallow bed were not exposed uniformly to the sample solution or to the eluent when the slider was being pulled from the elution position to the sample loading position and the reverse.

2.5.3 Shunting off flow When the Shallow Bed is Being Pulled from One Position to the Other

In the old system [54], when the slider was being pulled from the loading to the elution position, the right edge of the packing encountered the flowing eluent first and the eluent pushed this side down a little bit and caused it to dent. This results in the non-uniformity of bed thickness, and sometimes, loss of packing. In this study, V3 in Figure 2.2 was used to shunt off the flow when the bed was being pulled from the loading to the elution position and the reverse. Therefore, the eluent did not pass through the bed during the movement of the slider.

2.5.4 The Slider Valve

The center of the sorption rate measurement system is the slider valve and the shallow bed which are shown in Figure 2.3. The slider valve is not drawn to scale. The slider valve consists of three parts: the stainless steel valve body, made from 1/4 " thick stainless steel plates, the slider, and the Teflon face plates. The slider is a 2 mm thick, 13 mm wide and 113 mm long stainless steel frame, into which is inserted a 2.2 mm thick, 9 mm wide and 73 mm long Kel-F plate. Two holes of 3 mm diameter at 9.5 mm intervals at centers are drilled in the Kel-F insert part. One of the holes is the dummy hole. The other hole contains the shallow bed which is a small column of milligram amount of packing approximately 0.34 mm and 0.43 mm in height for PRP-1 and PRP-∞ respectively. The packing is supported at the bottom by one piece of stainless steel screen, that is 3 mm diameter, 0.076 mm thick and 2 μm pore size. On the top, the packing is held by two pieces of 2.8 mm i.d Zitex Teflon porous membranes. One is 0.2 mm thick and 10 to 20 μm pore size (H662-123), the other is 0.64 mm thick and 30 to 60 μm pore size (K1064-222). The slider is held in the valve body between two Teflon face plates which only contact the Kel-F insert. Screwed into the Teflon plates is a set of stainless steel plates. A piece of Teflon tape is placed between the steel and the Teflon plate to ensure a good seal. The two 3 mm i.d. stainless steel inlet tubes, the 3 mm i.d. stainless steel outlet and the 0.002" i.d. stainless steel outlet tube are silver soldered to the stainless steel plates. Four tension adjustment screws are used to seal the valve. The slider is moved forward and backward by two aluminum levers which are mounted on the aluminum back plate. One end of the slider is attached to the left side lever by an alloy cable, the other end of the slider is attached to the right side lever via a brass bar. The lever on the right side uses a hinged

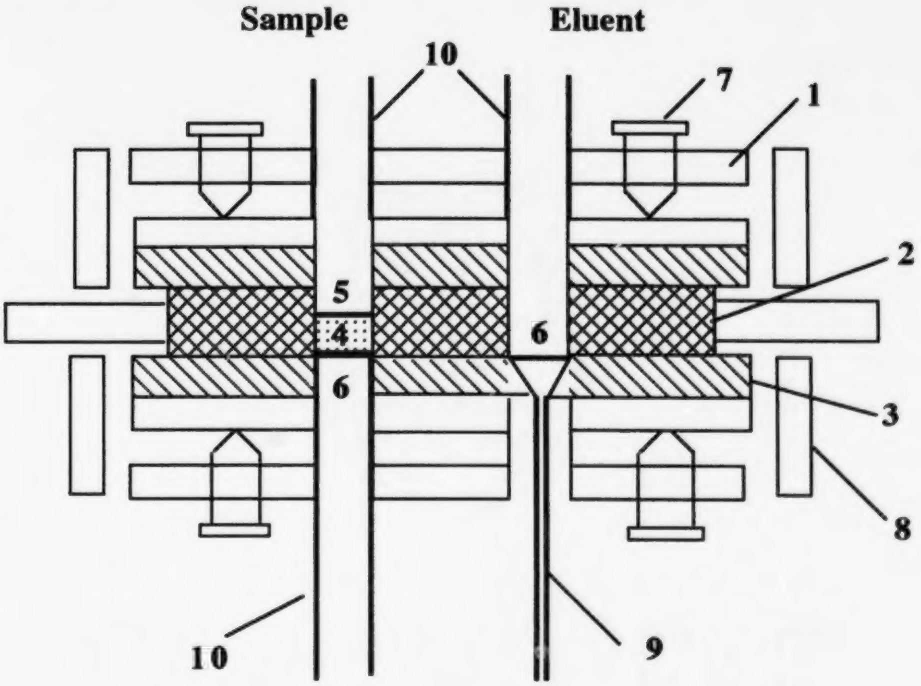
Sample
Eluent
10
7
1
2
5
4
6
6
3
8
10
9

1. Stainless Steel
2. Kel-F Insert
3. Teflon Face Plate
4. Bed Packing
5. Zitex Porous Membranes
6. 2μm s.s Screen
7. Tension Adjustment Screws
8. S.S. End Plate
9. 0.002" S. S. Tubing
10. 3 mm S.S. Tubing

Figure 2.3 Schematic diagram of the slider valve.

hook to catch the notch in the bar to change the position of the slider. The side view of the slider system is shown in Figure 2.4.

2.5.5 Procedures

The measurement of the sorption rates onto PRP-1 and PRP-∞ was accomplished by exposing the shallow bed of the packing of interest to a fast flowing stream of a sample solution for various periods of times.

First is the pre-conditioning step. The bed was initially located in the loading position as shown in Figure 2.5a. The bed was equilibrated by a sample solution which was being pumped through the left-hand inlet to the slider valve by constant N_2 pressure for about 60 seconds. The time during which a sample solution passed through the bed was controlled by V2. The pressure on the regulator of N_2 cylinder was always set as high as possible to get a high flow rate. The maximum pressure shown in the gauge was about 240 psi. The interstitial flow rate through the shallow bed, U (cm/s), was calculated as follows:

$$U = \frac{F(\mathrm{ml/min})}{\pi\, r^2\, \varepsilon_{inter}\, 60} \qquad (2.1)$$

where F is the flow rate through the shallow bed and was measured by timing the collection of solution in a buret as shown in Figure 2.2, r is the radius of the shallow bed which is 0.15 cm, ε_{inter} is the fraction of bed volume contained between the particles. For PRP-1, ε_{inter} is calculated using manufacturer's information concerning the column interparticle volume and the bed porosity was found to be 0.31. Since there is no information available about the physical properties for PRP-∞, a nonporous packing, from the manufacturer, ε_{inter} is used as 0.4 which is characteristics of most packings.

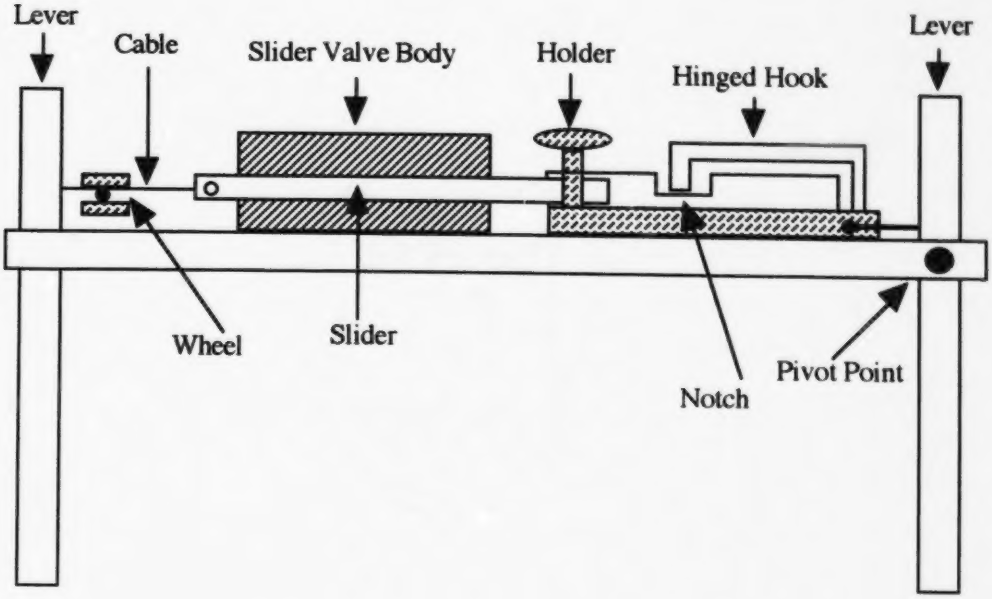
Lever
Cable
Slider Valve Body
Holder
Hinged Hook
Lever
Wheel
Slider
Notch
Pivot Point

Figure 2.4 Schematic side view of the whole shallow bed apparatus, including slider valve and the lever system used to move the slider.

When the four way valve V3 was set to bypass the bed, the slider was pulled to the elution position as shown in Figure 2.5b. Then V3 was set to allow flow of eluent through the bed. The sample sorbed on the packing was eluted.

Next, V3 was set to bypass the bed again, the slider was then pulled back to the loading position as illustrated in Figure 2.5c.

These steps were repeated for two more times. The purpose of this repetition was to pre-condition and stabilize the shallow bed and to get a constant and a known flow rate passing through the bed.

After the bed has been pre-conditioned in the above start-up cycle, measurement of the sorption curve started. The bed was usually exposed to the sample solution for times ranging from the minimum time of 0.04 (s) to a maximum of about 60 (s) at which time the sorption was very close to equilibrium. For each loading and elution, a peak with area proportional to the number of moles sorbed on the packing, after correcting for the amount in the hold up volume, was detected at 276 nm by a UV detector (Spectroflow 757, Kratos Analytical Instruments, Ramsey, NJ) and integrated by an integrator (HP 3390A, Hewlett packard). The UV detector was calibrated by injection of a series of standard naphthalene solutions into the analytical column by V4, a Rheodyne injection valve (part 7017, Rheodyne, Berkeley, CA). V3 was set to bypass the bed during the calibration process. The calibration curve, a plot of integrated area against the number of moles injected, was obtained.

A series of loadings and elutions in the shallow bed experiment produces in a sorption rate curve which is a plot of moles sorbed versus the exposure times.

2.6 The Hold-up Volume Measurement

The same apparatus was used as the one in the measurement of the sorption rate . The hold-up volume was measured by pumping a standard phloroglucinol solution through

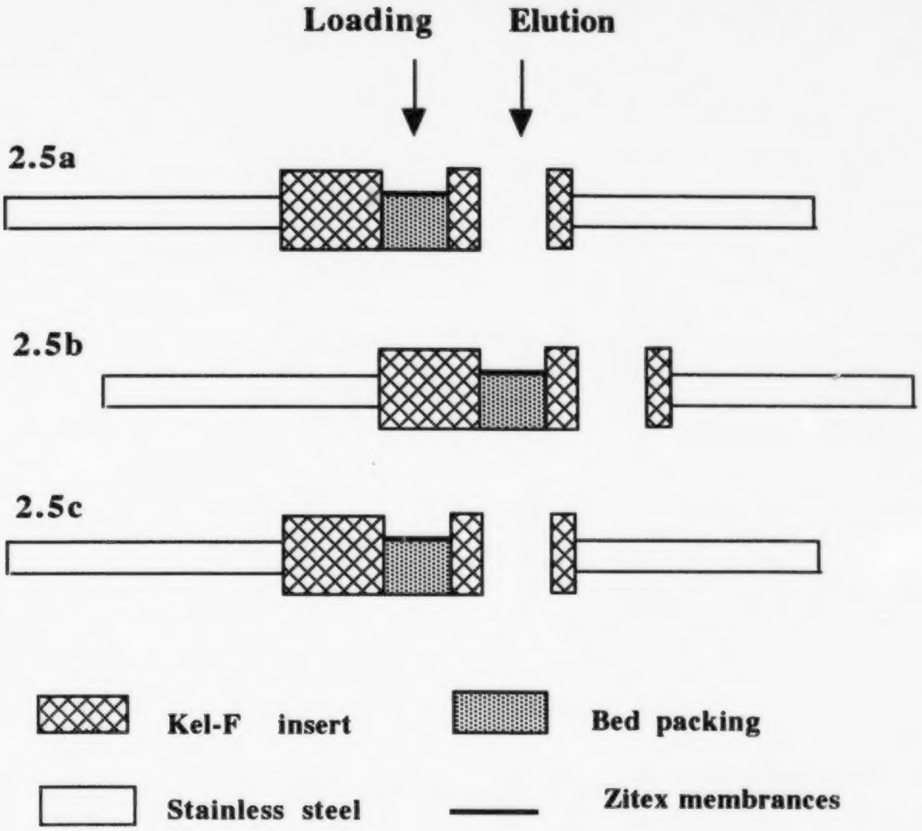
Loading
Elution
2.5a
2.5b
2.5c
Kel-F insert
Bed packing
Stainless steel
Zitex membrances

Figure 2.5 Schematic diagram showing the sequence of positions of the slider in the measurement of the sorption rate experiment. Details see 2.5.5

the bed for 60 seconds on PRP-1 and 90 seconds on PRP-∞ respectively. For detector calibration, the phloroglucinol was also injected onto the analytical column using V4, the injection valve.

2.7 Injector Loop Calibration

In the calculation of the hold-up volume, the volume of the injector, V4, was needed. The volume of the injector, V_{inj}, was determined by injecting anthraquinone solution with the loop. The HPLC column and the detector were disconnected from the injector V4. A concentration of 1.585 x10^{-4} M of anthraquinone in 100% MeOH was injected and collected into a volumetric flask. Three injections were made and the total volume collected was 3.00 ml, which was enough for determination of the absorbance in a 1.00 cm cell by a UV-Visible spectrophotometer (HP 8451A, Hewlett Packard). V_{inj} was calculated as follows:

$$V_{inj} \text{ x } C_m = \frac{\text{C x 3.00 ml}}{\text{3 injections}} \tag{2.2}$$

where C_m was a standard solution with a known concentration of 1.585 x10^{-4} M. The concentration C = (3.241±0.006) x 10^{-6} M, was determined from a calibration curve of anthraquionone. V_{inj} was determined to be 20.46 ± 0.95 μL. The standard deviation was calculated from error propagation at the 95% confidence level.

2.8 Naphthalene Sorption Isotherm Measurement

The isotherms of naphthalene on PRP-1 and PRP-∞ were measured using the shallow bed apparatus as illustrated in Figure 2.2 based on the "column equilibration method" [55]. The procedures are similar to those in the measurement of the sorption rate curves. In the experiment, a known amount of packing in the shallow bed was exposed to a known sample solution until the sample is at loading equilibrium between the mobile phase and the stationary phase. The loading equilibrium time was 60 seconds for PRP-1 and 90 seconds for PRP-∞. The number of moles eluted from the shallow bed, after correction for the sample contained in the hold up volume, was the amount sorbed on the packing.

2.9 Elution Chromatography

The experimental elution chromatograms which were needed for comparison with the predicted peaks were collected using a typical HPLC setup as illustrated in Figure 2.6. The HPLC pump, set in a constant flow mode, the inline filter, the injector valve and the UV detector at 254nm are the same as described in Section 2.5.5. The column used was a commercially available HPLC analytical column, PRP-1 (15o x 4.6 mm, part 79425-3145, Hamilton Inc. Reno, NV) packed with 10 μm spherical particles. Standard solutions of phloroglucinol and naphthalene were injected onto the column and the eluted peaks were collect by either a digital computer or by a chart recorder depending on the concentrations of the sample injected.

The peaks of phloroglucinol, an unretained compound, eluted from a column of PRP-1, were symmetric and narrow. The signal to background noise ratio was 28. The S/N was the ratio of the peak amplitude to the standard deviation of the baseline noise. Figure 2.7A shows the raw data of the elution profile of phloroglucinol at a mobile phase linear velocity of 0.3 cm/s using a 12 bit analog to digital convertor (National Instruments) data acquisition board placed in a Macintosh IIsi computer. The raw data was smoothed using the moving average function written in SpectroPlot [56] as shown in Figure 2.7B and transferred to Excel (Microsoft, 1990) where the raw data was further analyzed.

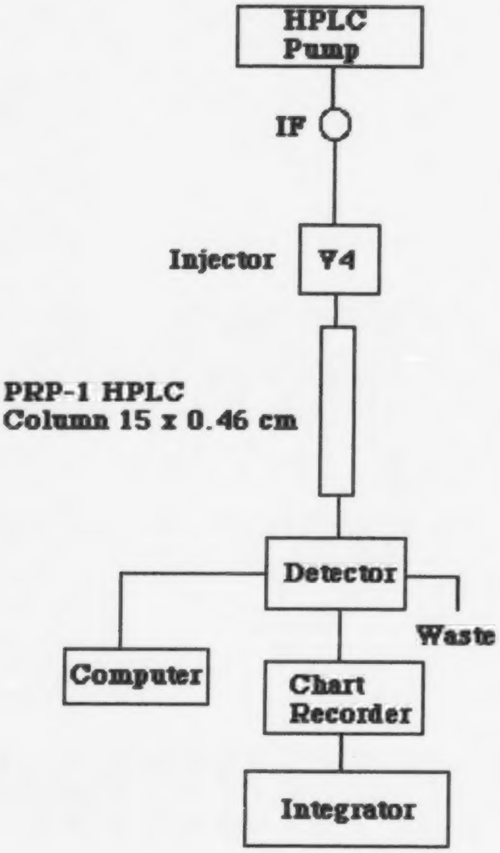
HPLC Pump
IF
Injector
V4
PRP-1 HPLC
Column 15 x 0.46 cm
Detector
Waste
Computer
Chart Recorder
Integrator

Figure 2.6 Schematic diagram of apparatus used in collection of the experimental elution profiles. Details see section 2.9.

The peak of 4 x10^{-5} M naphthalene, the maximum concentration within the linear region of the sorption isotherm, was asymmetric and broad. The signal to noise ratio was so low (about 1) that the peak acquired by the digital computer was barely recognized even after the signals were processed by a low pass filter and smoothed by the software programs written in SpectroPlot. Figure 2.8A shows the elution peak of naphthalene of 4.688 x 10^{-5} M at a mobile phase linear velocity of 0.4 cm/s as non-smoothed output from the data collection system. Figure 2.8B shows the smoothed output. As the concentration of naphthalene increases to 10^{-3} M, the peak can be acquired accurately by the digital system as shown in Figure 2.9. The S/N is 61. Therefore, the low concentration of naphthalene (10^{-5} M) was recorded on a chart recorder and digitized manually. Figure 2.10 shows a peak of naphthalene of 3.135 x 10^{-5} M recorded on a strip chart.

The low concentration of naphthalene (10^{-5} M) was required in the experiment, because the bandbroadening considered in this study is from kinetic effects which do not include the bandbroadening from the overloading of the column. The experimental elution profiles were measured at four mobile phase linear velocities. The peaks of phloroglucinol and naphthalene were characterized by moment analysis using the program written in MatLab (The MathWorks, Inc. 1991). The data from phloroglucinol were collected using a digital computer and the digital data were smoothed and calibrated linearly in the SpectroPlot and then transferred to Excel (Microsoft, 1990) where a subset data was chosen from limits as will be discussed in Section 5.3.3. The subset of data were then transferred to the MatLab where the first moments were calculated. For naphthalene, the manually digitized data was directly transferred to MatLab without any modification.

The moment analysis was carried out by two methods. For phloroglucinol, a numerical integration method was used, this method gave good precision and accuracy for the first moments. The second moments were calculated by graphical method because the digital data gave a very poor precision for the second moments due to the baseline noise. For naphthalene, where the number of data points was less, the digital data was fitted to an

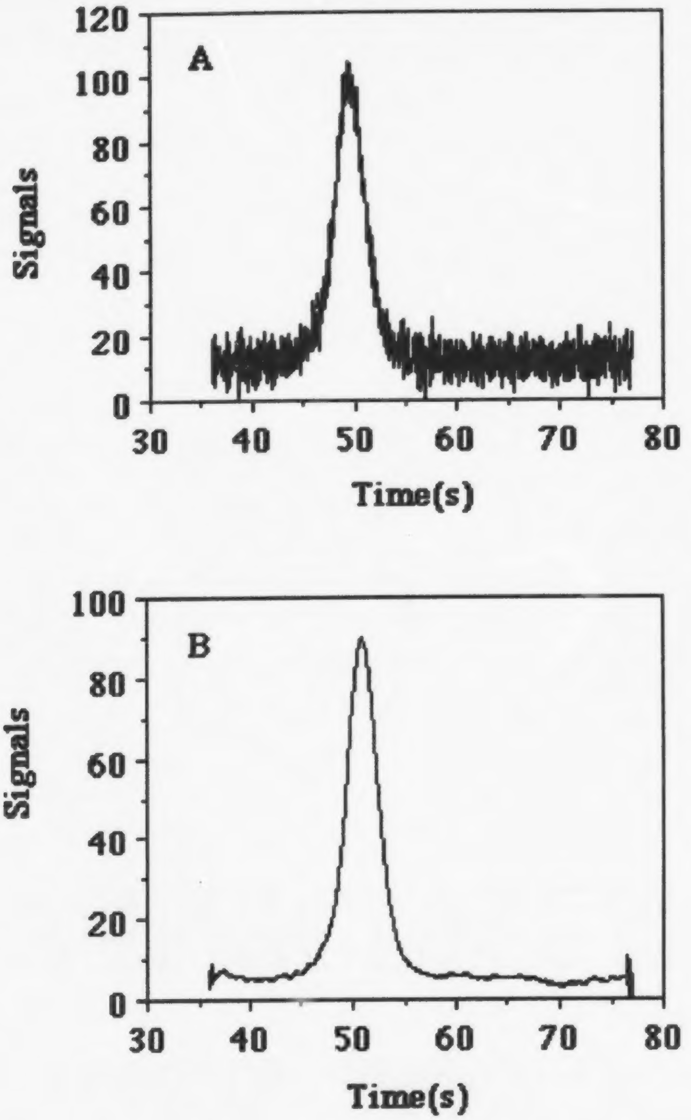

Figure 2.7 Chromatograms of 5.145 x 10^{-4} M phloroglucinol on a column of PRP-1 in 85% MeOH/H_2O at a mobile phase linear velocity of 0.3 cm/s. In A, the chromatogram is not a smoothed output from the data collection program written in SpectroPlot. In B, the chromatogram is a smoothed output from the data collection program written in SpectroPlot.

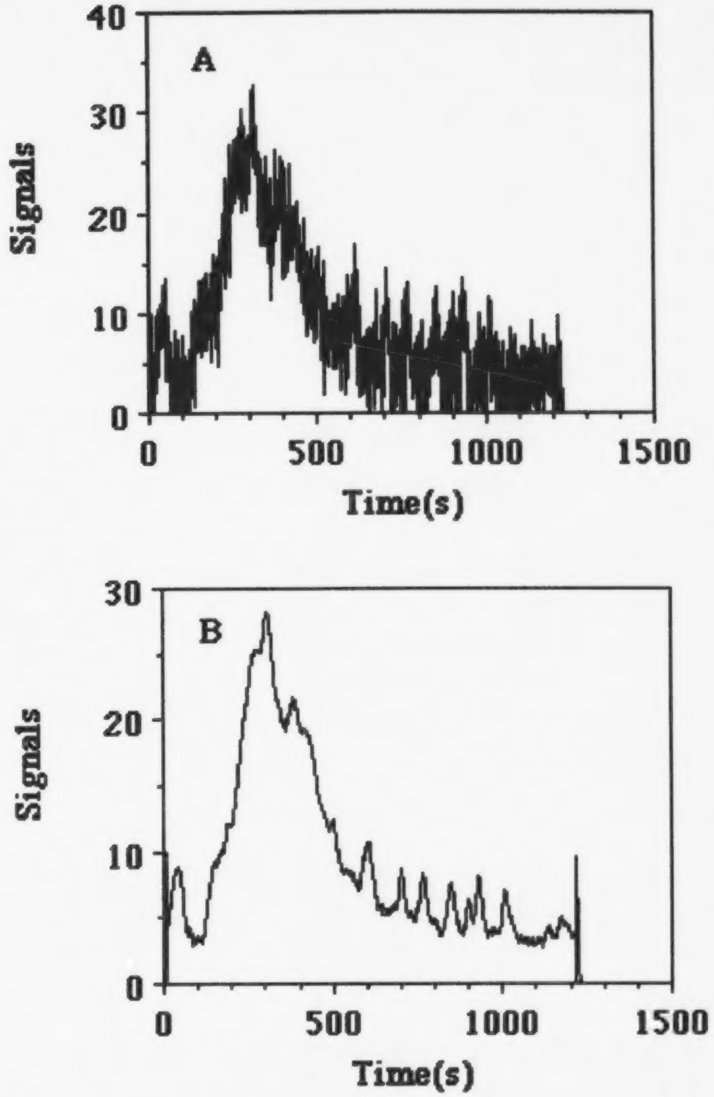

Figure 2.8 Chromatograms of 4.688 x10^{-5} M naphthalene on a column of PRP-1 in 85%MeOH/H_2O at a mobile phase linear velocity of 0.3 cm/s. In A, the chromatogram is not a smoothed output from the data collection program written in SpectroPlot. In B, the chromatogram is a smoothed output from the data collection program written in SpectroPlot.

exponentially modified Gaussian function (EMG) with a non-linear least squares regression. The program which was written in MatLab and called Expgauss then chose a user specified number of equally spaced data points which were used to fit the EMG function to the elution profile. Statistical moments were then calculated analytically from the EMG function.

2.10 Extra-Column Bandbroadening

The contributions of the extra-column components, such as tubing, detector and injector to the bandbroadening of naphthalene eluted from a column of PRP-1 were measured using the apparatus illustrated in Figure 2.11 with the column replaced by a zero dead volume coupling. In order to get a constant flow rate of a certain value, a nitrogen cylinder was used to provide a constant flow rate which was measured using a digital stopwatch (Cole-Parmer) and a buret. A standard solution of 5.057 x 10^{-4} M phloroglucinol in 85% MeOH/H_2O was injected and the signals were recorded on a strip chart recorder. The profiles were then hand digitized and transferred to MatLab (The MathWorks, Inc.1991) where the data was fitted to the EMG function from which the moments were calculated.

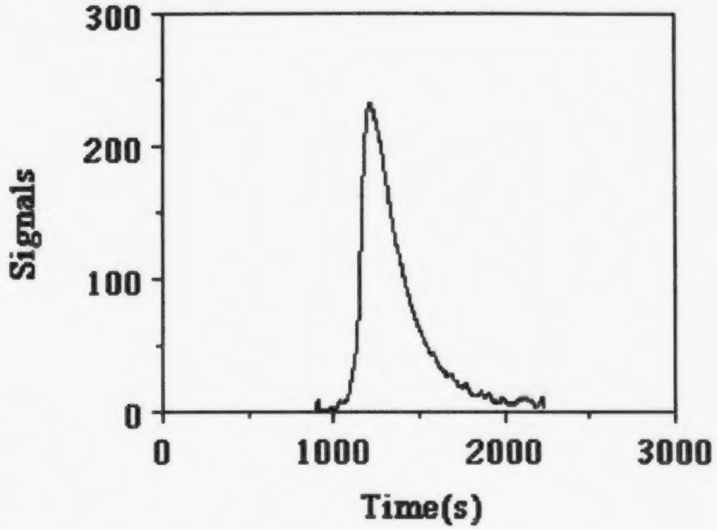

Figure 2.9 Chromatograms of 4.688 x 10^{-3} M naphthalene on a column of PRP-1 in 85%MeOH/H_2O at a mobile phase linear velocity of 0.3 cm/s. The chromatogram is a smoothed output from the data collection program written in SpectroPlot.

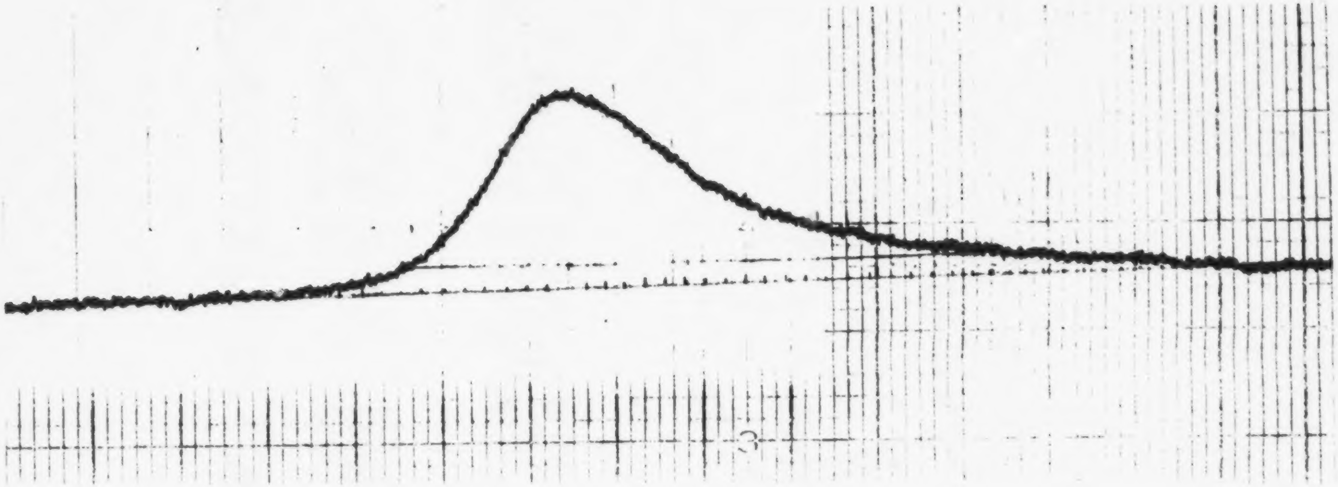

Figure 2.10 The chromatogram of 3.135×10^{-5} M naphthalene from a PRP-1 column at a mobile phase linear velocity of 0.1 cm/s. The profile was recorded on a strip chart.

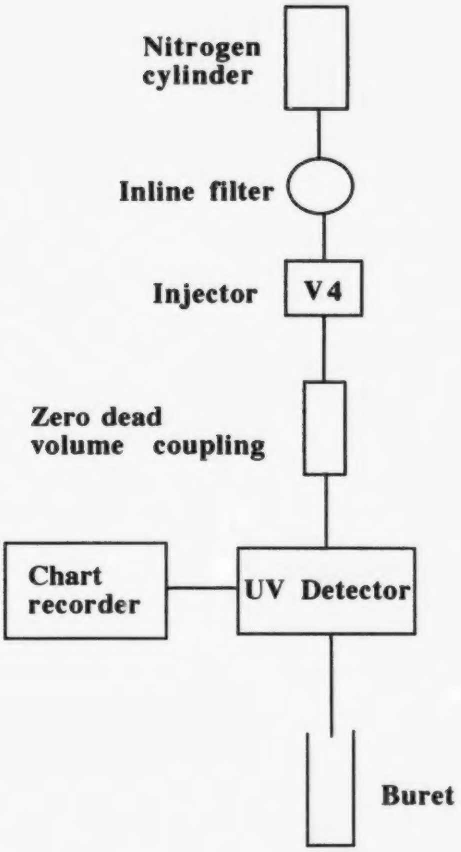
Nitrogen cylinder
Inline filter
Injector
V4
Zero dead volume coupling
Chart recorder
UV Detector
Buret

Figure 2.11 Schematic diagram of apparatus used in the measurement of the extra-column bandbroadening.

Chapter 3

Naphthalene Sorption Isotherm

3.1 Introduction

The location and shape of a peak in a chromatographic column is governed by two sources. The first is the thermodynamic equilibrium. The sample molecules distribute between the stationary phase and the mobile phase as they are travelling down the column. The migration rate, and therefore the retention time, t_R, are related to the equilibrium constant, in terms of the capacity factor, K'. If K' is independent of concentration, then equilibrium considerations do not affect the shape of the peak. If K' depends on concentrations, then equilibrium considerations affect the shape of a peak as well as its location. The second source is the non-thermodynamic effects of flow inequalities and kinetics. In chromatography, in the linear part of the isotherm, the bandbroadening and asymmetry of a peak are related to the plate height, $\overline{H}$, to which each non-thermodynamic process in a column contributes.

The sorption isotherms of naphthalene on PRP-1 and PRP-∞ were measured using the shallow bed apparatus based on the "column equilibration" method [55]. The Langumuir equation was fit to the data on PRP-1[57-59], and a linear equation was fit to the data on PRP-∞. The linear regions of the sorption isotherms, in which k' is a constant and independent of concentration, were used to select a concentration of naphthalene for use in the sorption rate measurement which will be presented in chapter 4.

3.2 Theory

A non-linear isotherm is one of the factors which control peak shape. The distribution isotherm and its effect on the chromatographic peak shape have been discussed in the literature [57-60].

An isotherm is a plot of the concentration of a sample in the stationary phase, C_s, versus the concentration in the mobile phase, C_m, at constant temperature. A typical isotherm is illustrated in Figure 3.1. The distribution coefficient of a sample is defined in equation 3.1:

$$K_D = \frac{C_s}{C_m} \tag{3.1}$$

The distribution coefficient is an equilibrium constant where a sample distributes itself between the two phases. K_D has units which depend on the units of C_s and C_m.

The value of the distribution coefficient at any particular concentration of a sample is the slope of the line drawn between the origin and the point on the isotherm corresponding to the appropriate concentration in the mobile phase. This is illustrated by a dashed line in Figure 3.1.

There are three types of simple isotherms: linear, convex and concave as shown in Figure 3.2. The elution chromatogram which would be expected from each isotherm is also drawn below in the same Figure.

The first type of isotherm is linear. A linear isotherm occurs when the concentration of a sample is effectively infinitely dilute. The distribution coefficient for a linear isotherm does not vary with the sample concentration in the mobile phase, i.e. it is a constant . The linear isotherm has no influence on the concentration-time profile of a peak. For linearity to occur, sample molecules must not interact with one another in either phase. Most sample solutions give a linear isotherm as the concentration of a sample approaches infinite dilution. It is the concentration of a sample in the column inlet rather than in the column outlet that should be within the linear region of the isotherm. The chromatographic peak shape resulting from a linear isotherm is Gaussian as shown in Figure 3.2. There is some bandbroadening due to the axial diffusion, non-uniform flow, and non-equilibrium due to the mass transfer resistance between phases. However, these processes broaden a peak virtually symmetrically in a long column.

The second type of isotherm is convex. The K_D decreases with an increase in sample concentration. Convex isotherms are the most commonly observed ones in chromatography. The amount sorbed in the stationary phase increases with concentration in the mobile phase and then approaches a plateau. This type of isotherm can sometimes be described by the Langmuir equation shown in equation 3.2 [57-59]:

$$C_s = \frac{a\,b\,C_m}{1+b\,C_m} \tag{3.2}$$

where a and b are constants.

The Langmuir sorption model was originally developed to represent chemisorption on a set of distinct localized adsorption sites with equivalent energy and it is assumed that each site can hold one adsorbate molecule and there is no interaction between molecules adsorbed on the neighboring sites [61].

The chromatographic peak associated with a convex isotherm is a tailed peak as drawn in Figure 3.2. The tailing of the peak can be understood by choosing two points on the isotherm. $K_{1,D}$, the distribution coefficient for point 1, is larger than $K_{2,D}$, the distribution coefficient for point 2, as seen in Figure 3.2. The average linear velocity, $\overline{U_i}$, of a retained sample is proportional to the mobile phase linear velocity in a column:

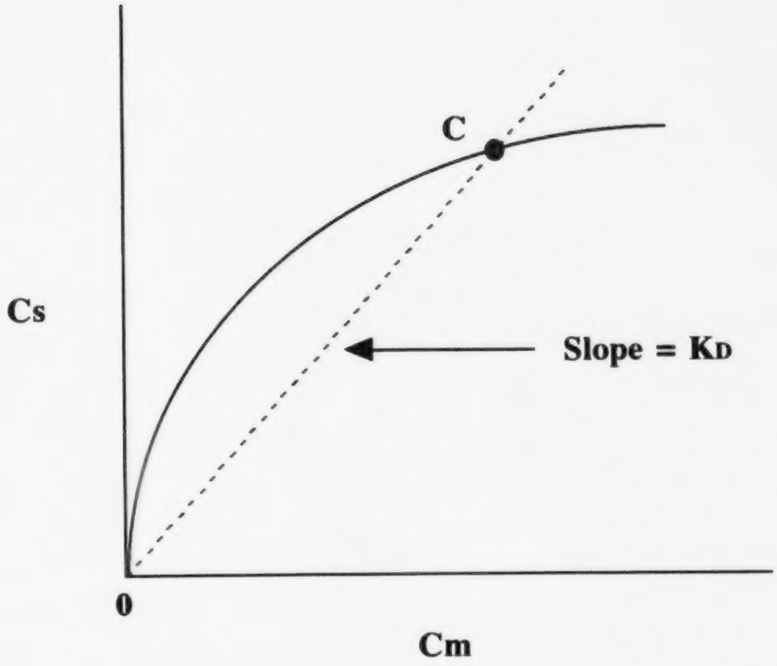

Figure 3.1 A typical sorption isotherm. The slope of the dashed line between the origin and point C is the distribution coefficient , K_D, for the solute at concentration C_m.

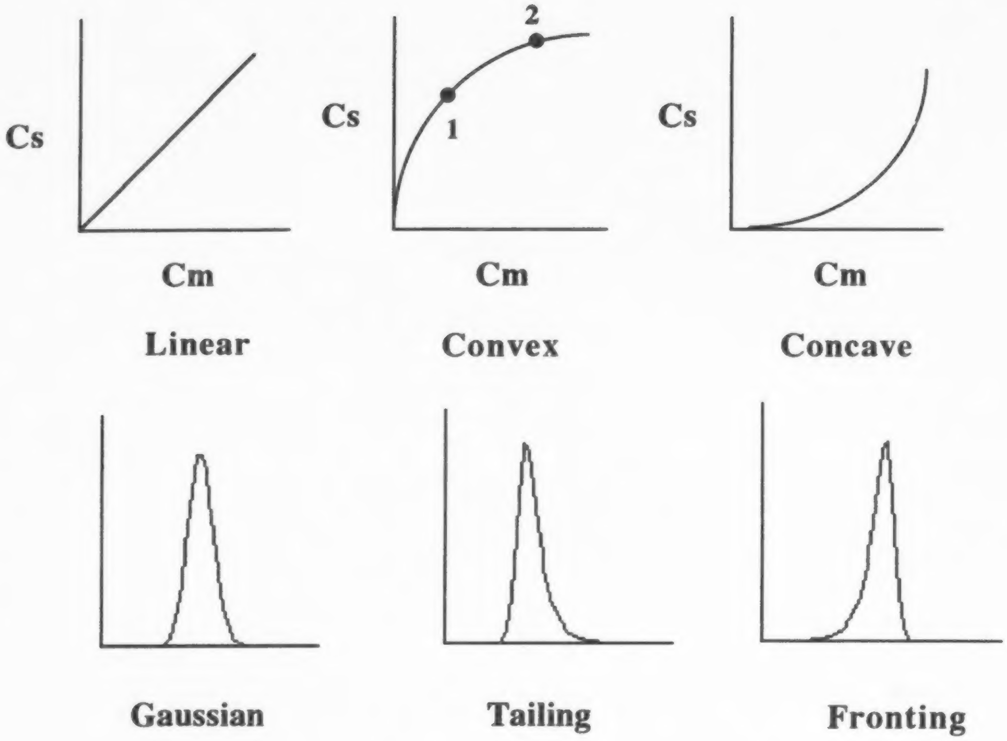
Cs
Cm
Linear
Cs
2
1
Cm
Convex
Cs
Cm
Concave
Gaussian
Tailing
Fronting

Figure 3.2 Shapes of common sorption isotherms and the corresponding elution peaks in chromatography.

$$\overline{U}_i = R\overline{U}_0 \tag{3.3}$$

$$R = \frac{V_m C_{i,m}}{V_m C_{i,m} + V_s C_{i,s}} = \frac{1}{1 + \frac{V_s C_{i,s}}{V_m C_{i,m}}} \tag{3.4}$$

where $\overline{U}_0$ is the average linear velocity for an unretained sample, R is the fraction of molecules in the mobile phase, V_s is the volume of the stationary phase, V_m is the total void volume (intra and inter particle). The capacity factor, K', is defined as shown in equation 3.5:

$$K' = \frac{C_{i,s} V_s}{C_{i,m} V_m} = K_D \frac{V_s}{V_m} \tag{3.5}$$

$$\overline{U}_i = \overline{U}_0 \frac{1}{1+K'} \tag{3.6}$$

The average linear velocity is inversely related to and K' and K_D as seen in equations 3.5 and 3.6. $\overline{U}1$ is smaller than $\overline{U}2$. This means the sample molecules at a high concentration move faster than the sample molecules at a lower concentration. Therefore, the region of a peak near the center of the band moves faster than the region of a peak toward the front and the back, causing the center of the band to catch up with the leading edge while the low concentration trailing edge moves more slowly and elutes as a tail.

The third type of isotherm is a concave isotherm as illustrated in Figure 3.2. A concave isotherm would give rise to a fronting peak using the same type of reasoning and is also shown Figure 3.2.

3.3 Measurement of the Isotherms

Methods used to measure sorption isotherm in GC [60, 62] have been discussed and the same techniques have also been applied to LC [63-65]. A commonly used method is frontal chromatography, including frontal analysis (FA). This method involves measurements made not at equilibrium.

In frontal analysis (FA) [60], a sample solution of a known concentration flows through a column packed with a known amount of sorbent. The concentration of the effluent solution is monitored. When the concentration of the effluent solution is equal to the concentration of the influent solution, total breakthrough has been achieved. A typical breakthrough curve is shown in Figure 3.3. The total amount of solute taken up by the sorbent is proportional to the area of *aed* shown in Figure 3.3.

The shape of the boundary is related to the shape of the isotherm curve. When the isotherm is linear, the shape of the breakthrough curve is sigmoid. The front (Figure 3.3) and rear boundary are symmetric. The breakthrough time is t_R which is the midpoint of the rising portion of the curve. For a convex isotherm, the shape of the front boundary is self-sharpening as shown in Figure 3.4a, and the shape of the rear boundary is diffuse as shown in Figure 3.4b. For a concave isotherm, the situation is reversed.

The shape of the breakthrough curve can be understood as follows: when the solution is first fed to the column, the sample will be sorbed at the top of the bed, and none of the sample comes out of the column. As the feed continues, the whole bed of sorbent begins to reach equilibrium with the sample solution. When this equilibrium is achieved (point e in Figure 3.3), the concentration of sample exiting the column is identical to that entering.

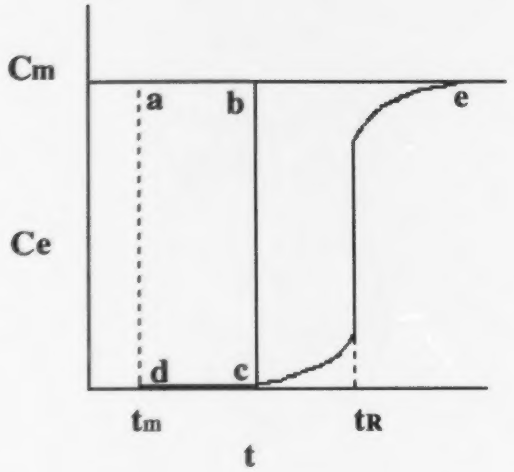

Figure 3.3 Breakthrough curve. Equilibrium between the mobile and stationary phase occurs at the plateau of point e. The concentration at point e is equal to the influent solution concentration. t_R is the retention time.

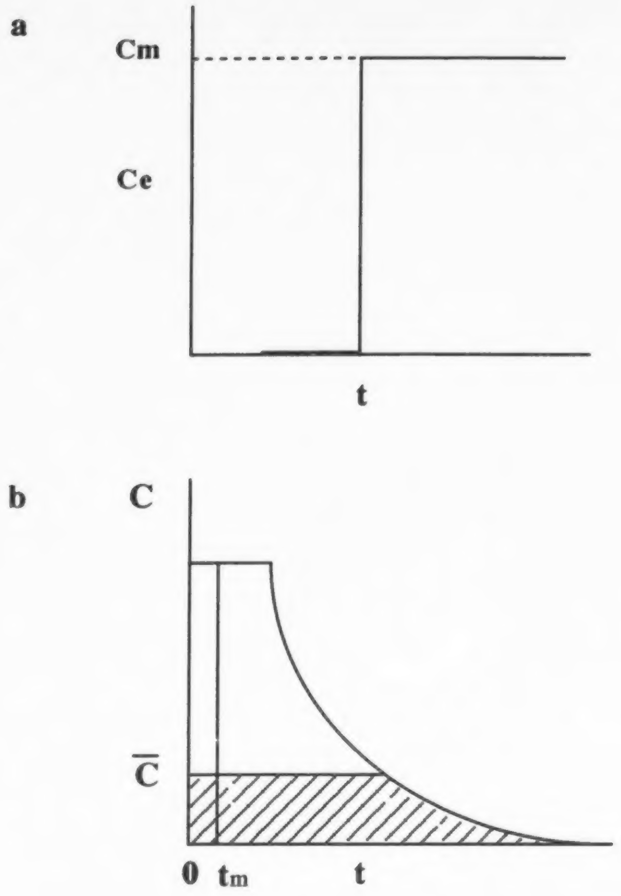

Figure 3.4 Frontal chromatograms. **a** is a selfsharpening front boundary. **b** is a diffuse rear boundary.

The amount of sample taken up by the sorbent when the breakthrough begins to occur at point c is the initial breakthrough and is proportional to the area of *abcd* in Figure 3.3. The area of interest in calculating C_s for a point on the isotherm is *aed*. In FA, a separate breakthrough curve for each point on the isotherm is carried out and therefore, this method needs more sample solution.

3.4 Principle of the Column Equilibration Method

In this work, the "column equilibration" method [55] was used to measure the sorption isotherms of naphthalene on PRP-1 and PRP-∞. The basic principles behind the column equilibrium technique are similar to those in frontal analysis. A shorter column packed with a known amount of sorbent is used instead of a larger analytical column. A known concentration of a sample solution is pumped through the short column to achieve total breakthrough. The amount sorbed at equilibrium is then eluted and determined. The amount eluted must be corrected by the amount present in the hold-up volume:

$$N_{sorb}=N_{elu}-N_{ex} \tag{3.7}$$

$$N_{ex}=C_m V_{hold\text{-}up\text{-}T} - V_p C_m = C_m V_{hold\text{-}up} \tag{3.8}$$

For PRP-1, V_p, the intra-particle pore volume of packing, is the product of the specific pore volume and the weight of the packing in the bed. For PRP-∞, V_p is zero. C_m is the concentration of the sample solution. $V_{hold\text{-}up\text{-}T}$ includes both inter and intraparticle volume as well as the spaces in, above and under the retaining screens. The $V_{hold\text{-}up\text{-}T}$ which was determined using the unretained compound phloroglucinol was calculated with equation 3.9.

$$\frac{A_{bed}}{V_{hold\text{-}up\text{-}T}} = \frac{A_{inj}}{V_{inj}} \tag{3.9}$$

A_{bed} is the area of a peak eluted from the shallow bed. A_{inj} is the area of a peak eluted from the injector. V_{inj} is the volume of the injector which has been calibrated as described in section 2.7. It is 20.46 ± 0.95µL.

The measured $V_{hold\text{-}up\text{-}T}$ was corrected by subtracting the intra-particle pore volume, V_p, of PRP-1. This correction, shown in equation 3.10, is necessary, because the sorption of a sample into the pores of the packing must be considered to be a part of the overall rate of sorption.

$$V_{hold\text{-}up} = V_{hold\text{-}up\text{-}T} - V_p \tag{3.10}$$

C_s, the concentration of a solute sorbed in the sorbent, is shown in equation 3.11:

$$C_s = \frac{N_{sorb}}{Wt} \tag{3.11}$$

where W_t is the weight of the sorbent.

3.5 Results and Discussion

3.5.1 Hold-up Volume for Naphthalene on PRP-1

The $V_{hold\text{-}up\text{-}T}$ for PRP-1 was measured by loading a standard solution of phloroglucinol in 85% MeOH/H_2O onto the shallow bed for 60 seconds. The same solution of phloroglucinol was also injected via the injector V4 as shown in Figure 2.2. The experimental parameters in the measurements of the $V_{hold\text{-}up\text{-}T}$ are shown in Table

3.1. The areas from the bed injection and from the injector are shown in Table 3.2. The average areas from bed and injector were used to calculate the $V_{hold\text{-}up}$. The hold-up volume determined using equations 3.9 and 3.10 is found to be 8.3 ± 0.8 μL. The standard deviation associated with the $V_{hold\text{-}up}$ was calculated from error propagation at the 95% confidence limit.

3.5.2 Hold-up Volume for Naphthalene on PRP-∞

The same procedures and apparatus were used in the measurement of the hold-up volume in PRP-∞. Since PRP-∞ does not have macropores, the hold-up volume includes the volume between the particles and the spaces within and below the retaining screen and the porous Zitex membranes. For PRP-∞, the $V_{hold\text{-}up\text{-}T}$ is equal to $V_{hold\text{-}up}$. The experimental parameters in the measurement of $V_{hold\text{-}up}$ are shown in Table 3.3. The areas from the shallow bed injection and the injector, V4, along with the standard deviations are shown in Table 3.4. The average areas from bed and injector were used to calculate the $V_{hold\text{-}up}$. The hold-up volume determined using equations 3.9 and 3.10 is found to be 5.8 ± 0.5 μL. The standard deviation associated with the $V_{hold\text{-}up}$ was calculated from error propagation at the 95% confidence limit.

3.5.3 Naphthalene Sorption Isotherm on PRP-1

The naphthalene sorption isotherm on PRP-1 was measured using the apparatus shown in Figure 2.2 and using the procedure described in section 2.5.5. The experimental parameters in the measurement of the sorption isotherm are shown in Table 3.5. The solid

Table 3.1 Experimental parameters for the measurement of the hold-up volume in the shallow bed of PRP-1 using 7.068 x 10^{-5} M phloroglucinol in 85% MeOH/H_2O.

Parameter	Value
PRP-1	1.19 ± 0.02 mg
F2	0.5 ml/min
Detector wavelength	276 nm
Detector range	0.1 A.U.F.S.
Recorder chart speed	0.2 In/min
Recorder range	0.1 V.F.S.
Sample solution temperature	25.1 ^{o}C ± 0.2 ^{o}C
Shallow bed temperature	25.2 ^{o}C ± 0.2 ^{o}C
Integrator ATT^2	-1
THRSH	-1
PK WD	0.04
$V_{hold-up}$	8.3 ± 0.8 μL

Table 3.2. The areas, A_{bed}, from injection of 7.068×10^{-5} M phloroglucinol onto the shallow bed of PRP-1 for 60 seconds, and the areas, A_{inj}, from the injector. The average area results were used to calculate the hold-up volume.

Run No.	A_{bed}	A_{inj}
1	13849	30271
2	13453	29088
3	13495	28676
4	13345	30295
5	13326	30855
Average	13494	29837
SD	211	914

a $V_{hold\text{-}up}$ was calculated with equations 3.9 and 3.10.

Table 3.3 Experimental parameters for the measurement of the hold-up volume in the shallow bed of PRP-∞ using 7.560×10^{-5} M phloroglucinol in 85% MeOH/H_2O.

Parameter	Value
PRP-∞	3.15 ± 0.02 mg
F2	0.5 ml/min
Detector wavelength	276 nm
Detector range	0.1 A.U.F.S.
Recorder chart speed	0.2 In/min
Recorder range	0.1 V.F.S.
Sample solution temperature	24.6 ^{o}C ± 0.2 ^{o}C
Shallow bed temperature	24.8 ^{o}C ± 0.2 ^{o}C
Integrator ATT^2	-1
THRSH	-2
PK WD	0.64
Vhold-up	5.8 ± 0.5 μL

Table 3.4 The areas, A_{bed}, from injection of 7.560×10^{-5} M phloroglucinol onto the shallow bed of PRP-∞ for 90 seconds, and the areas from the injector, A_{inj}. The average area results were used to calculate the hold-up volume.

Run No.	A_{bed}	A_{inj}
1	19884	66702
2	18202	68318
3	19043	69154
4	19319	69366
5	19906	69393
6	20806	NA
Average	19527	68587
SD	888	1141

a $V_{hold\text{-}up}$ was calculated with equations 3.9 and 3.10.

line in Figure 3.5 is a fit of the Langmuir equation to the data points with a nonlinear least squares regression. The data is shown in Table 3.6. The fitting parameters give a = (2.77 ± 0.49) x 10^{-5}, and b = (1.49 ± 0.258) x 10^{3} for the constants in equation 3.2. The isotherm is linear up to a solution concentration of approximately 4 x 10^{-5} M as illustrated in Figure 3.6. The slope of the linear part of the isotherm gives the distribution coefficient, K_D to be 0.0392L/g ± 0.0012L/g. The slope was calculated from the first four points with a correlation coefficient of 0.999. The sorption rate curve was measured at a solution concentration of 5 x 10^{-6} M which is clearly within the linear range of the sorption isotherm.

3.5.4 Naphthalene Sorption Isotherm on PRP-∞

The same method, apparatus and procedure as those on PRP-1 were used in the measurement of the sorption isotherm of naphthalene on PRP-∞. The experimental parameters are presented in Table 3.7. Figure 3.7 shows a linear fit to the experimental data points with a correlation coefficient of 0.999. The data is shown in Table 3.8. The slope of the linear fit gives the distribution coefficient, K_D to be (6.31 ± 0.08) x 10^{-3} L/g. undoubtedly, the isotherm on PRP-∞ would become non-linear at higher concentrations than those employed. However, since only the linear region was of interest, higher concentrations were not used.

Table 3.5 Experimental parameters in the measurement of the sorption isotherm of naphthalene onto PRP-1 in 85% MeOH/H_2O.

Parameter	Value
PRP-1	1.14 ± 0.02 mg
F2	0.5 ml/min
Detector wavelength	276 nm
Detector range	0.1 A.U.F.S.
Recorder chart speed	0.2 In/min
Recorder range	0.01 V.F.S.
Sample solution temperature	$25.2^{o}C \pm 0.2^{o}C$
Shallow bed temperature	$24.8^{o}C \pm 0.2^{o}C$
Integrator ATT^2	low con. -2, high conc.5
THRSH	low conc. -3, high conc.1
PK WD	0.04

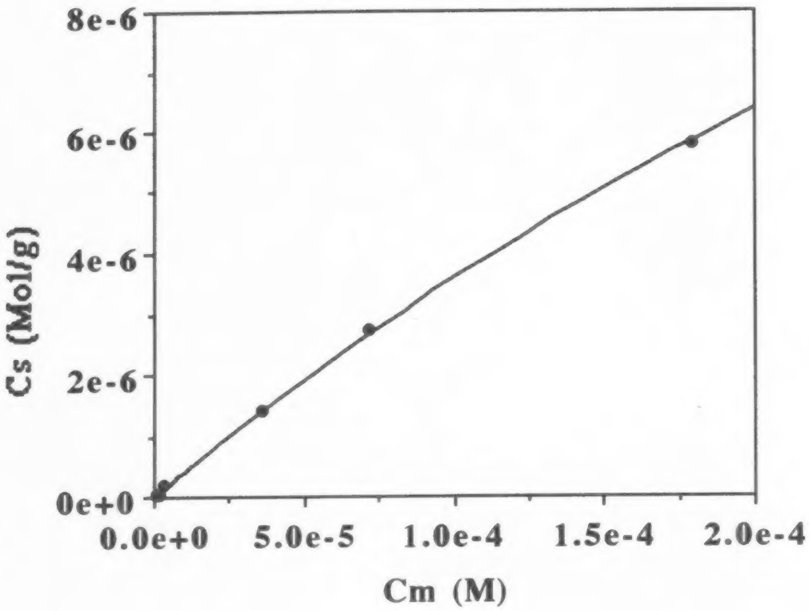

Figure 3.5 Naphthalene sorption isotherm on PRP-1. The solid line is the fit of Langmuir equation.

Table 3.6 The data of the sorption isotherm of naphthalene on PRP-1.

Run No.	Concentration (M)	Naphthalene sorbed (mol/g)
1	7.140×10^{-7}	2.622×10^{-8}
2		2.810×10^{-8}
1	1.942×10^{-6}	5.393×10^{-8}
2		5.285×10^{-8}
1	3.570×10^{-6}	1.920×10^{-7}
2		2.045×10^{-7}
1	3.570×10^{-5}	1.380×10^{-6}
2		1.410×10^{-6}
1	7.139×10^{-5}	2.794×10^{-6}
2		2.733×10^{-6}
1	1.785×10^{-4}	5.842×10^{-6}
2		5.761×10^{-6}

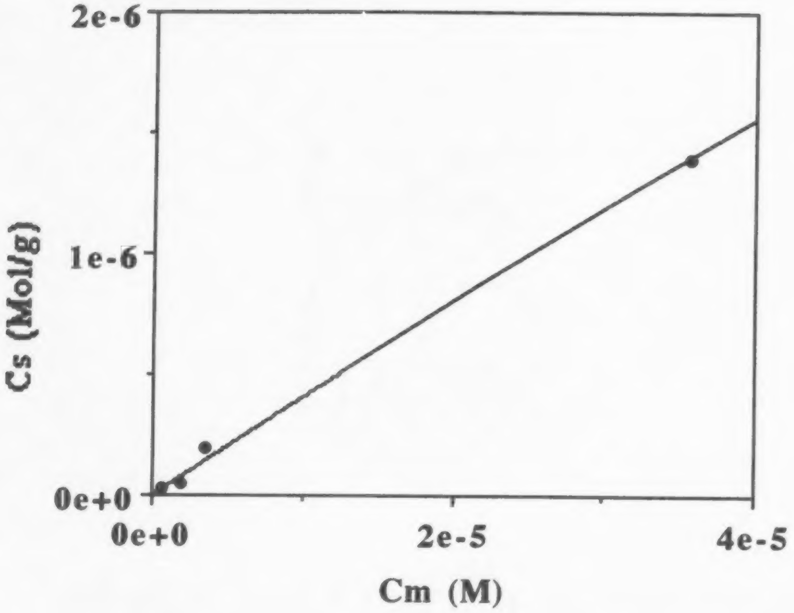

Figure 3.6 The linear part of the naphthalene sorption isotherm on PRP-1 in 85% MeOH/H_2O. The line shown is the result of a linear regression on these first four data points with a correlation coefficient of 0.999.

Table 3.7 Experimental parameters in the measurement of the sorption isotherm of naphthalene onto PRP-∞ in 85% MeOH/H_2O.

Parameter	Value
PRP-∞	3.67 ± 0.02 mg
F2	0.6 ml/min
Detector wavelength	276 nm
Detector range	0.1 A.U.F.S.
Recorder chart speed	0.2 In/min
Recorder range	0.01 V.F.S.
Sample solution temperature	25.0^oC ± 0.2^oC
Shallow bed temperature	24.8^oC ± 0.2^oC
Integrator ATT^2	low con.0, high conc.2
THRSH	0
PK WD	0.64

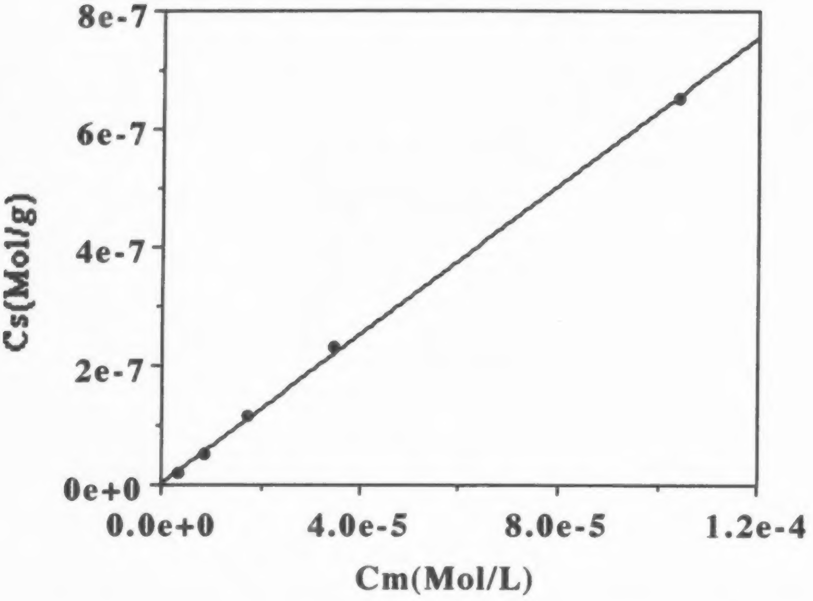

Figure 3.7 Naphthalene sorption isotherm on PRP-∞ in 85% MeOH/H_2O. The solid line is the result of a linear regression with a correlation coefficient of 0.999.

Table 3.8 The data of the sorption isotherm of naphthalene on PRP-∞.

Run No.	Concentration (M)	Naphthalene sorbed (mol/g)
1	3.452×10^{-6}	2.156×10^{-8}
2		2.003×10^{-8}
1	8.628×10^{-6}	5.572×10^{-8}
2		5.040×10^{-8}
3		4.43×10^{-8}
1	1.726×10^{-5}	1.146×10^{-7}
2		1.151×10^{-7}
3		1.127×10^{-7}
1	3.451×10^{-5}	2.381×10^{-7}
2		2.336×10^{-7}
3		2.200×10^{-7}
1	1.035×10^{-4}	6.261×10^{-7}
2		6.666×10^{-7}
3		6.627×10^{-7}

Chapter 4

Naphthalene Sorption Kinetics

4.1 Introduction

The bandbroadening and asymmetry of a peak eluted from a chromatographic column in the linear region of the isotherm are determined by the kinetic processes in the column. In order to study the origin of the bandbroadening and tailing of naphthalene in 85% MeOH/H_2O on PRP-1 and to predict the contribution of intra-particle sorption rate to elution peak shape, the intraparticle sorption rates of naphthalene onto PRP-1 were measured with the shallow bed technique in the linear region of the sorption isotherm. To predict the peak eluted from a HPLC column, the sorption rate data was fit to an empirical tri-exponential equation with non-linear least squares regression.

Chapter 5 will present the approaches used in the prediction of the elution profiles based on the sorption rate curves.

In chapter 6, the origin of the slow sorption rate of naphthalene on PRP-1 will be studied using the information from theoretical kinetic models and from the sorption rate curves of naphthalene on PRP-∞.

4.2 Theory

Generally speaking, a solute transporting from a bulk solution into a porous particle can experience any or all of the following processes as shown in Figure 4.1: a. film diffusion [66, 67]. b. intraparticle diffusion [61, 67-70]. c. adsorption onto the surface of the pore walls [69]. When a solute transports from a particle into the bulk solution, the above processes are reversed. A slowness of any of the processes can result in bandbroadening and tailing for a solute migrating in a column [69].

An important distinction to be made is that between film diffusion and all of the other steps described, including intraparticle diffusion and adsorption onto the surface of the pore walls. All of the later taken together, are responsible for the intraparticle sorption rate. Experimentally, it is easy to eliminate film diffusion by using a very high flow rate, as described below.

4.2.1 Film Diffusion

Before being sorbed onto porous particles, a solute initially in the mobile phase must first transport through a stagnant film around the particle by diffusion as shown in Figure 4.1. If diffusion through the film is the rate controlling step and other steps are fast, the total sorption rate will be governed by the following rate law shown in equation 4.1 [71]:

$$\frac{Q_t}{Q_\infty} = 1 - e^{-Rt} \tag{4.1}$$

where Q_t is the amount of solute sorbed at time t, Q_∞ is the amount of solute sorbed at equilibrium, and R is the rate constant [71]. For a spherical particle, R can be expressed as in equation 4.2 [71]:

$$R = \frac{3\, D_{film}}{r_0\, \Delta r_0\, K_D\, \rho} \tag{4.2}$$

where r_0 is the radius of the particle, Δr_0 is the film thickness, K_D is the distribution

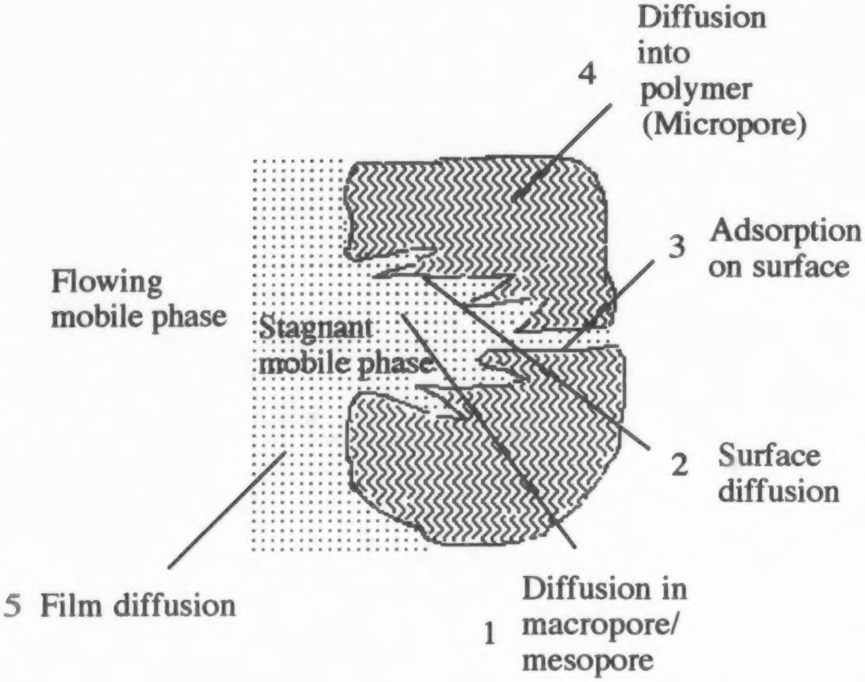
Diffusion into polymer (Micropore)
4
3
Adsorption on surface
Flowing mobile phase
Stagnant mobile phase
2
Surface diffusion
5 Film diffusion
Diffusion in macropore/ mesopore
1

Figure 4.1 Schematic diagram shows some possible steps which can occur in a porous particle. Intraparticle sorption includes both diffusion of a solute through pores / into polymers (1, 2, 4) and adsoprtion on pore walls/polymers (3), but not film diffusion (5).

constant with units of ml/g, ρ is the particle density, and D_{film} is the diffusion coefficient in the film. The film thickness can be calculated with empirical equations 4.3 and 4.4 [66]:

$$\Delta r_0 \approx \frac{0.2\ r_0}{1+70\ r_0 U} \quad \text{low flow rate} \qquad (4.3)$$

$$\Delta r_0 \approx \frac{0.0029}{U} \quad \text{high flow rate} \qquad (4.4)$$

where U is the interstitial linear velocity. The film thickness decreases with decreasing particle diameter at a constant U and with increasing flow rate. At a very high flow rate, the film thickness is negligible, so, the rate of the film diffusion is extremely fast. Since film diffusion and intraparticle sorption rate occur in series, the faster the film diffusion becomes, the smaller contribution it makes to the rate. At a sufficiently high linear velocity, rate control becomes exclusively intraparticle sorption.

4.2.2 Intraparticle Diffusion

Many commercial polymer sorbents consist of small microspheres formed into macrospheres. The macropores and mesopores are spaces between the microspheres or the aggregates of microspheres. The micropores are the spaces between the polymer chains. Intraparticle diffusion includes: step 1, diffusion through the solution in the macro/mesopores in the stagnant mobile phase and step 2, surface diffusion on the walls of macro/mesopores, and step 4, diffusion in the micropores as shown in Figure 4.1. The relative importance of the micropore and macropore resistances depends on the ratio of the diffusional time constants, which vary widely with the combination of solute and mobile phase. The time constant is proportional to the square of the particle radius. Variation of the particle size provides a simple and straightforward experimental test to confirm the nature of the control resistance [72].

4.2.3 Adsorption onto the Surface of the Pore Walls

The intraparticle diffusion steps discussed above are the mass transfer term. If the sorption rate is controlled by the adsorption step onto a single type of adsorption site rather than by mass transfer, the sorption rate equation is shown as follows [73, 74]:

$$\frac{Q_t}{Q_\infty} = 1 - e^{-k_{ad}\,t} \tag{4.5}$$

where k_{ad} is the first order adsorption rate constant. Adsorption is usually faster than diffusion [75, 76]. The adsorption step is shown as 3 in Figure 4.1.

4.2.4 The Shallow Bed Theory

The shallow bed mode was earlier described by Boyd [71] and it has been used to study the kinetics of sorption on ion exchange resins [77].

The shallow bed technique was used in this work to measure the sorption rates of naphthalene onto PRP-1 and PRP-∞. There are several kinetic steps in the sorption processes as illustrated in Figure 4.1. The kinetic rate measured with the shallow bed technique includes both intraparticle mass transfer and adsorption. For convenience, the term "sorption" is used to refer to the combined processes of pore diffusion and surface adsorption.

The sorption of a species i from a mobile phase onto one type of the sorption sites in the stationary zone is a reversible process with a forward and reverse rate constant k_f and k_r respectively:

$$i_m \underset{kr}{\overset{kf}{\rightleftharpoons}} i_s \tag{4.6}$$

Under reversible conditions, the observed sorption rate can be expressed as follows [78]:

$$\text{Rate} = k_f \times C_{i,m} - k_r \times C_{i,s} \tag{4.7}$$

The equilibrium constant, K_D, for the reversible reaction is the ratio of the forward rate constant to the reverse rate constant:

$$K_D = \frac{k_f}{k_r} \tag{4.8}$$

and

$$K' = K_D \phi \tag{4.9}$$

where K' is the capacity factor, and ϕ is the phase ratio of a column.

A high flow rate of sample through the shallow bed is required both to eliminate the contribution of film diffusion rate and to meet another important condition, the "infinite solution volume" condition [61. 66] also called the shallow bed condition. These conditions are met when the sample concentration in the effluent is essentially constant and equal to the concentration of the influent solution at all the times. If the shallow bed condition is met, every particle in the bed would encounter the mobile phase solution at the same concentration. There would be no sample concentration gradient along the bed in the mobile phase due to the sorption of a sample onto the stationary phase.

In order to obtain a higher flow rate, a short column was used to reduce the resistance of the bed. A short column is also necessary to minimize the time needed to sweep out the solution between particles in the bed with sample solution. In the shallow bed experiment, this step is assumed to occur instantaneously because of the very high flow rate. All the particles in the shallow bed experience the same solution at all times and will therefore undergo sorption processes at the same rate regardless of geographical location in the column.

Strictly speaking, the shallow bed condition is impossible to achieve because sample is being sorbed out of mobile phase. However, in practice, if the flow rate passing through the shallow bed is sufficiently faster than the rate of decrease in the concentration of a sample in the mobile phase, the sample concentration in the mobile phase is essentially constant. For fast sorption kinetics, a high flow rate is needed. In this study, the shallow bed condition was tested by measuring the amount of naphthalene sorbed at short times against the flow rates through the bed. This is a good test because the concentration in the mobile phase is reduced most rapidly early in the experiment.

It is interesting to compare a sorption rate curve and a breakthrough curve. The sorption rate curve is a plot of the sample concentration, in the stationary phase, C_s, versus time [61]. The sample concentration in the effluent is always constant when the shallow bed condition is met and is equal to the sample concentration in the influent. At a very short time, a small amount of sample has been sorbed onto the sorbent, but under the shallow bed condition, the amount sorbed does not cause any significant decrease in sample concentration in the mobile phase. At a long time, the sorbent approaches equilibrium with the mobile phase. A sorption rate curve is illustrated in Figure 4.2. The faster the sorption rate, the more steep the initial part of sorption rate curve.

The typical breakthrough curve is a plot of the sample concentration in the effluent, C_e, versus

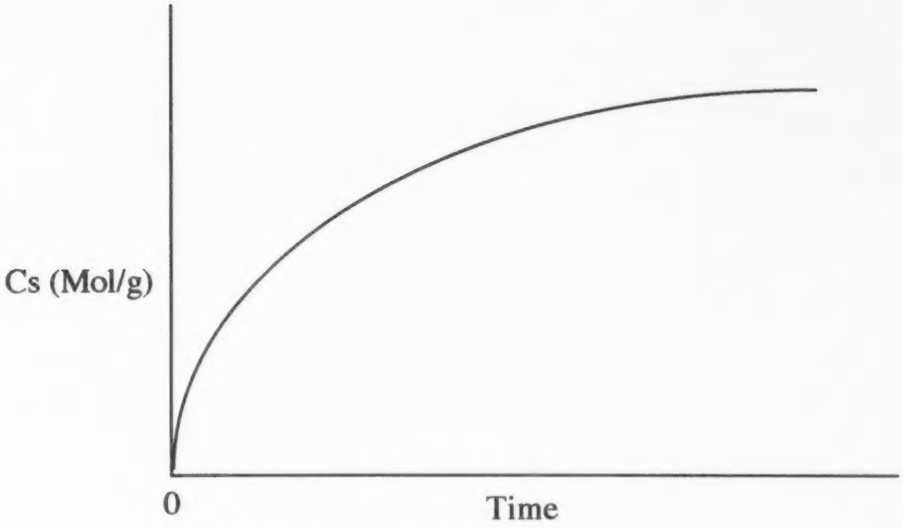

Figure 4.2 Diagrammatic sorption rate curve for a sample. Cs is the amount of the sample sorbed on the sorbent at a certain time

time. It is measured at relatively slow linear velocity so that the sorbent and solution are not far from load equilibrium. No sample is eluted and detected in the effluent before breakthrough. The concentration in the effluent changes continuously until the total breakthrough (point e in Figure 3.3) occurs where the sample is at equilibrium between the sorbent and the mobile phase. In contrast, at the high linear velocities used in a shallow bed, the sorbent and solution are far from equilibrium early in the experiment. The breakthrough for the shallow bed occurs at time zero. However, the sorbent is not at equilibrium with the sample solution. Equilibrium between sorbent and solution is slowly approached.

4.2.5 Empirical Tri-exponential Equation

In order to predict the peak which would elute from an analytical HPLC column of PRP-1, it was desired to fit the sorption rate data of naphthalene on PRP-1 to an empirical tri-exponential equation, using non-linear least squares regression [79]. The tri-exponential equation is not based on any theoretical model of particle or pore properties. The tri-exponential has the form shown in equation 4.10 [80]:

$$F = \frac{Q_t}{Q_\infty} = 1 - \frac{n_1}{n_0}\exp(-k_1 t) - \frac{n_2}{n_0}\exp(-k_2 t) - \frac{n_3}{n_0}\exp(-k_3 t) \tag{4.10}$$

where F is the fraction of solute sorbed at time t, n_1 through n_3 are moles of solute sorbed at equilibrium on each hypothetical type of site in a column, and k_1 through k_3 represent the sorption rate constants associated with each type of hypothetical sorption site of n_1 through n_3. In the linear region of the solute sorption isotherm, the values of n_1 through n_3 are proportional to the number of type 1 through type 3 hypothetical sorption sites. n_0 is proportional to the total number of the hypothetical sorption sites available for a solute in a column ($n_0 = n_1 + n_2 + n_3$). It should be realized that in reality a column could have more than three types of sorption sites, and the theoretical number of each hypothetical site could be more than n_1, n_2 and n_3.

It is important to note that no physical reality should be attached to the parameters in equation 4.10. It is only in a purely formal sense that there are different types of sites in a column. When describing the sorption rate curve with equation 4.10, it is not necessary to make any assumption about pore structure, mass transfer and so on. The tri-exponential equation is used instead of a mono-, or bi-exponential equation because it gives the best fit to the experimental sorption data for naphthalene on PRP-1 with the least number of exponential terms. It is also important to point out that the six parameters in the equation 4.10 are not independent, but are correlated.

The choice of a sum of exponential terms to describe the sorption rate curve is necessary because it is possible to predict the shapes of the hypothetical elution peaks that would arise separately from each of the exponential terms in equation 4.10. An exponential term is required in the calculation of the predicted peak using Giddings' probability equation [69, 83] because the probability equation was derived under the condition of reversible first order kinetics. Furthermore, it is possible to convolve all such peak shape contributions mathematically in order to predict the elution peak that would arise from the overall sorption rate.

4.3 Measurement of Sorption Rates

The sorption rate of a solute on HPLC stationary phases has been the subject of relatively few studies. It has proven to be an experimental challenge. Chromatography, relaxation and uptake rate methods are three different methods which have been previously applied to experimentally measure intraparticle sorption rates on chromatographic packings.

In a chromatographic method, a column packed with a sorbent is subjected to a perturbation in the inlet concentration of a solute, and an elution peak at the column outlet is measured. The plate height is calculated from the peak. A plot of the plate heights versus the mobile phase linear velocity is fitted to a theoretical equation such as the van Deemter equation shown in equation 4.11 [49, 84, 85].

$$\overline{H} = \frac{B}{\overline{U}_0} + A + C\,\overline{U}_0 \tag{4.11}$$

In term of chromatography, the intraparticle sorption rate which is related to the C term in the van Deemter equation, can be determined.

Muller and Carr [86] determined the rate constants for dissociation of sugar derivatives from silica immobilized concanavalin A using high performance liquid affinity chromatography. They used a theoretical plate height equation given by Horvath and Lin [87] to fit the plot of the plate height versus the mobile phase linear velocity. The kinetic term, including diffusion in the stagnant mobile phase and adsorption-desorption of a solute by the ligand in the stationary phase, was obtained by subtracting the non-kinetic term, including the axial dispersion and the non-uniform mobile phase linear velocity effects, from the overall kinetic effects. The non-kinetic term was either estimated by a non-adsorbed sugar with the same molecular weight and a similar chemical structure or by using various structural packing parameters from typical literature data for the packing.

Similarly, Groh and Halaze [85] determined the kinetic rate constants in the pores of a column filled with silica in size exclusion chromatography. The plot of the plate height versus the mobile phase linear velocity was fit to the van Deemter equation [84]. The total plate heights were measured using dry eluent where the solute can penetrate into the pores. The plate heights associated with the interstitial processes were measured with a wet eluent where the pores are filled with water and therefore which is impenetrable to the solute. The kinetic rate constants associated with the pores were obtained by subtraction of the interstitial plate heights from the total plate heights.

A similar technique was also used in affinity chromatography [88] where the peak split into a non-retained and a retained component. The fraction of a solute retained was plotted versus the mobile phase linear velocity. The slope gave the sum of the mass transfer resistances and the adsorption-desorption resistance. Under a situation where one of the resistances can be determined experimentally, the other can be obtained by subtraction.

For the measurement of the intraparticle sorption rate by the chromatographic method, the experimental setup is simple, a normal HPLC system is required. In the situation that the adsorption-desorption is fast, the mass transfer process is the limiting step. The total mass transfer resistance can be determined and the individual mass transfer resistance, such as external film diffusion, macropore diffusion and micropore diffusion, can be obtained by varying the size of a particle. On the other hand, if adsorption-desorption is the limiting step, the mass transfer term is negligible and can not be accurately measured [89].

The ease with which the kinetic term and the axial dispersion term can be determined depends on the relative magnitude of the resistances. If the kinetic term is small, the dispersion of a sample will be caused mainly by the axial dispersion, and under this condition, it is not possible to derive any information concerning the kinetic resistances. Even when the kinetic term is dominant in the dispersion of a sample, plate heights from the non-kinetic term must be subtracted from the total plate heights. This will introduce errors when these non-kinetic terms are estimated using packing parameters.

Although the plate height theory is well developed, the accuracy in the calculation of the plate heights are complicated by such factors as extra-column effects [87], errors in the calculation of the statistical moments [90], and the dependency of some terms on the capacity factor, K' [87, 91, 92]. In addition, the chromatograms must be measured in the linear region of the isotherm, because the total plate heights are equal to the sum of several individual plate heights from each process which are independent of each other within the linear region of the isotherm [89].

In the relaxation method [93], a system is initially at equilibrium under a given set of conditions. One of the physical properties is suddenly changed and the system is no longer at equilibrium. It then relaxes to a new state of equilibrium. The speed with which it relaxes can be measured, usually by spectroscopy. There are various ways in which the equilibrium can be disturbed, such as pressure change and temperature change. By jumping the temperature or the pressure to perturb the equilibrium on a time scale faster than the fastest rate of reaction of the system, one can observe the system as it relaxes back to its new equilibrium and thereby determine the rates of the reaction.

The first direct measurement of sorption-desorption rates on an alkylated silica surface in ion pair chromatography was performed by Marshall and coworker [94] using a pressure jump relaxation kinetic method with a fluorescent solute. The sorption rate constant on the surface was found to be 1.4 x10^9 l/mol s. The desorption rate constants on silica surface investigated ranged from 600 s^{-1} to 2000 s^{-1} for different alkylated silicas. They also observed that the first fast rise in fluorescence intensity within 5 μs was followed by a second, slow fall in florescence intensity around 0.025 to 0.1 seconds. The time of the slow fluorescence decay was independent of the concentrations of ion pair in the solution, of the amount of silica and of the chemical modification. However, the complete relaxation time was dependent on the pore sizes of the silica used. For a large pore size silica, the relaxation time was larger. It suggested that the sample molecules may penetrate deeply into the particle.

The pressure relaxation method can be used to measure a very fast sorption-desorption rate of 50 to 80μs [94] . However, as the molecules penetrate into the pore deeply, it becomes harder to observe the fluorescence signals .

In another paper published by Marshall et al.[95], a temperature jump relaxation kinetic method was used to measure the sorption-desorption rate constant at the C_{18} surface on a 100μs time scale. The desorption rate constant on ODS surface was 4.9 x 10^8 l/mol s.

A slow relaxation at a longer time of 2 ms was also observed and was temporarily attributed to diffusion of molecules within the porous structures of the silica gel.

The last of the commonly used approaches for measuring the sorption rate is the uptake rate measurement. The uptake rate measurement can be performed in two modes. One is the batch mode, the other is the column mode. In the batch mode [96-98], a known weight of stationary phase is contacted with a solution of known concentration and volume of the sample at a constant temperature. Agitation is provided by stirring or shaking. The batch mode can be performed with either "infinite solution volume" where the fraction of solute sorbed out of the solution is very small, so that the concentration of the solute in the solution is essentially constant. The amount of sample sorbed on the sorbent has to be measured. The sorbent must be separated from the solution periodically, and the amount solute sorbed is eluted and determined. In "finite solution volume" where the fraction of a solute sorbed from the mobile phase is significant, either the concentration change in the solution or the amount sorbed on the sorbent may be measured.

In the batch method, a number of sample withdrawals are required for determining the uptake as a function of time. This method is used to measure relatively slow sorption rate. However, it consumes a small amount of sample solution and solvent. The apparatus is simple, the measurement at a certain time can be repeated, and therefore statistical errors can be reduced.

In the shallow bed column mode [66, 71, 77, 99-103], a very thin layer of sorbent is packed in a tube, and a known concentration of solution is forced through the bed at a high and constant flow rate for various periods of times. The uptake rates are measured under the "infinite solution volume" condition where the concentration of a solution in the effluent is nearly identical to that in the influent solution, and all of the sorbent particles in the bed are bathed in a solution containing the initial concentration of solute. The solute sorbed on the sorbent is then eluted and determined.

The shallow bed technique can be used to measure fast sorption rate. However, in the shallow bed technique, the apparatus is complex, more sample solution and eluent are used. In this work, the shallow bed technique was used in a modified form for the measurement of the sorption rates of naphthalene on PRP-1 and PRP-∞ .

4.4 Results and Discussion

4.4.1 Testing Switching Valve, V2, to Control the Exposure Times

The sorption rate of naphthalene onto 10μm diameter of PRP-1 was shown to be very fast. In an earlier, approximate measurement, over 30% of the equilibrium amount had been reported to be sorbed within 0.4 seconds [54]. It is important to measure the sorption rate curve accurately, especially at shorter times. A six way rotary valve was introduced to control the exposure time, because opening and closing a valve is much faster than pulling a slider with a lever. The minimum time, which is determined by the speed at which the valve could be opened and closed, is 0.04 second, which is ten times smaller than that in the previous study [54]. Valve V2 was placed right below the slider valve as shown in Figure 2.2. The question was whether the flow through the bed was really stopped when V2 was closed. To answer this question, the bed was left in the loading position for various periods of times when V2 was closed, while V1 was set to sample solution. The amount of a sample which enters the bed when valve V2 is closed, was independent of time as shown in Table 4.1.

During normal operation, 5 seconds was the minimum time with V2 closed. Table 4.2 shows the amount of phloroglucinol, a non-sorbed compound, entering the bed when V2 was opened. The amount of phloroglucinol in the bed with V2 closed (Table 4.1) is only 27% to 22% of that amount with V2 being opened from 0.2 to 2 seconds (Table 4.2). This amount of phloroglucinol has not reached the sorbent yet, because the height of the

Table 4.1 The amount of 9.744×10^{-5} M phloroglucinol in 85% MeOH/ H_2O in a bed of PRP-1 when valve V2 was closed.

Time (s)	Area
5	20072
10	18865
32	19204
40	20153
60	19615
Average ± SD	19582 ± 548

Table 4.2 The amount of 9.744×10^{-5} M phloroglucinol in 85% MeOH/H_2O in a bed of PRP-1 when the valve 2 was opened.

Time (s)	Area	RD % [a]
0.28	76928	26
0.32	73536	27
0.33	74507	26
0.66	80015	25
0.91	87554	22
1.2	88431	22
1.9	87887	22

[a] $$\mathrm{RD} = \frac{\text{Area (with V2 closed)}}{\text{Area (with V2 opened)}}$$

shallow bed is about 0.43 mm , and the height of the 2μm s.s retention screen at the bottom plus the space below the screen is about 0.15mm. The total height of the Kel-F insert in the slider, in which a hole is drilled to accommodate the shallow bed, is 2.2 mm. 27% of the total height of the hole is 0.6 mm. This means that the phloroglucinol containing solution moves only 0.6 mm into the hole before V2 is opened. Since, the top of the sorbent bed is about 1.6 mm down the hole, no phloroglucinol has come in contact with the sorbent before V2 is opened. The same should be true of the naphthalene containing solution. It is the amount sorbed on the packing that is of interest in the measurement of the sorption rate curve, but none contacts the packing before V2 is opened. Therefore, as desired, the sorption rate experiment begins only when V2 is opened.

4.4.2 Shunting off the Sample Flow Through the Bed

Uniformity of flow through the bed is also important in the measurement of the sorption rate. All the particles in the bed must be exposed simultaneously to either the eluent driven by the HPLC pump or to the sample solution driven by a constant pressure cylinder. The solution which flows through the bed was shunted off to bypass the bed when the slider was being pulled from the sample loading to the sample elution position or the reverse. If the eluent were not shunted off while the bed were being pulled from the loading to the elution position, all the particles in the bed would not contact the eluent simultaneously. Those particles on the right edge of the bed would encounter the eluent first, this will cause non-uniformity in the packing.

One important thing that needed to be checked was that the flow rates through the bed in the elution position must be constant regardless of the position to which V3 is switched. The area of the eluted solute peak seen in the detection, which is proportional to the amount of naphthalene sorbed on the packing, is also inversely proportional to the flow rate. Therefore, the flow rate must be kept constant during the times when the sorbed amount was being eluted from the sorbent. A constant elution flow rate ensures an accurate determination of the sorption amount.

The flow rate was tested when the bed was in both the loading and the elution positions while the valve V3 was set either to bypass or to flow through the bed. The flow rate of eluent driven by the HPLC pump was set to 0.5 ml/min, and the HPLC pump ran in a constant flow mode. Initially, the shallow bed was in the loading position, and the dummy hole was in the elution position. V3 was set to either bypass or flow through the dummy hole. The flow rates were the same in both positions of V3 as shown in Table 4.3a. There is no statistical difference between the two average flow rates according to the t-test. Next, the slider was moved to the elution position, and V3 was set to both bypass and flow through positions. Again, the flow rates were not altered by opening and closing V3 as shown in Table 4.3b according to the t-test. Therefore, the position of V3 does not affect the flow rate when the HPLC pump is run in the constant flow mode.

4.4.3 Testing the Shallow Bed Condition in PRP-1

One way to determine if the shallow bed condition is maintained in the experiment is to measure the effects of a change of the solution flow rate through the bed on the initial sorption rate curves. The effect will be greatest at the short exposure times where the sorption rate of naphthalene onto the sorbent is highest and the sample concentration in the mobile phase is more likely to be decreased by the sorption of the sample. If the flow rate of the sample solution through the bed is increased, the initial slope of the sorption rate curve will increase until the flow rate is fast enough to maintain the constant concentration in the mobile phase. If the flow rate of the sample solution is increased beyond this point, the sorption rate curve should not vary with flow rates. When this is true it ensures that the shallow bed condition is met, and also that the thickness of the film around the particle is small enough that film diffusion is negligible. The experimental parameters in the test of

Table 4.3a The dependence of flow rate, F2, in Figure 2.2 through the dummy hole on the position of V3. The shallow bed was placed in the sample loading position while V3 was set to either bypass or pass the bed. F2 was set at 0.5ml/min.

V3 was set to bypass the dummy hole

Volume collected (ml)	Time (min)	F2 (ml/min)
1.07	2.0336	0.526
1.04	2.0750	0.501
1.80	3.2992	0.546
	Average F2 ± SD	0.524 ± 0.02

V3 was set to pass the dummy hole

Volume collected (ml)	Time (min)	F2 (ml/min)
1.38	2.5446	0.542
1.29	2.3531	0.548
1.07	2.0508	0.522
	Average F2 ± SD	0.537 ± 0.01

Table 4.3b The dependence of flow rate, F2, in Figure 2.2 through the shallow bed on the position of V3. The shallow bed was placed in the sample elution position while V3 was set to either bypass or pass the bed. F2 was set at 0.5ml/min.

V3 was set to bypass the bed

Volume collected (ml)	Time (min)	F2 (ml/min)
1.73	3.2289	0.536
1.71	3.2490	0.526
2.17	4.2535	0.510
	Average F2 ± SD	0.524± 0.01

V3 was set to pass the bed

Volume collected (ml)	Time (min)	F2 (ml/min)
1.33	2.5035	0.531
1.59	3.1422	0.506
1.54	3.0579	0.504
	Average F2 ± SD	0.514± 0.02

the shallow bed condition for naphthalene on PRP-1 are shown in Table 4.4. Figure 4.3 shows the effects of varying the interstitial linear velocity of the sample solution through the shallow bed on the sorption rate curves within the first 0.7 seconds. The interstitial linear velocity is calculated with equation 2.1. During the initial 0.05 second, the sorption rate curves are approximately linear. The slopes was calculated by the lines corresponding to the points between the time zero and the time 0.05 seconds. The amount

sorbed within this time is 11.2 ± 2.1% of the equilibrium value. The slopes are presented as a function of the interstitial linear velocity in Table 4.5. It is seen that when $U > 16.4$ cm/s, the sorption rate is independent of U. This means that the bed of PRP-1 acts as a shallow bed and the observed sorption rate is equal to the intra-particle sorption rate. All the measurements of the sorption rate curve in this study were made at an interstitial linear velocity higher than 16.3 cm/s.

The volume of sample solution which passes through the spaces between the particles in the bed at the minimum exposure time of 0.04 seconds and the minimum interstitial linear velocity of 16.4 cm/s, (i.e. 21.16 ml/min), is 0.0144 ml. The interparticle volume which was calculated from the interparticle porosity and the weight of packing in the bed is about 8.26×10^{-4} mL. Therefore, about 17 interparticle volumes have passed through the shallow bed within 0.04 seconds. This corresponds to over 400 interstitial bed volumes per second.

4.4.4 Sorption Rate Curves of Naphthalene on PRP-1

Shown in Figure 4.4 is the sorption rate curve of naphthalene on PRP-1 for run 1, and shown in Figures 4.5, 4.6 and 4.7 are the sorption rate curves of naphthalene on PRP-1 for run 2, 3 and 4. The data in each Figure were normalized to the equilibrium value of n_0. The points are experimental. The solid line represents the tri-exponential equation which fits well over the entire sorption rate data. It is seen that about 50% of the total

Table 4.4 Experimental parameters in the measurement of the shallow bed condition in the bed of PRP-1. 4.8986 x 10^{-6} M naphthalene in 85% MeOH/H_2O was used.

Parameter	Value
PRP-1	1.12 ± 0.02 mg
F2	0.5 ml/min
Detector wavelength	276 nm
Detector range	0.02 A.U.F.S.
Recorder chart speed	0.2 In/min
Recorder range	0.01 V.F.S.
Sample solution temperate	25.2 ^{o}C ± 0.2 ^{o}C
Shallow bed temperate	25.1 ^{o}C ± 0.2 ^{o}C
Integrator ATT^2	3
THRSH	1
PK WD	0.16

Table 4.5 Dependence of the initial sorption rates of naphthalene on the interstitial linear velocity of a solution through the shallow bed of PRP-1.

U (cm/s)	Initial rate (mol/g/s)[a]
12.6	2.9×10^{-10}
16.4	6.3×10^{-10}
19.1	7.4×10^{-10}
20.6	6.9×10^{-10}
24.0	6.1×10^{-10}
28.5	6.9×10^{-10}

[a] Initial sorption rate is for the time of 0.05 seconds.

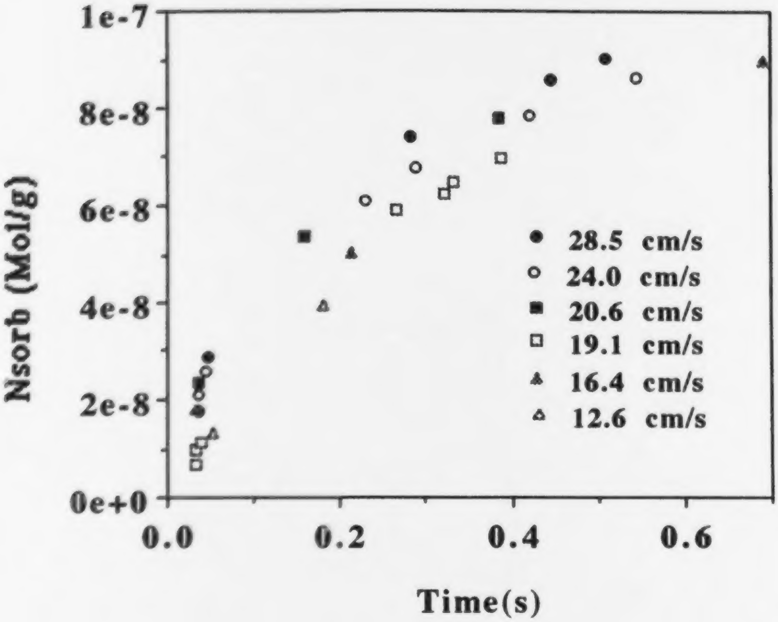

Figure 4.3 Testing the shallow bed condition in PRP-1. Amount sorbed for naphthalene in 85% MeOH/H_2O as a function of the interstitial velocity of sample solution through the shallow bed.

naphthalene was sorbed within 0.2 seconds and about 90% was sorbed within 1.0 second. There is a very slow increase after 1 second.

Also shown in Figure 4.4 are the individual contributions from each of the three terms in the tri-exponential equation. At shorter time, the first term, F_1, is a major contributor, and the second term, F_2, is the intermediate contributor to the sorption rate curve. The third term, F_3, is the major contributor at longer time when F1 and F2 are nearly at equilibrium.

The sorption rate studies were repeated four times. The constants n_i and k_i obtained from the tri-exponential fit of the sorption rate data are presented in Table 4.6. Different linear velocities were used in each of the four kinetic measurements of sorption, but all of them were high enough to achieve both the shallow bed condition and the intraparticle sorption rate control. When comparing the n_i and k_i value in Table 4.6, it is important to realize that these constants have no physical reality, but are merely empirical curve fitting parameters. The six constants in equation 4.10 are not fully independent of one another and the predicted peaks are determined by the six parameters together. As a result, agreement among these parameters from run to run is not required.

Table 4.6 also shows the error norms [81, 82] which is the square root of the square of the residue between the experimental and the theory. The error norms reflects the goodness of the tri-exponential fit. All the error norms for the kinetic sorption rate curves are very close to each other. The presented error norm for each kinetic run is the smallest as determined by fitting the data many times using a variety of initial estimates of n_3 and k_3, since the error norm is only sensitive to n_3 and k_3.

The presence of any significant amount of scatter in the experimental data creates some ambiguity in establishing the values of these six parameters. In particular, it was observed that the constants of k_3 and n_3 in the third term of the tri-exponential were the most sensitive to the experimental errors [80], because they always represent the slowly rising part of a sorption rate curve as shown in Figure 4.4. During the slow rising part, the amount sorbed changes very little, so that the sorbed amount suffers the most experimental errors. A nearly equally good fit of the rate data could be obtained with several combinations of k_3 and n_3. For the curve fitting itself, that is not a problem, because any good fit is acceptable. However, in the prediction of an elution peak using the parameters (chapter 5), different combinations of k_3 and n_3 will cause a problem because the shape of a peak is dependent on the values of k_3 and n_3. Therefore, a set of criteria have been used to select one correct combination of k_3 and n_3 which should be used in the prediction of an elution peak. Those criteria will be explored in Chapter 5.

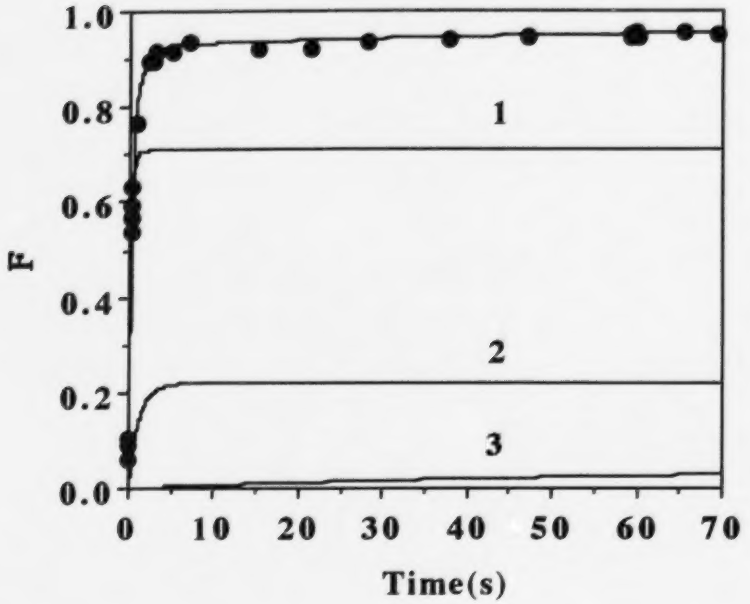

Figure 4.4 Sorption rate curve for naphthalene on PRP-1 in 85% MeOH/H_2O. (W_t = 1.20 mg). The experimental data points are overlaid by a solid line representing the tri-exponential equation. The data are normalized to the value at equilibrium. The tri-exponential constants for this sorption rate curve are shown in the first column in Table 4.6. Also shown are contributions from the three exponential terms to the overall sorption rate curve. Number 1, 2 and 3 are contributions to the curve from the first, second and third term.

Table 4.6 Constants from the tri-exponential equation 4.10 describing four separate sorption rate curves of naphthalene on a shallow bed of PRP-1.

Run No	1	2	3	4
U (cm/s)	19.1	24.0	20.6	17.6
n_0 (mol/g)	1.1×10^{-7}	1.1×10^{-7}	1.1×10^{-7}	8.9×10^{-8}
n_1 (mol/g)	7.8×10^{-8}	2.5×10^{-8}	5.7×10^{-8}	6.7×10^{-8}
n_2 (mol/g)	2.4×10^{-8}	7.8×10^{-8}	4.9×10^{-8}	1.4×10^{-8}
n_3 (mol/g)	5.6×10^{-9}	9.9×10^{-9}	6.7×10^{-9}	6.8×10^{-9}
k_1 (s^{-1})	4.23	19.6	11.1	3.95
k_2 (s^{-1})	0.853	2.70	1.37	0.608
k_3 (s^{-1})	0.0120	0.149	0.0309	0.0244
Error norm	6.4×10^{-9}	6.5×10^{-9}	5.4×10^{-9}	8.1×10^{-9}

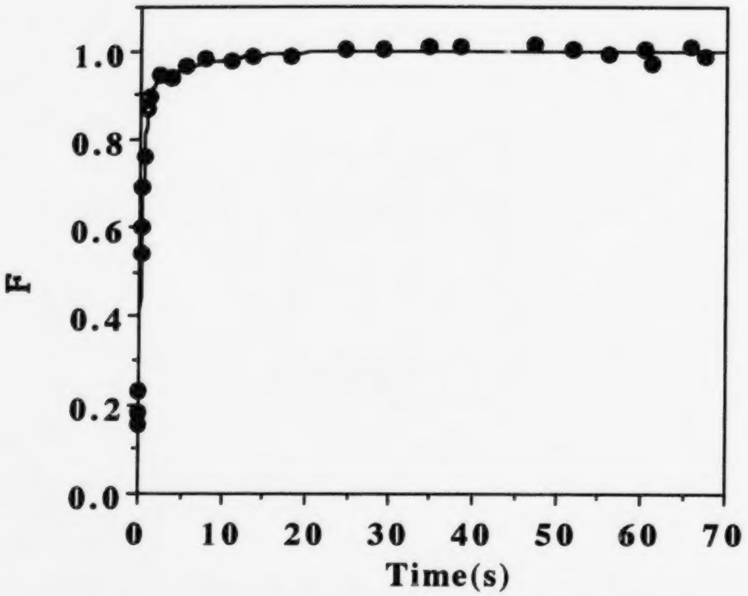

Figure 4.5 Sorption rate curve for naphthalene on PRP-1 in 85% MeOH/H_2O. (Wt = 1.12 mg). The experimental data points are overlaid by a solid line representing the tri-exponential equation. The data are normalized to the value at equilibrium. The tri-exponential constants for this sorption rate curve are shown in the second column in Table 4.6.

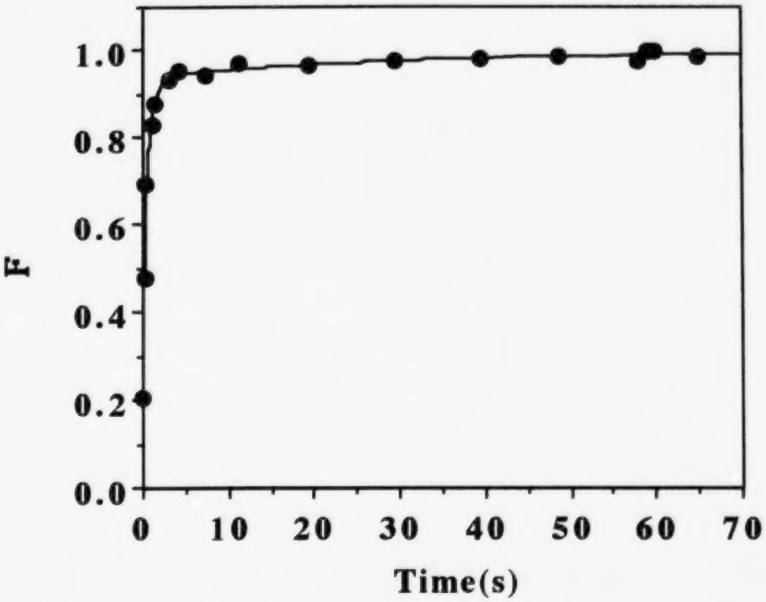

Figure 4.6 Sorption rate curve for naphthalene on PRP-1 in 85% MeOH/H_2O. (Wt = 1.12 mg). The experimental data points are overlaid by a solid line representing the tri-exponential equation. The data are normalized to the value at equilibrium. The tri-exponential constants for this sorption rate curve are shown in the third column in Table 4.6.

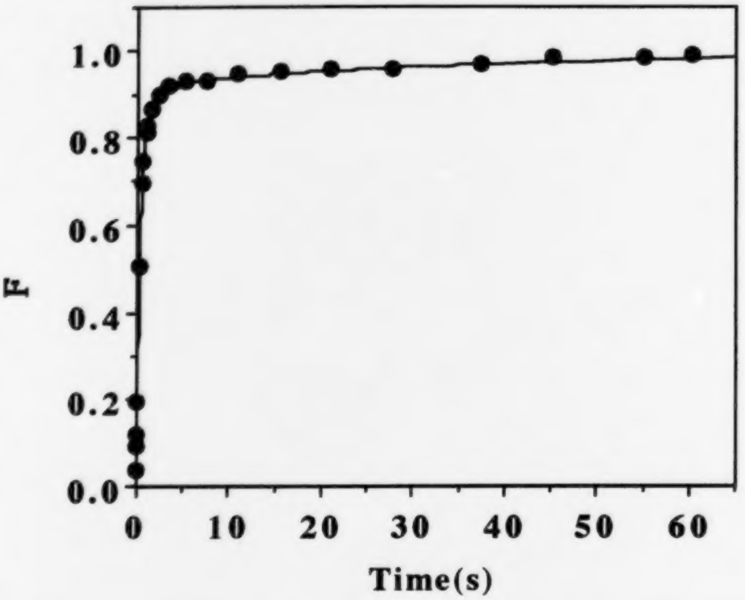

Figure 4.7 Sorption rate curve for naphthalene on PRP-1 in 85% MeOH/H_2O. (Wt = 1.00 mg). The experimental data points are overlaid by a solid line representing the tri-exponential equation. The data are normalized to the value at equilibrium. The tri-exponential constants for this sorption rate curve are shown in the fourth column in Table 4.6.

Chapter 5

Prediction of the Elution Peaks from the Sorption Rate Curves

5.1 Introduction

Bandbroadening and asymmetry are problems to the users of all forms of chromatography in areas such as analysis, physicochemical measurement and preparative scale separation. Narrow and symmetric peaks are desired in high efficiency chromatographic performance. Several physical processes and chemical reactions will affect the magnitude of bandbroadening and asymmetry. The contribution from each process to bandbroadening is equivalent to the relative plate height contribution from that process with respect to the overall plate height of the column.

In an "ideal" column and at an infinitely dilute concentration of a solute, a peak would maintain its initial profile unaltered as it migrates down a column. An infinitely narrow injected peak would still be infinitely narrow at the outlet of a column and the height equivalent to a theoretical plate (HETP) would be zero. This is called linear ideal chromatography.

In the real world, linear ideal chromatography does not exist. In a real column and at an infinite dilute concentration, an infinitely narrow injected peak would broaden and perhaps become asymmetric due to the spreading processes as it migrates down a column. This is called linear non-ideal chromatography.

Non-ideal peak broadening processes are usually classified into two groups. In the first group, there are those processes which are present in every column and therefore may be described as "normal" processes. These processes include axial diffusion, non-equilibrium due to resistance to mass transfer between phases, and spreading due to non-uniform flow paths in a packed column.

"Normal" processes tend to broaden a peak virtually symmetrically provided that the concentration gradients are the same on each side of the peak. That is, if the column contains a large number of plates and the solute is at infinite dilution.

In the second group, there are processes which are not present in every column and therefore can be described as "abnormal" process. This includes "slow kinetic process". The slow kinetic processes usually lead to more asymmetrical and tailed peaks than "normal processes" [60].

In this thesis, linear non-ideal chromatography with slow kinetic processes is studied. The normal non-ideal effects are much smaller compared to the slow kinetic processes. The effects of slow kinetics on the chromatographic peak shape were first modeled by Giddings using a two site model, on the basis of the statistical theory. In this thesis, prediction of an elution peak from a sorption rate curve is based on an extension of the Giddings' two site model.

5.2 Theory

5.2.1 Bandbroadening Processes in Liquid Chromatography

The phenomenon of bandbroadening in a packed column has been extensively treated in the literature [67-69, 87, 104-110].

The theoretical plate model is frequently used in describing the normal bandbroadening processes. Plate height is equal to the increase in the variance of the peak profile per unit length of column. It is expressed in equation 5.1:

$$\overline{H}_j = \sum_{j=1}^{i} \frac{\sigma^2_{x,j}}{x} \qquad (5.1)$$

where $\sigma^2_{x,j}$ is the variance in distance units, and X is the distance the sample has travelled down the column. When several independent peak spreading processes are present, the law of additivity applies [69]:

$$\sigma^2_{x,Total} = \sum_{j=1}^{i} \sigma^2_{x,j} \qquad (5.2)$$

and,

$$\overline{H}_{total} = \sum_{j=1}^{i} \overline{H}_j \qquad (5.3)$$

where j is the number of a bandbroadening process.

5.2.1.1 Longitudinal Diffusion

On injection of an infinitely narrow band of sample onto the top of a column, molecules diffuse away from the narrow band both forward and backward from the center of the band due to the Brownian thermal motion. The resultant profile of the sample is Gaussian and the variance of the diffusion is described by a modified Einstein equation 5.4 [69]:

$$\sigma^2 = 2\, \gamma\, D_m\, t_D \qquad (5.4)$$

and,

$$t_D = \frac{L}{U_0} \qquad (5.5)$$

The obstruction factor, γ , is about 0.5 to 0.8 in a packed column, and is added to the Einstein equation because the diffusion pathway is not straight among the particles. D_m is the solute diffusion coefficient in the mobile phase and has units of cm^2/s. t_D is the time that a sample takes to diffuse, $\overline{U}_0$ is the mobile phase linear velocity, and L is the length of a column. Substituting equation 5.5 into 5.4 [69], gives:

$$\frac{\sigma^2}{L} = \frac{2\,\gamma\, D_m}{\overline{U}_0} \tag{5.6}$$

Since the plate height is defined as variance per length, the plate height associated with the longitudinal diffusion is expressed in equation 5.7 [69]:

$$\overline{H}_{LD} = \frac{2\,\gamma\, D_m}{\overline{\overline{U}}_0} \tag{5.7}$$

It can be seen that longitudinal diffusion is inversely proportional to the mobile phase linear velocity and is significant at low linear velocity. For the flow rates commonly used in LC, longitudinal diffusion is negligible. Under some circumstance, longitudinal diffusion can also occur in the stationary phase, however, the diffusion coefficient in the stationary phase is small compared to D_m. Therefore, the magnitude of longitudinal diffusion in the stationary phase is also small.

5.2.1.2 Eddy Diffusion

Eddy diffusion is caused by the non-uniformity in the packing structure across the bed. The non-uniformity in packing is due to the differences in the particle sizes and shapes. There are many different possible velocities at which an individual molecule might move. There are mainly five types of flow non-uniformities in the bed according to Giddings. 1. Trans-particle effects which are the different velocities occurring on different sides of a particle. 2. Short range inter-channel effects which are the different velocities across a small number of particles. 3. Larger range inter-channel effects which are the velocity differences between regions separated by a layer number of particles. 4. Trans-channel effects which are the different velocities across a single interparticle channel in which the mobile phase velocity approaches a parabolic flow profile. 5. Trans-column velocity occurs near the walls of the column across the width of the column where, for example, the velocity may be faster than the velocity in the center. The non-uniformity of flow can be relaxed by lateral convective mass transfer of sample molecules between flow streams of various linear velocities.

The plate height associated with Eddy diffusion is expressed in equation 5.8 [69] :

$$\overline{H}_{Eddy} = 2\lambda d_p \tag{5.8}$$

where λ is a packing parameter, which decreases with increasing particle diameter due to it being easier to pack a column uniformly with larger particles. It has a typical value of 10. The parameter d_p is the diameter of a particle. Since the lateral convection diffusion results from the packing geometry only, $\overline{H}_{Eddy}$ is independent of mobile phase velocity.

5.2.1.3 Resistance to Mass Transfer in the Mobile Phase

As just discussed, in a packed bed, there are regions of different mobile phase velocities. Some molecules move at a higher velocity, some move at a lower velocity. Velocity inequality can be present across a single particle, across a group of particles and across the entire column. There are five types of flow velocities classified by Giddings as discussed in the section 5.2.1.2. These different velocities occur because of the non-homogeneity of the bed. Two lateral mass transfer processes can relax the non-uniform flow pattern: lateral convection which is included in the Eddy term and lateral diffusion which will be considered in this section.

If lateral diffusion occurred infinitely fast, the molecules would rapidly move laterally from higher velocity regions to lower velocity regions. All the molecules would experience identical average velocity. There would be no bandbroadening. However, lateral diffusion occurs at a finite rate so that there is a net bandbroadening effect. The plate height contribution from the lateral diffusion in the mobile phase is given in equation 5.9 [69] :

$$\overline{H}_m = \frac{\omega \ d_p^2 \overline{U}_0}{D_m} \qquad (5.9)$$

where ω is a packing factor which is small for a uniformly packed bed and usually has a value of about 5. It increases for irregularly shaped particles and decreases with increase in the particle size.

5.2.1.4 Coupling of the Eddy and the Lateral Diffusion Term

Eddy diffusion and lateral diffusion together relax non-uniform flow patterns in a packed bed and are not independent of each other [69]. When a molecule moves in the flow stream, the two processes occur simultaneously. The associated plate heights, however, can not be simply added. Giddings has combined the $\overline{H}_m$ and $\overline{H}_{Eddy}$ contributions as shown in equation 5.10 and referred to this as the coupled plate height term [69].

$$\overline{H}_{couple} = \left(\frac{1}{\overline{H}_{Eddy}} + \frac{1}{\overline{H}_m}\right)^{-1} \qquad (5.10)$$

When $\overline{H}_{Eddy} >> \overline{H}_m$, the coupling term will approach the value of $\overline{H}_m$. On the other hand, when $\overline{H}_{Eddy} << \overline{H}_m$, which usually occurs at high flow rate, the coupling term will approach $\overline{H}_{Eddy}$. The coupling term is not a rigorous solution to the combination of the two steps, but is a simplified manner of combining the two processes.

5.2.1.5 Resistance to Mass Transfer in the Stagnant Mobile Phase

Before a molecule is sorbed onto the stationary phase, it must diffuse through the stagnant mobile phase present in the pores of the particle. The mobile phase velocity in the stagnant mobile phase is zero. The sample molecules can move through the pores only by diffusion and the rate of diffusion is dependent on the diffusion coefficient of the sample in the mobile phase and on the geometry of the pores. The diffusion into and out of the stagnant mobile phase is not infinitely fast. Therefore, there is non-equilibrium between the stagnant mobile phase and the moving mobile phase. At the same time, molecules in the moving mobile phase are continuously migrating down the column. Thus, there is a zone of high concentration of sample in the leading half of the band in the mobile phase. Once the maximum of the band center passes the region, the mobile phase brings a lower concentration of sample into the region. Sample diffusion through the stagnant mobile phase to the moving mobile phase also takes time, therefore, the mobile phase and the stagnant mobile phase are not at equilibrium, and the trailing half of the band in the mobile phase contains a low concentration zone. In the stagnant mobile phase, the opposite situation exists. There is a concentration deficiency in the stagnant mobile phase for the leading half of the sample zone and a concentration excess for the back half. If the diffusion into or out of the stagnant mobile phase is not too slow, and the time a molecule takes to diffuse is less than half of the standard deviation of the peak, the non-equilibrium effect is not large, and a Gaussian peak will be observed [69, 83, 111].

Bandbroadening associated with the stagnant mobile phase is dependent upon the diffusion within the pores and upon the mobile phase linear velocity. The slower the rate of the diffusion, the more time a molecule takes to diffuse through the pores, and the molecules in the stagnant mobile phase fall far behind the moving mobile phase, the same thing happens when the mobile phase linear velocity is increased. The plate height contribution from the stagnant mobile phase is given in equation 5.11 [69]:

$$\overline{H}_{sm} = \frac{fct(f,K')\, d_p^2\, \overline{U}_0}{\gamma'\, D_m} \tag{5.11}$$

Where

$$fct = \frac{(1-f+K')^2}{30\,(1-f)\,(1+K')^2} \tag{5.12}$$

and

$$f = \frac{\varepsilon_{intra}}{\varepsilon_T} \tag{5.13}$$

Here, γ' is the obstruction factor which accounts for the tortuosity of the pores, and is less than 1. D_m and d_p have been previously defined. K' is denoted as the capacity factor, and f is the intraparticle porosity divided by the sum of the intra and interparticle porosity. It is usually around 0.5. In deriving equation 5.11, diffusion through the pores in a spherical particle is approximated by a first order (exponential) rate law by making the so-called "linear driving force" approximation in equation 6.7 in chapter 6. $\overline{H}_{sm}$ is only present in a column packed with porous particles.

5.2.1.6 Resistance to Mass Transfer in the Stationary Phase

Bandbroadening from this process is also caused by non-equilibrium between the mobile phase and the stationary phase. In this process, a molecule is adsorbed onto the stationary phase and becomes immobilized temporarily. Meanwhile, the molecules in the flowing zone of the mobile phase will continue to move down the column. Because the adsorption and desorption of a sample have a finite rate, the molecules, which are being adsorbed and desorbed, fall behind the moving band, causing band spreading. The amount that a zone spreads is proportional to the time the molecules spend on the stationary phase before the desorption occurs. The reasons for band spreading caused by this process are quite similar to those in section 5.2.1.5 in relation to $\overline{H}_{sm}$, except that the stationary phase takes the place of the stagnant mobile phase in the pores.

The plate height contribution from the rate of adsorption-desorption is given by equation 5.14 [69]:

$$\overline{H}_s = \frac{2K'}{(1+K')^2}\,\frac{\overline{U}_0}{k_d} \qquad (5.14)$$

where k_d is the desorption rate constant. In deriving this equation, the reversible adsorption-desoprtion process is asumed to follow a first order (exponential) rate law, as discussed in section 4.2.3 above.

5.2.1.7 Overall Column Bandbroadening

The overall bandbroadening in a packed column is the sum of the plate height contributions from each process which was discussed in the above sections. According to the additive law of the variance, the overall plate height is the sum of the plate heights associated with each bandbroadening process as shown in equation 5.15 [69]:

$$\overline{H} = \overline{H}_{LD} + \overline{H}_{couple} + \overline{H}_{sm} + \overline{H}_{s} \qquad (5.15)$$

5.2.1.8 Extra-Column Bandbroadening

In addition to the dispersion caused by the individual physical processes present in a column, there are also bandbroadening effects from the extra-column components such as the injector, connecting tubing, fittings, detector cell and the electronic readout system [60, 110, 111].

Radial concentration gradients due to the Laminar flow velocity profile in an open non-adsorbing tube produce band-spreading. Changes in tube diameter and in flow across connectors and fittings can cause both bandbroadening and exponential distortion of a peak. These regions act as mixing and diffusion chambers where convection and diffusion, laterally and longitudinally, occurs. A sample, entering these regions, tends to mix uniformly throughout the chamber. Such mixing and diffusion behavior can also occur in the injector and detector dead pockets. The peaks are exponentially distorted. Slow detector and electronic read out systems can also result in bandbroadening and asymmetry. The longer the response time, that is the time required for a signal to reach (1-1/e) or 63% of its finial value, the more bandbroadening and tailing that occurs.

Generally, it is desirable to keep extra-column bandbroadening to a minimum. Therefore, narrow, short tubing, plug injection, zero dead volume connectors, and fast detector response are necessary in high efficiency chromatography. In this work, the extra-column effect was reduced as much as possible. The extra-column bandbroadening was measured and compared with the bandbroadening from the column.

5.2.1.9 Total Plate Height

The total plate height measured experimentally on a column is the sum of the plate heights from the column and extra-column as shown in equation 5.16:

$$\overline{H} = \overline{H}_{LD} + \overline{H}_{couple} + \overline{H}_{sm} + \overline{H}_{s} + \overline{H}_{extra\text{-}column} \qquad (5.16)$$

$\overline{H}_{LD}$ is negligible at the velocities used in LC. In a well packed microparticulate column with moderately slow kinetic effects, $\overline{H}_{couple}$ is also small compared with $\overline{H}_{sm} + \overline{H}_{s}$. Therefore, the bandbroadening in a column is approximately expressed by equation 5.17 after the extra-column has been subtracted [69]:

$$\overline{H} \cong \overline{H}_{sm} \text{ and/or } \overline{H}_{s} \qquad (5.17)$$

Simple substitution for $\overline{H}_{sm}$ and $\overline{H}_{s}$ gives

$$\overline{H} = \frac{\text{fct}(f,K')\ d_p^2\,\overline{U}_0}{\gamma'\ D_m} \text{ and/ or } \frac{2K'}{(1+K')^2}\,\frac{\overline{U}_0}{k_d} \qquad (5.18)$$

which predicts that plate height is proportional to the mobile phase linear velocity.

It is important to note, however, that when very slow kinetic effects are present, in the form of very slow diffusion, then equation 5.11 representing $\overline{H}_{sm}$ is not correct. Equation 5.11 incorporates assumptions and considerations such as the linear driving force approximation and others. The correct treatment of $\overline{H}_{sm}$ in the case of very slow diffusion is discussed in chapter 6.

5.2.1.10 Concentration Overload Bandbroadening

When the solute concentration is sufficiently dilute, the sorption isotherm is linear, and K' is constant. Therefore, the linear isotherm has no influence on the peak shape. The peak is symmetric provided no slow kinetic processes are present. The overall average concentration of a peak decreases as it migrates along the column. The concentration of the peak inside the column is therefore always higher than that observed at the column outlet. Although the outlet concentration may be very dilute, the inlet concentration may be high enough, to fall in the non-linear region of the isotherm. In this case, the profile will rapidly develop asymmetry within a short distance of the inlet and that asymmetry remains as migration continues. In setting any criterion [60, 104] for isotherm linearity, the concentration at the inlet, not the outlet, should be considered.

In this thesis, the overloading of a column is studied by measuring the elution chromatograms at low and high concentration for naphthalene on PRP-1. The effects of the concentrations on the plate heights and the capacity factor K' are also studied.

5.2.1.11 Slow Kinetic Processes

The kinetic origin of tailing in chromatography was first addressed by Giddings [69, 83]. Slow kinetic processes can be regarded as exaggerated cases of a non-equilibrium between the the mobile phase and either the stationary or stagnant mobile phase in pores. The difference between the slow kinetic processes and the processes described in 5.2.1.5 and 5.2.1.6 is the extent of the non-equilibrium in the column. Slow kinetics may result in significant peak broadening, tailing and multiple zones even though the solute concentration is well within the linear region of the isotherm [69, 83, 111]. Examples of slow kinetic processes include both slow mass transfer diffusion of solute molecules into the micropores of the sorbents [49, 112], polymers [113, 114], organic gel matrix [48], ion exchanger resin [115], and deep droplets of liquid and slow adsorption-desorption of solute molecules onto the polymer surface, or a slow reaction of a solute on the stationary phase [116].

Slow kinetic processes often cause tailing of the eluted peak. A tailed peak may be imagined to consist of two parts: a symmetric peak, and a tail on the trailing side as shown in Figure 5.1 [60, 111]. The shape of a tailed peak resulting from slow kinetic processes has previously been investigated by varying the flow rate, temperature and the modifiers in the mobile phase. The area under an exponential tail was found to decrease but the length of the tail increased with the increase of the flow rate. The amount of tailing decreased with increase in temperature. However, in one case, for small molecules which can diffuse into the pores, the area under an exponential tail increased as the temperature increases [113]. The dependence of the apparent center of gravity of the tailed peak on the flow rate is complex. As the flow rate increases, a smaller portion of the molecules adsorb on the slow kinetic sites, so the retention volume of a peak decreases. At a very high flow rate, the slow kinetic sites are no longer available to the molecules due to the short time a solute spends in the column. The tail disappears and the retention volume becomes constant [60, 111].

Whether the apparent center of gravity of a peak depends on flow rate is decided by the relative value of the time constants for the desorption or adsorption step of the slow kinetics and by the value of half of the standard deviation of the peak [69, 83]. If the time constant for desorption or adsorption is greater than half of the standard deviation of the peak, the peak is not only broad but also forms an exponential tail.

It should be pointed out that it is not easy to distinguish between kinetic tailing and non-linear isotherm dependent tailing by just looking at the peak shape. However, non-linear tailing will decrease as the sample size is lowered, whereas kinetic tailing will be affected little by such a change. For kinetic tailing, the length of a tail will be especially prominent at high velocity [60, 69 , 83, 111].

5.2.2 Predicted Peaks from the Sorption Rate Curve

5.2.2.1 Selection of Experimental Conditions

As discussed in section 5.2.1, bandbroadening and asymmetry can result from several individual physical processes and chemical reactions occurring in a column and in the extra-column components. In the situation addressed in this thesis, the slow kinetic processes involved are intraparticle processes. Therefore, appropriate chromatographic conditions must be selected.

First, an aromatic compound, naphthalene, was selected as a probe because aromatic compounds often show extreme bandbroadening and asymmetry on a column of poly (styrenedivinylbenzene), and these effects have been suspected to arise from slow intraparticle processes. The solvent and eluent were 85% MeOH/H_2O in which naphthalene has a large capacity factor. This ensures that the bandbroadening and asymmetry of the observed elution peak are mainly caused by the kinetic processes.

Second, the concentration of a solute at the column inlet is within the linear region of the sorption isotherm to ensure linear chromatography.

Third, the capacity factor K' of naphthalene and the retention time, t_m, of unretained compound, phloroglucinol, must be obtained from the elution chromatograms [80].

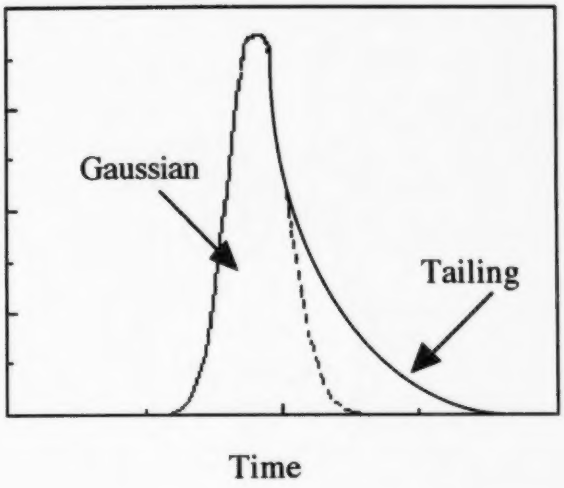

Figure 5.1 Schematic diagram of a tailed peak and its components of a tail and a Gaussian portion.

5.2.2.2 Models of the Elution Chromatographic Profiles

Generally, a mass balance equation is used to calculate an elution profile. The complexity of the mass balance equation depends on the sorption rate expression which reflects the mass transfer resistances in a column. For linear ideal chromatography, a simple mass balance equation can be written and can be solved analytically under the initial and boundary conditions. In this situation, the peak would maintain its original shape as it migrates down the column. For linear non-ideal chromatography, an analytical solution of the mass balance equation produces a Gaussian peak for infinitely narrow injected peak. Non-Gaussian peaks result from either non-linear or non-ideal chromatography or the combination of both. It is often difficult or impossible to find an analytical solution to the mass balance equation to describe these elution profiles.

In dealing with linear non-ideal chromatography with slow kinetic processes, a simple two site model was proposed by Giddings [69, 83]. This model is based on statistical theory [117, 118] and uses the methods of system theory which states that a chromatographic peak is a result of several processes which contribute in a characteristic way to the final peak shape, each process being characterized by an impulse response function (IRF). The final resultant profiles are the convolution of all the IRF's [69, 119-121]. In this work, the calculation of the predicted peak from the sorption rate curves which were fit to a tri-exponential equation draws heavily on the two site sorption model of kinetic tailing developed by Giddings.

Briefly, the two site model states that there are two different kinds of sorption sites with different sorption rates in the stationary phase. One type is normal sites which exhibit rapid kinetic exchange and result in the main chromatographic effects. A second type, a tail producing site, also exists which is relatively scarce and has a slow kinetic rate. The slow kinetic mechanism on the tail producing sites could be either the slow diffusion in the stagnant mobile phase in the pores or the slow adsorption-desorption onto the surface of the pore walls or the combination of the two steps. On each type of site, there is a first order adsorption-desorption rate constant. The shape of a profile from each site depends on the sorption rate constant. Some molecules have spent time not only on the normal sites but also on the slow exchange sites. For these molecules, the elution profile is the convolution of the profiles from the two sites. Other molecules pass through the column without being sorbed on the slow exchange sites. For them, the elution profile is the one obtained on the rapid exchange sites only. The overall elution profile is the weighted sum of these two profiles with convolution of a peak of an unretained compound.

In the present study, Giddings' model is extended to three sites. On each site, there is a first order adsorption-desorption rate constant corresponding to each term in the tri-exponential equation which was used to fit the sorption rate curve. It is imagined that a column of PRP-1 contains three hypothetical types of sites. The number of each type is n_i sites, where i refers to the type of sites, and is equal to 1, 2 or 3. It is imagined that the three different hypothetical types of sites have been sorted out of the column and collected together by type into three hypothetical columns that are placed in series. Each of the three hypothetical columns has the same length (L), linear velocity of the mobile phase ($\overline{U}_0$), retention time of an unretained compound, t_m, retention volume of an unretained compound, V_m, and sorbent weight (W_t) as the real chromatographic column has. The first order rate constant for each hypothetical column is k_i which is obtained from equation 4.10. For a reversible first order sorption, the rate constant is related to an adsorption rate constant $k_{a,i}$ and a desorption rate constant $k_{d,i}$ as given in equation 5.19 [80]:

$$k_i = k_{a,i} + k_{d,i} \tag{5.19}$$

The adsorption and desorption rate constants are also related to the capacity factor in equation 5.20 and 5.21 [80].

$$k_{a,i} = k_i \frac{K_i^{'}}{1+K_i^{'}} \tag{5.20}$$

$$k_{d,i} = k_i \frac{1}{1+K_i^{'}} \tag{5.21}$$

where $K_i^{'}$ is the capacity factor associated with each hypothetical column, and is expressed in equation 5.22 [80]:

$$K_i^{'} = \frac{n_i}{n_0} K' \tag{5.22}$$

where K' is the true capacity factor measured from the elution chromatogram and can be expressed in terms of the distribution coefficient as given by equation 5.23 [80].

$$K^{'} = K_D \, \phi \tag{5.23}$$

Here K_D is the distribution coefficient, and Φ is the phase ratio of a column. Both K_D and Φ are the same on each of the three hypothetical columns as they are on the real column.

If an impulse of a solute is injected onto any one of the three hypothetical columns alone, a fraction of solute molecules will pass through the column without being sorbed. This fraction of the solute molecules will elute as an impulse which is described by equation 5.24 [69, 83].

$$P_i^{'}(t_s) = \delta(t_s) \exp(-k_{a,i} \, t_m) \tag{5.24}$$

where δ(ts) is the Dirac impulse function representing an infinitely thin pulse, $k_{a,i}$ is the adsorption rate constant, and t_m is the retention time of an unretained compound. P'(ts), the probability distribution associated with the fraction of molecules passing through without being sorbed on the i hypothetical column, is related to the adsorption rate constant $k_{a,i}$ and indirectly to the mobile phase linear velocity via t_m. In a slower sorption process, $k_{a,i}$ is smaller, and the fraction of molecules that passes through the column without undergoing this slow process will increase. As the linear mobile phase velocity increases, t_m decreases, molecules spend less time in the column and have less time to undergo the slow sorption step. Therefore, the fraction of non-interacting molecules increases. In the present case for the sorption of naphthalene on PRP-1, it will later be seen that the non-interacting fractions associated with the hypothetical columns 1 and 2 are zero, because adsorption on these two types of sites is fast. Only on hypothetical site 3 is there a finite value of non-interacting fraction.

$P_i(ts)$, the probability distribution associated with the fraction of molecules which is sorbed during their moving through each hypothetical column, is also given by Giddings and is shown in equation 5.25 [69, 83]:

$$P_i(t_s) = \left(\frac{k_{a,i}\ k_{d,i}\ t_m}{t_s}\right)^{1/2} I_i\ (\sqrt{4k_{a,i}\ k_{d,i}\ t_m\ t_s}\ )\ \exp(-k_{a,i}t_m\ -k_{d,i}t_s\ ) \qquad (5.25)$$

Where

$$t_s = t - t_m \qquad (5.26)$$

Here, I_i is a Bessel function of imaginary argument for the parenthetic square root term. The elution peak profile that is predicted to elute from each hypothetical column is obtained by sum of $P_i'(ts)$ and $P_i(ts)$.

5.2.2.3 Overall Predicted Peak from the Individual Contribution on Each Hypothetical Column Using Mathematical Convolution

The overall peak predicted from a real chromatographic column is the convolution of the peaks from each hypothetical column. The mathematical expression of convolution is given in equation 5.27 [119-121]:

$$C_{overall}(t) = \int_0^{\infty} f_1(t')\ f_2\ (t\ -t')\ dt' \qquad (5.27)$$

$$t' = t + t_c \qquad (5.28)$$

where t_c is the center of gravity of the function f_2. f_1 is the input function describing an input profile. f_2 is the system impulse response function describing the concentration-time distribution that would exit the system if the input function had been an impulse. The overall profile, that is the convolution of f_1 and f_2, describes the concentration-time profile exiting the system when any input function f_1 is operated on by any response function f_2. In fact, either f_1 or f_2 can be the input or the response function. Figure 5.2 shows the convolution of an exponential response function, such as that from a detector cell, and a Gaussian input function which would enter the detector cell. The overall profile is an exponentially modified Gaussian. In the present case, on each hypothetical type of site, the response function for molecules interacting with these sites is described in equation 5.25.

It may be noted that convolution theory states that the product of convolution of a δ function with a response function is the response function itself, and is expressed in equation 5.29 [121].

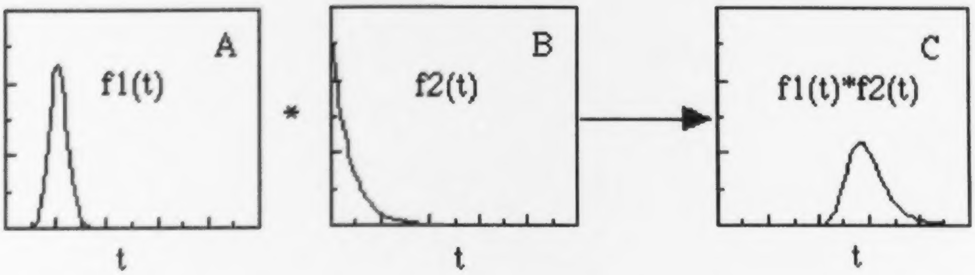

Figure 5.2 Schematic diagram of convolution of two impulse response functions. A is a Gaussian profile produced by injection of an impulse into a high efficiency chromatographic column. B is an exponential profile generated, for example, by injection of an impulse into a detector cell which acts as a mixing chamber.

$$\delta * f = f \tag{5.29}$$

Therefore, the convolution of a narrow input δ function with the response function $P_i(t_s)$ is equal to $P_i\ (t_s)$, so that equation 5.25 is an impulse response function.

The three hypothetical columns in series are illustrated at the top of Figure 5.3. The characteristics of the peaks from each hypothetical column are determined by the constants generated from the tri-exponential equation. The peaks for molecules being sorbed on each hypothetical site are shown in panels D, E and F in Figure 5.3. Panel F corresponds to the first exponential term in the tri-exponential equation, panel E and panel D are related to the second and third exponential terms respectively. Because fast sorption occurs on types 1 and 2 sites, the peaks in panel E and F are symmetric and Gaussian. The shapes of the peaks E and F reflect by the high values of k_1 and k_2 in equation 4.10. The peak in panel D which is calculated by equation 5.25 using the parameter k_3 and n_3 is essentially exponential. Therefore, it can be seen that the third term in the equation 4.10 mainly defines the tail of a peak. Panel H is the convolution of panel D, E and F.

The above analysis deals with the portion of molecules which interact with all these hypothetical types of sites. However, not all the molecules would get chance to interact with the third type of hypothetical site during the residence time of molecules in a column, as shown in Table 5.1. Run No. 1 in Table 4.6 is used to generate Table 5.1. The fraction which the molecules do not interact with the third hypothetical type of sites is not zero at all four mobile phase linear velocities. Panels A, B and C show the profiles eluted from each hypothetical type of site for the portion of molecules which do not interact with the slow sorption site 3. The peak in panel A is a spike impulse because molecules do not interact with the slow sorption site 3. However, the molecules do interact with the two fast sorption sites 1 and 2. Panel G shows the convolution of peaks in panel A, B and C.

The peak in panel I is the weighted sum of peaks in panel G and panel H. Before the summation, the areas of panels G and H are weighted

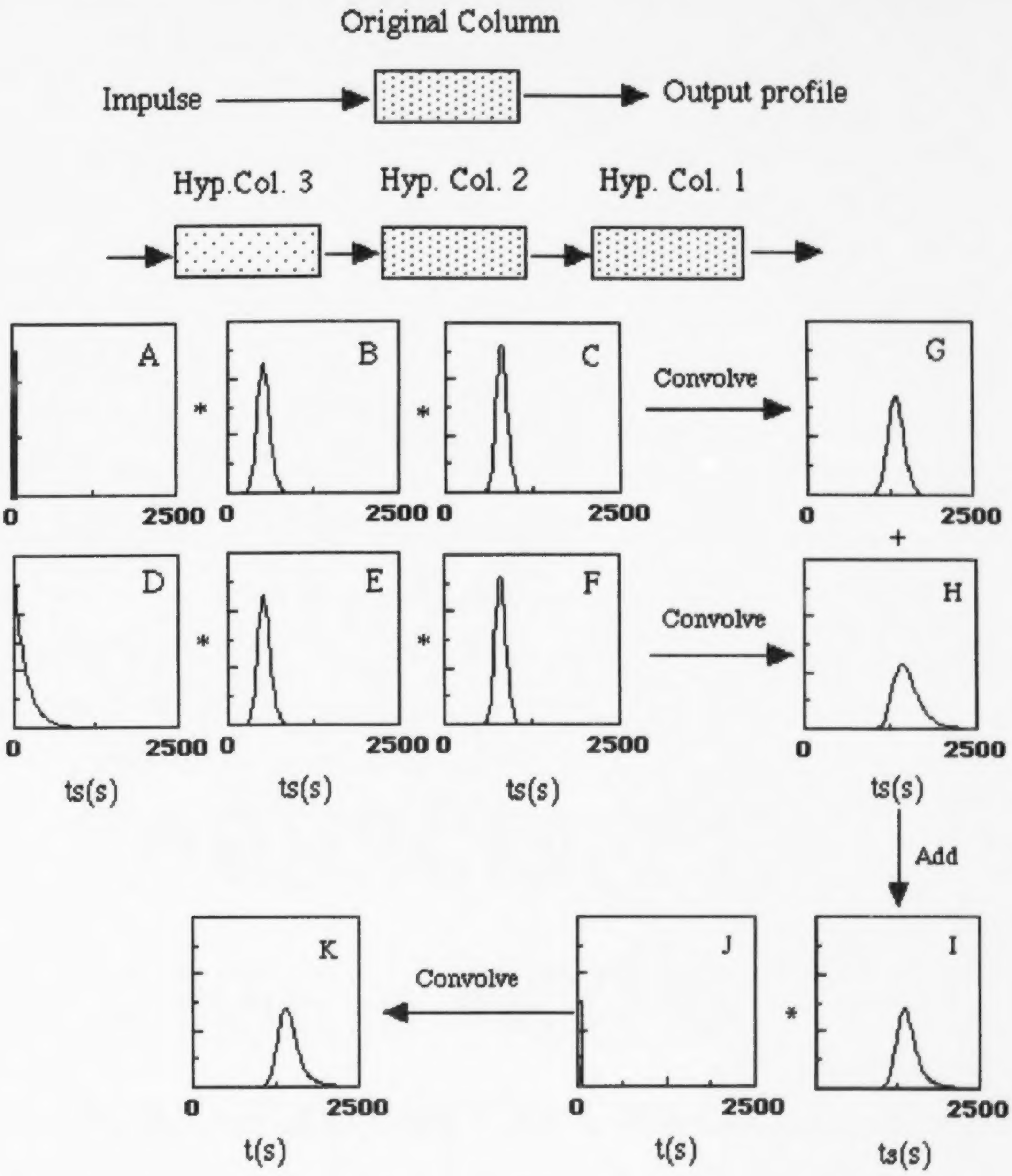
Original Column
Impulse
Output profile
Hyp.Col. 3
Hyp. Col. 2
Hyp. Col. 1
A
B
C
G
D
E
F
H
*
Convolve
+
0
2500
ts(s)
Add
K
J
I
t(s)
ts(s)

Figure 5.3 Prediction of the elution peak at a a mobile phase linear velocity of 0.3 cm/s for equation. The tri-exponential constants which are used to predict the peak are naphthalene whose sorption rate curve is described by a tri-exponential shown in the first column in Table 4.6.

respectively by the fraction of molecules that do not and that do interact with type 3 sites. For example, if the non-interacting fraction is 0.32, the area under profile H must be 68% of the total area. The scaled profiles are then summed to form the peak in panel I. The last step in the calculation of the final predicted peak is a convolution of the peak I with the peak J which is a profile of unretained compound, phloroglucinol. Peak J is very narrow. The variances of the phloroglucinol peaks are so small compared to the variances of the naphthalene peaks at all mobile phase linear velocities, as presented in Table 5.9 and Table 5.10, that the final convolution step increases the center of gravity of the peak I by t_m but a negligible increase in the variance. The finial predicted peak is shown in panel K.

It is should be recognized that the idea of three hypothetical types of sites is purely a convenience for the purpose of mathematical modeling based on the tri-exponential equation. In reality, the stationary phase probably possesses a wide spectrum of sorption sites [122].

5.2.3 Characterization of the Elution Profiles

5.2.3.1 Statistical Moment Analysis of Chromatographic Peaks

The principal factors which control peak shape have been discussed in section 5.2.1 in term of non-linearity, non-ideality and extra-column effects. Bandspreading and asymmetry of the peak results in different extents of peak distortion. Ideally symmetric peaks, which are rare in chromatography, follow a Gaussian distribution which is easily described and characterized. The time at which the maximum of a peak occurs is the retention time or the center of gravity of the peak. The variance is related to the peak width and can be easily calculated by various peak width measurements at different heights on the peak using graphical methods [123]. These quantities can be used to calculate the overall column efficiency.

Table 5.1 The non-interacting fraction at the four mobile phase linear velocities for run 1.

$\overline{U}_0$ (cm/s)	non-interacting fraction on hypothetical column 1[a]	non-interacting fraction hypothetical column 2[a]	non-interacting fraction hypothetical column 3 [a]
0.1	0[b]	0[b]	0.333
0.2	0	0	0.574
0.3	0	0	0.696
0.4	0	0	0.762

a non-interacting fraction is $\exp(-k_{a,i}\, t_m)$.

b When the values are smaller than 10^{-10}, they are defined as 0.

However, most chromatographic peaks do not follow a Gaussian distribution due to the physicochemical dispersion processes. It has been shown that the plate count of asymmetric peaks can easily be overestimated by more than 100% if a Gaussian based equation is employed [124], and all the variance of an asymmetric peak can be underestimated by more than 50% [125].

The theory of statistical moments provides a precise and meaningful way to characterize peaks of any shape [60, 126-131]. For a non-Gaussian peak, the differential mass balance equation is too complex to be solved analytically. Some mathematical methods, such as the Laplace transform, can be used to solve the differential equation. However, the solution, using the Laplace transform [121], must be back transformed which is very difficult. It is comparatively easy to obtain moments which give rise to a set of parameters characterizing a peak shape, from the solution of the Laplace transform. The zero moment, M_0, defines the peak area, the first moment, M_1, defines the center of gravity of a peak, the second moment, M_2, is the variance of a peak, the third moment, M_3, describes the skew of a peak, and the fourth moment, M_4, is excess of a peak. For a Gaussian peak, the moments higher than the second are equal to zero. Definition of M_0, M_1 and M_2 are given in equation 5.30, 5.31 and 5.32:

$$M_0 = \int_0^{\infty} h(t)\, dt \tag{5.30}$$

$$M_1 = \int_0^{\infty} \frac{t\, h(t)\, dt}{M_0} \tag{5.31}$$

$$M_2 = \int_0^{\infty} \frac{(t - M_1)^2\, h(t)\, dt}{M_0} \tag{5.32}$$

where h(t) is a mathematical function describing the concentration-time profile of a chromatographic peak. It is important to use the correct function to describe the peak shape, since a systematic error would be introduced if a wrong function were used. The exponentially modified Gaussian (EMG), a function obtained via the convolution of a Gaussian function and an exponential decay function has been widely used to describe asymmetric and tailing peaks. The EMG function is shown in equation 5.33 [90, 119, 126, 127, 129-131].

$$h_{EMG}(t) = A\frac{\sigma_G}{\tau}\sqrt{2}\exp\left[\frac{1}{2}\left(\frac{\sigma_G}{\tau}\right)^2 - \frac{t-t_G}{\tau}\right]\int_{-\infty}^{z/\sqrt{2}} \exp(-x^2)\,dx \tag{5.33}$$

Where

$$z = (t - t_G)/\sigma_G - \frac{\sigma_G}{\tau} \tag{5.34}$$

The EMG function is defined by three parameters: the center of gravity of Gaussian function, t_G; the standard deviation σ_G of the parent Gaussian function; and the time constant τ of the exponential function. The factor A determines the amplitude of the function. The integration term depends on the value of z. When $z > -3$, the identity shown in equation 5.35 is used to take the advantage of the built-in error function routine in the computer program.

$$\int_{-\infty}^{x} \exp(-y^2)dy = \frac{\sqrt{\pi}}{2}(1+\mathrm{erf}(x)) \tag{5.35}$$

When $z > -8$ and $\frac{\tau}{\sigma} > 0.2$, the integral can be approximated by a polynomial expression [130]. In this thesis, equation 5.35 is used to calculate the integral. The variable z is smallest at the starting of a peak, and for the rest of the peak, z will be larger than -3.

The moments of a peak can be calculated from the constants of the EMG function as shown in equation 5.36 and 5.37 [119]:

$$M_1 = V_G + V_\tau \tag{5.36}$$

$$M_2 = \sigma^2_{V,G} + V^2_\tau \tag{5.37}$$

Where V_G and $\sigma^2_{V,G}$ are the retention volume and the peak variance of the parent Gaussian peak in volume units . $V\tau$ and V^2_τ are the time constants and variance of the exponential function in volume units . The moments in volume units can be calculated from those in time units by multiplying the mobile phase flow rate. The column efficiency is expressed in equation 5.38:

$$\overline{H} = L\,\frac{M_2}{M_1^2} \tag{5.38}$$

Where L is the length of the chromatographic column.

The asymmetry factor, A.F, is calculated at 10% of the peak height using equation 5.39 [124, 130]:

$$A.F. = \frac{B}{A} \tag{5.39}$$

where B is the width of the back of the peak at 10% of the peak height. A is the width of the front of the peak at 10% of the peak height .

5.2.3.2 Characteristics of Kinetic Effects

The slow kinetic effects on the shape of a peak are chiefly observed by the effect of flow rate on the peak appearance and degree of peak tailing [60, 69, 83, 111]. The predicted peak calculated from run 1 in Table 4.6 is used to illustrate the effects of the flow rate on the peak shape.

The area and the height of the Gaussian portion of a tailing peak are calculated numerically from the peak in panel G in Figure 5.3 after correcting by the interacting fraction shown in Table 5.1, and are defined as a_G and h_G respectively. Similarly, the area and height of a tail calculated from the peak in panel H after corrected by the non-interacting fraction are defined as a_T and h_T separately.

Fractional tail area is the ratio of the tail area, a_T, to the sum of the tail area, a_T, and the Gaussian area, a_G. It is given in equation 5.40 [132]:

$$\text{Fractional tail area} = \frac{a_T}{a_T + a_G} \tag{5.40}$$

The fractional tail area reflects the number of molecules that interact with the tail producing sites. It is related to the elution time and the sorption rate constant of the slow kinetic process. The longer the molecules stay in the column, that is a longer retention time and a low flow rate, the more molecules that will participate in the slow process. Also, the larger the sorption rate constant of the slow process, the more molecules that will be sorbed onto the slow sites. Therefore, the fractional tailing area should increase with an increase in the sorption rate constant and with a decrease in flow rate.

The tail length, the degree of extension of the peak trailing edge, is given in equation 5.41 [132]:

$$\sigma_T' = \frac{\frac{h_G}{a_G}\sigma_G}{\frac{h_T}{a_T}} \qquad (5.41)$$

Where σ_G is the standard deviation of the Gaussian portion. The relative tail length is given in equation 5.42 [132]:

$$\text{Relative tail length} = \frac{\sigma_T'}{t_{R,G}} \qquad (5.42)$$

where $t_{R,G}$ is the retention time of the Gaussian portion. Using relative tail length, the tail lengths of peaks with different fractional tail area and Gaussian width are compared. The length is inversely proportional to the height of a tail. The relative tail length is related to the desorption rate constant in the tail producing sites. The slower the desorption rate in the tail producing sites, the longer the sorbed molecules take to return to the moving zone, and the longer the tail is on the trailing edge of the peak.

In addition, the relative width of the Gaussian portion is given in equation 5.43 [132]:

$$\text{Relative width} = \frac{\sigma_G}{t_{R,G}} \qquad (5.43)$$

and the relative height of a tail is given in equation 5.44 [132]:

$$\text{Relative height} = \frac{h_T}{h_G} \qquad (5.44)$$

5.3 Results and Discussion

5.3.1 Extra-column Bandbroadening

The bandbroadening of a naphthalene peak in the extra-column components was measured by injection of 5.057 x 10^{-4} M phloroglucinol in 85% MeOH/H_2O using the apparatus shown in Figure 2.11. The column was replaced by a zero dead volume coupling. Table 5.2 presents the experimental parameters used in the collection of the chromatographic signals. The elution profiles were recorded on a strip chart recorder, and digitized manually. The digitized data was used to calculate the moments using a program in MatLab (The MatWorks, 1991). The moments were calculated from the EMG function which gives a good fit to the experimental data. Figure 5.4 shows the extra-column elution profiles at a mobile phase flow rate of 0.587 ml/min. The elution profiles shown as points are overlaid by solid lines of the EMG function. Profile A is the elution profile for run 1, and profile B is for run 2. The peaks are tailed, the asymmetry factors in terms of $\frac{\tau}{\sigma}$ are around 1.7 [123]. This is because the spaces in the injector and detector cell act as mixing and diffusion chambers [126, 128, 133], in which a sample experiences rapid convection and longitudinal and lateral diffusion which result in exponentially tailed peaks.

In the worst case, a detector and injector act as a mixing chamber. The variance of a peak is equal to the square volume of the detector and injector, and is independent of the flow rate.

The bandbroadening of a peak from a straight tubing is given by Golay [133]:

$$\sigma_v^2 = \frac{\pi\, r^4\, L\, F}{24\, D_m} \tag{5.45}$$

Table 5.2 Experimental parameters in the collection of the elution profiles of 5.057 x 10^{-4} M phloroglucinol in 85% MeOH/H_2O from the extra-column units.

Parameter	Value
Pressure from nitrogen cylinder	50.5 psi
F	0.587 ± 0.01 ml/min
Detector wavelength	276 nm
Detector range	0.05 A.U.F.S.
Recorder chart speed	10 In/min
Recorder range	0.01 V.F.S.

where σ_v^2 is the variance of a peak from the tubing in volume units which is calculated from the variance in time units by multiplying the flow rate, F is the flow rate in units of mL/min, r is the radius of the tubing, and L is the length of the tubing. D_m is the diffusion coefficient of a solute in the solution. Therefore, the higher the flow rate, the wider the peak. The radius and the length of the tubing are very small, therefore, the variance of a peak from the dispersion in the tubing is smaller than those from the detector and injector.

In order to obtain a high column efficiency, it is desirable to keep the bandbroadening contribution from the extra-column components as small as possible. Usually, the variances from the extra-column are kept to 10% or less of those in a column. Table 5.3 shows the extra-column variances at a mobile phase flow rate of 0.587 ml/min and the total variances at four mobile phase flow rates. The extra-column bandbroadening is only 0.02% of the total variances at the mobile phase flow rate of 0.5 ml/min. Although the flow rates in the measurements of the extra-column bandbroadening and the naphthalene elution chromatograph are different, this will not make a significant difference. The volume bandbroadening from the tubing, which is proportional to the flow rate, is very small, and the bandbroadening from the detector and injector is nearly independent of the flow rate as discussed above. The retention times, t_m, of the unretained compound will be smaller after they have been corrected by the retention times in the extra-column components. However, the capacity factor of naphthalene, K', will increase a little bit according to equation 5.46. The net effect is very small on the predicted peak as shown in Figure 5.5. The predicted peak is calculated using the parameters in column 1 in Table 4.6 at a mobile phase linear velocity of 0.4 cm/s.

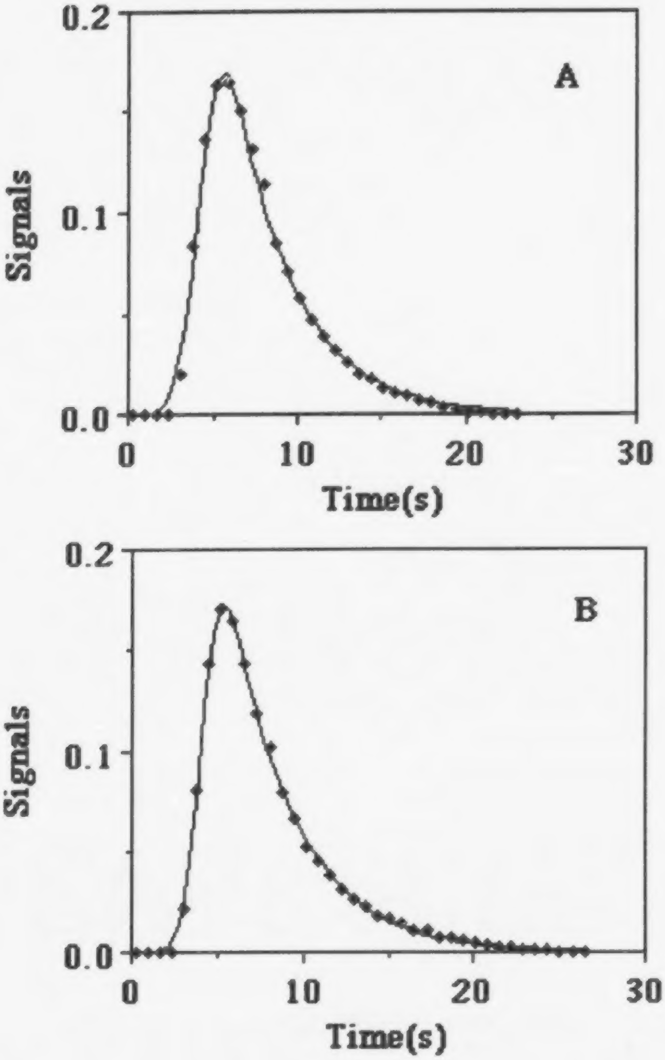

Figure 5.4 Chromatograms of 5.057×10^{-4} M phloroglucinol in 85% MeOH/H_2O from the extra-column components. The experimental points are overlaid by solid lines of EMG fits. Profile A is from run 1 and profile B is from run 2. The mobile phase flow rate is 0.587 ml/min.

Table 5.3 The variance from the extra-column components measured using 5.057 x 10^{-4} M phloroglucinol and the total variances for 3.135 x10^{-5} M naphthalene in a column of PRP-1 at four mobile phase linear velocities. The standard deviations were calculated from duplicate injections.

F (ml/min)	σ_v^2 (ml^2) (Total)	SD (ml^2)
0.5	9.1	0.2
1.0	9.5	0.9
1.5	15	3
2.0	17	4
0.587	1.39 x 10^{-3} [a]	5 x 10^{-5}

a From extra-column components.

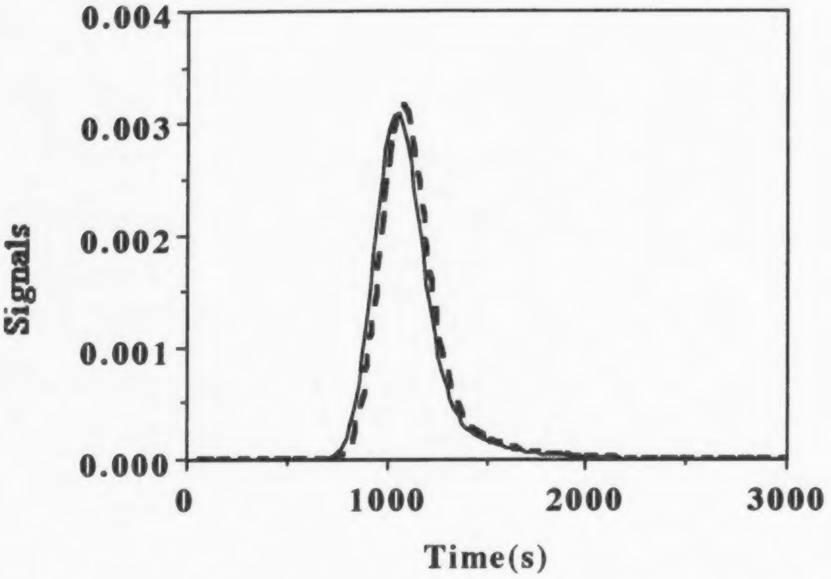

Figure 5.5 The predicted peak (------) of naphthalene after corrected by the extra-column bandbroadening and the predicted peak (———) without correction from the extra-column bandbroadening at the mobile phase linear velocity of 0.4 cm/s.

The contribution from the extra-column bandbroadening is so small that it is not corrected in the later calculation of the chromatographic figures of merit for the naphthalene elution profiles.

5.3.2 Concentration Overload Bandbroadening

A non-linear isotherm due to a high concentration can also cause an asymmetric peak [57, 60, 110, 111]. In this work, bandbroadening and asymmetry that result only from the kinetic processes in a column are of interest. Therefore, the concentration overload bandbroadening must be avoided.

Either of two ways can be chosen to select the concentration of a solution which will not overload a column. One way is to run the sorption isotherm, and then choose a concentration within the linear region of the isotherm. The other way is to examine the effects of the concentration on the shape of the peak, as characterized by the chromatographic figures of merit. The capacity factor, K', should be independent of the concentrations within the linear region of the sorption isotherm [60, 110, 111]. The K' was measured by varying the concentration of naphthalene from 10^{-3} to 10^{-5} M at a mobile phase linear velocity of 0.3cm/s. The K' was calculated using equation 5.46:

$$K' = \frac{t_{max} - t_m}{t_m} \tag{5.46}$$

where t_m is the first moment of the unretained compound of phloroglucinol, t_{max} is the retention time of peak maximum for naphthalene. Figure 5.6 shows the plot of K' versus the concentration of naphthalene. The data are shown in Table 5.4. As expected for a convex sorption isotherm, K' increases with decreasing concentration until it approaches a constant in the linear region of the isotherm. There are no significant differences in K' at concentrations of 1.57 x 10^{-5} M and 3.14 x10^{-5} according to the t-test. Therefore, when the concentration is smaller than about 3 x 10^{-5} M, K' becomes a constant and independent of the concentration of naphthalene. This agrees with the results from the sorption isotherm (Figure 3.6). The plate height versus the concentration should be constant when K' becomes constant at a certain mobile phase linear velocity. The plate heights were calculated by an empirical equation proposed by Foley and Dosery [130]. This empirical equation is based on an exponentially modified Gaussian function and employs only graphically measurable parameters such as retention time of the peak maximum, t_{max}, the peak width at 10% of the peak height, $w_{0.1}$, and the empirical asymmetry factor of B/A. The plate height was then calculated with equation 5.47:

$$\overline{H} = \frac{L}{N} = \left[41.7 \frac{\left(\frac{t_{max}}{w_{0.1}}\right)^2}{(B/A + 1.25)}\right]^{-1} L \tag{5.47}$$

The reason for using the empirical equation to calculate the plate height is that the profiles of low concentration naphthalene, a highly retained compound on PRP-1, can not be accurately digitized by the 12 bit analog to digital converter at a concentration within the linear region of the isotherm due to the very low S/N ratio.

This can be seen as follows : previous Figure 2.9 shows the elution profile of naphthalene on PRP-1 at a concentration of 10^{-3} M after being smoothed by a moving average of 21 points. The profile has a high value of S/N. The peak can be accurately digitized. The parameters in the collection of the elution profiles of 4.688 x10^{-3} M naphthalene on a column of PRP-1 at four mobile phase linear velocities are shown in Table 5.5. However, as the concentration decreases to 4 x 10^{-5} M which is the upper limit of the concentration within the linear region of the sorption isotherm, the signals appear too noisy to be recognized as shown in previous Figure 2.8a, even after the signals were

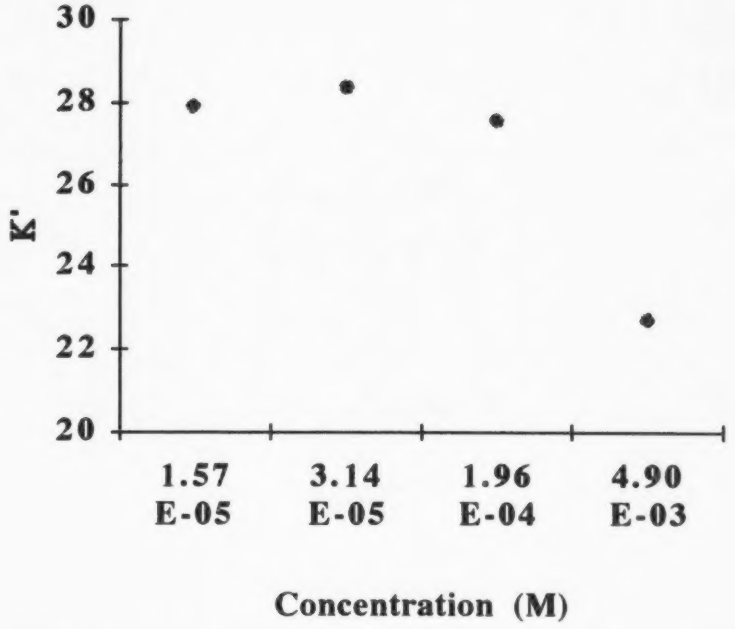

Figure 5.6 The dependence of capacity factors on the concentrations of naphthalene in 85 % MeOH/H_2O on a column of PRP-1. The standard deviations were from duplicate injections. The capacity factors were calculated at a mobile phase linear velocity of 0.3 cm/s.

Table 5.4 The dependence of capacity factors on the concentrations of naphthalene in 85 % MeOH/H_2O on a column of PRP-1. The standard deviations were from duplicate injections. The capacity factors were calculated at a mobile phase linear velocity of 0.3 cm/s.

Concentration (M)	K '	SD
4.90×10^{-3}	22.69	0.25
1.96×10^{-4}	27.54	0.27
3.14×10^{-5}	28.32	0.53
1.57×10^{-5}	27.86	0.17

processed using a low pass filter and a moving average program in the SpectroPlot [56]. The peaks are highly distorted as shown in Figure 2.8b.

Although the peaks of naphthalene at a low concentration can be recorded on a chart and then hand digitized as will be seen in section 5.3.4, it is not necessary to carry out this time consuming and tedious processes in this section. Instead, the quicker graphical approach implied in equation 5.47 was used here. The plot of plate height versus the concentration at mobile phase linear velocity of 0.3 cm/s is shown in Figure 5.7 and the data is shown in Table 5.6. The standard deviations were calculated from duplicate injections. The SD includes the errors in obtaining the parameters graphically, such as errors associated with t_{max}, B, and A from the chart. SD is relatively low. The plate height decreases with concentration until it becomes constant. There are no significant difference in the plate heights at 3.14×10^{-5} M and 1.57×10^{-5} M concentrations according to the t-test. These results agree with those from the sorption isotherm (Figure 3.6) and the capacity factor (Figure 5.6).

Figure 5.8 shows the elution profiles of naphthalene at concentration of 4.688×10^{-3} M and 3.135×10^{-5} M. The profile A at a high concentration is more tailed, the t_{max} is shorter, and the peak width is larger, these are expected for a peak from an overloaded column. The profile B at 3.135×10^{-5} M is more symmetrical and less tailed with a larger t_{max}. The elution profile of 3.135×10^{-5} M naphthalene on a PRP-1 column was used to compare with the predicted peaks.

Table 5.5 The experimental parameters in the collection of the elution profiles of 4.688×10^{-3} M naphthalene in 85% MeOH/H_2O on a column of PRP-1 at four mobile phase linear velocities with an analog to digital converter (LAB NB).

$\overline{U}_0$ (cm/s)	Sample	Data Point	Sampling Rate (sec)	Gain	Start Time[a]
0.1	Naph.	2048	2	50	52'55"[b]
0.2	Naph	2048	1.5	50	24'48"
0.3	Naph	1024	1.3	50	15'22"
0.4	Naph	1024	1.3	50	11'02"

[a] start time is the time before the data acquisition starts.

[b] ' is minute, " is second.

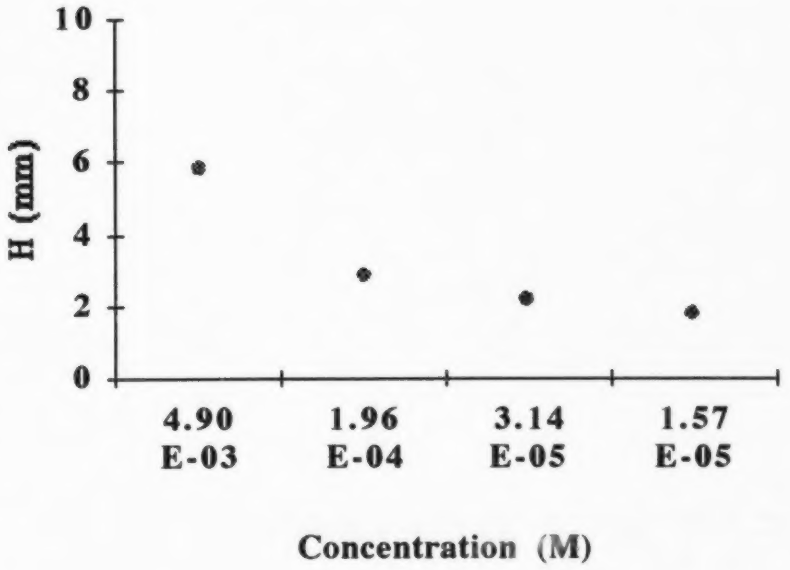

Figure 5.7 The plate heights of naphthalene on PRP-1 in 85% MeOH/H_2O as a function of the concentrations. The plate heights were calculated at a mobile phase linear velocity of 0.3 cm/s using equation 5.47.

Table 5.6 The dependence of the plate heights on the concentrations of naphthalene in 85 % MeOH/H_2O on a column of PRP-1. The standard deviations were from duplicate injections.

Concentration (M)	$\overline{H}$ (mm)	SD
4.9×10^{-3}	5.81	0.51
1.96×10^{-4}	2.82	0.32
3.14×10^{-5}	2.18	0.17
1.57×10^{-5}	1.79	0.10

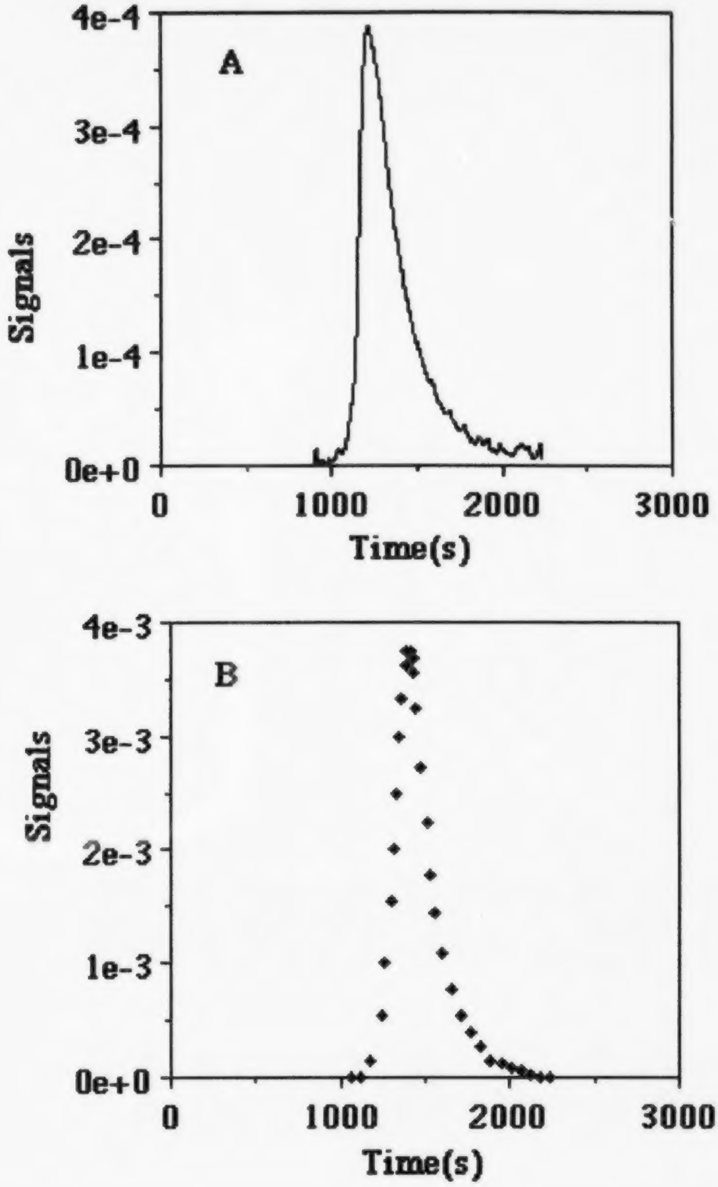

Figure 5.8 Chromatograms of naphthalene on an analytical column of PRP-1 in 85% MeOH/H_2O at a mobile phase linear velocity of 0.3 cm/s. A. The chromatogram of 4.688 x 10^{-3} M naphthalene shown as a smoothed output from the data collection program written in SpectroPlot. B. The chromatogram of 3.135 x 10^{-3} M naphthalene.

5.3.3 Axial Dispersion and Non-Uniform Flow Pattern

The calculation of the predicted peaks from the intraparticle sorption rate curves assumes that bandbroadening and asymmetry from axial dispersion and non-uniform flow patterns in a packed column are negligible compared to the kinetic effects as are the extra-column and the nonlinear isotherm effects. In a chromatographic column, these two processes are definitely present. However, the magnitude of the bandbroadening of naphthalene alone from the two processes can be shown to be small compared with the kinetic effects for naphthalene in the column of PRP-1.

Phloroglucinol, a highly polar and hydrophilic compound which was used to estimate extra-column bandbroadening, is not sorbed on PRP-1 and can be used to indirectly estimate the contributions from the axial dispersion and the non-uniform flow pattern. The bandbroadening of phloroglucinol eluting from a column of PRP-1 arises from extra-column components and from the axial dispersion and the non-uniform flow in a column.

A 5.145 x 10^{-4} M solution of phloroglucinol was injected onto PRP-1 column. The signal was fed into a LAB-NB analog to digital converter. The experimental parameters in the collection of the phloroglucinol peak are shown in Table 5.7. Phloroglucinol, an unretained compound, shows a symmetric and narrow peak on PRP-1 as shown in previous Figure 2.7A, with a signal to noise ratio of 28. The profile in Figure 2.7A is at $\overline{U}_0$ of 0.3 cm/s. Figure 5.9 A shows the profile at $\overline{U}_0$ of 0.1cm/s, profiles B and C in the same Figure show the elution profiles at $\overline{U}_0$ of 0.2 and 0.4 cm/s. After the signals were smoothed by a moving average of 21 points in SpectroPlot, the digital data were transferred to Excel where a data subset was chosen to calculate the first moments by the numerical integration. The data subset was selected by setting the first data point at about 1% of the peak maximum before the peak maximum and the final data point at about 1% of the peak maximum after the peak maximum [54, 80, 90]. The detailed limits used in selecting the beginning and the end of the baselines for the data subset for all the linear velocities are shown in Table 5.8.

The first moments, M_1, calculated from the numerical integration give good precision as seen from the standard deviations in the second column in Table 5.9. However, for the second moments, M_2, which are more sensitive to the baseline noise, the numerical integration gave a very poor precision. Using the EMG function can avoid the baseline noise, unfortunately , the EMG function gave a very poor fit to the profiles of phloroglucinol. Therefore, the M_2 was calculated by the graphical tangents [134] method where the baseline width is four times the standard deviation of the peak. The second moments at four mobile phase linear velocities are shown in the third column in Table 5.9. The second moments, that is the variances of the phloroglucinol peaks are very close to the value of 1.39×10^{-3} ml^2 at F = 0.587 ml/min from the extra-column components (Table 5.3). This indicates that bandbroadening of phloroglucinol peaks is mainly from the extra-column effects and that the axial dispersion and non-uniform flow bandbroadening is even smaller than those due to the extra-column effects.

The asymmetry factors measured at 10% of the peak height are also shown in Table 5.9. All of the asymmetry factors are around one which means phloroglucinol peak is Gaussian.

After the first moment of phloroglucinol is known, the mobile phase linear velocity can be calculated using equation 5.48 [3, 69]:

$$\overline{U}_0 = \frac{L}{M_1} \tag{5.48}$$

The first moments M_1 of phloroglucinol in Table 5.9 are also used as t_m in equation 5.25 to calculate the predicted peaks.

Table 5.7 The experimental parameters in the collection of the elution profiles of 5.145×10^{-4} M phloroglucinol in 85% MeOH/H_2O on a column of PRP-1 at four mobile phase linear velocities with an analog to digital converter (LAB NB).

$\overline{U}_0$ (cm/s)	Sample	Data Points	Sampling Rate (ms)	Gain	Start Time[a]
0.1	Phl	1048	110	100	1'50" [b]
0.2	Phl	1024	60	100	40"
0.3	Phl	1024	40	100	40"
0.4	Phl	1024	30	100	28"

a start time is the time before the data acquisition starts.

b ' is minute, " is second

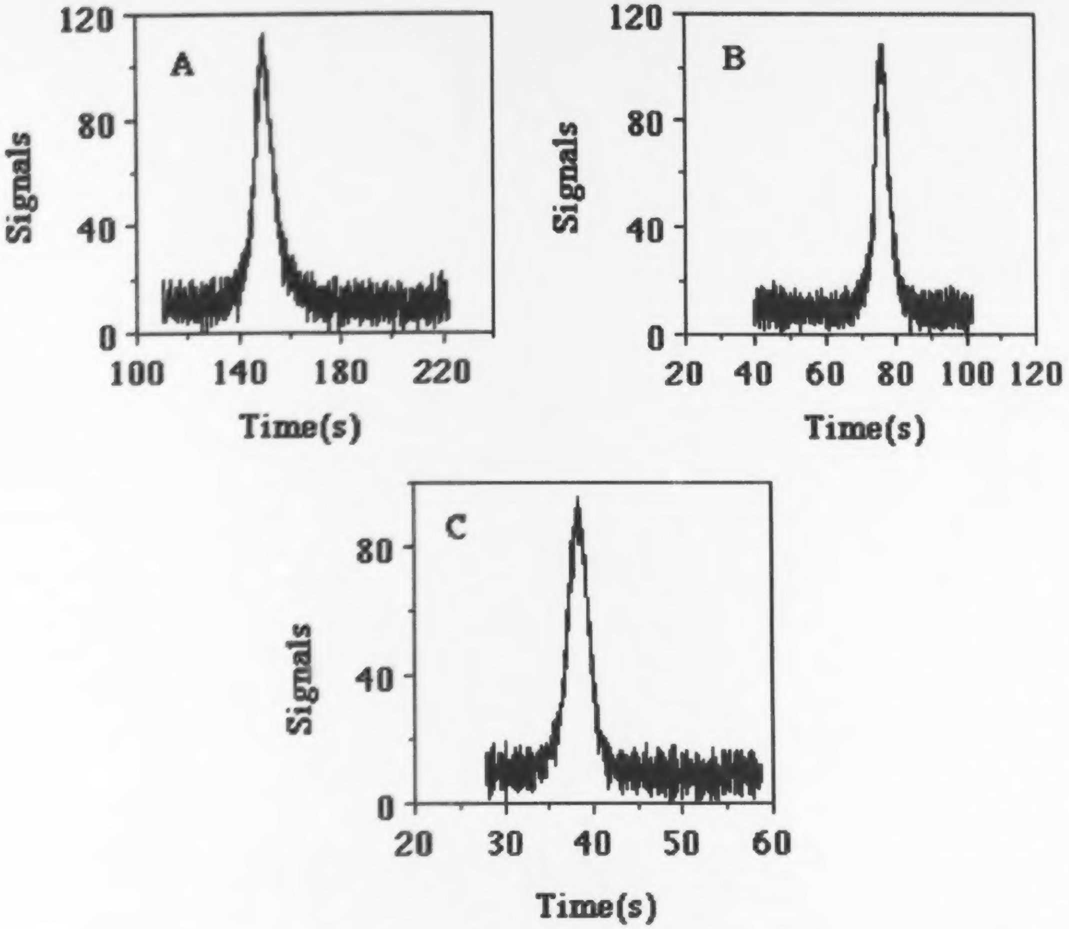

Figure 5.9 Elution profiles of 5.145 x 10^{-4} M phloroglucinol on a column of PRP-1. Profile A is the unsmoothed output at mobile phase linear velocity of 0.1 cm/s. Profiles B and C are outputs at mobile phase linear velocity of 0.2 and 0.4 cm/s

Table 5.8 The baseline setting in the measurement of the moments of peaks from 5.145×10^{-4} M phloroglucinol at four mobile phase linear velocities.

$\overline{U}_0$(cm/s)	Beginning [a]	Ending [a]
0.1	1.4%	1.6%
0.2	1.4%	1.8%
0.3	1.1%	1.0%
0.4	1.1%	1.0%

[a] The percentage of peak maximum.

Table 5.9 The first, second moments and the asymmetry factors at 10% of the peak height of 5.145 x 10^{-4} M phloroglucinol in 85% MeOH/H_2O on a column of PRP-1 at four mobile phase linear velocities. The standard deviations were from replicate injections.

$\overline{U}_0$ (cm/s)	M_1 (s)	M_2 (ml^2)	A. F.
0.1	153 ± 2	$1.12 \times 10^{-3} \pm 2.1 \times 10^{-4}$	1.21 ± 0.13
0.2	77.3 ± 0.5	$1.74 \times 10^{-3} \pm 2.7 \times 10^{-4}$	1.07 ± 0
0.3	50.5 ± 0.5	$1.91 \times 10^{-3} \pm 2.8 \times 10^{-4}$	0.967 ± 0.05
0.4	37.9 ± 0.7	$2.01 \times 10^{-3} \pm 3.3 \times 10^{-4}$	0.984 ± 0.02

5.3.4 The Elution Chromatograms of Naphthalene on PRP-1

The elution chromatograms were obtained by injection of 3.135 x 10^{-5} M naphthalene onto a PRP-1 column. The signals were recorded on a strip chart recorder and then hand digitized. The reasons for hand digitizing method was discussed in section 2.9 and 5.3.2.

At each flow rate, duplicate injections were made. The digital data were fit with the EMG function which was used to calculate the moments. The EMG fit was used to avoid the baseline setting errors as discussed before.

Introducing an EMG function to the experimental data could cause a systematic error. Fortunately, the EMG function fits the elution profiles of naphthalene from a column of PRP-1 quite well as shown in panels A, B, C and D in Figure 5.10 at the four mobile phase linear velocities investigated. The solid lines are the EMG fit, the symbols are experimental data. The figures of merit for the observed peaks are shown in Table 5.10.

The SD in Table 5.10 includes not only the experimental errors in collection of the elution profiles but also the errors in the hand digitizing process and the EMG fits. Generally speaking, the SD is small except for the very shape-sensitive parameters $\sigma^2_{V,G}$, V^2_τ and A.F. Figure 5.11 shows the plot of the observed plate height versus the mobile phase linear velocity. The plot shows that the plate height increases with the mobile phase linear velocity, which is a characteristic of slow intra-particle mass transfer. A strictly linear increase, such as would be expected from the simplified $\overline{H}_{sm}$ term in equation 5.11, is not expected for a system which exhibits asymmetric peaks.

The first moments of the elution profiles of phloroglucinol and naphthalene were used to calculate the capacity factors using equation 5.49 [3, 69]:

$$K' = \frac{M_1(\text{Naph})-M_1(\text{Phl})}{M_1(\text{Phl})} \qquad (5.49)$$

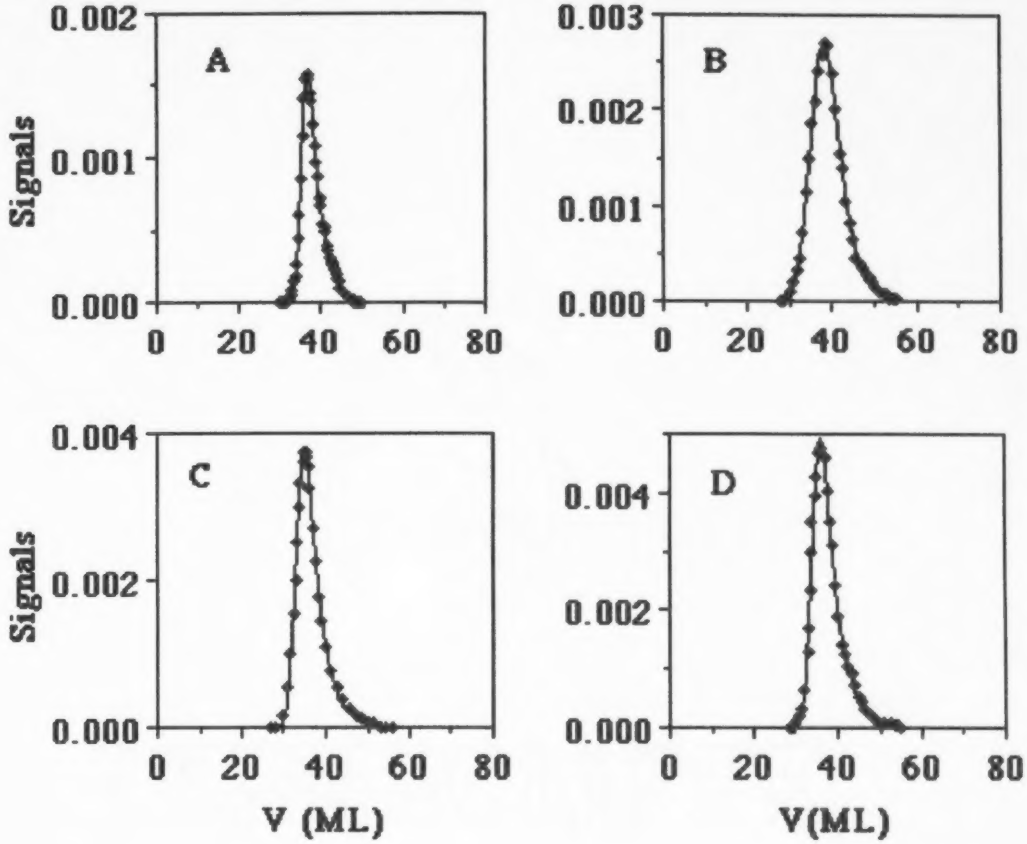

Figure 5.10 EMG fits of the elution profiles of 3.135 x 10^{-5} M naphthalene in 85% MeOH/H_2O on PRP-1. The solid lines represent the EMG fit. The symbols represent the experimental profiles. In A. The EMG fit and the experimental elution profile at a mobile phase linear velocity of 0.1 cm/s. Profiles B, C and D are the EMG fit and the experimental elution profiles at $\overline{U}_0$ of 0.2, 0.3 and 0.4 cm/s.

Table 5.10 Chromatographic figures of merit for the observed elution profiles of 3.135×10^{-5} M naphthalene on a column of PRP-1 at the four mobile phase linear velocities.

$\overline{U}_0$ (cm/s)	No.	V_R (ML)	V_G (ML)	V_τ (ML)	$\sigma^2_{V,G}$ $(ML)^2$	σ^2_V $(ML)^2$	V^2_τ $(ML)^2$	A.F.
0.1	1	38.18	35.36	2.82	1.28	9.24	7.99	2.3
	2	39.36	36.71	2.65	1.97	8.96	7.01	2.1
SD		0.83	0.95	0.12	0.49	0.20	0.69	0.1
0.2	1	37.44	34.57	2.87	1.98	10.2	8.22	1.9
	2	38.15	35.58	2.57	2.25	8.83	6.58	1.9
SD		0.50	0.71	0.21	0.19	0.97	1.16	0.0
0.3	1	36.62	33.38	3.24	2.37	12.88	10.5	2.2
	2	39.60	35.75	3.85	2.63	17.4	14.7	2.3
SD		2.11	1.68	0.43	0.18	3.2	2.9	0.1
0.4	1	37.92	34.47	3.47	2.18	14.2	12.0	2.2
	2	37.19	32.65	4.54	2.17	22.8	20.0	2.6
SD		0.52	1.29	0.47	0.01	3.7	5.6	0.3

Table 5.11 shows the capacity factors measured from the elution profiles at four mobile linear velocities. For each flow rate, K' was calculated from duplicate injections. K' is independent of flow rate as it should be. The average value of K' at four mobile phase linear velocities was used in the calculation of the predicted peak using equation 5.25.

5.3.5 Predicted Elution Peaks from the Sorption Rate Curves of Naphthalene on PRP-1

The predicted peaks are based on the information from the sorption rate curves of naphthalene on PRP-1 and were calculated using equations 5.24 and 5.25 as described in section 5.2.2 employing the parameters k_i and n_i from Table 4.6. A typical predicted peak has been shown in panel K in Figure 5.3. The first moment of the unretained compound of phloroglucinol, t_m, and the capacity factor of naphthalene in 85% MeOH/H_2O on PRP-1, K', which are used in the calculation of the predicted peak using equation 5.25, are shown in Table 5.9 and Table 5.11 respectively. n_i and k_i are shown in column 1, 2, 3 and 4 in Table 4.6.

The elution peaks predicted for a mobile phase linear velocity of 0.3 cm/s, based on k_i and n_i values are illustrated in Figure 5.12. Here curve A is the profile predicted from run 1 and curves B, C, and D are the profiles predicted from run 2, 3, and 4 respectively. All the profiles are normalized to area one. In general, the four peaks are very similar to one another in terms of V_R, width and shape, although the peak in panel B, from run 2, is less tailed than the others. The profiles with a small k_3 and a larger n_3 give rise to a longer tail. Run 2 has the largest k_3 and the shortest tail.

A qualitative comparison among the predicted peaks can be carried out by the chromatographic figures of merit calculated from the EMG curve fit. Figure 5.13 shows the predicted peak and the EMG fit at a mobile phase linear velocity of 0.3 cm/s. Curve A is from run 1 and curves B, C, and D are from run 2, 3 and 4 respectively. The solid lines

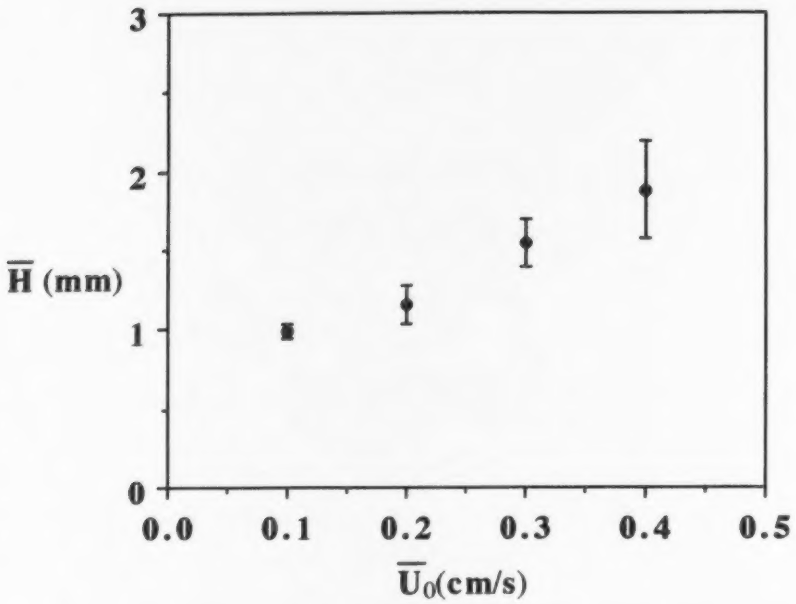

Figure 5.11 The observed plate heights of 3.135×10^{-5} M naphthalene in 85% MeOH/H_2O on an analytical column of PRP-1 as a function of the mobile phase linear velocities. The plate heights were calculated from the moments of the EMG fit. The error bars are one standard deviation from duplicate measurements.

Table 5.11 The capacity factors calculated from the EMG fit for 3.135×10^{-5} M naphthalene in 85% MeOH/H_2O on a column of PRP-1 at the four mobile phase linear velocities. The standard deviations were from duplicate injections.

$\overline{U}_0$ (cm/s)	K'	SD
0.1	28.90	0.34
0.2	28.04	0.23
0.3	28.01	0.30
0.4	28.98	0.51

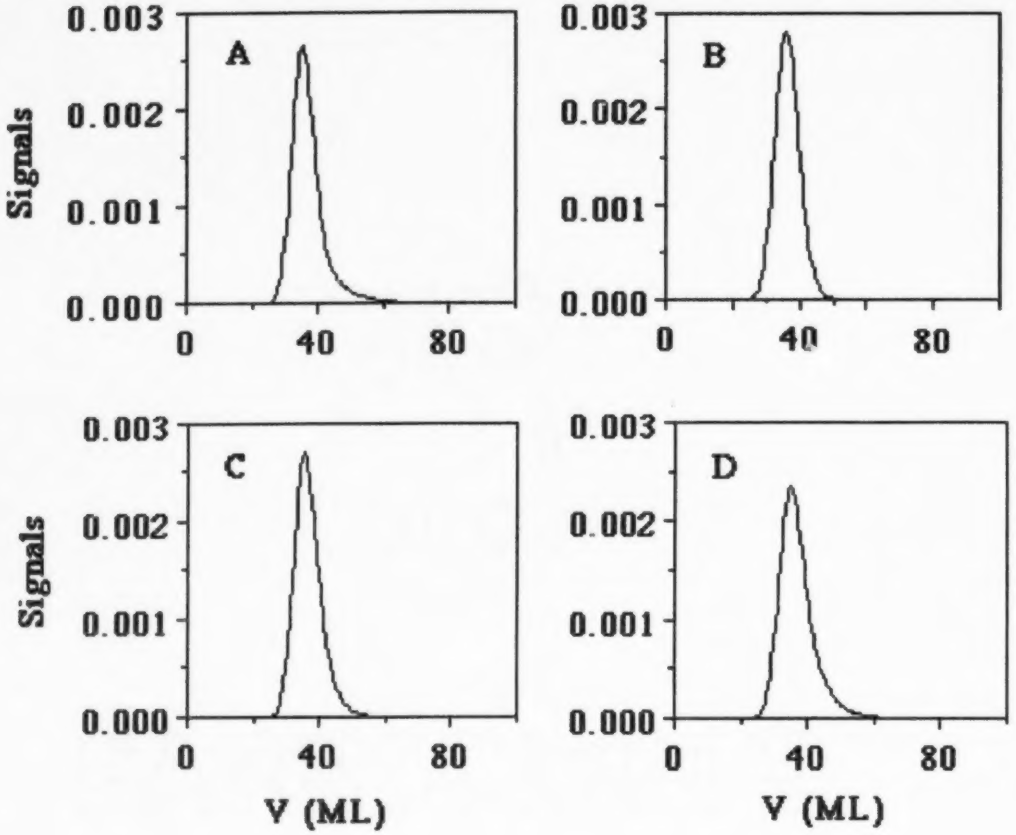

Figure 5.12 The predicted profiles from the four replicate sorption rate measurements for naphthalene on PRP-1 at $\overline{U}_0$ of 0.3 cm/s. A is the predicted profiles using the tri-exponential constants shown in column 1 in Table 4.6. B, C and D are profiles predicted by the constants shown in column 2, 3 and 4 respectively in Table 4.6.

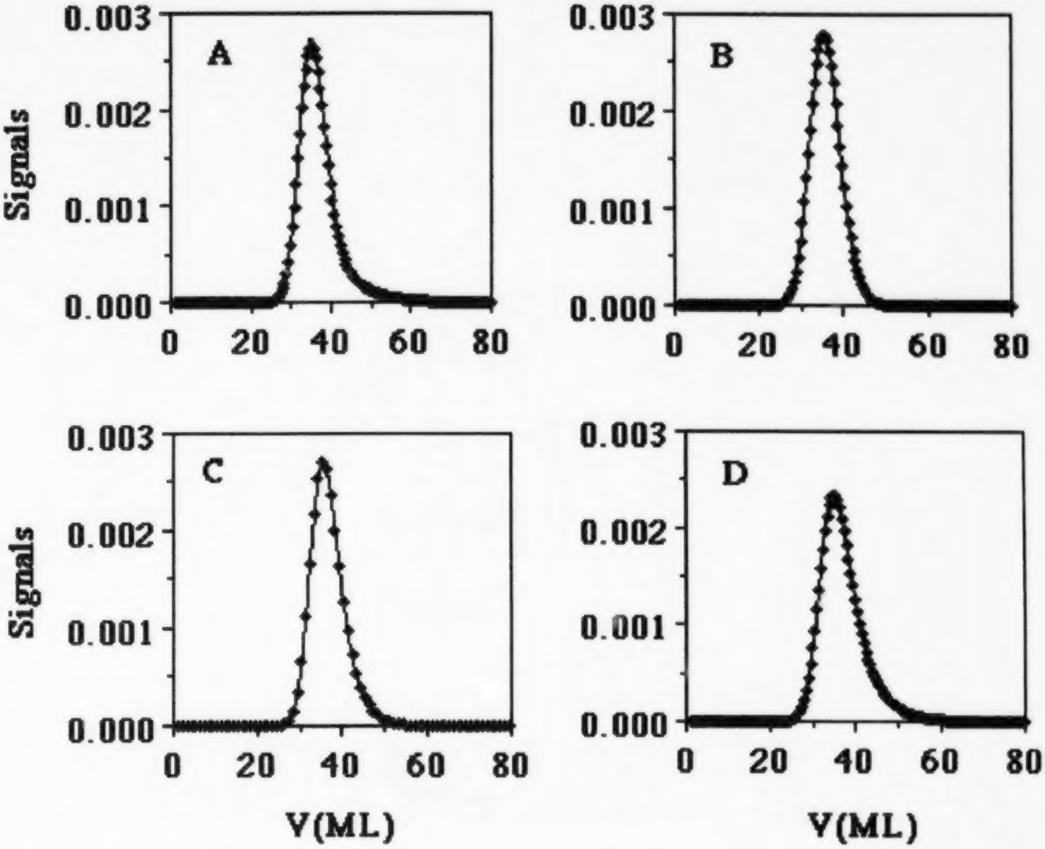

Figure 5.13 The EMG fits of the predicted profiles from the four replicate sorption rate measurements for naphthalene on PRP-1 at $\overline{U}_0$ of 0.3 cm/s. The solid lines are the EMG fits. The symbol are the predicted peaks. The peak A, B, C and D show the EMG fits and the predicted profiles using the tri-exponential constants shown in column 1, 2, 3 and 4 respectively in Table 4.6.

are the EMG fits which give a good description of the predicted peaks. The EMG characteristics for all the predicted profiles at the four mobile phase linear velocities are presented in Table 5.12.

A good precision is obtained for the centers of gravity of the predicted peak, a relatively large difference exists for V_τ and $\sigma^2_{v,G}$. The use of an EMG function to represent chromatographic peaks can avoid extreme ambiguities which would arise from baseline errors. However, such an arbitrary division of a peak into Gussian and an exponential components is quite sensitive to samll differences in peak shape, particularly to the uncertainties in the tailing part which is associated with the uncertainties in determination of the slow sorption step in the kinetic study.

The SD in Table 5.12 includes all the error contributions from the overall experiment, including the contribution from the sorption rate measurement, the contribution from the processes used to predict the elution profiles and the contribution from the EMG fitting routine. Overall, the precision is good except for the exponential component for run 2.

Figure 5.14 shows the plot of the predicted plate height versus the mobile phase linear velocity. The error bars are one standard deviation which was calculated from four predicted peaks. The data is shown in Table 5.13. As for the observed elution peaks in Figure 5.11, the plate height increases with flow rate.

The asymmetry factors measured at 10% of the peak height are shown in Table 5.14.

Table 5.12 Chromatographic figures of merit for the predicted elution profiles of naphthalene on a column of PRP-1 at four mobile phase linear velocities. The predicted peaks were from four replicate sorption rate curves measured by the shallow bed technique.

$\overline{U}_0$ (cm/s)	No.	V_R (ML)	V_G (ML)	V_τ (ML)	$\sigma^2_{V,G}$ $(ML)^2$	σ^2_V $(ML)^2$	V^2_τ $(ML)^2$
0.1	1	37.98	34.64	2.74	2.83	10.4	7.51
	2	36.52	34.98	0.95	3.61	4.51	0.91
	3	37.49	35.66	1.83	3.48	6.81	3.35
	4	37.45	34.78	2.67	4.28	7.11	7.13
SD		0.61	0.45	0.84	0.59	2.42	3.16
0.2	1	37.49	34.17	3.32	4.79	15.8	11.0
	2	36.52	34.98	1.53	6.94	9.44	2.36
	3	37.37	34.88	2.85	5.66	13.8	8.12
	4	37.76	33.87	3.10	6.29	15.9	9.61
SD		0.54	0.54	0.8	0.92	3.02	3.8
0.3	1	36.44	32.95	3.45	6.80	18.9	12.2
	2	36.39	34.38	2.02	9.75	13.8	4.06
	3	36.84	33.34	3.47	7.21	19.2	12.0
	4	36.82	32.35	3.90	7.90	23.1	15.2
SD		0.24	0.85	0.82	1.3	3.81	4.77
0.4	1	37.43	33.77	3.65	9.07	22.4	13.3
	2	36.50	34.03	2.43	12.2	18.8	6.08
	3	36.89	32.93	3.96	8.86	24.5	15.7
	4	37.75	31.86	4.58	9.81	30.8	20.9
SD		0.56	0.98	0.90	1.53	5.03	6.16

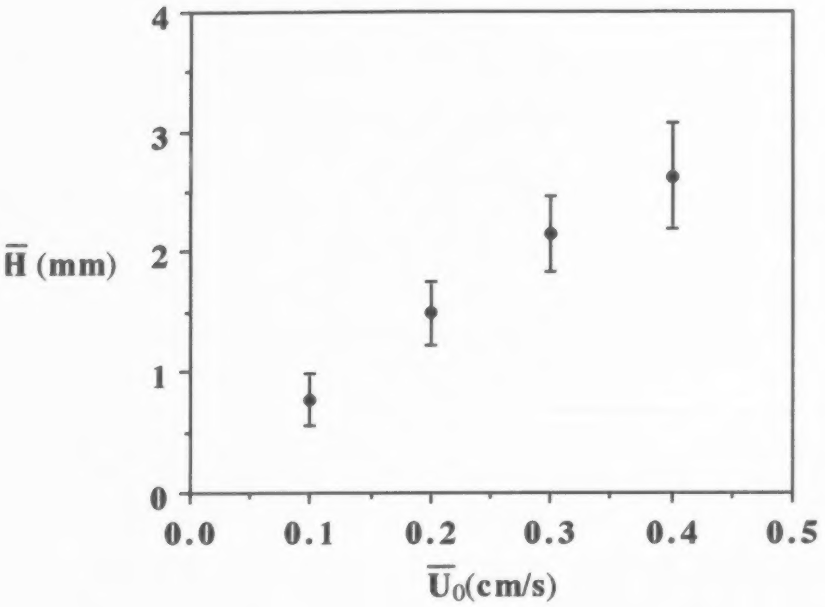

Figure 5.14 The plate heights of the predicted peaks from the four replicate sorption rate measurements for naphthalene in 85% MeOH/H_2O on PRP-1 as a function of the mobile phase linear velocities. The predicted plate heights were from EMG fit. The error bars are one standard deviation from duplicate measurements.

Table 5.13 The predicted plate heights from the EMG fit at four mobile phase linear velocities. The standard deviations were from four replicate sorption rate curves.

$\overline{U}_0$ (cm/s)	$\overline{H}$ (mm)	SD
0.1	0.8	0.2
0.2	1.5	0.2
0.3	2.2	0.3
0.4	2.6	0.4

Table 5.14 The asymmetry factors calculated at 10% of the peak height from the EMG fit for the predicted peaks of naphthalene on PRP-1. The standard deviations were from four replicate sorption rate curves.

$\overline{U}_0$ (cm/s)	Run No.	A.F.
0.1	1	1.8
	2	1.2
	3	1.4
	4	1.5
SD		0.60
0.2	1	1.6
	2	1.1
	3	1.5
	4	1.7
SD		0.41
0.3	1	1.6
	2	1.2
	3	1.6
	4	1.7
SD		0.22
0.4	1	1.4
	2	1.2
	3	1.5
	4	1.6
SD		0.17

5.3.6 Comparison of the Predicted and the Observed Elution Profiles on PRP-1

This section examines how the predicted profiles (PRE) match the observed elution peaks (OBS) of naphthalene on PRP-1. In Figure 5.15, panel A shows a predicted peak (a solid line) and an observed peaks (points) at a mobile phase linear velocity of 0.1 cm/s. Panel B, C, and D in the same Figure show the predicted and observed peaks at other mobile phase linear velocities of 0.2 cm/s, 0.3cm/s and 0.4 cm/s respectively. The predicted peaks in Figure 5.15 were calculated from the rate data from run 1 in Table 4.6. The predicted peaks (solid lines) along with the observed peaks (points) in Figure 5.16, 5.17 and 5.18 were calculated from the rate data from runs 2, 3 and run 4 in Table 4.6. Both the predicted and the observed peaks were normalized to area one.

In general, all the predicted peaks match the observed peaks very well. The tailing portions of the predicted peaks are almost coincident with those of the observed peaks at all mobile phase linear velocities using data from all the four kinetic runs, except at the two low flow rates for run 2. The centers of gravity of the predicted peaks also closely match those of the observed ones. At the highest mobile phase linear velocity of 0.4 cm/s, the front of the predicted peaks do not match those of the observed ones. All the predicted peaks are shorter and slightly broader than the observed ones. The predicted and observed peaks can also be quantitatively compared in term of chromatographic figures of merit calculated from the EMG fits. The relative difference in the chromatographic figures of merit defined in equation 5.50 are shown in Table 5.15:

$$\Delta_i = \frac{\text{PRE - OBS}}{\text{OBS}} \text{x}100\% \qquad (5.50)$$

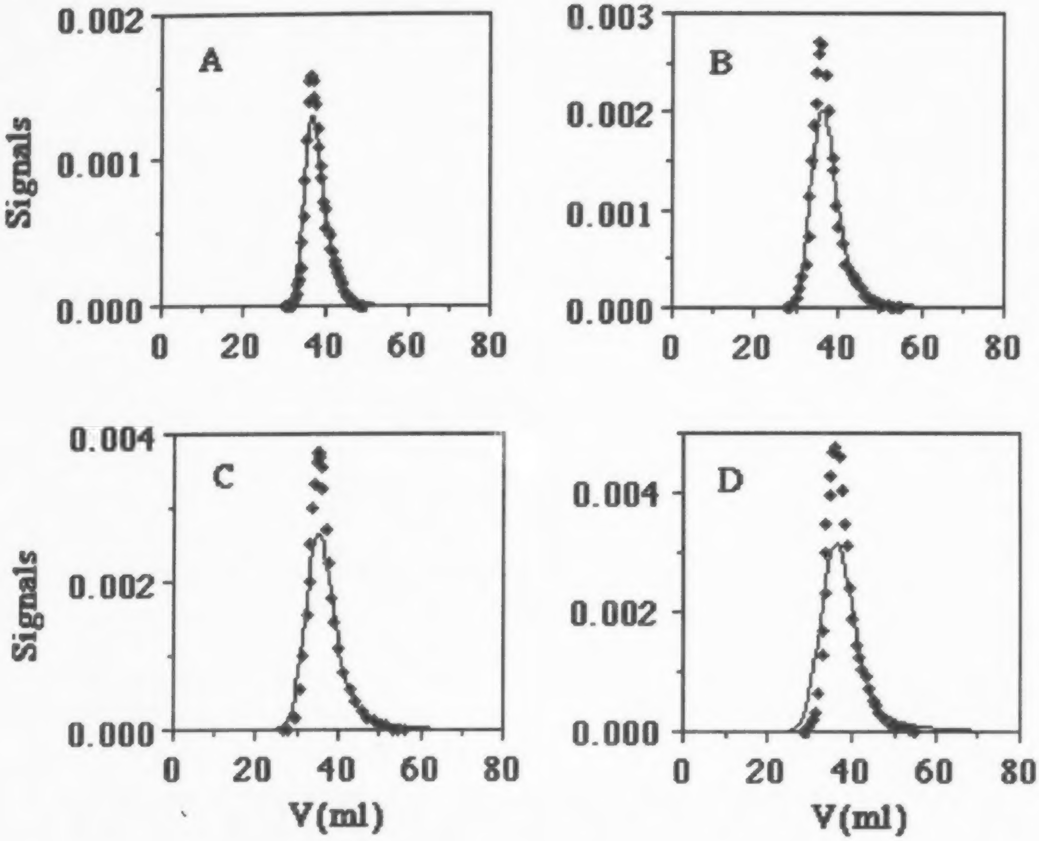

Figure 5.15 The predicted profiles (solid lines) and the observed peaks (symbols) at four mobile phase linear velocities. The observed peaks are obtained by injection of 3.135 x 10^{-5} M naphthalene in 85% MeOH/H_2O on PRP-1 . The predicted peaks are predicted using the tri-exponential constants in column 1 in Table 4.6. Panel A shows the predicted and the observed peaks at $\overline{U}_0$ of 0.1 cm/s. Panels B, C, and D show the observed and predicted peaks at $\overline{U}_0$ of 0.2, 0.3 and 0.4 cm/s.

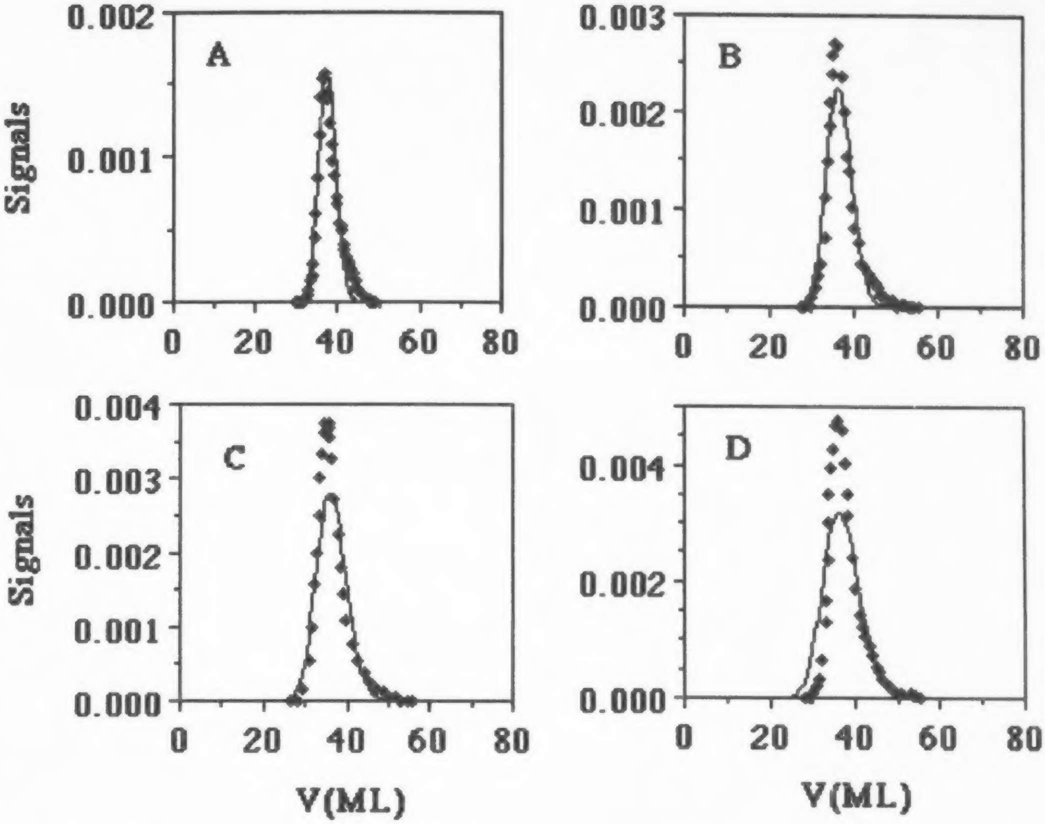

Figure 5.16 The predicted profiles (solid lines) and the observed peaks (symbols) at four mobile phase linear velocities. The observed peaks are obtained by injection of 3.135×10^{-5} M naphthalene in 85% MeOH/H_2O on PRP-1 . The predicted peaks are predicted using the tri-exponential constants in column 2 in Table 4.6. Panel A shows the predicted and the observed peaks at $\overline{U}_0$ of 0.1 cm/s. Panels B, C, and D show the observed and predicted peaks at $\overline{U}_0$ of 0.2, 0.3 and 0.4 cm/s.

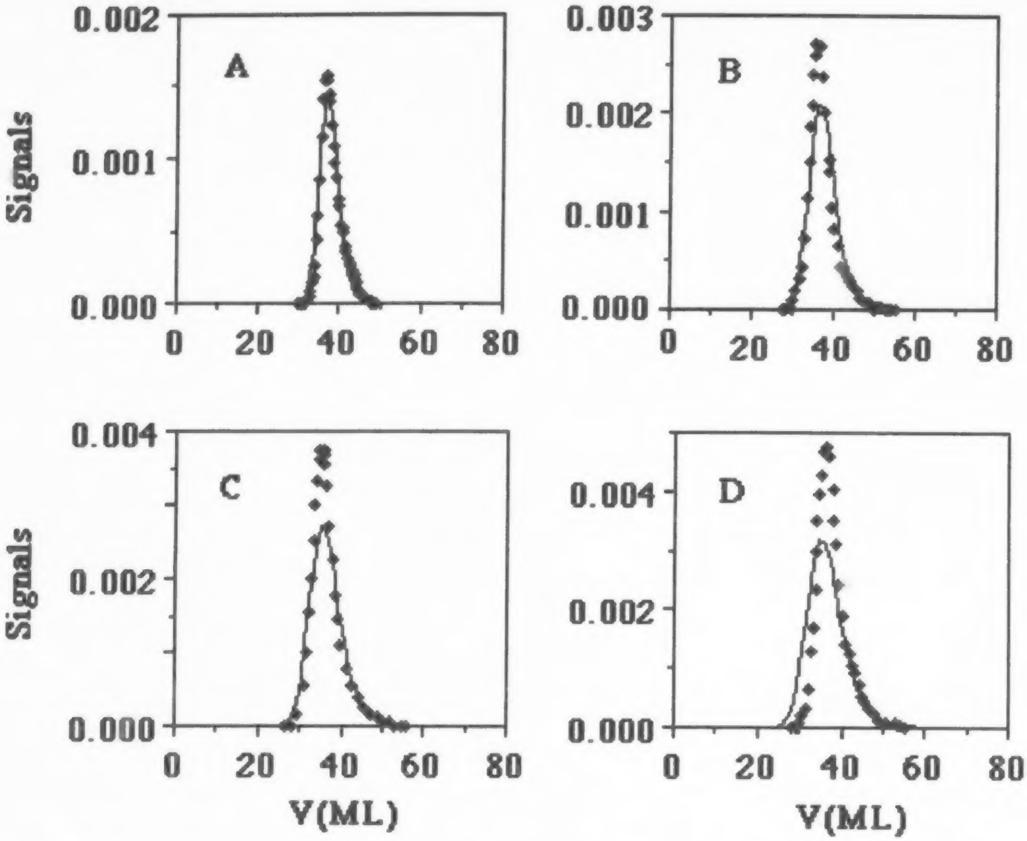

Figure 5.17 The predicted profiles (solid lines) and the observed peaks (symbols) at four mobile phase linear velocities. The observed peaks are obtained by injection of 3.135 x 10^{-5} M naphthalene in 85% MeOH/H_2O on PRP-1 . The predicted peaks are predicted using the tri-exponential constants in column 3 in Table 4.6. Panel A shows the predicted and the observed peaks at $\overline{U}_0$ of 0.1 cm/s. Panels B, C, and D show the observed and predicted peaks at $\overline{U}_0$ of 0.2, 0.3 and 0.4 cm/s.

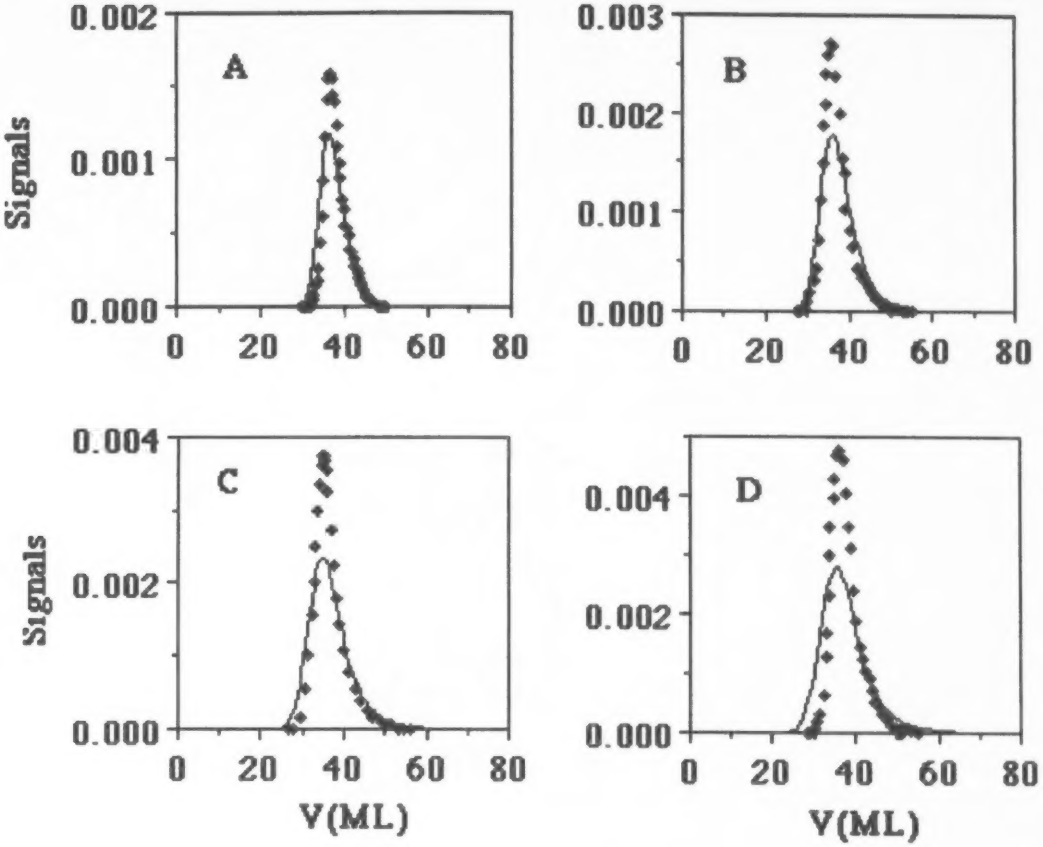

Figure 5.18 The predicted profiles (solid lines) and the observed peaks (symbols) at four mobile phase linear velocities. The observed peaks are obtained by injection of 3.135 x 10^{-5} M naphthalene in 85% MeOH/H_2O on PRP-1 . The predicted peaks are predicted using the tri-exponential constants in column 4 in Table 4.6. Panel A shows the predicted and the observed peaks at $\overline{U}_0$ of 0.1 cm/s. Panels B, C, and D show the observed and predicted peaks at $\overline{U}_0$ of 0.2, 0.3 and 0.4 cm/s.

Δ represents the relative difference, and i is any of figure of merit between the predicted and observed peaks. Δ_i was calculated using the average values shown in Table 5.10 and Table 5.12.

The relative differences in the centers of gravity, V_R, between the observed and the predicted peaks are less than 4% at the four mobile phase linear velocities. The relative differences in the centers of gravity, V_G, of the Gaussian portion are less than 4%. The relative differences in the V_τ are less than 25%. The relative differences in the variances, σ^2_V, which are the sum of the variances of the Gaussian portion, $\sigma^2_{v,G}$, and the variances of the tailing portion , V^2_τ, of the peak are relatively larger. This is mainly due to the large difference in the variances of the Gaussian portion of a peak. It is seen that the relative differences in the variances of the Gaussian portion, $\sigma^2_{v,G}$, is as high as 359%.

In order to understand the large difference associated with the variances of the Gaussian portion of a peak, it is necessary to understand the origin of the predicted peak shape. Each of the distributions predicted for the three hypothetical types of sites were investigated. The tri-exponential constants used in this discussion were previously shown in the first column in Table 4.6. The profiles used for the following discussion were obtained at the mobile phase linear velocity of 0.3 cm/s.

Figure 5.19 shows the distributions P1, P2 and P3, calculated from the three terms of the tri-exponential using equation 5.25. P1, P2 and P3 are not scaled. The first term, P1, which is associated with the largest rate constant k_1 and the largest number of

Table 5.15 The relative differences in the figures of merit between the observed and the predicted peaks at four mobile phase linear velocities.

$\overline{U}_0$ (cm/s)	ΔV_R (%)	ΔV_G (%)	ΔV_τ (%)	$\Delta\sigma^2_{V,G}$ (%)	$\Delta\sigma^2_V$ (%)	ΔV^2_τ (%)
0.1	-3.7	-2.8	-25	118	-21	37
0.2	-1.3	-1.7	1.0	179	44	30
0.3	-3.9	-3.8	10	217	24	14
0.4	0.4	1.2	-8.5	359	41	13

$$\Delta_i = \frac{\text{PRE-OBS}}{\text{OBS}} \text{X} 100\%$$

hypothetical sites n_1 (except run 2 which has $n_2 > n_1$) generates a profile which is Gaussian and the second narrowest of the three , and it is located at the furthest right on the time axis. P2, which is associated with the second largest rate constant k_2 and the second largest number of hypothetical sites n_2, generates a profile which is Gaussian and the narrowest of the three, and it is located further left on the time axis. P3 with the smallest rate constant and number of sites produces a tailing peak and is located the furthest left on the time axis.

The profiles in Figure 5.19 are interesting in terms of their contributions to the shape of the final predicted peaks. The major source of the tailing of the profiles is the contribution from the distribution due to the slowest process, P3. The distribution due to the fast and the intermediate processes, P1 and P2, are likely to be the major source of the width of the profiles except near the baseline. The distributions P1 and P2 along with the observed profiles are shown in Figure 5.20 and Figure 5.21. The distributions P1 and P2 have been artificially shifted down the time axis so that the peak maxima coincide . All of the distributions and the observed peaks are normalized to area one.

As shown in Figure 5.20, the distribution P1 matches the main part of the observed peak very well, although, the width of the observed peak is slightly overestimated by P1. Figure 5.21 shows the distribution P2 as well as the observed peak. The distribution P2 matches the main part of the observed peak well but not as well as the P1 does. The distribution P2 is much higher than the observed peak. Figure 5.22 shows the distribution P1_2, the convolution of P1 and P2. It is shorter and wider than the observed peak. Through the above analysis, it is shown that the large relative differences in the variances of the Gaussian portion between the OBS and the PRE peaks are due to P1 and P2 distributions. It should be pointed out that the six parameters in the tri-exponential equation is not independent of each other, therefore, P1, P2 and P3 are correlated to each other, a larger uncertainty in n_3 and k_3 can cause a large uncertainty in P3, therefore, in P1 and P2. In addition, the values of V_τ and σ_G are more sensitive to the EMG fitting errors which also cause large difference between the PRE and OBS. The shapes of the tailing parts of

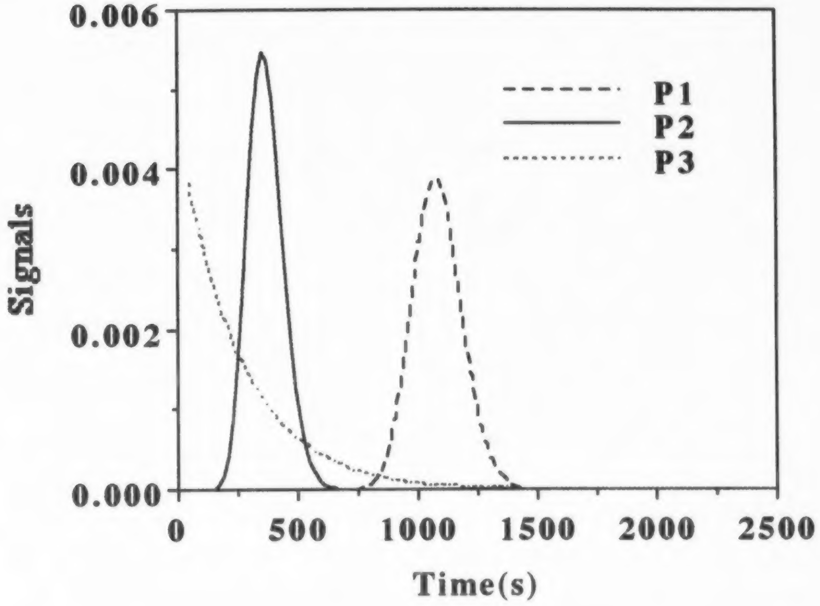

Figure 5.19 The non-scaled probability distributions of P1, P2 and P3 which were calculated from equation 5.25 using the tri-exponential constants shown in column 1 in Table 4.6. The distribution P1 is associated with the hypothetical sites in which the rate process described only by the first term in the tri-exponential. The distributions P2 and P3 are associated with the hypothetical sites in which the rate processes described by the second and the third term in the tri-exponential.

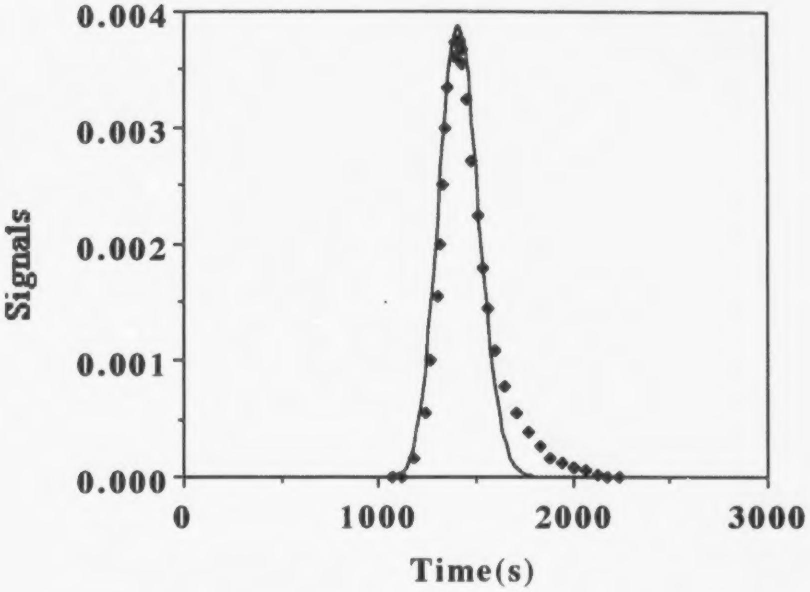

Figure 5.20 The probability distribution P1 (solid line) and the observed predicted peak (symbols) at the mobile phase linear velocity of 0.3 cm/s. The P1 is shifted down the time axis so that the peak maximum overlaps with that of the observed elution profile. The observed peak is the result of injection of 3.135 x 10^{-5} M naphthalene on PRP-1 in 85 %MeOH/H_2O.

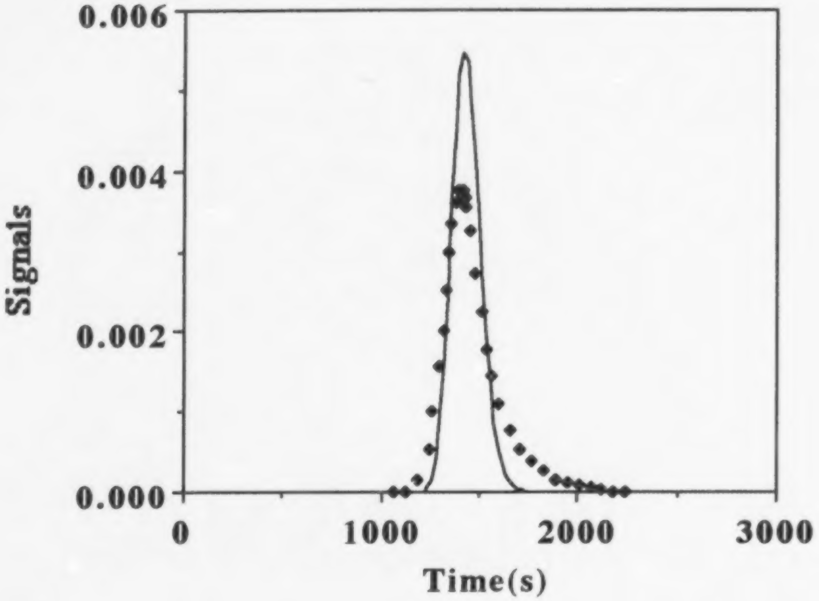

Figure 5.21 The probability distribution P2 (solid line) and the observed predicted peak (symbols) at the mobile phase linear velocity of 0.3 cm/s. The P2 is shifted down the time axis so that the peak maximum overlaps with that of the observed elution profile. The observed peak is the result of injection of 3.135 x 10^{-5} M naphthalene on PRP-1 in 85 %MeOH/H_2O.

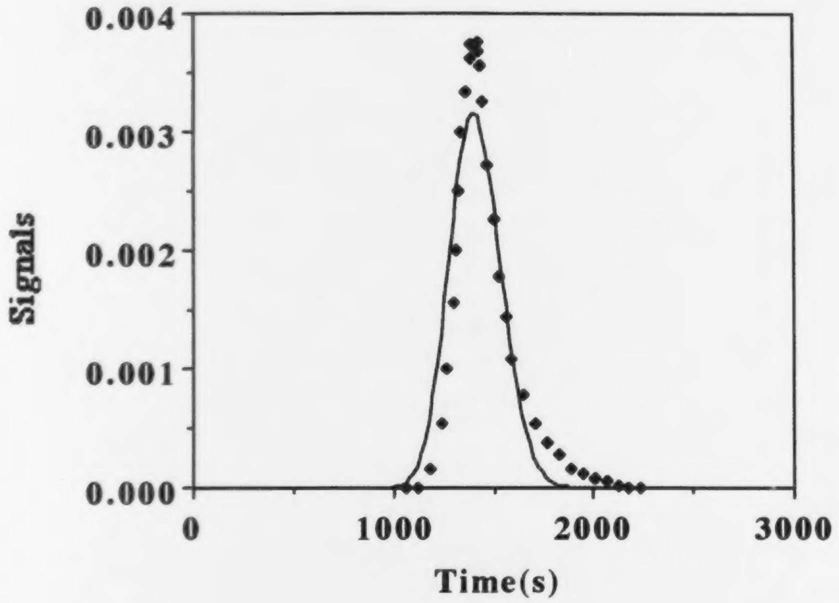

Figure 5.22 The probability distribution P1_2 (solid line), convolution of P1 and P2, and the observed peak (symbols) at the mobile phase linear velocity of 0.3 cm/s. The P1_2 is shifted down the time axis so that the peak maximum overlaps with that of the observed elution profile. The observed peak is the result of injection of 3.135 x 10^{-5} M naphthalene on PRP-1 in 85 % MeOH/H_2O.

the distributions P1, P2 and P1_2 do not match the tailing parts of the observed peaks, since the distributions of P1, P2 and P1_2 are essentially symmetric. This suggests that the kinetic tailing, which can be matched well by P3, is mainly due to the slow sorption rate defined by the third exponential term in equation 4.10. A plot of the observed and predicted plate heights against the mobile phase linear velocity along with the standard deviations are shown in Figure 5.23. The observed plate heights are shown in Table 5.16. The predicted plate heights were shown previously in Table 5.13. The standard deviations for the observed peaks were calculated from duplicate runs. The standard deviations for the predicted peaks were calculated from four replicate runs. The error bars shown in Figure 5.23 are one standard deviation.

The predicted plate heights are close to the observed plate heights, but they are larger than the observed ones except that at $\overline{U}_0$ of 0.1 cm/s, this is mainly due to the larger $\sigma^2_{v,G}$ associated with the predicted peaks.

5.3.7 The plate height in the stagnant mobile phase from Giddings' Equation.

As discussed in Section 5.2.1.5, the contribution to bandbroadening from the stagnant mobile phase can be described theoretically by equation 5.11 [69] which is based on the "linear driving force" approximation where the diffusion in the pores is described with a single exponential equation with a diffusion coefficient of D_m in the bulk solution, and there is no hindered diffusion. Substituting typical column parameters into equation 5.11, the bandbroadening from $\overline{H}_{sm}$ is calculated. The parameters used are $\gamma' = 2/3$ [135], K'=28.48, from the elution chromatogram, f = 0.52, and $D_m = 1.12 \times 10^{-5}$ cm^2/s estimated from Wilke-Chang equation [136].

The plate heights calculated from the theoretical equation 5.11, the observed plate heights, and the predicted plate heights are presented in Table 5.17 for four mobile phase

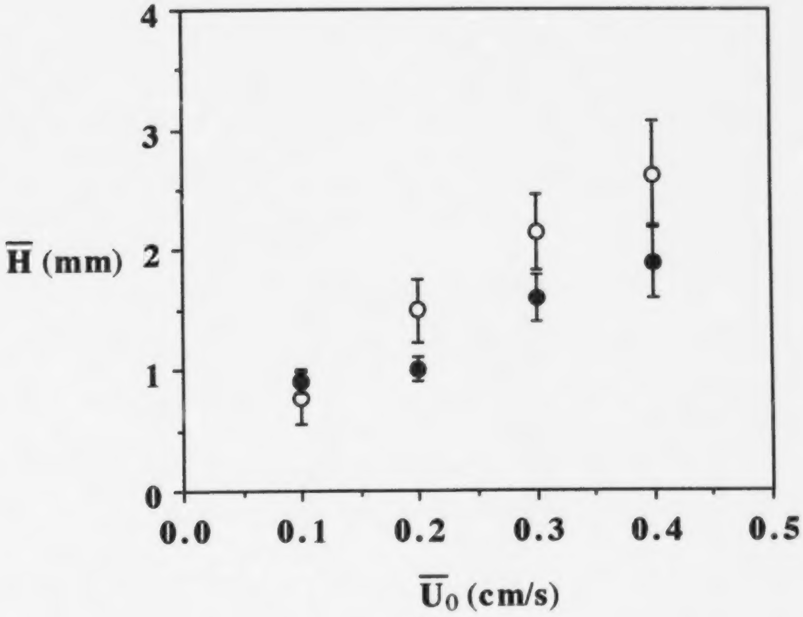

Figure 5.23 The observed(●) and predicted (O) plate heights as a function of the mobile phase linear velocity for naphthalene on PRR-1 in 85% MeOH/H_2O. The predicted plate heights are calculated from the moments of the EMG fits for the peaks which are calculated from the four sorption rate curves. The observed plate heights were calculated from the moments of EMG fits by duplicate injections of 3.135 x 10^{-5} M naphthalene on PRP-1. The error bars are one standard deviation from replicate measurements of the observed and predicted peaks.

Table 5.16 The observed plate heights from the EMG fit at the four mobile phase linear velocities. The standard deviations were from duplicate injections.

$\overline{U}_0$ (cm/s)	$\overline{H}$ (mm)	SD
0.1	0.9	0.1
0.2	1.0	0.1
0.3	1.6	0.2
0.4	1.9	0.5

Table 5.17 Comparison of the predicted, observed and the theoretical ($\overline{H}_{sm}$) plate heights at four mobile phase linear velocities. The standard deviations of the observed plate heights were from duplicate injections. The standard deviations of the predicted plate heights were from four replicate sorption rate curves.

$\overline{U}_0$ (cm/s)	$\overline{H}$(OBS) (mm)[a]	SD	$\overline{H}$(PRE) (mm)[b]	SD	$\overline{H}_{sm}$(Theory) (mm)[c]
0.1	0.9	0.1	0.8	0.2	0.0096
0.2	1.0	0.1	1.5	0.2	0.018
0.3	1.6	0.2	2.2	0.3	0.026
0.4	1.9	0.5	2.6	0.4	0.034

a Plate heights from the EMG fit.

b Plate heights predicted in this work.

c Plate heights from Giddings' equation.

linear velocities. The plate heights from Giddings' equation 5.11 are over 100 times smaller than the observed ones.

However, the plate heights from peaks predicted from the measured sorption rates, as discussed above, are much closer to those of the observed ones. Sorption of naphthalene on PRP-1 occurs both in macropores and in micropores. A single diffusion coefficient or a linear driving force model can not represent the sorption of naphthalene on PRP-1 accurately as will be discussed in Chapter 6.

The asymmetry factors measured at 10% of the peak heights for the observed peaks are shown in Table 5.18. The predicted A. F. shown in the previous Table 5.14 are slightly lower than the observed ones.

5.3.8 Kinetic Tailing

The effects of kinetic tailing can be examined by varying flow rates. The fractional tail area, $a_T/(a_T+a_G)$, the relative length of the tail $\frac{\sigma_G}{t_{R,G}}$, the relative height of the tail, $\frac{h_T}{h_G}$, and the normalized standard deviations of the Gaussian portion of the tailed peak $\frac{\sigma_G}{t_{R,G}}$, at four mobile phase linear velocities are shown in Table 5.19. The values of the parameters used in obtaining the characteristics in Table 5.19 are shown in Table 5.20.

The fractional tail areas decrease with an increase in flow rate because the fractional tail area is proportional to the number of molecules participating in the slow sorption step. As the flow rate increases, the molecules spend less time in a column, therefore, fewer molecules will undergo the slow sorption step. The relative length of the tail increases with an increase in the mobile phase linear velocities because the molecules being desorbed from the slow kinetic process will fall further behind the rest of the molecules in the mobile phase as the flow rate increases. Therefore, the relative length of the tail increases. The normalized standard deviations of the Gaussian portion of a peak increases with flow rate,

Table 5.18 The asymmetry factors calculated at 10% of the peak heights from the EMG fit for the observed peaks of naphthalene on PRP-1. The standard deviations were from replicate injections.

$\overline{U}_0$ (cm/s)	Run No.	A.F.
0.1	1	2.03
	2	2.30
	SD	0.19
0.2	1	1.85
	2	1.90
	3	1.85
	SD	0.03
0.3	1	2.34
	2	2.15
	SD	0.13
0.4	1	2.57
	2	2.17
	3	2.01
	SD	0.29

Table 5.19 The dependence of fractional areas, relative heights, relative lengths of peak tails, and the relative standard deviations of the Gaussian parts of a predicted peak on the mobile phase linear velocity. The predicted peak was from run 1 in Table 4.6.

$\overline{U}_0$ (cm/s)	$a_T/(a_T+a_G)$	h_T/h_G	$\sigma'_G/t_{R,G}$	$\sigma_G/t_{R,G}$
0.1	0.02	0.01	0.08	0.049
0.2	0.01	0.005	0.12	0.068
0.3	0.003	0.002	0.13	0.083
0.4	0.002	0.001	0.14	0.093

Table 5.20 The parameters used in the calculation of the characteristics for the tailing and the Gaussian parts in Table 5.19 at the four mobile phase linear velocities. The predicted peak was from run 1 in Table 4.6.

$\overline{U}_0$ (cm/s)	a_T	a_G	h_T	h_G	$\sigma_G'(s)$	$\sigma_G(s)$	$t_G(s)$
0.1	0.074	4.23	8.7×10^{-5}	7.6×10^{-3}	316	207	4210
0.2	0.003	0.314	4.3×10^{-6}	8.0×10^{-4}	260	146	2152
0.3	0.001	0.276	1.9×10^{-6}	8.4×10^{-4}	186	116	1409
0.4	0.0004	0.245	1.0×10^{-6}	9.4×10^{-4}	153	100	1067

meaning the Gaussian portion becomes wider with the flow rates as expected.

5.3.9 Criteria for Selecting a Correct Combination of n_3 and k_3 for the Predicted Peaks

As mentioned in section 4.4.4, the sorption rate data of naphthalene on PRP-1 was fit to an empirical tri-exponential equation by adjusting the six parameters n_1, n_2, n_3, k_1, k_2 and k_3 to minimize the error norm which is the square root of the square of the residue. The presence of any scatter in the experimental data creates some uncertainty in the values of the six parameters. In particular, it was observed that the values of k_3 and n_3 were quite sensitive to the input values [80]. In addition to the scatter in the experimental data, the six parameters are not independent of one another. This means a nearly equally good fit of the rate curves can be obtained with a higher n_3 and a lower k_3 as with a lower n_3 and a higher k_3. The different possible combinations of n_3 and k_3 will create serious ambiguity when the six parameters are used to predict the elution peak.

The criteria which should be used to select a correct combination of n_3 and k_3 are explored in this section using the kinetic run 3 in Table 4.6. Table 5.21 shows the input values of n_3 and k_3 along with the corresponding output values of n_3 and k_3 arising from the curve fitting program which runs a non-linear least squares regression. The values of n_3 vary from 10^{-7} to 10^{-13}, while the k_3 changes from 10^{-4} to 84. The tri-exponential fit (solid line) in Figure 5.24A is the result of using a n_3 of 3.07×10^{-13} and k_3 of 84.41 for No.8. Shown in Figure 5.24B is the tri-exponential fit using a n_3 of 4.65×10^{-8} and k_3 of 1.81×10^{-3} for No.2. n_1,n_2 and k_1 and k_2 vary slightly for the two in Figure 5.24. Visually, the two tri-exponential equations give almost the same good fit for these two combinations of n_3 and k_3 except the fit in Figure 5.24A flattes quickly and the fit in Figure 5.24B rises slowly to approach equilibrium. In addition, the fit in Figure 5.24B gives a smaller error norm as shown in Table 5.21.

Table 5.21 The effects of the estimated input values of n_3 and k_3 on the observed n_3 and k_3 values which were from the curve fitting program with a non-linear least squares regression. The sorption rate curve used was run 3 in Table 4.6.

No.	n_3 (input)	k_3 (input)	n_3 (observed)	k_3 (observed)	Error norm 10^9
1	7.66×10^{-7}	2.26×10^{-4}	3.69×10^{-7}	2.14×10^{-4}	5.6
2	3.71×10^{-8}	2.14×10^{-3}	4.65×10^{-8}	1.81×10^{-3}	5.6
3	3.71×10^{-9}	2.14×10^{-2}	7.22×10^{-9}	2.29×10^{-2}	5.4
4[a]	5.17×10^{-9}	3.14×10^{-2}	6.75×10^{-9}	3.09×10^{-2}	5.4
5	3.71×10^{-10}	0.214	1.28×10^{-9}	2.36×10^{-2}	7.4
6	7.66×10^{-11}	2.26	9.24×10^{-11}	1.73	7.9
7	1.0×10^{-12}	10	1.31×10^{-12}	10.7	8.0
8	1.0×10^{-13}	100	3.07×10^{-13}	84.4	8.0

[a] The parameters in run 4 were used in the calculation of the predicted peaks.

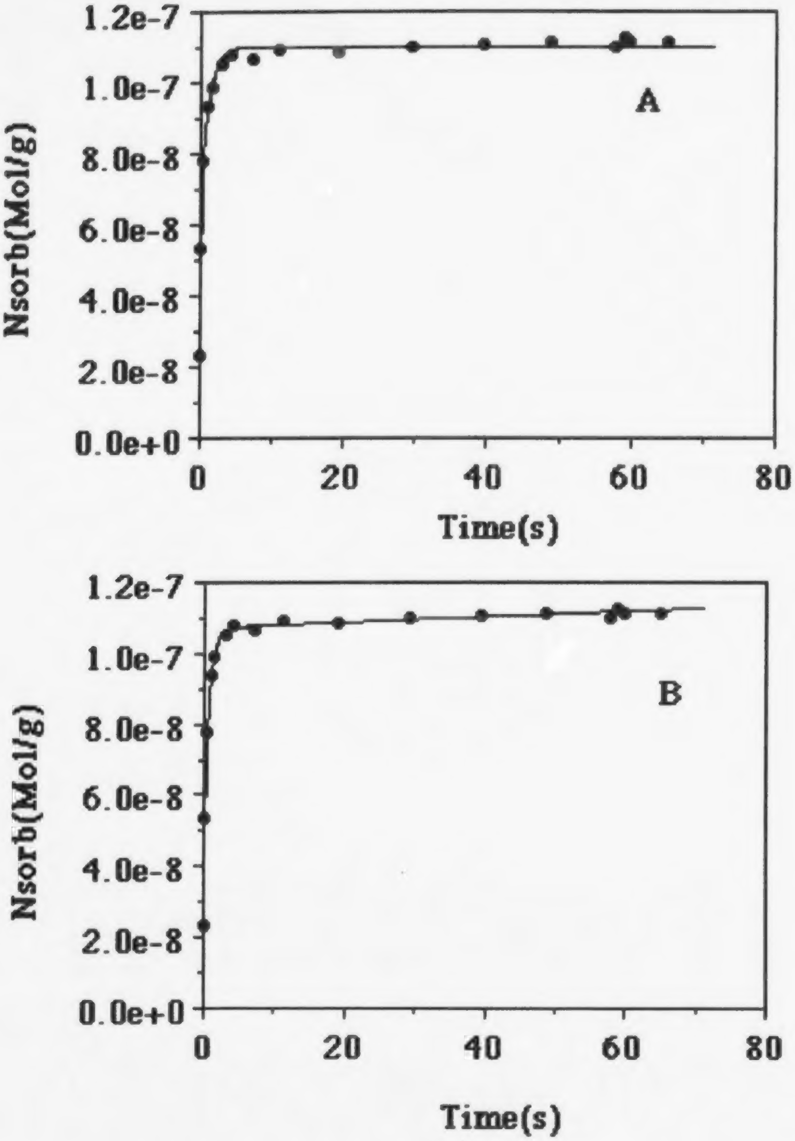

Figure 5.24 The experimental sorption rate data for run 3 in Table 4.6 and the two tri-exponential fits. In A, the solid line was generated using the value of n_3 and k_3 from No.8 in Table 5.21. The error norm is 8 x 10^{-9}. In B, the solid line was generated using the values of n_3 and k_3 from No.2 in Table 5.21. The error norm is 5.6 x 10^{-9}.

Figure 5.25A shows the predicted peak calculated from the parameters generated by the tri-exponential fit in Figure 5.24A, and Figure 5.25B shows the predicted peak calculated using the parameters from the tri-exponential fit in Figure 5.24B. Obviously, these two predicted peaks are quite different. In Figure 5.25A, the profile with a large k_3 and a small n_3 is broad and is located further right on the time axis. However, the profile in Figure 5.25B with a small k_3 and a large n_3 is a narrow peak and located further left on the time axis. Some criteria must be established to select the correct n_3 and k_3.

The first criterion used to select the correct n_3 and k_3 is the error norm. The smaller the error norm, the better the tri-exponential fit. In Table 5.21, among the eight combinations of n_3 and k_3, four kinetic runs have error norm of 7 to 8 x 10^{-9} including No. 5, 6, 7 and 8, and four runs have error norm of 5 x 10^{-9}, including run 1, 2, 3, 4. Therefore, run 5, 6, 7 and 8 were first excluded due to a relative large error norm associated with the curve fitting routine.

Among the four runs left, No. 3 and 4 have slightly smaller error norms than No. 1 and 2. No. 3 and 4 predict very similar peaks as shown in Figure 5.26. Curve A from No.3 gives a slightly longer tail than Curve B from No.4 due to a slightly smaller k_3. Therefore, among these two runs which one should be used to predict the elution peak?

A large value for n_3 means that the true equilibrium value of C_s is much larger than the value observed after 70 seconds, and the corresponding small value of k_3 means that equilibrium will be approached very slowly at a time reached by great extrapolation of the data in the nearly flat region of the rate curve. Such extrapolation to values well beyond the data set is never justified.

Therefore, the k_3 should be the largest and n_3 should be the smallest among all the combinations of n_3 and k_3 which also give smaller error norms, because only with a large k_3 and a small n_3, will the measured sorption rate curve be close to the equilibrium within the shortest and finite time. When k_3 is small, the experimental data were extrapolated greatly to reach equilibrium. The uncertainty in the experimental data, especially in the

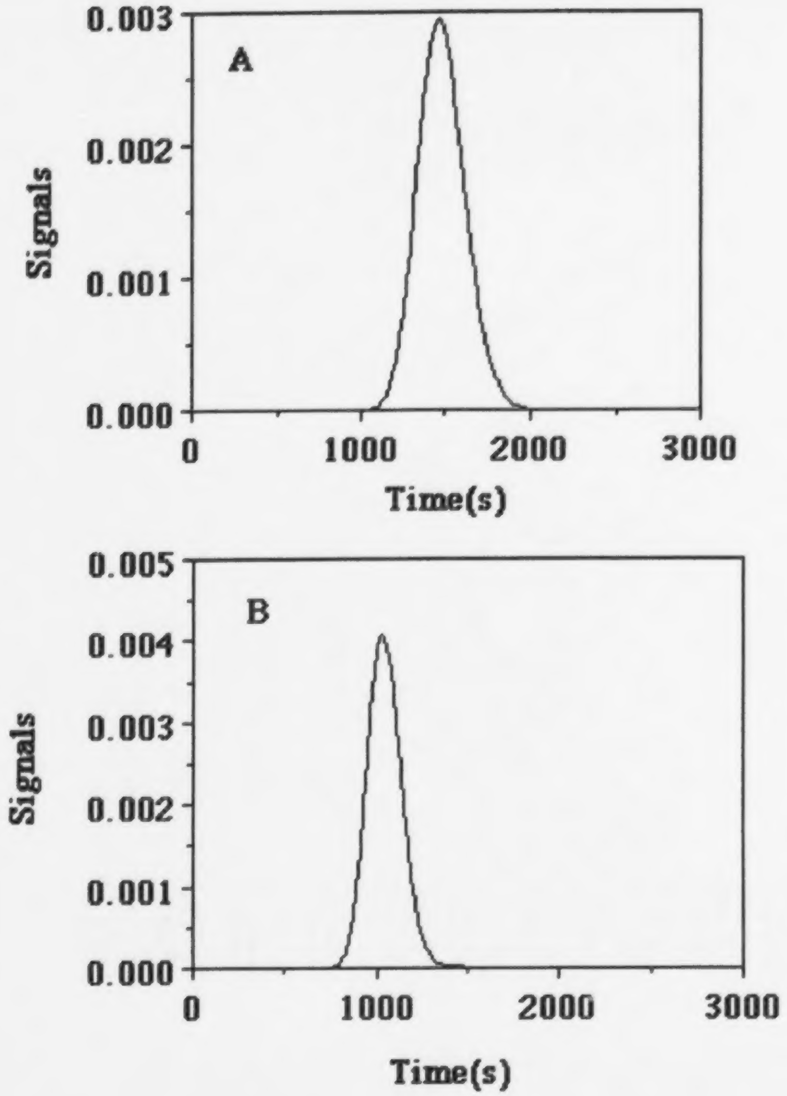

Figure 5.25 In A is the predicted elution profile calculated from the tri-exponential fit from Figure 5.24A using the values of n_3 and k_3 shown as No. 8 in Table 5.21 at $\overline{U}_0$ of 0.3 cm/s. In B is the predicted elution profiles calculated from the tri-exponential fit from Figure 5.24 B using the values of n_3 and k_3 shown as No. 2 in Table 5.21 at $\overline{U}_0$ of 0.3 cm/s.

slow step approaching equilibrium, makes the extrapolation unjustified. When k_3 is the largest, and n_3 is the smallest, n_0 should be the smallest, as can be seen in Table 5.22 for No.1, 2, 3 and 4. No.4 has the smallest n_3 and n_0, meaning we do not have to extrapolate the experimental data long a way to sorption equilibrium in the measurements of the sorption rate curves. Therefore, the peak from No.4 is predicted to elute from a column of PRP-1 for naphthalene in 85%MeOH/H_2O.

Therefore, the final two criteria which should be used together to select the right combination of n_3 and k_3 in the calculation of a predicted peak are both a smaller error norm and the smallest n_3 (or the largest k_3).

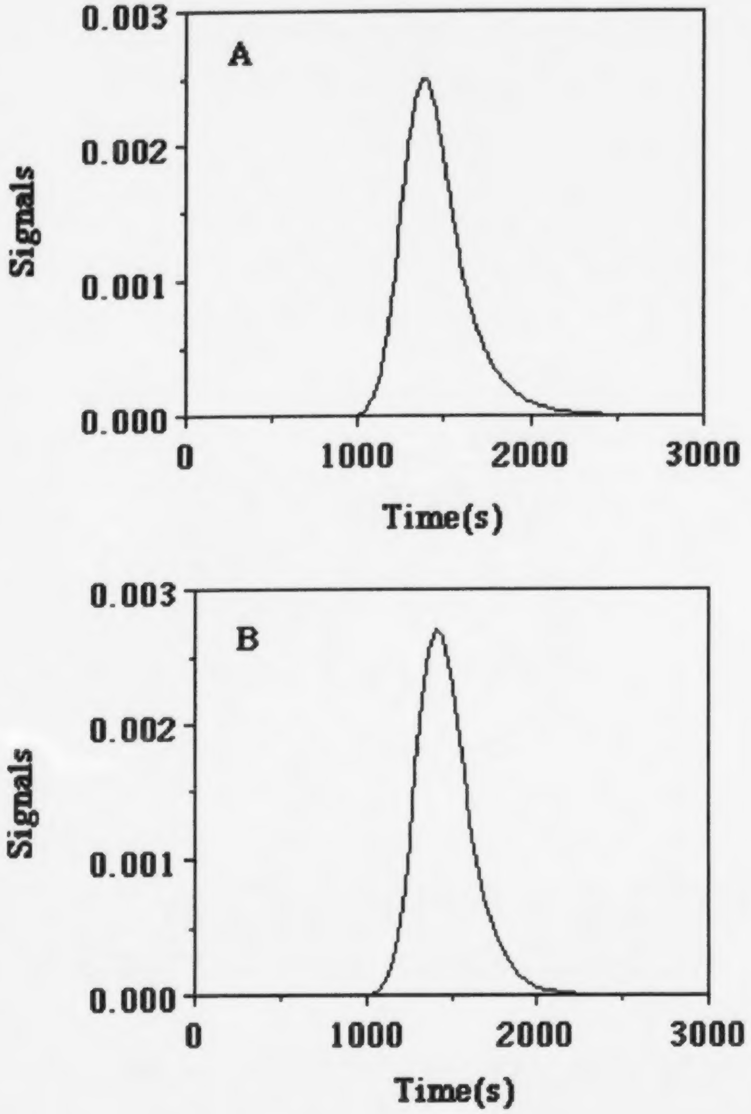

Figure 5.26 Predicted peaks calculated from the experimental sorption rate data of run 3 in Table 4.6 using the value of n_3 and k_3 as shown in Table 5.21 at the mobile phase linear velocity of 0.3 cm/s. Profile A is the predicted peak using the values of n_3 and k_3 as No.3 in Table 5.21. Profile B is the predicted peak using the values of n_3 and k_3 as No.4 in Table 5.21.

Table 5.22 The values of n_0 and n_3 for the four runs with small error norms.

No.	Error norm	n_0	n_3
1	5.6×10^{-9}	4.765×10^{-7}	3.69×10^{-7}
2	5.6×10^{-9}	1.536×10^{-7}	4.65×10^{-8}
3	5.4×10^{-9}	1.136×10^{-7}	7.22×10^{-9}
4[a]	5.4×10^{-9}	1.128×10^{-7}	6.75×10^{-9}

No.4 was used to calculate the predicted peaks.

Chapter 6

Origin of Bandbroadening of Naphthalene on PRP-1

6.1 Introduction

As discussed in Chapter 4 and Chapter 5, there is a slow step in the sorption of naphthalene on PRP-1 in 85% MeOH/H_2O. This slow step causes the severe bandbroadening and tailing in the elution peak of naphthalene. This chapter is to discover what causes the slow sorption of naphthalene in PRP-1.

Generally speaking, there are four possible reasons which have been proposed to explain the slow sorption, as presented in chapter 1.

1. Stagnant zones in the pores of the packing material, because of a poor contact between the eluent and the polymer surface [25].

2. Shrinking and swelling of the particles upon solvent switching which causes channeling in the bed [1].

3. Strong interactions of pi electrons in the PS-DVB with the pi electrons in the solutes [13].

4. Slow diffusion of solutes into the polymer matrix or, in other words, diffusion into micropores [48, 49].

The first effect is related to the diffusion in the stagnant mobile phase present in the pores of the particles. The effect 2 is associated with non-uniform flow due to the non-homogenity of the packing. The effect 3 corresponds to adsorption onto very active sites of the packing. The effect 4 is the intraparticle micropore diffusion which is most likely responsible for the slow sorption of naphthalene on PRP-1.

In order to discover the origin of the slow sorption, the sorption rate curves of naphthalene on PRP-1 must be quantified by a theoretical kinetic model. A commonly used intraparticle diffusion model with a single diffusion coefficient is the Crank model [66, 96, 137]. The Crank model has been used to analyze sorption rate data on sulfonated polystyrene ion exchanger [90], on phenol-formaldehyde ion exchanger [71], on polymeric poly(styrenedivinylbenzene) XAD-2 and XAD-4 adsorbents [100], and on 5A zeolite [138]. Therefore, the sorption rates of naphthalene on PRP-1 was first fit to the Crank model with a single diffusion coefficient. As will be seen below, the Crank model does not give a perfect fit over the entire sorption rate curve.

Sorption on a sorbent with a bidisperse pore distribution has been observed in several cases. Some organic compounds sorbed by activated carbon in a microcolumn have shown a two stage behavior [70, 96, 139, 140]. The sorption of sulfur dioxide by a PS-DVB macroreticular ion exchanger, Amberlyst 21, has been characterized by two stage behavior [141]. The sorption of phenol and its derivatives on activated carbon and on polystyrene sorbents, XAD-4 and XAD-2, has been found to be a two stage sorption process [97, 139]. Such behavior has also been observed with molecular sieves and palletized microporous catalyst such as zeolite.

It was proposed that PRP-1 has micropores(<20Å) in addition to macro and mesopores. The sorption rate curves on PRP-1 were therefore described by a bidisperse pore distribution model proposed by Ruckenstein [141] which gives a better fit to the experimental data.

The sorption rates of naphthalene on PRP-∞, a nominally nonporous PS-DVB packing, were also measured by the shallow bed technique. It was initially believed that PRP-∞ has the same matrix as the PRP-1 due to the same monomers used in the polymerization. The sorption rate curves of naphthalene on PRP-∞ were characterized by a monodisperse pore distribution model, the Crank model [66, 96, 137], because PRP-∞ has no macropores but it has micropores due to the size of the crosslinking monomer, divinybenzene.

The sizes of micropores in PRP-∞ is compared with those in PRP-1. The sizes of the two PS-DVB packings are estimated using a hydrodynamic model for the hindered diffusion. In addition, the sorption isotherms of naphthalene on PRP-1 and PRP-∞ are also compared.

6.2 Theory

6.2.1 Isothermal Macropore Diffusion Control (Crank Model)

If the macropore resistance is dominant in the mass transfer, there will be a concentration profile through the macrospheres, and the sorption rate will therefore depend on the gross particle size. Macropore diffusion was shown previously in Figure 4.1 as steps 1, 2 and 3. Under the conditions of a linear isotherm and a local equilibrium between the sorbed phase and the fluid phase within the macropores at any specified radial position, a differential mass balance equation for a solid spherical shell which reflects Fick's second law of diffusion is given in equation 6.1, 6.2 and 6.3 [66, 96, 137].

$$\frac{\partial Q}{\partial t} = D_{a,eff} \left(\frac{\partial^2 Q}{\partial R^2} + \frac{2}{R}\frac{\partial Q}{\partial R}\right) \tag{6.1}$$

$$D_{a,eff} = \frac{D_a}{\left(1+\frac{\rho K_{a,D}}{\varepsilon_a}\right)} \tag{6.2}$$

$$Q_{ave} = \frac{3}{R_a^3}\int_0^{R_a} Q\, R^2 dR \tag{6.3}$$

where Q is the concentration of a solute in the sorbed phase at time t. Q_{ave} is the average concentration of a solute in the sorbed phase. D_a is the macropore diffusivity and $D_{a,eff}$ is effective macropore diffusivity. R_a is the radius of a particle. $K_{a,D}$, having unit of L/g, is the distribution coefficient associated with adsorption on the walls of the macropores. ε_a, the macropore porosity, is the ratio of the macropore volume to the particle volume. ρ, the density of a particle, is the ratio of the weight of a particle to the volume of a particle.

The initial and boundary conditions for a step change in the surface concentration are shown as follows:

$$C\,(R,\,0) = C_0 \qquad\qquad C\,(R_a,t) = C_\infty \tag{6.4}$$

$$Q(R,0) = Q_0 \qquad\qquad Q(R_a,t) = Q_\infty \tag{6.5}$$

$$\left(\frac{\partial C}{\partial R}\right)_{R=0} = \left(\frac{\partial Q}{\partial R}\right)_{R=0} = 0 \tag{6.6}$$

where C_0, C_∞ and C are the concentrations of a solute in the mobile phase at initial, equilibrium and time t. Q_0 and Q_∞ are the concentrations of a solute in the sorbed phase at initial and equilibrium. The solution of the above mass balance equation is expressed in equation 6.7 which is also called the Crank model:

$$\frac{Q_{ave}-Q_0}{Q_\infty - Q_0} = \frac{Q_{a,t}}{Q_{a,\infty}} = 1 - \frac{6}{\pi^2}\sum_{n=1}^{\infty}\frac{1}{n^2}\exp(-\,n^2\,B_a\,t) \tag{6.7}$$

and

$$B_a = \frac{\pi^2\,D_{a,eff}}{R_a^2} \tag{6.8}$$

where $Q_{a,t}$ is the macropore uptake at time t, $Q_{a,\infty}$ is the macropore uptake at equilibrium, Q_0 and Q_∞ are the concentrations of a solute in the sorbed phase at time zero and equilibrium respectively. Other parameters are defined as before.

Equation 6.7 is derived for the isothermal sorption where the heat transfer is sufficiently rapid relative to the sorption rates and under the condition of "infinite solution volume" where the fraction of a solute sorbed out of the mobile phase is very small, then the solute concentration is essentially constant in the mobile phase.

6.2.2 Isothermal Micropore Diffusion Control (Crank Model)

When the macropore sorption is sufficiently faster than the micropore sorption, the concentration profile through all the macrosphere is uniform. The micropore sorption process is shown as step 4 in the previous Figure 4.1.

For a linear sorption isotherm and a spherical microsphere, and if the sorption is performed under "infinite solution volume" and isothermal condition, a similar differential mass balance equation to the equation 6.1 is applied to the micropore controlled sorption rate. The initial and boundary conditions are also similar to equation 6.4, 6.5 and 6.6. The intraparticle micropore sorption rate with a single effective diffusion coefficient is shown in the equation 6.9 [66, 96, 137]:

$$\frac{Q_{ave}-Q_0}{Q_\infty - Q_0} = \frac{Q_{i,t}}{Q_{i,\infty}} = 1 - \frac{6}{\pi^2} \sum_{n=1}^{\infty} \frac{1}{n^2} \exp(-\, n^2 B_i\, t) \tag{6.9}$$

and

$$B_i = \frac{\pi^2 D_{i,eff}}{R_i^2} \tag{6.10}$$

where $Q_{i,t}$ is the micropore uptake at time t. $D_{i,eff}$ is the effective micropore diffusivity with $K_{a,D}$ and ε_a, in equation 6.2 replaced by ε_i and $K_{i,D}$. R_i is the radius of the microspheres, and $Q_{i,\infty}$ is the micropore uptake at equilibrium. Other parameters were defined before.

However, if the sorption in the macropores is not at equilibrium when the micropore uptake starts, macropore and micropore sorption are not independent of each other during the entire sorption. The above method can not be used for the evaluation of the macropore and micropore diffusivities [141]. The overall sorption rate will depend on both time constants.

6.2.3 Bidisperse Pore Diffusion Control (Ruckenstein Model)

Many models for the description of sorption by a bidisperse porous sorbent have been developed on the basis of various combinations of mass transfer resistance and isotherm relations. The earlier interests in the modeling of bidisperse pore diffusion is related to the evaluation of the effectiveness factors for synthetic zeolites and catalyst pellets [142-145]. Bidisperse pore diffusion models for the description of sorption rates of gas, vapor and organic compounds by an ion exchanger [97, 141], a molecular sieve and activated carbon have been reported for both the bed column [97, 141] and batch reactor [74, 97, 140]. Recently, the irreversible adsorption of an adsorbate in a bidisperse pore system has been modeled using a Turner pore structure model [146].

The solution for a mass balance equation consisting of two mass transfer resistances is very complex, and the mass balance equation is difficult to be solved analytically. However, for one situation, where the macropore sorption is very fast but finite compared with the micropore sorption, but it is not at equilibrium when the micropore sorption starts, a simplified bidisperse model is used to account for the two resistances to mass transfer where one resistance is essentially small compared with the other.

In this work, a model proposed by Ruckenstein [141], describing the competing effects of macropore and micropore sorption in PRP-1, is used. The sorption occurs both in the macropores and micropores under the condition where the macropore sorption is faster than the micropore sorption. A picture of a bidisperse pore distribution structure is shown in Figure 6.1, and the bidisperse pore diffusion model is expressed in equation

6.11:

$$\frac{Q_t}{Q_\infty}=\frac{[1-\frac{6}{\pi^2}\sum_{n=1}^{\infty}\frac{1}{n^2}\exp(-n^2\pi^2\gamma\ t)]+\frac{\beta}{3\alpha}[1-\frac{6}{\pi^2}\sum_{n=1}^{\infty}\frac{1}{n^2}\exp(-n^2\pi^2\gamma\ \alpha\ t)]}{1+\frac{\beta}{3\alpha}} \qquad (6.11)$$

$$\gamma=\frac{D_{a,eff}}{R_a^2} \qquad (6.12)$$

$$\alpha=\frac{D_{i,eff}\,R_a^2}{D_{a,eff}\,R_i^2} \qquad (6.13)$$

$$\beta=\frac{3(1-\varepsilon_a)\varepsilon_i}{\varepsilon_a}\times\frac{R_a^2 D_i}{R_i^2 D_a} \qquad (6.14)$$

where ε_i, the porosity of micropores, is the ratio of the micropore volume to the particle volume. D_i is the micropore diffusivity. Other parameters are defined before.

6.2.4 Comparison of Different Kinetic Equations

In order to evaluate the goodness of fit of various kinetic models in fitting the sorption rate curves of naphthalene on PRP-1 and PRP-∞, the error analysis between the models and the measured experimental data is carried out as follows:

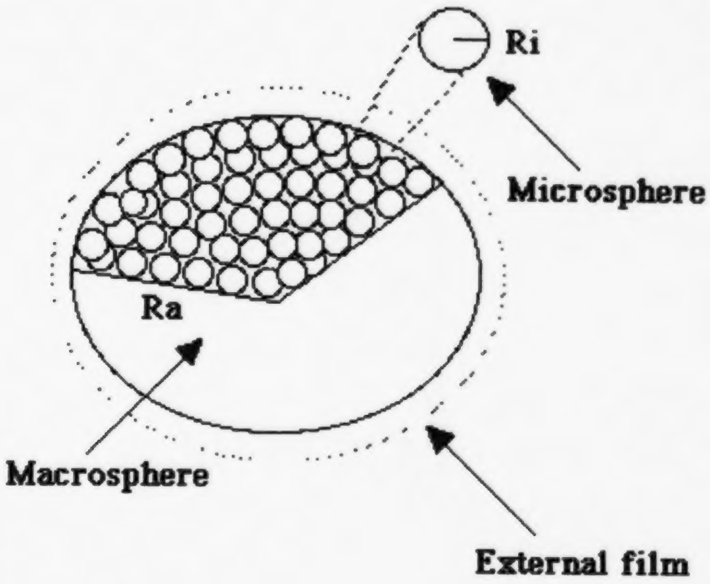
Ri
Microsphere
Ra
Macrosphere
External film

Figure 6.1 Schematic diagram of a bidisperse sorbent particle consisting of macrospheres and microspheres.

$$\text{Error} = \sum \left(\frac{(Q_t)_{pred}-(Q_t)_{exp}}{(Q_t)_{exp}}\right)^2/(N-n) \qquad (6.15)$$

where N is the number of data. n is the number of the parameters in an equation.

6.2.5 Hydrodynamic Theory for Hindered Diffusion

6.2.5.1 Introduction

The diffusivity of a solute within a pore of dimensions comparable to those of the solute molecule is generally found to be less than its value in unbounded liquid. This phenomenon is known as "hindered" or "restricted" diffusion. The decrease of the diffusion coefficient for a solute in a pore compared with the diffusion coefficient (D_m) in the bulk solution is due to two combined hindrance effects: (1) The additional hydrodynamic resistance above that in the bulk solution hinders the movement of a solute molecule through the pore due to the presence of the pore walls. (2) Steric interactions between the solute and the pore walls cause the solute to be effectively excluded from a fraction of the pore volume, this leads to an equilibrium partition coefficient (Φ) less than one due to the solute concentration inside the pore being less than that outside the pore.

Theoretical models of hindered diffusion in the micropores have generally been based on a hydrodynamic approach for a solid sphere in an array of identical cylindrical pores. Several theoretical descriptions of hydrodynamic treatments for liquid phase mass transfer in the pores have been discussed by Been [147], Anderson and Quinn [148], Brenner and Gaydos [149], and Malone and Anderson [150].

The concept of the steric and hydrodynamic hindrance to mass transfer in the micropores has found extensive use in fields such as characterization of biological structures [151], gel permeation chromatography [152], hydrodynamic chromatography

[153], heterogeneous catalysis and membrane separations [154].

6.2.5.2 Basic Assumptions [149, 155, 156]

The hindered diffusion of solutes is viewed as taking place through a porous medium which is modeled as an array of identical uncharged cylindrical pores. The molecules of solutes are rigid spheres, uncharged and sufficiently larger than those of solvents so that the solutes can be treated as particles having both Brownian and hydrodynamic characteristics, while solvents can be viewed as a continuum. The bulk solution is assumed to be sufficiently dilute to neglect all solute-solute interactions. No significant adsorption of solute onto the walls of pores and no chemical interactions between the solutes and the walls of pores occur.

6.2.5.3 Physical Picture for a Rigid Spherical Uncharged Solute in a Cylindrical Pore

The initial physical situation for a solute in a liquid-filled pore is shown in Figure 6.2. λ is the ratio of the solute radius to pore radius, r_s/r_o. β is the dimensionless radial position, r/r_o. U is the velocity of a solute molecule in the pore. In the case of an ideal hydrodynamic model, D_i/D_m is given by equation 6.16 [150]:

$$\frac{D_i}{D_m} = K^{-1}\,\Phi \tag{6.16}$$

$$\Phi\,(\lambda,\beta) = \frac{\langle C_o \rangle}{C_o} = \frac{\langle C_L \rangle}{C_L} = 2\int_0^{1-\lambda} e^{-\frac{E}{RT}}\,\beta\, d\beta \tag{6.17}$$

C_o, C_L are the solute concentrations at a pore entrance and in the bulk solution, $<C_o>$ and

$<C_L>$ are concentrations of a solute averaged over a pore cross section at a pore entrance and exit. E is a potential describing long range interactions between the solute and the pore walls. D_m is the diffusion coefficient in the mobile phase. Φ is the partition coefficient, the ratio of the average intrapore concentration to the concentration in the bulk solution at equilibrium. An important specific case is that of purely steric interactions between the solute and the pore walls (E=0).

$$\Phi\ (\lambda,0) = (1-\lambda)^2 \tag{6.18}$$

This result means that since the center of the solute molecule can not get closer than r_s to the pore walls, only the fraction $(1-\lambda)$ [148] of the pore cross section is accessible to the solute. Equation 6.17 is given by Brenner and Gaydos [149], and equation 6.18 has been obtained by various authors using either geometric [157, 158] or statistical thermodynamic [150] arguments.

K, is the "enhanced drag coefficient" in the pore. K^{-1} is also called the hydrodynamic coefficient which is the ratio of the drag on a particle in an unbounded medium to the drag within the pore [155]. K^{-1} is given as [149, 150]:

$$K^{-1}(\lambda,\beta) = \frac{\int_o^{1-\lambda} \frac{f_\infty}{f(\lambda,\beta)} e^{-\frac{E}{RT}} \beta d\beta}{\int_o^{1-\lambda} e^{-\frac{E}{RT}} \beta d\beta} \tag{6.19}$$

where f_∞ and $f(\lambda,\beta)$ are molecular friction coefficients in the bulk solution and in the pores. In general, it is assumed that $f\ (\lambda,\ 0\ )$ adequately approximates $f(\lambda,\beta)$.

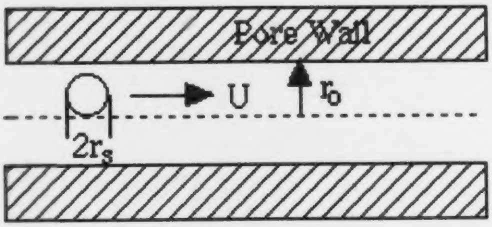
Pore Wall
U
r_o
$2r_s$

Figure 6.2 Schematic diagram of a spherical solute in a cylindrical pore.

6.2.5.4 Hydrodynamic Coefficient K^{-1} in the Hydrodynamic Model

The application of the hydrodynamic theory of hindered diffusion has been impeded to some extent by a lack of complete hydrodynamic information. As indicated by equation 6.19, K^{-1} not only depends on the solute sizes but also on the radial positions of the solute. It can be determined, in principle, by computing the drag on a sphere translating parallel to the cylindrical pore axis with fluid velocity of 0.

A wide range of values λ (< 1) is possible. However, for the axisymmetric case, in which the solute is translating on the centerline ($\beta = 0$) only, it is assumed that the centerline $K^{-1}(\lambda,0)$ adequately approximates $K^{-1}(\lambda,\beta)$. Evidence that centerline values $K^{-1}(\lambda,0)$ may lead to reasonably accurate estimates for $K^{-1}(\lambda,\beta)$ has led to a wide spread use of the "centerline approximation". For E=0 and uncharged solutes, equation 6.19 becomes:

$$K^{-1}(\lambda,0) = \frac{f_\infty}{f} \qquad (6.20)$$

An early relation equivalent to equation 6.20 for the diffusional hindrance factor was given by Pappenheimer et al [159] for $0 < \lambda \leq 0.4$. For larger values of λ ($0 \leq \lambda \leq 0.9$), the numerical calculation of K^{-1} values by Haberman and Sayre[160], Wang and Skalak [161] and Paine and Scherr [155] gave more accurate centerline values. The centerline values of K^{-1} given by Paine and Scherr [155] were used in this work.

6.3 Results and Discussion

6.3.1 Intraparticle Monodisperse Pore Diffusion Model (Crank Model) for Naphthalene on PRP-1

Attempts to fit the naphthalene sorption rate curves on PRP-1 using the Crank model (equation 6.7) with a single effective intraparticle diffusion coefficient led to inconsistency between the observed kinetic behavior and the model. The experimental data points are not exactly overlaid by the solid line of the Crank model over the entire sorption rate curve, as shown in Figure 6.3. The model overestimates the sorption rate between 2 seconds and 10 seconds, and underestimates the sorption rate after 40 seconds where the line is below most of the experimental points. For sorption of naphthalene on PRP-1, the Crank model only adequately represents the experimental data up to about 88% of the sorption within about the first second.

This can be seen more clearly in the linearized version of the Crank model which is a plot of $B_a t$ verse t. B_a is expressed in equation 6.8. B_a was calculated by substituting the sorption amount at time t from each experimental data point into equation 6.7. The $Q_{a,\infty}$ was the sorption amount at equilibrium. The linearized version of the Crank model should result in a straight line through origin. The first five points are approximately a straight line up to the first second which corresponds to 88% of total sorption as illustrated in Figure 6.4. However, the line curves off after about 88% of sorption. In other porous sorbents, the deviation of the experimental data from the model is often attributed to "hindered" diffusion phenomena as the sorbent approaches saturation [97, 100, 139, 140].

Figure 6.3 and Figure 6.4 show that it is inadequate to use a single diffusion coefficient to describe the entire sorption rate of naphthalene on PRP-1. The problem with the Crank model is that a constant diffusion coefficient is operative through the whole sorption process. However, this seams not to be true for naphthalene sorption on PRP-1.

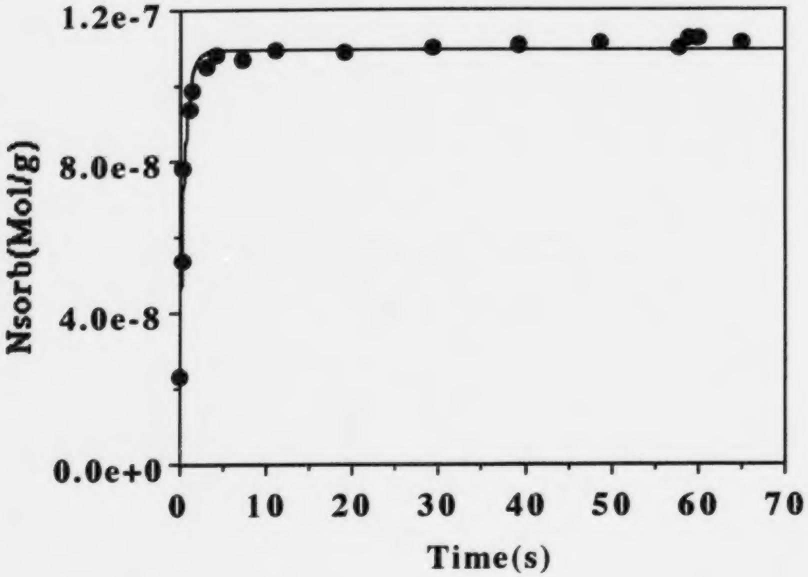

Figure 6.3 The experimental sorption rate data for naphthalene on PRP-1 in 85% $MeOH/H_2O$ are overlaid by a solid line which is generated by using the Crank model (6.7) with a single diffusion coefficient. The experimental data are run 3 in Table 4.6.

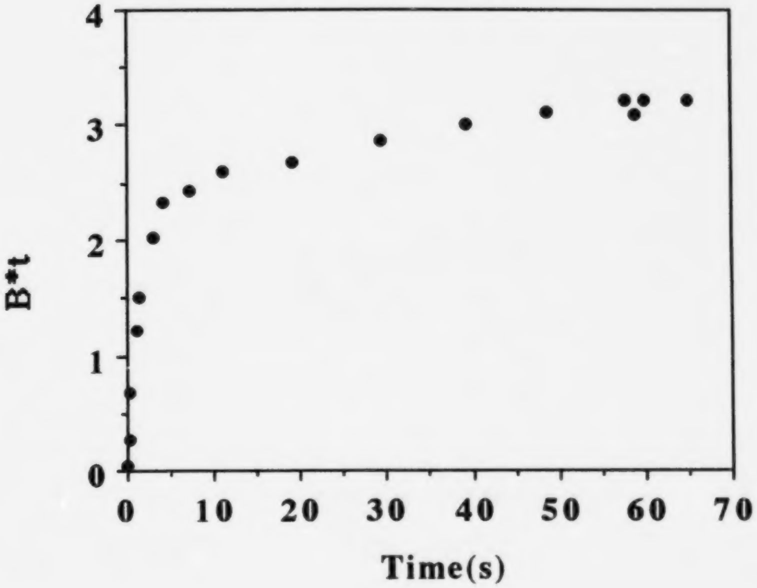

Figure 6.4 The linearized version of the Crank model for naphthalene on PRP-1 in 85%MeOH/H_2O. The B value is calculated from equation 6.8 using the experimental sorption data of run 3 in Table 4.6.

6.3.2 Intraparticle Bidisperse Pore Diffusion Model (Ruckenstein Model) for Naphthalene on PRP-1

The experimentally measured sorption rate of naphthalene on PRP-1 can be successfully described by an empirical tri-exponential equation 4.10. Unfortunately, the parameters obtained from the tri-exponential equation have no physical reality because the tri-exponential equation is not based on any theoretical model of a particle and a pore.

The purpose of fitting the sorption rate data of naphthalene on PRP-1 to the bidisperse pore model is to see if two diffusion processes better describe the sorption rate curve. The slow second step could be due to the diffusion into the polymer matrix or micropores between the polymer chains.

The sorption rate curve of naphthalene on PRP-1 was fit to the bidisperse model shown in equation 6.11 with a nonlinear least squares regression. An excellent agreement between the experimental data (symbols) and the bidisperse model (solid line) has been obtained as shown in Figure 6.5. The bidisperse model gives a much better fit than the Crank model. The parameters from the fitting program are $\gamma\alpha$, $\beta/3\alpha$, $\gamma$and Q_∞ which are shown in Table 6.1. The standard deviations are from the curve fitting program.

The parameters α, β and γ in the bidisperse model have simple physical meanings. The parameter α can be written as [141]:

$$\alpha = \frac{\dfrac{D_{i,eff}}{R_i^2}}{\dfrac{D_{a,eff}}{R_a^2}} = \frac{t_a}{t_i} \qquad (6.21)$$

where t_a is the time a solute spends in the macropores, and t_i is the time required by a solute in the micropore sorption. Therefore, α represents the ratio of the time scales of the entire sorption taking place in the macropores and micropores. A large value of α means that macropore sorption process is rate limiting and a very small value (α <<1) indicates that micropore sorption is rate controlling. α <<1 indicates that micropore diffusion is the controlling step in the sorption of naphthalene on PRP-1.

The parameter β can be rewritten [141]:

$$\beta = \frac{3(1-\varepsilon_a)\varepsilon_i}{\varepsilon_a}\,\alpha\,\frac{(1+\frac{\rho\,K_{i,D}}{\varepsilon_i})}{(1+\frac{\rho\,K_{a,D}}{\varepsilon_a})} \qquad (6.22)$$

$K_{i,D}$, having units of L/g, is the distribution coefficient associated with the micropores. The number 3 is related to the shape of a spherical particle. Therefore, β/α gives information concerning the ratio of the micropore and macropore uptake at equilibrium. At the sorption equilibrium, their ratio is $\beta/3\alpha$ for a spherical particle. A very small value of β/α indicates a negligible micropore uptake while a large value means the macropore sorption amount is negligible.

The amount of naphthalene sorbed in the macropores is (89 ± 4)% of the total capacity. The micropore uptake is (11± 4)% of the total capacity at the concentration investigated. This explains why the Crank model describes the sorption of naphthalene on PRP-1 up to about 88% of the total sorption.

The parameter γ is related to the effective diffusion coefficient in the macropores and can be expressed as [141]:

$$\gamma = \frac{D_{a,eff}}{R_a^2} \qquad (6.23)$$

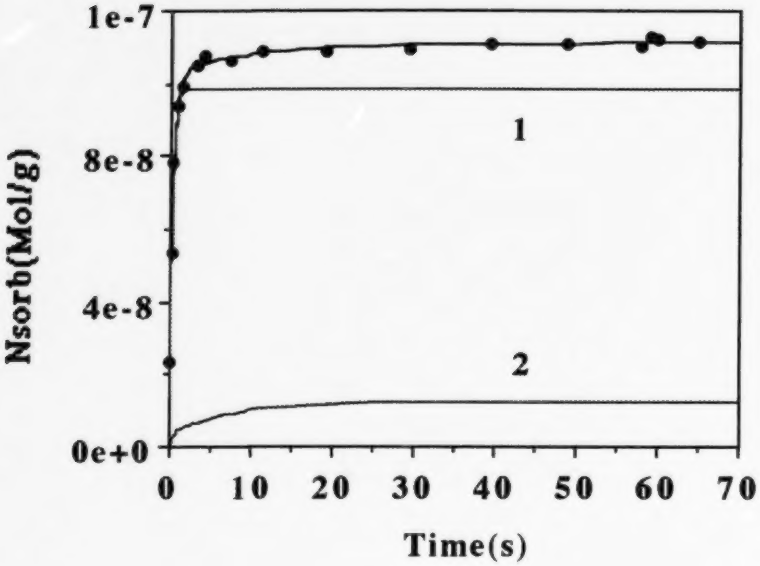

Figure 6.5 The sorption rate curve of naphthalene on PRP-1 in 85% MeOH/H_2O. The experimental data points are overlaid by a solid line representing the bidisperse pore distribution model 6.11 proposed by Ruckenstein. The experimental sorption data are for run 3 in Table 4.6. Line 1 is the macropore sorption and line 2 is the micropore sorption.

Table 6.1 The parameters from the Ruckenstein bidisperse pore distribution model for the sorption of naphthalene on PRP-1. The standard deviations were from the non-linear least squares fitting routine.

Parameter	γ (s^{-1})[a]	$\beta/3\alpha$[b]	$\alpha\gamma$ (s^{-1})[c]	Q_∞ (mol/g)	Error
Value	0.218	0.128	9.4×10^{-3}	1.11×10^{-7}	0.052
SD	0.022	0.051	7.4×10^{-3}	9.04×10^{-10}	

[a] $\gamma = \frac{D_{a,\mathrm{eff}}}{R_a^2}$

[b] $\frac{\beta}{3\alpha} = \frac{\text{Mol. in micropores at equi.}}{\text{Mol. in macropores at equi.}}$

[c] $\alpha\gamma = \frac{D_{i,\mathrm{eff}}}{R_i^2}$

6.3.3 Comparison of the Different Kinetic Models for Naphthalene on PRP-1

The sorption rate curve of naphthalene on PRP-1 in 85% MeOH/H_2O has been analyzed by the intraparticle monodisperse pore distribution model (Crank), the intraparticle bidisperse pore distribution model (Ruckenstein), and the empirical tri-exponential equation (as in chapter 4). The goodness of the model fitting to the sorption rate data was evaluated by equation 6.15. The results of the error analysis for the corresponding models are listed in Table 6.2. The empirical tri-exponential equation gives a slightly better fit than the bidisperse model which gives a better fit than the Crank model. The parameters generated by the tri-exponential equation do not have any physical reality which can describe the sorption processes for naphthalene on PRP-1. The bidisperse pore distribution model (Ruckenstein) gives a better fit than the monopore distribution model (Crank), because it has two diffusion coefficients which more accurately reflect the sorption process for naphthalene on PRP-1. Molecules diffuse in the macropores with a relative large diffusion coefficient and diffuse in the micropores with a small diffusion coefficient. The parameters from the bidisperse pore distribution model were used to calculate the diffusion coefficients of naphthalene on PRP-1. As the parameters increase, a model will become complex and is less useful. In addition, when parameters are not independent of one another, it will be more difficulty to interpret the physical meaning of those parameters.

6.3.4 Calculation of the Diffusion Coefficient (D_m) of Naphthalene in the Bulk Solution Via the Wilke-Chang Equation

The diffusion coefficient for free diffusion of a solute in solvents has been predicted by many equations. Most work has centered on empirical equations. The Wilke-Chang [136] equation 6.24 is the most widely quoted in the calculation of the diffusion coefficients in a solution.

$$D_m = 7.4 \times 10^{-8} (\Psi_b M_b)^{0.5} \frac{T}{\eta V_a^{0.6}} \qquad (6.24)$$

Ψ_b is a solvent association factor having value of 1.9 for methanol and 2.6 for water [162]. M_b is the molecular weight of the solvent. For a mixture of solvents, ($\Psi_b M_b$) is the arithmetic average values for constituent pure solvents weighted according to their volume fractions in solvent mixture. T is the temperature (K). η, the viscosity of 85% MeOH/H_2O, is 0.89 cp [162]. Va, the molar volume of naphthalene, is 111.6 cm^3/mol[163]. The calculated diffusion coefficient for naphthalene in the bulk solution is 1.12×10^{-5} cm^2/s at a temperature of 25 °C.

6.3.5 Diffusion Coefficients of Naphthalene in the Macropores and Micropores of PRP-1

The effective macropore diffusion coefficient for naphthalene on PRP-1 was calculated via equation 6.23, using R_a= 5×10^{-4} cm for the 10μm diameter spherical particles of PRP-1. The value is shown in Table 6.3. The standard deviation was

Table 6.2 Comparison of different models for the sorption rate curves of naphthalene on a shallow bed of PRP-1. The error is calculated with equation 6.15.

Model	Bidisperse pore distribution model	Tri-exponential equation	Crank model
Error	0.052	0.049	0.057
n	4	6	2

calculated from that of parameter γ. The measured macropore effective diffusion coefficient of $5.5 \times 10^{-8} \pm 5.6 \times 10^{-9}$ cm^2/s for naphthalene on PRP-1 is in the same order of magnitude as that of 2.1×10^{-8} cm^2/s [97] for phenol on XAD-4, a porous PS-DVB polymer.

The effective macropore diffusion coefficient is used to estimate the free diffusion coefficient of naphthalene, D_m, in the bulk solution, after it is corrected by the instantaneously adsorption on the pore walls and by the hindrance and the tortuosity factors using the following equation [68]:

$$D_{a,eff} = \frac{D_m \lambda'}{\theta \left(1 + \frac{K_{a,D}\,\rho}{\varepsilon_a}\right)} \tag{5.25}$$

where θ, the tortuosity factor, is usually 5, λ', the hindrance factor, is 1 for macropores. $K_{a,D}$ is the distribution coefficient of naphthalene in the macropores and is the ratio of C_s, $9.87 \times 10^{-8} \pm 4.3 \times 10^{-9}$ mol/g to C_m, 4.8986×10^{-6} mol/L, for PRP-1. $K_{a,D}$ is found to be 20.1 ± 0.9 ml/g. ρ, the particle density, was calculated to be 0.61g/ml using the weight of a particle and the volume of a particle. ε_a, the macropore porosity, was calculated to be 0.48 using the volume of the macropores and the volume of a particle. The estimated D_m from the measured effective diffusion coefficient is $(7.3 \pm 0.8) \times 10^{-6}$ cm^2/s. The D_m estimated from the Wilke-Chang equation 6.24 is 1.12×10^{-5} cm^2/s. The diffusion coefficient of naphthalene in the bulk solution is close 1.5 times as much as that in the macropores of PRP-1. Therefore, the diffusion in the macropores of PRP-1 is not hindered.

Table 6.3 The macropore and the micropore diffusion parameters for naphthalene in PRP-1. The standard deviations were calculated from error propagation based on standard deviations associated with the parameters shown in Table 6.1.

Da,eff (cm^2/s)	SD	$\frac{D_{i,eff}}{R_i^2}$ (s^{-1})	SD
5.5×10^{-8}	5.6×10^{-9}	9.4×10^{-3}	7.4×10^{-3}

The effective diffusion coefficient in the micropores can be calculated using the following equation [141]:

$$\frac{D_{i,eff}}{R_i^2} = \alpha\gamma \tag{6.26}$$

Because the diameter of a microsphere is not known. $D_{i,eff}$ can only be estimated by making an assumption of the radius of microsphere. Table 6.4 show the radii of microspheres varying from 0.01μm to 5μm which is the radius of a PRP-1 particle, and the corresponding micropore diffusion coefficients ranging from 9.4 x 10^{-15} to 2.4 x 10^{-9} cm^2/s. Weber and Sun have measured the ratio of a micropore effective surface diffusion coefficient to the square radius of the microsphere, it is 9.8 x 10^{-7} cm^2/s for phenol on activated carbon. If the a microsphere radius of 0.01μm were used, the micropore diffusion coefficient would be 9.8 x 10^{-19} cm^2/s. The corresponding macropore effective diffusion coefficient is 8.6 x 10^{-9} cm^2/s [139]. Buchholz and Kruckels have obtained a micropore surface diffusion coefficient of 2 x 10^{-15} cm^2/s for 2,4-dichlorophenol on activated carbon, and the corresponding macropore diffusivity is in the order of 3-6 x 10^{-8} cm^2/s [164]. Ruckenstein has measured the effective micropore diffusion coefficients of 10^{-12}-10^{-19} cm^2/s for various gases on an Amberlyst 21, a PS-DVB polymer [141]. It has been found that the uptake by polystyrene resins is faster than that by activated carbon [97]. The diffusion coefficient of naphthalene in the micropores of PRP-1 is much smaller than that in the macropores. Therefore, the slow sorption for naphthalene on PRP-1 must be related to the sorption in the micropores or matrix, as will be discussed from section 6.3.7 to section 6.3.9.

Table 6.4 Dependence of the effective micropore diffusion coefficient for naphthalene in 85% MeOH/H_2O in PRP-1 on the estimated radii of the microspheres.

R_i (μm)	$D_{i,eff}$ (cm^2/s)
0.01	9.4×10^{-15}
0.1	9.4×10^{-13}
1	9.4×10^{-11}
2	3.8×10^{-10}
5	2.4×10^{-9}

6.3.6 Sorption Rate Curves of Naphthalene on PRP-∞

The sorption rate curves of naphthalene on PRP-∞ were also investigated. The sorption rate curves were not used to predict a peak eluted from an analytical column, because the large diameter of PRP-∞ makes it less useful as a commercial HPLC sorbent. However, the sorption rate curves were measured to determine the diffusion coefficient in the micropores of PRP-∞, which has the same chemical composition as PRP-1, but is a non-macroporous sphere and has a larger diameter than PRP-1. It was thought that PRP-∞ might have the same micropore structures as PRP-1 due to the size of the crosslinking monomer, divinylbenzene. It was chosen to represent the matrix of PRP-1.

6.3.6.1 Testing the Shallow Bed Condition in PRP-∞

The sorption rate of naphthalene on PRP-∞ is slower than that on PRP-1. Therefore, it is easier to meet the shallow bed condition in the experiment. The same apparatus and procedures as those used for PRP-1 were used for testing the shallow bed condition. The experimental parameters are shown in Table 6.5.

In Figure 6.6, the amount of naphthalene sorbed versus the linear velocity, over the first 25 seconds is presented. The sorption rate curves do not vary significantly with the linear velocities investigated when the interstitial velocity is larger than 37.4 cm/s. The initial sorption amount at five interstitial linear velocities was compared over the first 10 seconds, during which the sorption rate curves were approximately linear. The slopes calculated from the straight lines between the origin and the points within 10 seconds as a function of the linear velocities are shown in Table 6.6. It is seen when U> 37 cm/s, a complete shallow bed condition has been achieved. In the subsequent kinetic study, the sorption rates of naphthalene onto PRP-∞ were measured at a linear velocity larger than 37 cm/s.

Table 6.5 Experimental parameters in the measurement of the shallow bed condition in PRP-∞.

Parameter	Value
PRP-∞	3.20 ± 0.02 mg
F2	0.5 ml/min
Detector wavelength	276 nm
Detector range	0.1 A.U.F.S.
Recorder chart speed	0.2 In/min
Recorder range	0.1 V.F.S.
Sample solution temperature	24.7°C ± 0.2° C
Shallow bed temperature	24.9 °C ± 0.2 °C
Integrator ATT^2	short time -4, long time -2
THRSH	short time -3, long time -1
PK WD	0.64

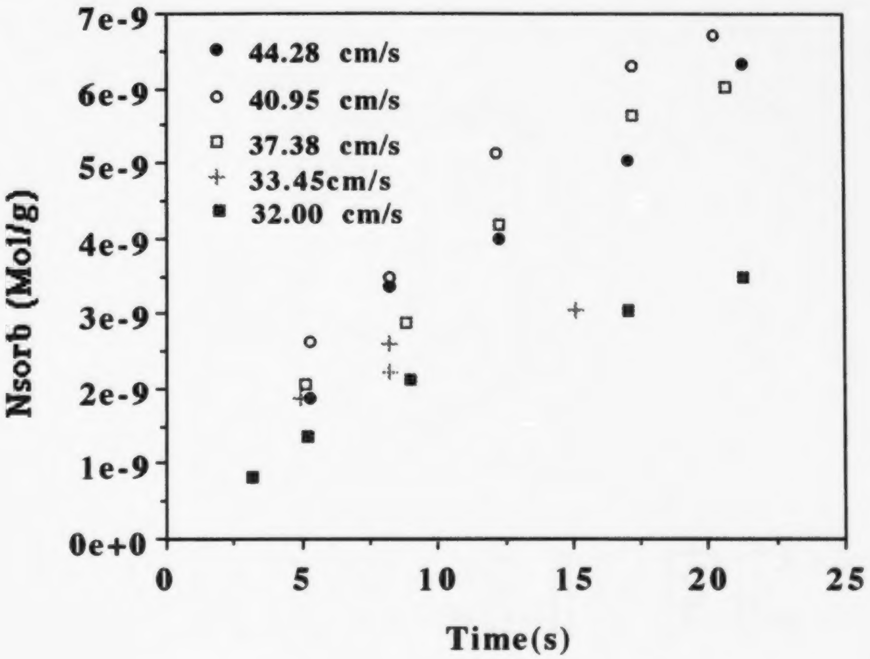

Figure 6.6 Testing the shallow bed condition in PRP-∞. Amount sorbed for naphthalene on PRP-∞ in 85%MeOH/H_2O as a function of interstitial velocity of sample solution through the shallow bed.

Table 6.6 Dependence of the initial sorption rates of naphthalene on interstitial linear velocity of a solution through the shallow bed of PRP-∞.

U (cm/s)	Initial sorption rate (mol/g/s) [a]
32.00	1.6×10^{-10}
33.45	2.4×10^{-10}
37.38	4.0×10^{-10}
40.95	4.3×10^{-10}
44.28	3.3×10^{-10}

[a] Initial sorption rate is for the time of 10 seconds

6.3.6.2 Intraparticle Monodisperse Pore Distribution Model (Crank Model) for Naphthalene on PRP-∞

Because PRP-∞ is expected to contain only micropores, the sorption rate data of naphthalene on PRP-∞ were first fit to the Crank model which describes intraparticle diffusion onto a monodisperse pore distribution sorbent. Figure 6.7 illustrates the experimental data (points) and the Crank model (solid line) for run 1. A good agreement is now found between the Crank model and the data over the whole sorption rate curve. Figure 6.8 shows that the linearized version of the Crank model equation 6.8 gives a straight line, as expected for monodisperse pore diffusion. Figures 6.9 and 6.10 present the Crank model fits to sorption curves of run 2 and run 3. The error analysis results are shown in Table 6.7. Also shown in the same table are the effective diffusion coefficients, $D_{i,eff}$, and the uptake at equilibrium, Q_∞, along with the standard deviations which were calculated from the curve fitting routine. The effective diffusion coefficients and the Q_∞ are slightly different among the runs but all are within a couple of standard deviations of one another.

6.3.6.3 The Empirical Tri-exponential Equation for Naphthalene on PRP-∞

The sorption rates of naphthalene on PRP-∞ were also fit to the empirical tri-exponential equation 4.10, although the parameters generated by the tri-exponential were not used to calculate the predicted peaks. It is of interest to see how well the tri-exponential can fit the data. Figure 6.11 shows the tri-exponential fit shown as a solid line, and the data shown as points for run 1. Figure 6.12 and 6.13 present the tri-exponential fit for run 2 and run 3. A good agreement has been obtained between the experimental data and the tri-exponential equation over the entire region of the sorption rate curves. Table 6.8 presents the constants obtained from the tri-exponential fit.

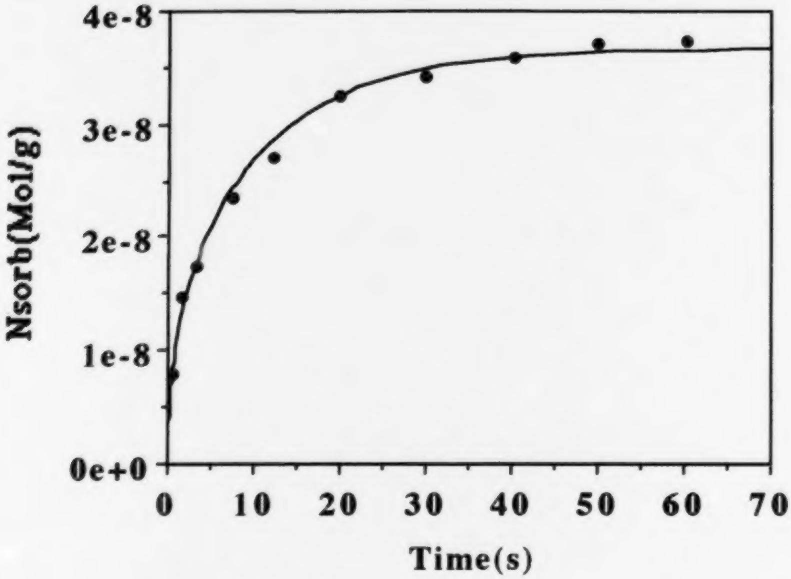

Figure 6.7 The sorption rate curve for naphthalene on PRP-∞ in 85% MeOH/H_2O. The experimental data points are overlaid by a solid line representing the Crank model 6.9. The fitting parameters are shown for run 1 in Table 6.7.

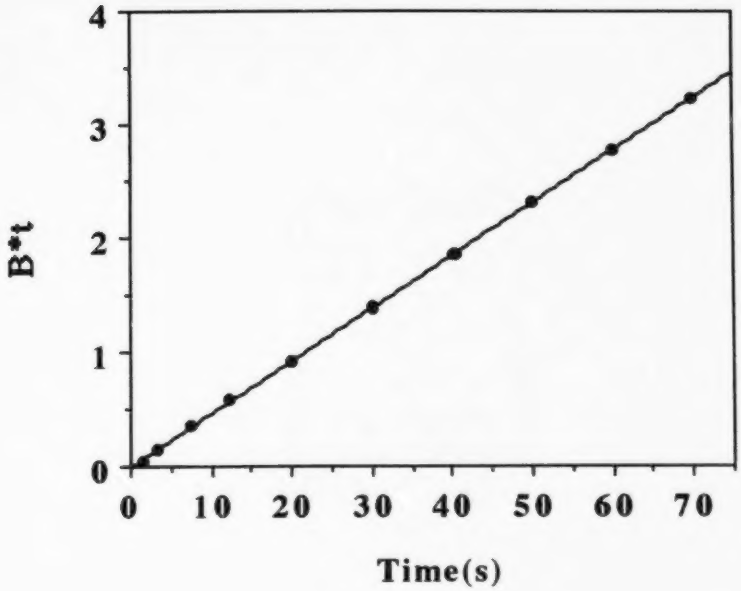

Figure 6.8 The linearized version of the Crank model for naphthalene on PRP-∞ in 85%MeOH/H_2O. The B value is calculated from equation 6.8 using the experimental sorption data of run 1 in Table 6.7.

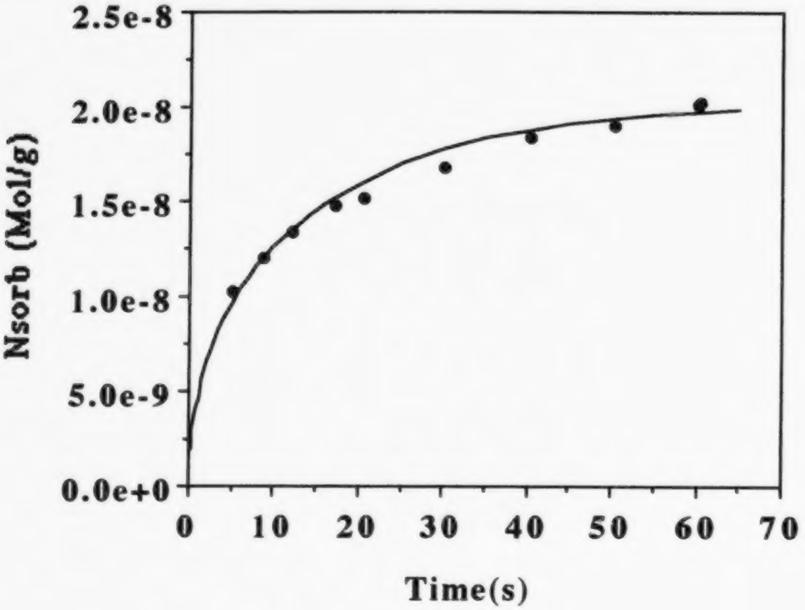

Figure 6.9 The sorption rate curve for naphthalene on PRP-∞ in 85% MeOH/H_2O. The experimental data points are overlaid by a solid line representing the Crank model 6.9. The fitting parameters are shown for run 2 in Table 6.7.

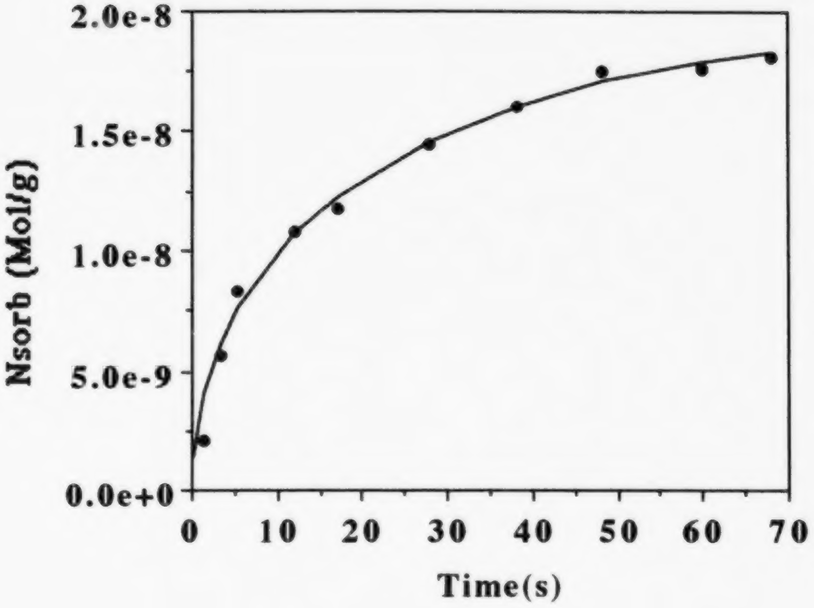

Figure 6.10 The sorption rate curve for naphthalene on PRP-∞ in 85% MeOH/H_2O. The experimental data points are overlaid by a solid line representing the Crank model 6.9. The fitting parameters are shown for run 3 in Table 6.7.

Table 6.7 The micropore effective diffusion coefficients and the sorption amount at equilibrium from Crank model for sorption rate curves of naphthalene on PRP-∞. The standard deviations were from the non-linear least squares fitting routine.

Run No	Q_∞ (mol/g)[a]	$D_{i,eff}$ (s^{-1})[b]	Error [c]
1 SD	3.77×10^{-8} 1.01×10^{-9}	8.62×10^{-9} 9.36×10^{-10}	0.002
2 SD	2.03×10^{-8} 8.13×10^{-10}	5.31×10^{-9} 8.27×10^{-10}	0.004
3 SD	1.97×10^{-8} 1.35×10^{-9}	3.17×10^{-9} 7.81×10^{-10}	0.109

[a] The amount sorbed at equilibrium.

[b] The radius of a particle of PRP-∞ is 10μm.

[c] It was calculated with equation 6.15.

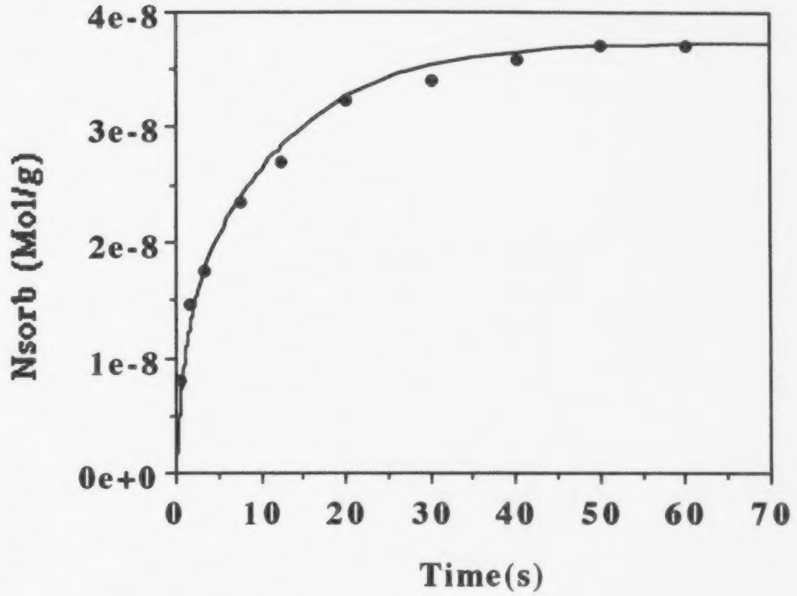

Figure 6.11 The sorption rate curve for naphthalene on PRP-∞ in 85%MeOH/H_2O. The experimental data points are overlaid by a solid line representing the tri-exponential equation. The fitting parameters are presented in Table 6.8. The experimental sorption rate data are for run 1 in Table 6.7.

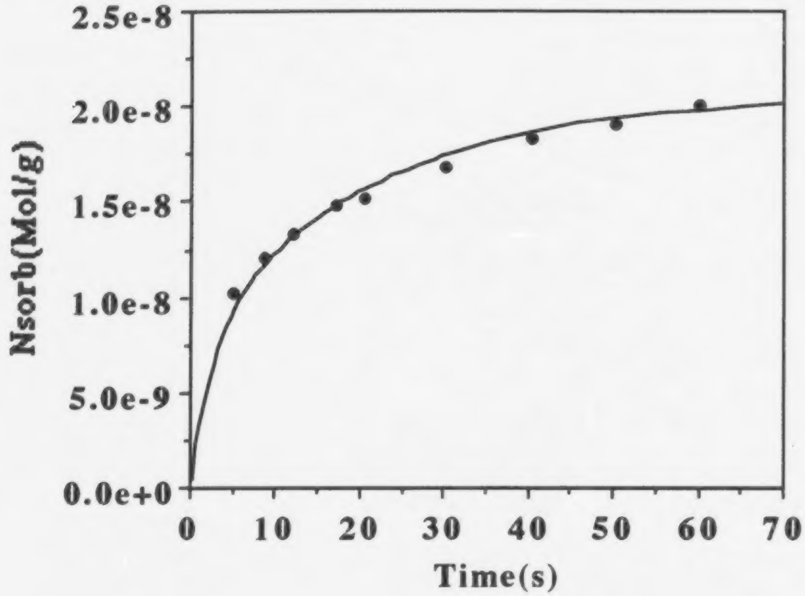

Figure 6.12 The sorption rate curve for naphthalene on PRP-∞ in 85%MeOH/H_2O. The experimental data points are overlaid by a solid line representing the tri-exponential equation. The fitting parameters are presented in Table 6.8. The experimental sorption rate data are for run 2 in Table 6.7.

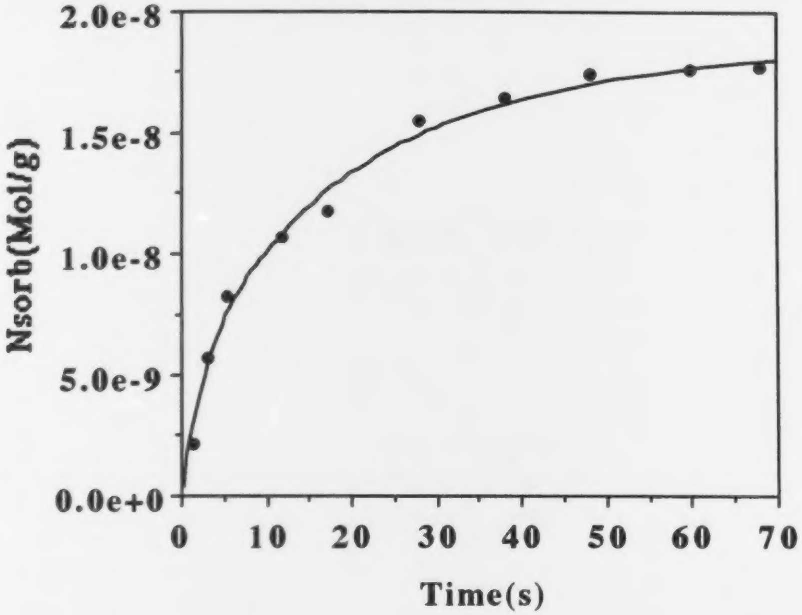

Figure 6.13 The sorption rate curve for naphthalene on PRP-∞ in 85%MeOH/H_2O. The experimental data points are overlaid by a solid line representing the tri-exponential equation. The fitting parameters are presented in Table 6.8. The experimental sorption rate data are for run 3 in Table 6.7.

Table 6.8 Constants from the tri-exponential fit for the sorption rate curves of naphthalene on a shallow bed of PRP-∞.

Run No	1	2	3
U(cm/s)	43.5	43.8	44.3
n_0 (mol/g)	3.7×10^{-8}	2.1×10^{-8}	1.8×10^{-8}
n_1 (mol/g)	1.1×10^{-8}	7.7×10^{-9}	5.3×10^{-9}
n_2 (mol/g)	2.2×10^{-8}	1.3×10^{-8}	1.3×10^{-8}
n_3 (mol/g)	3.4×10^{-9}	8.6×10^{-12}	9.1×10^{-12}
k_1 (s^{-1})	22.6	0.376	0.376
k_2 (s^{-1})	0.084	0.047	0.047
k_3 (s^{-1})	0.084	0.004	0.005
error norm	6.1×10^{-9}	1.5×10^{-9}	1.6×10^{-9}

6.3.6.4 Simplified First Order Rate Law

Use of theoretical rate laws of intraparticle diffusion to predict chromatographic elution peaks is rather complex, even in comparatively simple limiting cases such as the Crank and Ruckenstein equations. In a rigorous quantitative treatment of more complicated systems, tremendous mathematical difficulties are encountered. So, various simplified rate laws have been given. One of the simplified rate law which is often used in the quantitative treatment of chromatographic columns is based on the "linear driving force", which is the first term of the Crank equation [66, 89, 165, 166]. It assumes that the rate, at any time , is proportional to the distance the system is away from equilibrium. For particle-diffusion rate control, departure from equilibrium is given by the difference between the average internal concentration and the concentration at the surface which is at equilibrium with the solution. The linear driving force rate law is expressed in equation 6.27 [167]:

$$-\frac{dC}{dt} = \frac{15D_{eff}}{R^2}(C - \overline{C}) \tag{6.27}$$

The integrated form is :

$$F = 1 - e^{-kt} \tag{6.28}$$

$$k = \frac{15D_{eff}}{R^2} \tag{6.29}$$

Here, k is the first order rate constant , F is the fraction of moles sorbed at equilibrium, and R is the radius of a particle. C is the concentration in the solution, and $\overline{C}$ is the mean value of internal concentration in the particle. D_{eff} is the effective internal diffusion coefficient which describes the rate of transport of a solute from the outer surface of a particle into the interior.

6.3.6.5 Intraparticle Diffusion Model Based on Linear Driving Force (Mono-exponential Equation)

The linear rate model, using the "linear driving force" idea [66, 89, 167, 168] is expressed as a monoexponential in equation 6.28. Figure 6.14 presents the fit (solid line) of the sorption rate data (points) for naphthalene on PRP-∞ for run 1 to the monoexponential equation 6.28. The rate constant, k, from the non-linear least squares curve fit, is found to be (0.246 ± 0.045) s^{-1}. Substituting 0.246 (s^{-1}) for k and 10μm for R in PRP-∞ into equation 6.29, the $D_{i,eff}$, based on the "linear driving force" idea, is 1.64 x 10^{-8} cm^2/s. The measured average value of $D_{i,eff}$ from the Crank model is (5.7 ± 2.7) x 10^{-9} cm^2/s. Although the values of $D_{i,eff}$ from the two models are not very different from each other, the "linear driving force" model gives a very poor description of the overall observed sorption rate data of naphthalene on PRP-∞ as seen in Figure 6.14. The monoexponential equation underestimates the sorption rate up to 44% of sorption and overestimates the sorption rate from 44% to 97% of sorption.

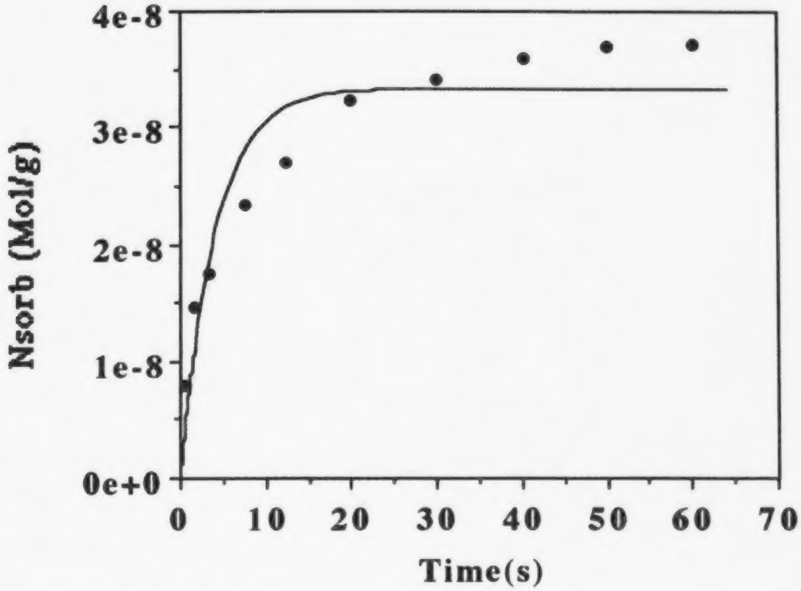

Figure 6.14. The sorption rate curve for naphthalene on PRP-∞ in 85 % MeOH/H_2O. The experimental data points are overlaid by a solid line representing the monoexponential equation 6.28.

6.3.6.6 Comparison of the Different Kinetic Models for Naphthalene on PRP-∞.

The error analysis was carried out for the Crank model and the empirical tri-exponential equation using equation 6.15. Table 6.9 shows the error analysis results for different models. The smaller the error, the better the model fits the experimental data. The tri-exponential equation gives better fit for run 1 and run 3. However, for run 2, the Crank model gives a smaller error, this is probably due to the scatter of the experiment data. The "linear driving force" model gives a rather poor fit to the sorption rate data as just by visual inspection from Figure 6.14, therefore, the error was not calculated

6.3.6.7 Diffusion Coefficient of Naphthalene in the Micropores of PRP-∞

The diffusion coefficients were obtained by fitting the experimental data to the Crank model with a non-linear least squares regression. As shown in Figure 6.11, 6.12 and 6.13, the sorption data were successfully described by the Crank model. The values of the effective diffusion coefficients of naphthalene in the micropores of PRP-∞ along with the standard deviations have been shown in the previous Table 6.7. The diffusion coefficient of naphthalene in the micropores of PRP-∞ is significantly smaller than the diffusion coefficient of naphthalene in the bulk solution. The significant decrease in the diffusion coefficient can be explained by the hindered diffusion of naphthalene in the micropores of PRP-∞, as discussed in the next section.

Table 6.9 Comparison of different models for sorption rate curves of naphthalene on a shallow bed of PRP-∞. The error is calculated with equation 6.15.

Run No	Crank	Tri-exponential
1	0.002	0.0006
2	0.004	0.008
3	0.109	0.036

6.3.7 Hydrodynamic Model for Hindered Diffusion of Naphthalene in the Micropores of PRP-∞

The reduction of the diffusion coefficient of a solute within a pore of a comparable size is generally due to two effects as discussed in 6.2.5.1. Under the basic assumptions described in section 6.2.5.2, D_i/D_m is given by equation 6.30 which is the combination of equations 6.16 and 6.18.

$$D_i = D_m \frac{(1-\lambda)^2}{K} = D_m \lambda_i' \tag{6.30}$$

This equation is used only with $\lambda < 0.9$ [155]. λ_i' is the hindrance factor, D_m is the diffusion coefficient from Wilke-Chang equation 6.24. D_i is the hindered diffusion coefficient in the micropores of PRP-∞, which can be calculated from the experimentally measured $D_{i,eff}$ after it is corrected by the tortuosity factor and the instantaneous adsorption on the surface of the stationary phase [137]. An equation similar to equation 6.25 is expressed in equation 6.31:

$$D_{i,eff} = \frac{D_m \lambda_i'}{\theta\left(1 + \frac{K_{i,D}\,\rho}{\varepsilon_a}\right)} \tag{6.31}$$

and

$$\lambda_i' = \frac{(1-\lambda)^2}{K} \tag{6.32}$$

$$K_{i,D} = \frac{Q_{i,\infty}}{C_m} \tag{6.33}$$

where $K_{i,D}$, the distribution coefficient in the micropores, can be determined from the amount of naphthalene sorbed at equilibrium ($Q_{i,\infty}$) and the concentration in the mobile phase (C_m). It was measured to be 6.3 ± 0.1 ml/g (section 3.5.4). ρ, the particle density of PRP-∞, is 1.2g/cm^3 for poly(styrene-divinylbenzene)[50]. ε_i, the micropore porosity of PRP-∞, is calculated as the product of the specific pore volume of " solid" poly(styrene-divinylbenzene)(0.3 ml/g) [49] times ρ. ε_i is estimated to be 0.38. θ, the tortuosity factor, is 5 [168]. K and λ were defined before. $D_{i,eff}$ is calculated from the Crank model. Substituting all the parameters into equation 6.31, the average value of D_i, i.e. $D_m\lambda_i'$, for naphthalene on PRP-∞ is (6.0± 2.6) x 10^{-7}cm^2/s.

Substituting D_m into equation 6.30, λ_i' can be calculated. Therefore, λ, the ratio of a solute radius to the micropore radius, can be calculated from equation 6.32. K depends on λ and can be found from a table given by Paine and Scherr [155]. The accurate value of λ can be found by trial and error to minimize the difference between the observed D_i and the D_i calculated from equation 6.30 using different values of K and λ. λ does not vary continuously but in unit of 0.02 in the table given by Paine and Scherr [155]. Table 6.10 presents a set of λ, K and the corresponding D_i along with the observed D_i. The van der Waals radius of naphthalene is 3.08 Å [163]. Therefore, the radius of a micropore in PRP-∞ is estimated to be (6.4 ± 0.9)Å.

Table 6.10 Dependence of hindrance diffusion coefficients, D_i, on the values of λ and K.

λ^a	K	D_i (cm^2/s)^b	D_i (cm^2/s)^c
0.42	3.864578	9.55×10^{-7}	
0.44	4.34741	8.08×10^{-7}	
0.46	4.8088	6.79×10^{-7}	
0.48	5.34141	5.67 x 10-7	$(6.0 \pm 2.6) \times 10^{-7}$
0.50	5.95938	4.70×10^{-7}	
0.54	7.52686	3.15×10^{-7}	

a $\lambda = \frac{r_s}{r_o}$

b From equation 6.30.

c From equation 6.31 using the average experimentally measured $D_{i,eff}$ from Crank model (Table 6.7).

6.3.8 Comparison of the Diffusion Coefficients in the Micropores of PRP-1 and PRP-∞

PRP-∞ was chosen because it was initially considered to be the matrix of PRP-1. The rate constants, $D_{i,eff}/R_i^2$, in the micropores for naphthalene sorption on PRP-1 and PRP-∞ are very close. These are given in Table 6.11. The plots of the micropore sorption rate curve for PRP-1 and of the sorption rate curve for PRP-∞ are shown in Figure 6.15. The slow sorption rate in the matrix of PRP-1 and PRP-∞ are quite similar as seen from the fact that the sorption rate curves are almost parallel in Figure 6.15.

The ratio of the effective micropore diffusion coefficient to the square radius of a microsphere, i.e. $D_{i,eff}/R_i^2$, in PRP-1 was obtained from the Ruckenstein model. However, the radius of a microsphere in PRP-1 is not known. The microsphere radius must be in the range from 0.01μm to 5 μm because the macropores have a radius of about 35 Å and the particle has a radius of 5μm. Therefore, a set of $D_{i,eff}$ is obtained from a set of estimated R_i, and so is a set of D_i. After D_i is known, λ can be estimated, therefore, the radius of a micropore in PRP-1 can be estimated. Equation 6.30 is used for $\lambda < 0.9$. However, when $\lambda > 0.9$, the following equation must be used [169]:

$$D_i = D_m \, 0.984 \, (1-\lambda)^{9/2} \tag{6.34}$$

The effective micropore diffusion coefficients, $D_{i,eff}$, in PRP-1 can also be corrected by the instantaneous sorption in the same way as that in PRP-∞ using equation 6.31. The parameters used in the correction are shown in Table 6.11 for both PRP-1 and PRP-∞. Shown in Table 6.12 are a set of $D_{i,eff}$ and hindered diffusion coefficients, D_i, based on a set of R_i. For a given D_i, λ can be estimated in the same way as that for PRP-∞ using either equation 6.30 or equation 6.34. A set of λ and the corresponding microsphere radii of PRP-1 are also shown in Table 6.12. The radius of a naphthalene molecule is 3.08 Å [163].

From Table 6.12, it is seen that the hinderance diffusion coefficient, D_i, significantly depends on the value of λ, the ratio of the solute radius to the micropore radius. D_i varies from 10^{-13} cm^2/s to 10^{-7}cm^2/s for a change in λ from 0.977 to 0.64, and a change in the radius of micropore from 3.15 to 4.81 Å. Also shown, in the last row in Table 6.12, is the hinderance diffusion coefficient of naphthalene in the micropores of PRP-∞ and the corresponding average radius of micropores. If the microsphere radius of PRP-1 is 1μm which is one fifth of the radius of PRP-1 particles, the corresponding D_i is 4.5×10^{-9} cm^2/s which is much smaller than D_i in the micropores of PRP-∞ (6.0×10^{-7} cm^2/s). This large difference in D_i between PRP-1 and PRP-∞ corresponds to a difference in micropore radius between the two sorbents of only 2.6 Å.

The above analysis clearly shows that a small difference in the micropore size can cause a large difference in the hinderance diffusion coefficient, D_i, for the two PS-DVB packings.

Table 6.11 The parameters used in the estimation of micropore diffusion coefficients from the effective micropore diffusion coefficients for naphthalene on PRP-1 and PRP-∞.

Parameter	PRP-1	PRP-∞
$\frac{D_{i,\,eff}}{R_i^2}$ (s^{-1})	$(9.4 \pm 7.4) \times 10^{-3}$ [a]	$(5.7 \pm 2.7) \times 10^{-3}$ [b]
$C_{i,s}$ (mol/g)	$(1.2 \pm 0.4) \times 10^{-8}$	$(3.2 \pm 0.1) \times 10^{-8}$
$C_{i,m}$ (mol/L)	4.899×10^{-6}	5.023×10^{-6}
ρ (g/ml)	0.61	1.2
$K_{i,D}$ (ml/g)	2.5 ± 0.9	6.3 ± 0.1
ε_i	0.18	0.38

a From the Ruckenstien model.

b Average value from Table 6.7. The radius of PRP-∞ is 10μm.

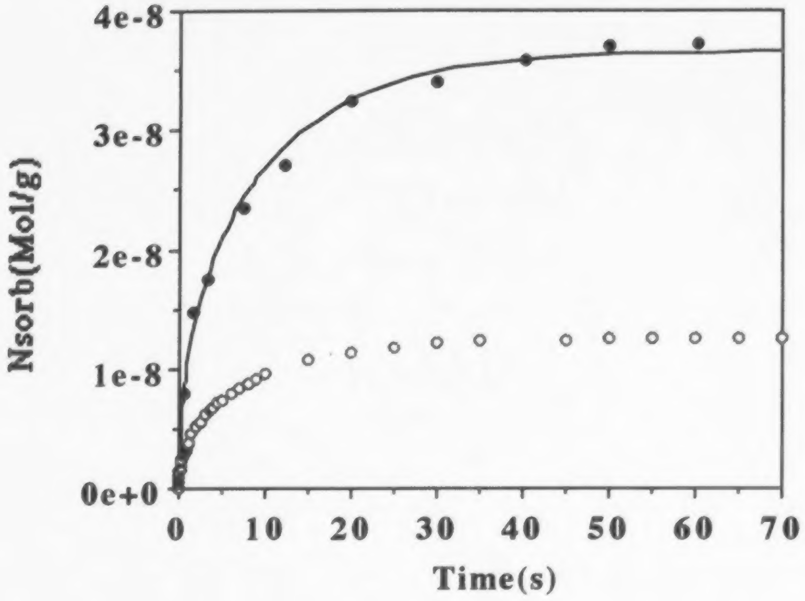

Figure 6.15 The sorption rates of naphthalene in 85% MeOH/H_2O on PRP-∞ (•) and in the micropores of PRP-1 (o). The sorption data points are overlaid by Crank model.

Table 6.12 The dependence of the micropore diffusion coefficients and the micropore sizes on the microsphere radius in PRP-1 along with the observed micropore diffusion coefficient and the radius of micropores in PRP-∞.

R_i (μm)	$D_{i,eff}$ (cm^2/s)[a]	D_i (cm^2/s)[b]	D_i/D_m [c]	λ	r_p (Å)[f]
0.01	9.4×10^{-15}	4.5×10^{-13}	4×10^{-8}	0.977[d]	3.15
0.1	9.4×10^{-13}	4.5×10^{-11}	4×10^{-6}	0.973[d]	3.29
1	9.4×10^{-11}	4.5×10^{-9}	4×10^{-4}	0.80[e]	3.85
2	3.8×10^{-10}	1.8×10^{-8}	1.6×10^{-3}	0.74[e]	4.16
5	2.4×10^{-9}	1.1×10^{-7}	9.8×10^{-3}	0.64[e]	4.81
10[g]	5.7×10^{-9}	6.0×10^{-7}	5.36×10^{-2}	0.48[g]	6.4

a Also presented in the second column in Table 6.4.

b From equation 6.31.

c From equation 6.30 where D_m is 1.12 x 10-5 cm^2/s from Wilke-Chang equation 6.24.

d From equation 6.33, when $\lambda > 0.9$.

e From equation 6.30 by trial and error, when $\lambda < 0.9$.

f $r_s = 3.08$ Å for radius of naphthalene molecules.

g Values for PRP-∞. The radius of PRP-∞ is 10μm.

6.3.9 Comparison of the Sorption Isotherms of Naphthalene on PRP-1 and PRP-∞

The sorption isotherms of naphthalene on PRP-1 and PRP-∞ in 85% MeOH/H_2O are shown in Figure 6.16. The solid lines are the interpolations of the experimental data. The linear range of the isotherm is 0-4 x 10^{-5} M for PRP-1. Undoubtedly, the isotherm of naphthalene on PRP-∞ will approach a plateau at high concentrations. However, only the linear range of the isotherm was measured in this study.

The large amount of naphthalene sorbed on PRP-∞ indicates that naphthalene molecules have been sorbed into the micropores. From the ratio of the slopes of the two isotherms (section 3.5.5 and 3.5.4), the total amount of naphthalene sorbed in both macropores and micropores on PRP-1 is 6 times that on PRP-∞ at the concentrations investigated However, from the bidisperse pore diffusion model, only 11% of the total amount of naphthalene sorbed is in the micropores of PRP-1. Therefore, the amount sorbed in the micropores of PRP-1 is about 0.7 times that on PRP-∞. This suggests that naphthalene is also sorbed into the polymer matrix of PRP-1.

Considering the large difference in the specific surface areas between PRP-1 (415m^2/g) and PRP-∞ (0.29 m^2/g) and the closeness of the amount sorbed, the surface area is not a useful parameter for characterizing sorption on PRP-1 and PRP-∞ with respect to naphthalene.

A solute which has a similar solubility parameter, δ, to a sorbent is sometimes defined as a solvent. The solubility parameter for naphthalene is 20.2 (J $cm^{-3})^{1/2}$ [170] which is very close to the solubility parameter for poly(styrene-divinylbenzene) of 18.6 (J $cm^{-3})^{1/2}$ [171]. Therefore, it is possible for naphthalene, a solvent and having a similar chemical structure to polystyrene, to penetrate deeply into the polymers. The similar phenomenon has been found for trichloroethylene, a solvent, on a nonmacroporous polystyrene [101]. Also, it has been found that the chromatographic retention volumes of solutes on poly(styrene-divinylbenzene) polymers are nearly the same, although their specific surface areas differ greatly [48].

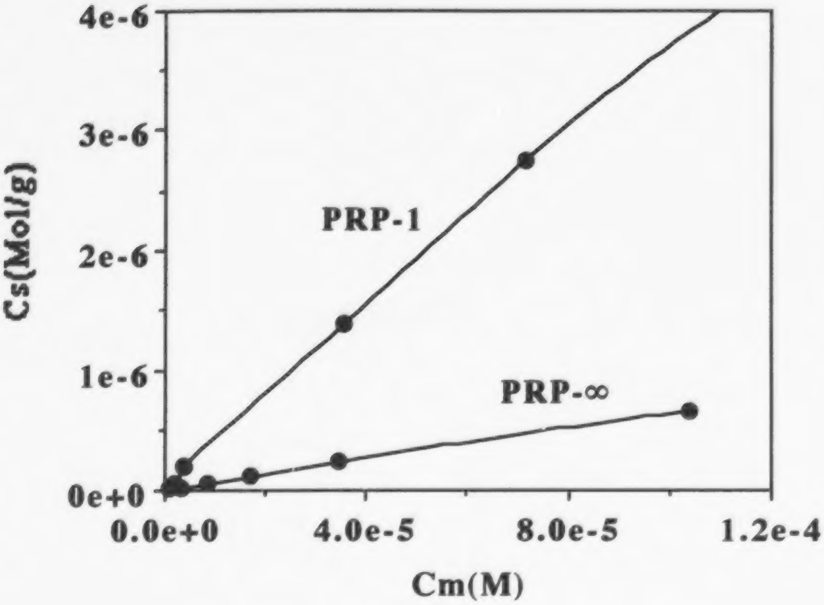

Figure 6.16 The sorption isotherms of naphthalene in 85% MeOH/H_2O on PRP-1 and PRP-∞. The solid lines are interpolations.

Chapter 7

Conclusions and Future Work

7.1 Conclusions

The work presented in this thesis concentrated on four areas:

1. The development and improvement of the shallow bed apparatus used in the measurement of the sorption rates of naphthalene on poly(styrene-divinylbenzene) copolymers of PRP-1, a HPLC packing, and PRP-∞. 2. The use of a 12 bit Lab-NB analog to digital converter placed in a Macintosh computer in the collection of the elution profiles of phloroglucinol on a column of PRP-1. 3. The use of a theoretical model which is based on statistic theory and mathematical convolution to predict elution profiles from sorption rates measured in the shallow bed experiment. 4. The origin of the slow step in the sorption rates of naphthalene on PRP-1, and consequently, the cause of the severe bandbroadening and tailing present in the elution profiles, is investigated.

In area 1, a number of changes were made to the shallow bed design used by Litwinson [54] including a lever system and the Kel-F insert in the slider. The most important is the introduction of a rotary valve which reduces the minimum exposure time from the previous 0.4 to 0.04 seconds in the measurement of the sorption rates of naphthalene on PRP-1. Therefore, the initial sorption rates are measured more accurately. The effects of the systematic errors on the steeply rising portion of the sorption rate curve are greatly reduced. Also, non-uniformity of the packing in the bed is reduced by introducing a slider valve which shunts off the eluent flowing through the bed when the slider is moved from the loading to the elution position and the reverse. So that all the particles in the bed are exposed to the eluent and sample solution at the same time. In area 2, the digital data collection system consisting of a 12 bit analog to digital converter and a

Macintosh computer are used in the collection of the elution profiles of phloroglucinol. No requirement needed to transfer of the data between IBM clone to a Macintosh as it was performed previously. The translation of data was tedious and prone to errors. Data translation was required because data collected in Macintosh can be used directly to easily calculate the statistical moments using programs written for a Macintosh. Unfortunately, the present data collection system can not be used to acquire the elution profiles of naphthalene at a low concentration of 10^{-5} M on a PRP-1 column. A low concentration of naphthalene, a highly retained compound on PRP-1, gives a very low signal. The signals are greatly distorted after they are smoothed by the software programs written in the data collection system. Therefore, a signal conditioning hardware, an amplifier, should be used to improve the accuracy in the collection of the digital data of naphthalene at a low concentration on a column of PRP-1 in further work.

In the third area, a theoretical model was evaluated which uses the results of the sorption rate curves from the shallow bed experiments to predict elution peak shapes. Comparison of the predicted and the observed elution profiles in term of chromatographic figures of merit and by visual inspection shows the model successfully predicts the elution profiles, particularly, the tailing parts of the observed peaks are well matched by the predicted peaks. The third term in the tri-exponential fit, which is mainly associated with the slow sorption at long time approaching equilibrium for naphthalene on PRP-1, defines the tail of the predicted peaks. Therefore , the tailing is from the slow intraparticle sorption of naphthalene on PRP-1.

In the fourth area, the origin of the slow sorption for naphthalene on PRP-1, and consequently, the origin of the bandbroadening and tailing, is investigated. The experimentally measured sorption rate curve of naphthalene on PRP-1 clearly suggests two distinct stages of kinetic behavior, a fast initial sorption followed by a slow sorption approaching to equilibrium. Therefore, PRP-1 is perceived to have a bidisperse pore distribution structure consisting of macropores which are large compared to the size of the solute, and which provide unhindered access to the solute, and of micropores which are comparable in size to that of the solute so that solute diffusion in that pore is severely hindered. The sorption rate curve of naphthalene on PRP-1 is fit well by a bidisperse model, the Ruckenstein model with two diffusion coefficients. The diffusion coefficients in the macropores and micropores are calculated from this model. The measured diffusion coefficient of naphthalene in the stagnant mobile phase present in the macropores is very close to that in the bulk solution. This indicates that diffusion in the macropores of PRP-1 is not hindered. The rate constant associated with the diffusion in the micropores is measured, the micropore diffusion coefficient can be calculated when the radius of a microsphere in PRP-1 is known. Because the radius of a microsphere is not known, the micropore diffusion coefficient is estimated using a set of estimated radii of the microspheres. A hydrodynamic model for hindered diffusion is used to estimate the size of a micropore in PRP-1 by using the micropore diffusion coefficient. The micropore radius is 3.85 Å if the radius of a microsphere of PRP-1 is assumed to be 1μm, and the corresponding micropore diffusion coefficient, D_i, is 4.5×10^{-9} cm^2/s.

The sorption rate of naphthalene on PRP-∞, a nominally non-porous PS-DVB, is also studied using the shallow bed apparatus. The sorption rate curve is fit well by a monodisperse pore diffusion model, the Crank model with a single diffusion coefficient. The micropore diffusion coefficient of naphthalene in PRP-∞ is calculated from the Crank model. The magnitude of the micropore diffusion coefficient for naphthalene on PRP-∞ indicates there is also a slow diffusion into the micropores. The average radius of the micropores in PRP-∞ is estimated to be 6.4 Å using the hydrodynamic model from the measured micropore diffusion coefficient.

The sizes of the micropores in PRP-1 and PRP-∞ are not very different, (the micropores in PRP-∞ is only about 1.5 times those in PRP-1). Therefore, the two PS-DVB packings have very similar matrix structures. Although the micropore sizes are similar for the two PS-DVB packings, the micropore diffusion coefficient in PRP-1 is over

200 times smaller than that in PRP-∞ if the radius of a microsphere in PRP-1 is assumed to be 1μm which is one fifth of a PRP-1 particle radius. This suggests that the diffusion in the micropores in PRP-1 is more hindered than diffusion in the micropores in PRP-∞. The assumption of a smaller radius than 1μm for the microsphere in PRP-1 will give a smaller micropore diffusion coefficient so that a larger difference in the micropore diffusion coefficients between PRP-1 and PRP-∞ will exist.

7.2 Future Work

The shallow bed apparatus developed in this work can be used to measure sorption rate curves for other compounds on other packings. For monodisperse pore diffusion, the Crank model can be used to calculate the diffusion coefficient, and for bidisperse pore diffusion, the Ruckenstein model can be used. The hydrodynamic model for hindered diffusion can be further evaluated in calculating the pore size of other packing using the measured diffusion coefficients of other compounds by the shallow bed apparatus.

The high sorption capacity of naphthalene on PRP-∞ suggests naphthalene molecules penetrate into the matrix of PRP-∞. A compound, which will not be sorbed into the matrix, could be tested further to prove the micropore diffusion. Also, the study of the swelling properties of PRP-∞ using a solvent which can wet PS-DVB would be useful to understand the high sorption capacity of PRP-∞. Both experiments are under way in this laboratory.

1. Melander, W. R. and Horvath, Cs. *In High -Performance Liquid Chromatography Advances and Perspectives*, Ed. by Horvath, Cs., Volume 2, Academic Press Inc., London, **1980**, Chapter 1.
2. Krstulovic, A. M. and Brown, P. R. *In Reversed-phase High Performance Liquid Chromatography : Theory, Practice and Biomedical Applications*, Wiley, Tronto, **1982**, Chapter 4.
3. Snyder, L. R. and Kirkland, J. J. *Introduction to Modern Liquid Chromatography*, Wiley, Toronto, **1979**, Chapter 7.
4. Grieser, M. D. and Pietrzyk, D. J. *Anal. Chem.*,**1973**, 44, 1348.
5. Kohler, J.; Chase, D. B.; Farlee, R. D.; Vega, A. J. and Kirkland, J. J. *J. Chromatogr.*, **1986**, 352, 275.
6. Sokolowski, A. and Wahlund, K. G. *J. Chromatogr.*, **1980**, 189, 299.
7. Sadek, P. C. and Carr, P. W. *J. Chromatogr. Sci.*, **1983**, 21, 314.
8. Grobe-Rhode, C.; Kicinski, H. G. and Kettrup, A. *J. Chromatogra.*, **1988**, 26, 209.
9. Nice, E. C.; Capp, M. W.; Cooke, N. and O'Hare, M. J. *J. Chromatogr.*, **1981**, 218, 569.
10. Cole, L. A. and Dorsey, J. G. *Anal. Chem.*,**1990**, 62, 16.
11. Rigney, M. P.; Weber, T. P. and Carr, P. W. *J. Chromatogr.*, **1989**, 484, 273.
12. Bien-Vogelsang, B.; Deege, A.; Figge, H., Kohler, J. and Schombourg, G. *J. Chromatogr.*, **1984**, 19, 170.
13. Benson, J. R. and Woo, D. J. *J. Chromatogr. Sci.*, **1984**, 22, 386.
14. Moor, J. *J. Polymer Sci.*, **1964**, Part A2, 835.
15. Lloyd, L. L. *J. Chromatogr.*, **1991**, 544, 201.
16. Lee, D. P. and Kindsvater, J. H. *Anal. Chem.*, **1980,** 52, 2425.
17. Dawkins, J. V.; Lloyd, L. L. and Warner, F. P. *J. Chromatogr.*, **1986**, 352,

157.

18. Smith, R. M. *J. Chromatogr.*, **1984**, 291, 372.

19. Popl, M.; Dolansky, V. and Fahnrich, J. *J. Chromatogr.*, **1978**, 148, 195.

20. Smejkal, F.; Popl, M.; Cihova, A. and Zazvorakova, M. *J. Chromatogr.*, **1980**, 197, 147.

21. Tanaka, N.; Ebata, T. Hashizume; K. Hosoya, K. and Araki, M. *J. Chromatogr.*, **1989**,475, 195.

22. Chu, C. H. and Pietrzyk, D. J. *Anal. Chem.*, **1981**, 49, 757.

23. Robinson, J. L.; Robinson, W. J.; Marshall, M. J.; Barnes, A. D.; Johnson, K. J. and Salas, D. S. *J. Chromatogr.*, **1980**, 189, 145.

24. Mori, S. *Anal. Chem.*, **1977**, 50, 745.

25. Smith, R. M. and Garside, D. R. *J. Chromatogr.*, **1987**, 407, 19.

26. Lee, D. P. *J. Chromatogr.*, **1988**, 443, 143.

27. Yang, Y. B. and Verzele, M. *J. Chromatogr.*, **1987**, 387, 197.

28. Rolls, W. A. and Jagodzinski, J. J. *J. Chromatogr.*, **1992**, 59, 89.

29. Sun, J. J. and Fritz, J. S. *J. Chromatogr.*, **1990**, 522, 95.

30 Tweeten, K. A. and Tweeten, T. N. *J. Chromatogr.*, **1986**, 359, 111.

31. Moats, W. A. *J. Chromatogr.*, **1986**, 366, 69.

32. Kibwage, I. O. and Roets, E. *J. Chromatogr.*, **1985**, 333, 275.

33 Paeson, J.; Roets, E. and Hoogmartens, J.*Chromatogra.*, **1991**, 32, 162.

34. Hoogmartens, J and De Beer, J. O. *J. Pharm. Biomed. Anal.*, **1993**, 11, 1293.

35. Stewart, J. T. and Hoogmartens, J. *J. Pharm. Biomed. Anal.*, **1993**, 11, 970.

36. Hoogmartens, J. *J. Pharm. Biomed. Anal.*, **1992**, 10, 845.

37. Roets, E. and Hoogmartens, J. *J. Chromatogr*, **1993**, 628, 49.

38. Gawdzok, B. *J. Chromatogr.*, **1992**, 600, 115.

39. Yuan, D. and Pietrzyk, D. J. *J. Chromatogr.*, **1990**, 509, 357.

40. Betti, A.; Lodi, G.; and Coppi, S. *J. Chromatogr.*, **1990**, 513, 219.

41. Hosoya, K.; Kimata, K.; Tanaka, N.; Araki, T.; Terashima, M.; and Frechet, M. J. *J. Liq. Chromatogr.*, **1993**, 16, 3059.

42. Jucger, D. A. *J. Org. Chem.*, **1988**, 53, 3985.

43. Weiner, M. P.; Thannhauser, T. W.; Laity, J. H.; Bennig, M. E.; Lee, D. P. and Scheraga, H. A. *Nucleic Acids Res.*, **1988**, 16, 8185.

44 Reh, E. and Kapfer, U. *Chromatographia*, **1990**, 30, 663.

45. Huber, C. G.; Oefner, P. J. and Bonn, G. K. *Anal. Biochem.*, **1993**, 212, 351.

46. Huber, C. G.; Oefner, P. J. and Bonn, G. K. *Chromatogra.*, **1993**, 37, 653.

47. Bowers, L. D. and Pedigo, S. *J. Chromatogr.*, **1986**, 371, 243.

48. Deng, L. R.; Hu, X.; Wu, Q.; Meng, Q.; Li, Y. and Zhang, Y. *Scientia Sinica series B.*, **1982**, 9, 905.

49. Nevejans, F. and Verzele, M. *J. Chromatogr.*, **1987**, 406, 325.

50. Jacobelli, H.; Bartholin, M. and Guyot. A. *J. Appl. Polymer Sci.*, **1979**, 23, 927.

51. Nevejans, F. and Verzele, M. *Chromatogrpahia* , **1985**, 20, 173.

52. Jerabek, K. *Anal. Chem.*, **1985**, 57, 1598.

53. Dawkins, J. V.; LLoyd, L. L. and Warner, F. P. *J. Chromatogr.*, **1986**, 352, 157.

54. Litwinson, L. L. M. Sc. Thesis, University of Alberta, Edmonton, Canada, **1991**.

55. May, S.; Hux, R. and Cantwell, F. F. *Anal. Chem.*, **1982**, 54, 1279.

56. King, G. B. and Horlick, G. *Spectrochimica Acta*, **1992**, 47B, E353.

57. Miller, J. M. *Separation Methods in Chemical Analysis*, Wiley, Toronto, **1975**, Chapter, 5.

58. Snyder, L. R. *Principles of Adsorption Chromatography*, Marcel Dekker, New York, **1968**, Chapter, 3.

59. Karger, B. L.; Snyder, L. R. and Horvath, Cs. *An Introduction to Separation Science*, Wiley, Toronto, **1973**, Chapter 2, 5.

60. Conder, J. and Young, C. L. *Physicochemical Measurement by Gas Chromatography*, Wiley, Toronto, **1979,** Chapter 2,9.

61. Ruthven, D. M. *Principles of Adsorption and Adsorption Processes, Wiley, Toronto*, **1984**, Chapter 4.

62. Huber, J. F. K. and Gerritse, R. G. *J. Chromatogr.*, **1971**, 58, 137.

63. Jacobson, J. A.; Frenz, J. and Horvath, Cs. *J. Chromatogr.*, **1984**, 316, 53.

64. Jonsson, J. A. and Lovkvist, P. *J. Chromatogr.*, **1987**, 408, 1.

65. Roles, J.; Guiochon, G. *J. Chromatogr.*, **1992**, 591, 233.

66. Helfferich, F, *Ion Exchange*, McGraw-Hill, New York, **1962**, Chpater 6, 9.

67. Horvath, Cs and Lin, H. J. *J. Chromatogr.*, **1976**, 126, 401.

68. Frey, D. D.; Schweinheim, E. and Horvath, Cs. *Biotechnol, Prog.*, **1993**, 9, 273.

69. Giddings, J. *Dynamics of Chromatography*, Dekker, New York, **1965**, Chapter 2, 6.

70. Peel, R. G. and Benedek, A. *J. Environ. Eng. Div. Amer. Civil Eng.*, **1980**, 106, 797.

71. Boyd, G. E.; Adamson, A. W. and Myers, Jr. L.S. *J. Amer. Chem. Soc.*, **1947**, 69, 2836.

72. Ruthven, D. M. *Principles of Adsorption and Adsorption Processes*, Wiley, Toronto, **1984**, Chapter 5.

73 Lenhoff, A. M. *J. Chromatogr.*, **1987**, 384, 285.

74 Famularo, J., Mueller, J. A. and Pannu, A. S. *J. Water Pollut. Control Fed.*, **1980**, 52, 2019.

75 Weber, T. W. and Chakravorti, R. K. *AIChE.* J., **1974**, 20, 228.

76. Vassiliou, B. and Dranoff, J.S. *AIChE J.*, **1962**, 8, 248.

77. Riveros, P. A. and Cooper, W. C. *Solvent Extraction and Ion Exchange*, **1988**, 6, 479.

78. Levine, I. *Physical Chemistry*, McGraw-Hill, Toronto, **1983**, Chapter, 17.

79. MATlab^{TM}, The Mathwoeks Inc. Natick, MA.

80. Gowanlock, D.; Bailey, R. and Cantwell, F. F. *J. Chromatogr.*, Submitted for publication, **1995.**

81. Lochmuller, C. H.; Colborn, A. S.; Hunicutt, M. L. and Harris, J. *J. Amer. Chem. Soc.*, **1984**, 106, 4077.

82. Bevington, P. P. *Data Reduction and Error Analysis for the Physical Sciences*, McGraw-Hill, New York, **1969**, Chapter 11.

83. Giddings, J. C. *Anal. Chem.*, **1963**, 35, 1999.

84. van Deemter, J. J.; Zuiderwy, F. J. and Klinkenberg, A. *Chem. Eng. Sci.*, **1956**, 5, 271.

85. Groh, R. and Halasz, I. *Anal. Chem.*, **1981**, 53, 1325.

86. Muller, A. J. and Carr. P. W. *J. Chromatogr.*, **1984**, 284, 33.

87. Horvath, Cs. and Lin, H. J. Chromatogr., **1978**, 149, 43.

88. Hage, D. S.; Walters, R. R. and Hethcote, H. W. *Anal. Chem.*, **1986**, 58, 274.

89. Ruthven, D. M. *Principles of Adsorption and adsorption processes,* Wiley, Toronto, **1984**, Chapter 8.

90. Anderson, D. J. and Walters, R. R. *J. Chromatogr. Sci.*, **1984**, 22, 353.

91. Katz, E.; Ogan, K. L. and Scott, R.P.W. *J. Chromatogr.*, **1983**, 270, 51.

92. Stout, R. W.; DeStefano, J. J. and Snyder, L. R. *J. Chromatogr.*, **1983**, 282, 263.

93. Laidler, K. *J. Chemical Kinetics*, **1987**, Chapter 2.

94. Marshall, D. B.; Burns, J. W. and Connolly, D. E. *J. Chromatogr.*, **1986**, 360, 13.

95. Waite, S. W.; Marshall, D. B. and Harris, J. M. *Anal. Chem.*, **1994**, 66, 2052.

96. Ruthven, D. M. *Principles of Adsorption and Adsorption Processes*, Wiley, Toronto, **1984**, Chapter 5.

97. Van Vliet, B. M.; Weber, Jr. W. J. and Hozumi, H. *Water Research*, **1980**, 14,

1719.

98. Costa, C. and Rodrigues, A. *In Fundamettals of Adsorption*, Ed. by Muers, A. L. and Belforte, G. *Engineering Foundations*, **1983**, 163.

99. Reichenberg, D. *J. Am. Chem. Soc.*, **1953**, 75, 589.

100. Aguwa, A. A.; Patterson, J. w.; Haas, C. N. and Noll, K. E. J. *Water Pollut. Control Fed.*, **1984**, 56, 442.

101. Cornel, P.; Sontheimer, H.; Summers, R. S. and Roberts, P. V. *Chem. Eng. Sci.*, **1986**, 41, 1801.

102. Friedrich, M.; Seidel, A. and Gelbin, D. *AIChE.* J., **1985**, 31, 324.

103. Weber, W. J. and Liu, K. T. *Chem. Eng. Commun.*, **1980**, 6, 49.

104. Conder, J. R. J. *High Resolution Chromatogr. and Chromatogr. Communications*, **1982**, 5, 341.

105. Chen, J. C. and Weber, S. G. *Anal. Chem.*, **1983**, 55, 127.

106. Done, J. N. and Knox, J. H. *J. Chromatogr. Sci.*, **1972**, 10, 606.

107. Kennedy, G. J. and Knox, J. H. *J. Chromatogr. Sci.*, **1972**, 10, 549.

108. Huber, J. F. K. *J. Chromatogr. Sci.* **1969**, 7, 85.

109. Crombeen, J. P.; Poppe, H. and Kraak, J. C. *Chromatographia*, **1986**, 22, 319.

110. Snyder, L. R. and Kirkland, J. J. *Introduction to Modern Liquid Chromatography* Wiley,Toronto, **1979**, Chapter 19.

111. Conder, J. R. J. *High Resolution Chromatogr. and Chromatogr. Commun.*, **1982**, 5, 397.

112. Oberholtzer, J. E. and Rogers, L. B. *Anal. Chem.*, **1969**, 41, 1590.

113. Galin, M. and Guillet, J. E. *J. Polymer Sci.*, **1973**, 11, 233.

114. Courval, G. J. and Gray, D. G. *Macromolecules*, **1975**, 8, 916.

115. Sen Sarma, R. N.; Anders, E. and Miller, J. M. *J. Phy. Chem.*, **1959**, 63, 559.

116. Conder, J. R. *Anal. Chem.*, **1971**, 43, 367.

117. Giddings, J. C. and Erying, H. *J. Phys. Chem.*, **1955**, 59, 416.

118. Giddings, J. C. and Erying, H. J. *J. Chem. Phys.*, **1957**, 26, 169.

119. Yau, W. W. *Anal. Chem.*, **1977**, 49, 395.

120. Chesler, S. N. and Cram, S. P. *Anal. Chem.*, **1973**, 45, 1354.

121. Jonsson, J. A. *In Chromatography Theory and Basic Principles*, Marcel Dekker, Inc., New York, **1987**, Chapter 2.

122. McQuarrie, D. A. *J. Chem. Phys.*, **1963**, 38, 437.

123. Bidlingmeyer, B. A. and Warren, Jr. F. V. *Anal. Chem.* **1984**, 56, 1583A.

124. Kirkland, J. J.; Yau, W. W.; Stoklosa, H. J. and Dilks, C. H. *J. Chromatogr. Sci.*, **1977**, 15, 303.

125. Pauls, R. E. and Rogers, L. B. *Sep. Sci.*, **1977**, 12, 395.

126. Sternberg, J. C. *In advances in Chromatography*, Vol. 2, **1966**, Chapter 6.

127. Reilley, C. N.; Hildebrand, G. P. and Ashley, Jr. J. W. *Anal. Chem.*, **1962**, 34, 1198.

128. Karger, B. L. snyder, L. R. and Horvath, Cs. *An Introdection to Separation Science*, Wiley, Toronto, **1973**, Chapter, 3.

129. Foley, J. P. and Dorsey, J. G. *J. Chromatogr. Sci.*, **1984**, 22, 40.

130. Foley, J. P. and Dorsey, J. G. *Anal. Chem.*, **1983**, 55, 730.

131. Chesler, S. M. and Cram, S. P. *Anal. Chem.*, **1971**, 44, 2240.

132. Ohkuma, T. and Hara, S. *J. Chromatogr.*, **1987**, 400, 47.

133. Atwood, J. G. and Golay, M. *J Chromatogr.*, **1981**, 218, 97.

134. Cantwell, F.F. Chemistry 421 notes, **1992**.

135. Knox, J. H. *J. Chromatogr. Sci.*, **1977**, 15, 352.

136. Wilke, C. R. and Chang, P. *AIChE.* J, **1955**, 1, 264.

137. Crank, J. *Mathematics of Diffusion*, Oxford Unit Press, London **1957**, Chapter, 12.

138 Ruthven, D, M. and Garg, D. R. *Chem. Eng. Sci.*, **1972**, 27, 417.

139. Weber, J. W. and Liang, S. *Envir. Prog.*, **1983**, 2, 167.

140. Peel, R.G.; Benedek, A. and Crowe, C. *AIChE. J.*, **1981,** 27, 26.

141. Ruckenstein, E.; Vaidyanathan, A.S. and Youngquist, G.R. *Chem. Eng. Sci.*, **1971,** 26, 1305.

142. Mingle, J.O. and Smith, J. M. *AIChE. J.* **1961,** 7, 243.

143. Carberry, J. J. *AIChE. J.*, **1962,** 8, 557.

144. Wakao, N. and Smith, J. M. *Chem. Eng. Sci.*, **1962,** 17, 825.

145. Doong, S. J. and Yang, R. T. *AIChE. J.*, **1987**, 3.

146. Petersen, E. E. *AIChE. J.*, **1991**, 37, 671.

147. Bean, C. P. In "*Membranes*", Eisenman, G. Ed., Marcel Dekker, New York, **1972**, Vol. 1, Chapter 1.

148. Anderson, J. L. and Quinn, J. A. *Biophys.* J., **1974**, 14, 130.

149. Brenner, H. and Gaydos, L. J. *J. Colloid. Interf. Sci.*, **1977**, 58, 312.

150. Malone, D. M. and Anderson, J. L. *Chem. Eng. Sci.*, **1978**, 33, 1429.

151. Solomon, A. K. *J. Gen. Physiol.*, **1968**, 51, 335s.

152. Akers, G. K. *Advan. Protein Chem.*, **1970**, 24, 343.

153. Prieve, D. C. and Hoysan, P. M. *J. Colloid Interf. Sci.*, **1978**, 64, 201.

154. Craig, L. C. Science, **1964**, 144, 1093

155. Paine, P. L. and Scherr, P. *Biophys. J.*, **1975**, 15, 1087.

156. Deen, W. M. *AIChE J.*, **1987**, 33, 1409.

157. Renkin, E. M. *J. Gen. Physiol.*, **1954**, 38, 225.

158. Giddings, J. C.; Kucera, C. E.; Russell, C. P. and Myers, M. N. *J. Phys. Chem.* **1968**, 72, 4397.

159. Pappenheimer, J. R.; Renkin, E. M. and Borrero, L. M. *Am. J. Physiol.*, **1951**, 167, 13.

160. Haberman, N. L.; Sayre, R.M. *David W. Taylar Model Basin Rept. No. 1143, U.S.Dept. Navy,* Washington, DC, **1958.**

161. Wang, H. and Skalak, R. *J. Fluid Mech.*, **1969**, 38, 75.

162. Snyder, L. R. J. *Chromatogr. Sci.*, 1977, 15, 441

163. Edward, J. T. *J. Chem. Edu.*, **1970**, 47, 261.

164. Buchholz, H. and Kruchels, W. *Verfahrenstechnik*, **1976**, 10, 290.

165. Lin, B. C.; Golshan-Shirazi, S. and Guiochon, G. *J. Phys. Chem.*, **1989**, 93, 3363.

166. Golshan-Shirazi, S. Lin, B.C. and Guiochon, G. *J.Phys.Chem.*, **1989**, 93, 6871.

167. Clueckauf, E. and Coates, J. I. *J. Chem. Soc.*, 1947, 269, 1315.

168 Colton, C. N.; Satlerfield, C.N. and Lai, C. J. *AIChE. J.*, **1975**, 21, 289.

169. Mavrovouniotis, G. M. and Brenner, H. *J. Colloid Interf. Sci.*, **1988**, 124, 269.

170. Nicholson, J. W. *The Chem. of Polymers*, The Royal Soc. of Chem. **1991**, Chapter 5.

171. Hughes, L. J. and Britt, G. E. *J. Appl. Polymer Sci.* **1961**, 5, 3377.

APPENDIX 1

The program used in the tri-exponential fit to the sorption rate data. The program written in MatLab is called MultiExpFit. It was written by David Gowanlock.

```
clear
echo off
clc

Data = ...
[0 0
1 1
2 2];

DataLocation = menu('Where is the data located?','In the data section of this program','In
a seperate file, Data.dat');
if DataLocation==1
                    Xcolumn = input('Which column corresponds to the X values? ');
                    Ycolumn = input('Which column corresponds to the Y values? ');
elseif DataLocation==2
  clear Data;
                    load Data.dat
                    Xcolumn = input('Which column corresponds to the X values? ');
                    Ycolumn = input('Which column corresponds to the Y values? ');
end

global Data
global Xcolumn
global Ycolumn

t = Data(:,Xcolumn);
y = Data(:,Ycolumn);
plot(t,y,'o'),title('Input Data'),pause
```

```
newfit = 1;
while newfit==1
clear f tol
  EquType = menu('Choose a fit equation','Monoexponential','Biexponential',
'Triexponential','None of the above.  I want out.');

  if EquType==1
    fixlim = menu('Do you want to fix the limiting value?','Yes','No');
   if fixlim==1
   load tempmonolim;
      monolim = input(['old limit = ' num2str(monoexplim) '   new limit = ']);
     if ~isempty(monolim)
       monoexplim = monolim;
      end
      loop = 1;
      while loop==1
        Tri = menu('Choose one (must do Parameter Estimate before Initiate Curve
Fit)','Parameter Estimate','Initiate Curve Fit');
         if Tri==1
           [lam] = MonoexpEstLim(lam,monoexplim);
           save tempmonolim lam monoexplim;
         elseif Tri==2
           loop = 0;
                                                                [lam,f,tol] =
MonoexpFitlim(lam,monoexplim);
           save tempmonolim lam monoexplim;
          end                          %end of 'Tri' if
      end                                      %end of 'loop' while

   elseif fixlim==2
   load tempmono;
   loop = 1;
   while loop==1
     Mono = menu('Choose one (must do Parameter Estimate before Initiate Curve
Fit)','Parameter Estimate','Initiate Curve Fit');
```

```
       if Mono==1
         [lam] = MonoexpEst(lam);
         save tempmono lam;
       elseif Mono==2
         loop = 0;
                                                          [lam,f,tol] =
MonoexpFit(lam);
         save tempmono lam;
       end                          %end of 'Mono' if
     end                                 %end of 'loop' while
     end                          %end of 'fixlim' if

  elseif EquType==2
     fixlim = menu('Do you want to fix the limiting value?','Yes','No');
    if fixlim==1
    load tempbilim;
      bilim = input(['old limit = ' num2str(biexplim) '   new limit = ']);
      if ~isempty(bilim)
        biexplim = bilim;
      end
      loop = 1;
      while loop==1
        Tri = menu('Choose one (must do Parameter Estimate before Initiate Curve
Fit)','Parameter Estimate','Initiate Curve Fit');
        if Tri==1
          [lam] = BiexpEstLim(lam,biexplim);
          save tempbilim lam biexplim;
        elseif Tri==2
          loop = 0;
                                                          [lam,f,tol] =
BiexpFitlim(lam,biexplim);
          save tempbilim lam biexplim;
        end                         %end of 'Tri' if
      end                                        %end of 'loop' while

    elseif fixlim==2
```

```
   load tempbi;
   loop = 1;
   while loop==1
     Bi = menu('Choose one (must do Parameter Estimate before Initiate Curve
Fit)','Parameter Estimate','Initiate Curve Fit');
      if Bi==1
        [lam] = BiexpEst(lam);
        save tempbi lam;
      elseif Bi==2
        loop = 0;
                                                                        [lam,f,tol] =
BiexpFit(lam);
        save tempbi lam;
      end                          %end of 'Bi' if
   end                                %end of 'loop' while
   end                           %end of 'fixlim' if

  elseif EquType==3
    fixlim = menu('Do you want to fix the limiting value?','Yes','No');
   if fixlim==1
   load temptrilim;
     trilim = input(['old limit = ' num2str(triexplim) '   new limit = ']);
    if ~isempty(trilim)
      triexplim = trilim;
     end
     loop = 1;
     while loop==1
       Tri = menu('Choose one (must do Parameter Estimate before Initiate Curve
Fit)','Parameter Estimate','Initiate Curve Fit');
        if Tri==1
         [lam] = TriexpEstLim(lam,triexplim);
         save temptrilim lam triexplim;
        elseif Tri==2
          loop = 0;
                                                                          [lam,f,tol] =
TriexpFitlim(lam,triexplim);
```

```
            save temptrilim lam triexplim;
           end                              %end of 'Tri' if
         end                                          %end of 'loop' while

       elseif fixlim==2
       load temptri;
         loop = 1;
         while loop==1
           Tri = menu('Choose one (must do Parameter Estimate before Initiate Curve
Fit)','Parameter Estimate','Initiate Curve Fit');
            if Tri==1
              [lam] = TriexpEst(lam);
              save temptri lam;
            elseif Tri==2
              loop = 0;
                                                                          [lam,f,tol] =
TriexpFit(lam);
              save temptri lam;
            end                             %end of 'Tri' if
          end                                          %end of 'loop' while
        end                                %end of 'fixlim' if

    elseif EquType==4
      newfit = 0;
     LaterMan;
    end                                     %end of 'EquType' if
    if newfit==1
      fitplot = menu('Do You want to print a plot?','Yes','No');
      if fitplot==1
        lamlen = length(lam);
        LinFac = 1;
         graphtitle = input('Enter a graph title. ','s');
        if lamlen==1
          MonoLimPlot(lam,LinFac,graphtitle,monoexplim,f,tol);
        elseif lamlen==2
          LinFac = fzeromod('MonoexpLinFac',1,lam);
        MonoPlot(lam,LinFac,graphtitle,1,f,tol);
      elseif lamlen==3
        BiLimPlot(lam,LinFac,graphtitle,biexplim,f,tol);
      elseif lamlen==4
        LinFac = fzeromod('BiexpLinFac',1,lam);
        BiPlot(lam,LinFac,graphtitle,1,f,tol);
      elseif lamlen==5
        TriLimPlot(lam,LinFac,graphtitle,triexplim,f,tol);
      elseif lamlen==6
        LinFac = fzeromod('TriexpLinFac',1,lam);
        TriPlot(lam,LinFac,graphtitle,1,f,tol);
      end                        %end of 'lamlen' if
      prtsc
    elseif fitplot==2

    end                          %end of 'fitplot' if
  end                            %end of 'newfit' if
end
                                                                  %end of
'newfit' while
```

TriexpEstLim

```
function[lam] = TriexpEst(lam)
%
n1 = input(['old n1 = ' num2str(lam(1)) '   new n1 = ']);
if ~isempty(n1)
  lam(1) = n1;
end

n2 = input(['old n2 = ' num2str(lam(2)) '   new n2 = ']);
if ~isempty(n2)
  lam(2) = n2;
end

n3 = input(['old n3 = ' num2str(lam(3)) '   new n3 = ']);
if ~isempty(n3)
  lam(3) = n3;
end
```

```
k1 = input(['old k1 = ' num2str(lam(4)) '   new k1 = ']);
if ~isempty(k1)
  lam(4) = k1;
end

k2 = input(['old k2 = ' num2str(lam(5)) '   new k2 = ']);
if ~isempty(k2)
  lam(5) = k2;
end

k3 = input(['old k3 = ' num2str(lam(6)) '   new k3 = ']);
if ~isempty(k3)
  lam(6) = k3;
end


t = Data(:,Xcolumn);
y = Data(:,Ycolumn);

t1 = 0:.5:max(t);
y1 = (lam(1) + lam(2) + lam(3)) - (lam(1) .* exp(-1 .* lam(4) .* t1))...
 - (lam(2) .* exp(-1 .* lam(5) .* t1)) - (lam(3) .* exp(-1 .* lam(6) .* t1));
plot(t1,y1,t,y,'o')
```

TriexpFitlam

```
function[lam,f,tol] = TriexpFit(lam)
%
tol = input('enter tolerance (0.1 default) ');
if isempty(tol)
  tol = 0.1;
end

[lam,f] = fmins('triexponential',lam,tol);
```

TriexpFit

```
function[lam,f,tol] = TriexpFit(lam)
%
tol = input('enter tolerance (0.1 default) ');
if isempty(tol)
  tol = 0.1;
end

[lam,f] = fmins('triexponential',lam,tol);
```

TriLimPlot

```
function TriLimPlot(lam,li,graphtitle,n0,f,tol)
t = Data(:,Xcolumn);
y = Data(:,Ycolumn);
```

```
t1 = 0:.25:max(t);
y1 = li .* ((n0) - (lam(1) .* exp(-1 .* lam(3) .* t1))...
- (lam(2) .* exp(-1 .* lam(4) .* t1)) - ((n0-lam(1)-lam(2))...
 .* exp(-1 .* lam(5) .* t1)));

plot(t1,y1,t,y,'o')
xt = max(t)/2;
yt = max(y)/2;
n0 = li * n0;
n1 = li * lam(1);
n2 = li * lam(2);
n3 = li * (n0-lam(1)-lam(2));
k1 = lam(3);
k2 = lam(4);
k3 = lam(5);
```

TriPlot

```
function TriPlot(lam,li,graphtitle,n0,f,tol)
t = Data(:,Xcolumn);
y = Data(:,Ycolumn);

t1 = 0:.25:max(t);
y1 = li .* ((lam(1) + lam(2) + lam(3)) - (lam(1) .* exp(-1 .* lam(4) .* t1))...
- (lam(2) .* exp(-1 .* lam(5) .* t1)) - (lam(3) .* exp(-1 .* lam(6) .* t1)));

plot(t1,y1,t,y,'o')
xt = max(t)/2;
yt = max(y)/2;
n0 = li * (lam(1) + lam(2) + lam(3));
n1 = li * lam(1);
n2 = li * lam(2);
n3 = li * lam(3);
k1 = lam(4);
k2 = lam(5);
k3 = lam(6);
```

Fzeromod

```
function [b,lam] = fzeromod(FunFcn,x,lam,tol,trace)
%FZEROZero of a function of one variable.
%	FZERO(F,X) finds a zero of f(x).  F is a string containing the
%	name of a real-valued function of a single real variable.  X is
%	a starting guess.  The value returned is near a point where F
%	changes sign.  For example, FZERO('sin',3) is pi.  Note the
%	quotes around sin.  Ordinarily, functions are defined in M-files.
%
```

```
%       name of a real-valued function of a single real variable.  X is
%       a starting guess.  The value returned is near a point where F
%       changes sign.  For example, FZERO('sin',3) is pi.  Note the
%       quotes around sin.  Ordinarily, functions are defined in M-files.
%
%       An optional third argument sets the relative tolerance for the
%       convergence test.  The presence of an nonzero optional fourth
%       argument triggers a printing trace of the steps.

%       C.B. Moler 1-19-86
%       Revised CBM 3-25-87, LS 12-01-88.
%       Copyright (c) 1986-88 by the MathWorks, Inc.

% This algorithm was originated by T. Dekker.  An Algol 60 version,
% with some improvements, is given by Richard Brent in "Algorithms for
% Minimization Without Derivatives", Prentice-Hall, 1973.  A Fortran
% version is in Forsythe, Malcolm and Moler, "Computer Methods
% for Mathematical Computations", Prentice-Hall, 1976.

% Initialization

if nargin < 4, trace = 0; tol = eps; end
if nargin == 4, trace = 0; end
if trace, clc, end
if x ~= 0, dx = x/20;
else, dx = 1/20;
end
a = x - dx;  fa = feval(FunFcn,a,lam);
if trace, home, init = [a fa], end
b = x + dx;  fb = feval(FunFcn,b,lam);
if trace, home, init = [b fb], end

% Find change of sign.

while (fa > 0) == (fb > 0)
  dx = 2*dx;
  a = x - dx;  fa = feval(FunFcn,a,lam);
  if trace, home, sign = [a fa], end
  if (fa > 0) ~= (fb > 0), break, end
  b = x + dx;  fb = feval(FunFcn,b,lam);
  if trace, home, sign = [b fb], end
end

fc = fb;
% Main loop, exit from middle of the loop
while fb ~= 0
  % Insure that b is the best result so far, a is the previous
  % value of b, and c is on the opposite of the zero from b.
  if (fb > 0) == (fc > 0)
    c = a;  fc = fa;
    d = b - a;  e = d;
  end
  if abs(fc) < abs(fb)
    a = b;    b = c;    c = a;
    fa = fb;  fb = fc;  fc = fa;
  end

  % Convergence test and possible exit
  m = 0.5*(c - b);
  toler = 2.0*tol*max(abs(b),1.0);
  if (abs(m) <= toler) + (fb == 0.0), break, end

  % Choose bisection or interpolation
  if (abs(e) < toler) + (abs(fa) <= abs(fb))
  % Bisection
    d = m;  e = m;
  else
  % Interpolation
    s = fb/fa;
    if (a == c)
    % Linear interpolation
      p = 2.0*m*s;
```

```
        q = 1.0 - s;
      else
      % Inverse quadratic interpolation
        q = fa/fc;
        r = fb/fc;
        p = s*(2.0*m*q*(q - r) - (b - a)*(r - 1.0));
        q = (q - 1.0)*(r - 1.0)*(s - 1.0);
      end;
      if p > 0, q = -q; else p = -p; end;
      % Is interpolated point acceptable
      if (2.0*p < 3.0*m*q - abs(toler*q)) * (p < abs(0.5*e*q))
        e = d;  d = p/q;
      else
        d = m;  e = m;
      end;
    end % Interpolation

    % Next point
    a = b;
    fa = fb;
    if abs(d) > toler, b = b + d;
    else if b > c, b = b - toler;
        else b = b + toler;
        end
    end
    fb = feval(FunFcn,b,lam);
    if trace, home, step = [b fb], end
  end % Main loop
```

APPENDIX 2

The program shown in Appendix 2 is used in the calculation of the predicted peaks. The program written in MatLab is called Elution in which the three sites July 94 version is used. The program was written by David Gowanlock.

```
clc
clear
% ELEUTION CHROMATOGRAM FROM KINETIC CURVE
% David Gowanlock  May 31, 1991
% Modified        July 94        (attenuation of k')
%
% The folowing is written to predict eleution chromatogram profiles
% from shallow bed kinetic plots.  In this case the shallow bed kinetic
% plots have been fit to a triexponential of the following form:
%
% n_observed = n0 - (n1 * exp(-k1 * t)) - (n2 * exp(-k2 * t))
%               - (n3 * exp(-k3 * t))
%
%                        1 = fast sites
%                        2 = intermediate sites
%                        3 = slow sites
%
% The equation used to produce the eleution profiles corresponding
% to each of the above type of sites is given in the following reference
% (see function probdist):
%
%   equation (1), page 1999
%   J. C. Giddings, Anal. Chem., Vol. 35, Page 1999, Dec. 1963
%
% Variable List
%   k_prime = k'
%   k = rate constant from kinetic curve
%   n = fraction of a particular type of site
%   ord = order of bessel function
%   ts = t - tm
%   tm = time for mobile phase
%   t = time from injection
%   ka = adsorption rate constant
%   kd = desorption rate constant
%   Pts = probability distribution with respect to time
%   nanalrt = used to detect NaN warnings that can arise in the
%           calculation of bessel values in the function probdist
%                                       stepsz = stepsize along the time axis
%   fr_no_sl = fraction not interacting with the slow sites
%           (fraction not slow)
%   fr_sl = fraction interacting with the slow sites
%         (fraction slow)
%   theor_ratio = theoretical ratio of solute iteracting with slow sites to
%               solute not interacting with slow sites
%   act_ratio = theoretical ratio of solute iteracting with slow sites to
%               solute not interacting with slow sites
%   maxsz = maximum value of range of ts1 and ts2 values
%

%-----------------------------------------------------------------
%  This section is where the inital parameters used throughout the rest
%  of the program are entered.
%
stepsz = 20;
maxsz = 8001
k_prime = 28.48
k1 =19.41
k2 =2.713
k3 =0.148
n1 =0.2224
n2 =0.688
n3 =0.089
tm =37.94
```

```
n0 = n1 + n2 + n3

%-----------------------------------------------------------------
% The following calculates the elution profile for the fast sites.
%
ord1 = 1;
ts1 = 1:stepsz:maxsz;
k_prime1 = k_prime .* n1 ./ n0
ka1 = k1 ./ (1 + (k_prime1 .^ (-1)))
kd1 = k1 ./ (k_prime1 + 1)
tm1 = tm

[Pts1,nanalrt1] = probdistrib(ts1,ka1,kd1,tm1,ord1);

%-----------------------------------------------------------------
% The following calculates the eleution profile for the intermediate sites.
%
ord2 = 1;
ts2 = 1:stepsz:maxsz;
k_prime2 = k_prime .* n2 ./ n0
ka2 = k2 ./ (1 + (k_prime2 .^ (-1)))
kd2 = k2 ./ (k_prime2 + 1)
tm2 = tm

[Pts2,nanalrt2] = probdistrib(ts2,ka2,kd2,tm2,ord2);

%-----------------------------------------------------------------
% The following calculates the elution profile for the slow sites
%
ord3 = 1;
ts3 = 1:stepsz:2.*maxsz;
k_prime3 = k_prime .* n3 ./ n0
ka3 = k3 ./ (1 + (k_prime3 .^ (-1)))
kd3 = k3 ./ (k_prime3 + 1)
tm3 = tm
```

```
[Pts3,nanalrt3] = probdistrib(ts3,ka3,kd3,tm3,ord3);

%----------------------------------------------------------------
% The following convolves the elution profiles and plots the results
% along with the elution profiles for each type of sight acting alone.
%
Pts1_2 = conv(Pts1,Pts2);
ts1_2 = 1:stepsz:2.*(maxsz-.5);
Pts1_2_3 = conv(Pts1_2,Pts3);
ts1_2_3 = 1:stepsz:4.*(maxsz-.5);
ymax = max([max(Pts1),max(Pts2),max(Pts3)])
P1s = 1.0 .* Pts1 .* ymax ./ max(Pts1);
P2s = .7 .* Pts2 .* ymax ./ max(Pts2);
P3s = .3 .* Pts3 .* ymax ./ max(Pts3);
P1_2s = .5 .* Pts1_2 .* ymax ./ max(Pts1_2);
P1_2_3s = .4 .* Pts1_2_3 .* ymax ./ max(Pts1_2_3);
axis([0,0.2.*maxsz,0,1.05.*ymax])
plot(ts1,P1s,ts2,P2s,ts3,P3s,ts1_2,P1_2s,ts1_2_3,P1_2_3s)
%plot(ts1,P1s,ts2,P2s,ts3,P3s)
%xlabel('ts'), ylabel('P(ts)')
%-------------------------------------------------------
%t3= ts3 + tm;
%axis;
%plot(t3,P3s)
%xlabel('t'), ylabel('P(t)')
%x = t3';
%y = P3s';
%z = [x y];
%save plot.dat z /ascii;
%pause

%----------------------------------------------------------------
% Integration of the peaks
%
area1_2 = integrate_2pt(ts1_2,Pts1_2)
area1_2_3 = integrate_2pt(ts1_2_3,Pts1_2_3)
```

```
%area1 = integrate_2pt(ts1,Pts1)
%area2 = integrate_2pt(ts2,Pts2)
%area3 = integrate_2pt(ts3,Pts3)

%-----------------------------------------------------------------
% This section scales the convolution of 1 & 2 with the convolution of 1, 2, & 3
%
fr_no_sl = exp(-1 .* ka3 .* tm3);
fr_sl = 1.0 - fr_no_sl;
theor_ratio = fr_sl ./ fr_no_sl;
act_ratio = area1_2_3 ./ area1_2;
correction = theor_ratio ./ act_ratio;
Pts1_2_3 = Pts1_2_3 .* correction;
area1_2_3 = integrate_2pt(ts1_2_3,Pts1_2_3)
axis;
plot(ts1_2,Pts1_2,ts1_2_3,Pts1_2_3)
xlabel('ts'), ylabel('P(ts)')
pause

%-----------------------------------------------------------------
%  This section addes the convolution of 1 & 2  to the convolution of 1, 2, & 3
%
for l= 1:length(Pts1_2);
Ptsnet(l) = Pts1_2(l) + Pts1_2_3(l);
end
axis([0,max(ts1_2),0,1.05.*max(Ptsnet)])
plot(ts1_2,Pts1_2,ts1_2_3,Pts1_2_3,ts1_2,Ptsnet)
xlabel('ts'), ylabel('P(ts)')
pause

%-----------------------------------------------------------------
%  This section plots the elution profile from time of injection, not ts
%   (ts = t - tm)
%
t1_2 = ts1_2 + tm;
axis;
```

```
plot(t1_2,Ptsnet)
xlabel('t'), ylabel('P(t)')
x = t1_2';
y = Ptsnet';
z = [x y];
save plot.dat z /ascii;


%--------------------------------------------------------------------
% This section normalizes the plots
% (t/tr) & (area = 1)
%
%pause
%[m0,m1,m2,m3] = moments(t1_2,Ptsnet);
%tnorm = t1_2./m1;
%[m0,m1,m2,m3] = moments(tnorm,Ptsnet);
%PtsScaled = Ptsnet ./ m0;
%[m0,m1,m2,m3] = moments(tnorm,PtsScaled)
%plot(tnorm,PtsScaled)
%xlabel('t/tr'), ylabel('P(t)')
```

APPENDIX 3

The program shown bellow is used in the EMG curve fit from which the moments are calculated from the EMG function. The program written in MatLab is called Expgaus & Moments. It was written by David Gowanlock.

```
echo off
clc
clear

Data = ...
[    ];

numberofpoints = 60;

%pause           % Strike any key for plot.
t = Data(:,1);
y = Data(:,2);
[Ymax,indexYmax] = max(y);
[Ymin1,indexYmin1] = min(y(1:indexYmax));
[Ymin2,index] = min(y(indexYmax:length(y)));
indexYmin2 = index + indexYmax - 1;

[M0,M1,M2,M3] = moments(t,y);

retenttime_exp = (M3 ./ 2) .^ 0.3333
retenttime_gaus = M1 - retenttime_exp
variance_exp = retenttime_exp .^ 2
variance_gaus = M2 - variance_exp

fit_indecies = linspace(1,length(y),numberofpoints);
round(fit_indecies);
global FitData_t
```

```
FitData_t = t(fit_indecies);
global FitData_y
FitData_y = y(fit_indecies) ./ M0; % area of dist. normalized to unit area
axis;
plot(t,y./ MO, FitData_t,FitData_y,'o');

lam = [retenttime_gaus retenttime_exp (variance_gaus .^ 0.5)]';
lam = fmins('fitmy',lam,.1)

FitData_y = y(fit_indecies);

global lam_global
lam_global = lam;


lin_scaling_factor = fzero('exp_fit_diff',M0)

mintime = min(t);
maxtime = max(t);
miny = 0.0;
maxy = max(y);

t_curvefit = mintime:1:maxtime;

y_curvefit = lin_scaling_factor .* (exp(lam(3).^2 ./ (2 .* lam(2).^2)) .* ...
exp((lam(1) - t_curvefit) ./ lam(2)) ./ (2 .* lam(2)) .* ...
(1 + erf((t_curvefit-lam(1)-lam(3).^2 ./ lam(2)) ./( sqrt(2) .* lam(3)))));

axis([mintime maxtime miny (maxy .* 1.08)]);
plot(t,y,'--',FitData_t,FitData_y,'o',t_curvefit,y_curvefit);
%plot(t,y,'--',FitData_t,FitData_y,'o');

x =t_curvefit';
y =y_curvefit';
z = [x y];
save plot.dat z /ascii;
```

```
xlabel('Time (sec)');
ylabel('Signals');
text(.65,.8,'numeric','sc')
text(.8,.8,'fit','sc')
text(.5,.7,'gaus tr','sc')
text(.5,.65,'gs sd.dv.','sc')
text(.5,.6,'exp tr','sc')
text(.65,.7,num2str(retenttime_gaus),'sc')
text(.65,.65,num2str(variance_gaus .^ 0.5),'sc')
text(.65,.6,num2str(retenttime_exp),'sc')
text(.8,.7,num2str(lam(1)),'sc')
text(.8,.65,num2str(lam(3)),'sc')
text(.8,.6,num2str(lam(2)),'sc')
text(.75,.5,num2str(lin_scaling_factor),'sc')
text(.55,.5,'linear scaling','sc')
```

APPENDIX 4

The program shown bellow is used to fit the sorption rate of naphthalene on PRP-1 to the Ruckenstein model. The program written in BASIC is called RATELAWLI2. The program is from Dr. Jordan's group.

```
10 REM NON LINEAR LEAST SQUARES PROGRAM FOR SINGLE EXPONENTIAL
20 OPTION BASE 0
590 DEFINT I,J,K,L,M,N,C,R
600 DEFSNG X,Y,F,B,V,P
610 DEFDBL T,S,D,G
620 DIM B(10),Y(100),X(3,100),G(10),P(10),S(10),B1(10),B2(10),B8(10),D(20,10)

730 K0=4:REM PRINT"ENTER NUMBER OF PARAMETERS"

731  INPUT "ENTER PARAM. 1 GAMA = ";B(1)
732  INPUT "ENTER PARAM. 2 BATA = ";B(2)
733  INPUT "ENTER PARAM. 3 ALPHA = ";B(3)
732  INPUT "ENTER PARAM.  4 M∞ = ";B(4)

734  REM INPUT "ENTER PARAM. 1 DIFFUSION COEF = ";B(1)
735 REM INPUT "ENTER PARAM. 2 CONSTANT = ";B(3)
736  REM INPUT "ENTER PARAM. 3 M∞ = ";B(2)


740 IF K0>10 THEN PRINT"10 PARAMETERS MAXIMUM":GOTO 730
750 PRINT"ENTER NUMBER OF FIXED PARAMETERS";:INPUT I0
760 IF I0<0 THEN PRINT"MUST BE GREATER THAN ZERO":GOTO 750
762 IF I0>10 THEN PRINT"MUST BE LESS THAN 10":GOTO 750
820 IF I0=0 THEN GOTO 850
822 FOR I=1 TO I0
824 PRINT"ENTER PARAMETER INDEX";:INPUT I2(I)
828 NEXT I
```

```
850 R$="N":I4=15:S$="N":A$="N"
855 REM GOTO 930
860 PRINT "DO YOU WANT DETAILED PRINTING?  Y/N ";:INPUT R$
890 PRINT"MAXIMUM NUMBER OF ITERATIONS ?";:INPUT I4
900 PRINT " POSITIVE VALUES ONLY ? Y/N ";:INPUT S$
930 INPUT"RELATIVE RESIDUALS ?  Y/N  ";E$:GOTO 1077
940 INPUT"USING ANALYTICAL DERIVATIVES ? Y/N ";A$
1070 FOR I=1 TO K0
1072 PRINT"VALUE OF PARAMETER";I;"?";:INPUT B(I)
1076 NEXT I
1077 INPUT"ENTER NUMBER OF DATA SETS=";DATSET
1078 FOR SET=1 TO DATSET
1079 READ T$,N0,M0
1080 FOR I=1 TO N0
1084 READ Y(I)
1090 FOR J=1 TO M0
1100 READ X(J,I)
1110 NEXT J

1120 NEXT I


1250 REM SECTION 1B-DISPLAY INPUT DATA *******
1260 PRINT"INPUT DATA":PRINT
1280 PRINT"TITLE:  ";T$: PRINT
1290 PRINT"No. OF DATA POINTS: ";N0;"No. OF PARAMETERS ";K0
1300 PRINT"No. OF FIXED PARAMETERS:  ";I0;"    No. OF INDEPENDENT
VARIABLES: ";M0
1310 IF I0>0 THEN PRINT"INDICES OF FIXED PARAMETERS: " ELSE GOTO 1340
1320 FOR I=1 TO I0:PRINT I2(I);:NEXT I:PRINT:PRINT
1340 IF R$="Y" THEN PRINT"DETAILED PRINTING" ELSE PRINT "BRIEF
PRINTING"
1360 PRINT"MAXIMUM ITERATIONS:  ";I4
1400 PRINT
1420 PRINT"INITIAL PARAMETERS":FOR I=1 TO K0:PRINT B(I);:NEXT I:PRINT
```

```
1430 LPRINT "DATA POINTS": PRINT "   I              T                  Y  "
1440 FOR I=1 TO N0
1450  PRINT USING " ##.###^^^^ "; I, X(1,I),Y(I)
1470 NEXT I
1480 I3=0
1490 GOTO 1500
1500 REM SECTION 2 CALCULATION OF PTP MATRIX
1515 I3=I3+1
1520 FOR I=1 TO K0:G(I)=0:FOR J=1 TO K0:D(I,J)=0
1524 NEXT J: NEXT I
1530 PRINT:PRINT"ITERATION NUMBER =";I3


1540 IF R$="Y" THEN PRINT:PRINT"Y(OBS)    Y(CALC)    DIFF"

1550 P=0
1560 FOR I=1 TO N0
1570 GOSUB 2090
1572 IF E$="Y" THEN FOR J=1 TO K0:P(J)=P(J)/Y(I):NEXT J:F=F/Y(I)
1574 P=P+F*F
1580 FOR J=1 TO K0:G(J)=G(J)+F*P(J)
1590 FOR K=J TO K0:D(J,K)=D(J,K)+P(J)*P(K):NEXT K:NEXT J:NEXT I



1600 P=P/(N0-K0+I0)
1604 PRINT "VARIANCE = ";P
1610 FOR J=1 TO K0:FOR K=J+1 TO K0:D(K,J)=D(J,K):NEXT K:NEXT J
1611 REM  ADDITION FOR FIXED PARAMETER ************
1612 FOR I=1 TO I0:G(I2(I))=0:FOR J=1 TO K0:D(I2(I),J)=0:D(J,I2(I))=0:NEXT J
1614 D(I2(I),I2(I))=1:NEXT I
1620 REM GET INVERSE OF D MATRIX AND SOLVE DB*****
1640 GOSUB 1810
1650 PRINT:PRINT"PARAMETER   VALUE        CORRECTION        NEW VALUE
STD DEV"
1660 FOR I=1 TO K0
```

```
1670 B0=0
1680 FOR J=1 TO K0:B0=B0+D(I,J)*G(J):NEXT J
1690 B1(I)=B0:NEXT I
1700 D$="Y"
1710 FOR J=1 TO K0
1720 B0=B(J):B(J)=B(J)+B1(J)
1722 REM POSITIVE PARAMETER RESTRICTION **********
1724 IF S$="Y" AND B(J)<0 THEN B(J)=0
1726 IF D(J,J)=1 THEN S0=0 ELSE S0=SQR(D(J,J)*P)
1730 IF (ABS(B1(J))>.5*S0) OR ABS(B1(J))>.001*ABS(B(J)) THEN D$="N"
1740 IF S$="Y" THEN B(J)=ABS(B(J))
1750 PRINT "B(";J;")       ";:PRINT USING "##.####^^^^      ";B0,B1(J),B(J),S0
1752 NEXT J
1754 IF D$="N" AND I3<I4 THEN 1500
1756 IF D$="Y" THEN LPRINT"CONVERGENCE IN ";I3;"ITERATIONS":ELSE
LPRINT"NO CONVERGENCE AFTER";I3;"ITERATIONS"
1758 LPRINT: LPRINT " TITLE : ";T$:LPRINT
1760 LPRINT:FOR N=1 TO K0 :LPRINT "  B(";N;")= ";B(N);:NEXT N:LPRINT
1762 LPRINT
1791 LPRINT"   [X]        Yobs          Ycalc            DIFF":LPRINT
1792 FOR I=1 TO N0
1794 GOSUB 2090
1796 LPRINT USING "##.###^^^^      "; X(1,I),Y(I),F1,F
1797 NEXT I
1798 LPRINT:LPRINT"STD ERROR=";SQR(P);:IF E$="Y" THEN LPRINT"
RELATIVE RESIDUALS" ELSE LPRINT "    ABSOLUTE RESIDUALS";:
1799 IF A$="Y" THEN LPRINT "  ANAL. DERIVATIVES" ELSE LPRINT "    EST.
DERIVATIVES"
1800 GOTO 2500
1810 REM MATRIX INVERTER*******
1820 FOR I1=1 TO K0
1830 R1=I1:C1=I1:Z=ABS(D(I1,I1))
1840 FOR J=I1 TO K0
1850 FOR K=I1 TO K0
1860 B1=ABS(D(J,K))
1870 IF B1>Z THEN Z=B1:R1=K:C1=J
```

```
1880 NEXT K: NEXT J
1890 C9(I1)=C1:R(I1)=R1
1900 IF C1<>I1 THEN FOR J=1 TO K0:T=D(I1,J):D(I1,J)=D(C1,J):D(C1,J)=T:NEXT J
1910 IF R1<>I1 THEN FOR J=1 TO K0:T=D(J,I1):D(J,I1)=D(J,R1):D(J,R1)=T:NEXT J
1920 T=1/D(I1,I1)
1930 FOR J=1 TO K0:D(I1,J)=T*D(I1,J):NEXT J
1940 D(I1,I1)=T
1950 FOR J=1 TO K0
1960 IF J=I1 THEN 1990
1970 T=D(J,I1):D(J,I1)=0
1980 FOR K=1 TO K0:D(J,K)=D(J,K)-T*D(I1,K):NEXT K
1990 NEXT J
2000 NEXT I1
2010 FOR I1=1 TO K0-1
2020 I2=K0-I1
2030 C1=C9(I2)
2040 IF C1<>I2 THEN FOR J=1 TO K0:T=D(J,C1):D(J,C1)=D(J,I2):D(J,I2)=T:NEXT J
2050 R1=R(I2)
2060 IF R1<>I2 THEN FOR J=1 TO K0:T=D(R1,J):D(R1,J)=D(I2,J):D(I2,J)=T:NEXT J
2070 NEXT I1
2080 RETURN
2090 REM COMBINATION OF FINDF, ANALP, AND ESTP SUBROUTINES
2100 GOSUB 2400
2102 F1=F:IF A$="Y" THEN GOTO 2140
2104 FOR J=1 TO K0:B(J)=1.05*B(J):GOSUB 2400:F2=F:B(J)=.95*B(J)/1.05:GOSUB
2400:B(J)=B(J)/.95
:P(J)=(F2-F)/(.1*B(J)):NEXT J
2110 GOTO 2180
2140 REM ENTER ANALYTICAL DERIVATIVES IN 2150 TO 2170**********
2150 P(1)=1
2152 P(2)=-EXP(-B(3)*X(1,I))
2154 P(3)=-B(2)*X(1,I)*P(2)
2180 F=Y(I)-F1
2200 IF R$="Y" THEN PRINT USING"#.###^^^^  ";X(1,I),X(2,I),X(3,I),Y(I),F1,F
2230 RETURN
2400 REM FUNCTION DEFINED IN STATEMENTS 2420 TO 2440
```

```
2415 PI=3.14156:  FA=1:FB=1:NN=50 :BB=.001: RR =.0005
2420 FOR LL=1 TO NN
2430   FA=FA-6/PI^2/(LL^2)*EXP(-LL^2*PI^2*B(1)*X(1,I))
2435  FB=FB-6/PI^2/(LL^2)*EXP(-LL^2*PI^2*B(3)*X(1,I))
2440   NEXT LL
2445   FD=(FA+1/3*B(2)*FB)/(1+1/3*B(2))
2450  REM FA=FA-6/PI^2/LL^2*EXP(-PI^2*LL^2*B(1)*X(1,I)/0.000324)
2455  REM NEXT LL
2455  REM FA=FA+B(2)
2460 REM F=FA*B(3)
2465  F=FD*B(4)
2470 REM F=FD


2480 RETURN
2500 REM  ERROR ANALYSIS RESULTS**********
2730 PRINT:PRINT"CORRELATION MATRIX":PRINT
2740 FOR I=1 TO K0:FOR J=1 TO K0:LPRINT USING"   #.###
";D(I,J)/SQR(D(I,I)*D(J,J));:NEXT J:LPRINT:NEXT I
2750 PRINT:PRINT:PRINT"CONFIDENCE LIMITS COMPUTED USING T =";
2770 REM GET T VALUE FROM SUBROUTINE 4000*********
2790 N1=1:N2=N0-K0+I0:GOSUB 4000:T=SQR(F9):LPRINT USING "  #.##
";T;:LPRINT "AND F =";
2800 N1=K0-I0:GOSUB 4000:LPRINT USING "  #.##  ";F9:LPRINT
2801 LPRINT "NO   PARAMETER     STANDARD     LINEAR     NON-LINEAR"
2802 LPRINT "      VALUE        DEVIATION    ERROR        ERROR"
2810 FOR J=1 TO K0
2820 IF D(J,J)=1 THEN S0=0:ELSE S0=SQR(P*D(J,J))
2830 IF S0=0 THEN LPRINT USING "##";J;:LPRINT USING "
##.####^^^^";B(J);:LPRINT "     PARAMETER NOT VARIED" ELSE LPRINT USING
"##";J;:LPRINT USING "    ##.####^^^^";B(J),S0,S0*T,S0*SQR(F9*(K0-I0))
2840 NEXT J
2844 NEXT SET
2850 END
```

```
2920 RESTORE
4000 REM TO EVALUATE CONFIDENCE LIMIT PARAMETERS ************
4010 REM  F(N1,N2) FOR 95 % CONFIDENCE LIMITS  AS F9
4040 IF 2*INT(N1/2)=N1 OR 2*INT(N2/2)=N2 THEN GOTO 4070
4050 IF N2>N1 THEN  IN1=N1:IN2=N2-1 ELSE IN1=N1-1:IN2=N2
4060 GOTO 4080
4070 IN1=N1:IN2=N2
4080 IF 2*INT(N1/2)=N1 THEN Y1=0:N3=IN1-2 ELSE Y1=1:N3=IN2-2
4090 N4=N3/2
4100 F1=3:F5=F1:GOSUB 4170:X1=Q9
4110 F2=5:F5=F2:GOSUB 4170:X2=Q9
4120 F5=(F2-F1)*(.05-X1)/(X2-X1)+F1
4130 IF F5<0 THEN F5=0
4140 GOSUB 4170
4150 IF ABS(Q9-X1)>ABS(Q9-X2) THEN X1=Q9:F1=F5 ELSE X2=Q9:F2=F5
4160 IF ABS(Q9-.05)>.0005 THEN 4120 ELSE F9=F5:RETURN
4170 REM EVALUATE Q(F,N1,N2) USING ABRAMOWITZ & STEGUIN FORMULA
***
4200 N8=IN2+IN1-4
4210 N7=N3:Q9=1
4220 X8=IN2/(IN2+IN1*F5)
4230 IF 2*INT(N1/2)=N1 THEN X4=1-X8:Y2=SQR(X8)^IN2 ELSE X4=X8:Y2=-
SQR(1-X8)^IN1
4240 FOR I=1 TO N4
4250 Q9=1+Q9*X4*N8/N7
4260 N8=N8-2:N7=N7-2
4270 NEXT I
4280 Q9=Y1+Y2*Q9
4290 RETURN
```